

Electric and Magnetic Coupling Phenomena at Oxide Interfaces

Von der Fakultät für Physik und Geowissenschaften
der Universität Leipzig
genehmigte

DISSERTATION

zur Erlangung des akademischen Grades

doctor rerum naturalium
Dr. rer. nat.

vorgelegt

von M. Sc. Francis Bern

geboren am 11.09.1984 in Filderstadt

Gutachter: Prof. Dr. Michael Ziese
Prof. Dr. Lambert Alff

Tag der Verleihung 25. Mai 2018

Bibliographische Beschreibung

Bern, Francis:

*Electric and Magnetic Coupling Phenomena
at Oxide Interfaces*

Universität Leipzig, Dissertation

140+xii S., 376 Lit., 42 Abb., 1 Anhang

Bibliographische Beschreibung:

Bern, Francis

Electric and Magnetic Coupling Phenomena at Oxide Interfaces

Universität Leipzig, Dissertation

140+xii S., 376 Lit., 42 Abb., 1 Anhang

Referat:

Perovskit-Oxide weisen eine große Bandbreite an physikalischen Eigenschaften bei gleichzeitig hoher struktureller Qualität in kleinsten Dimensionen auf. Die dramatischen Veränderungen ihrer Eigenschaften bei nur geringer Variation der stöchiometrischen Zusammensetzung sind sowohl für ein tieferes physikalisches Verständnis als auch für mögliche Anwendungsperspektiven interessant.

In der vorliegenden Arbeit wurde der Einfluss von Ladungsübertragung an Grenzflächen, Anisotropiemodifikation durch Verspannung und Oberflächeneffekte sowie magnetische und strukturelle Kopplung untersucht. Aufgrund ihrer kontrastierenden Eigenschaften im Hinblick auf Ferromagnetismus und Ladungstransport wurden dotiertes Lanthanmanganat und Strontiumruthenat (SRO) für die Untersuchungen ausgewählt. Durch ihre hervorragenden Wachstumseigenschaften mit fehlerlosen Grenzflächen auf atomarer Ebene erlauben sie als Modellsystem die Untersuchung elektronischer, magnetischer und struktureller Kopplung in Perovskit-Oxiden – mit folgenden Ergebnissen:

Durch Ladungsübertragung an Grenzflächen wird Ferromagnetismus in Schichten von weniger als vier Einheitszellen in Manganaten stabilisiert.

Die mikroskopische Struktur der Systeme kann aus der Analyse der durch die Anisotropie bedingten Symmetrie der winkelabhängigen Magnetotransportmessungen erschlossen werden.

Bei abnehmender Schichtdicke verringert sich die intrinsische orthorhombische Symmetrie in SRO zugunsten einer tetragonalen aufgrund der Symmetriebrechung an der Grenzfläche. Die Untersuchungen des anormalen Hall Effekts unterstreichen seine Tensor-Natur und zeigen eine Abhängigkeit des Vorzeichens sowohl von der magnetischen Anisotropie als auch der mikroskopischen Schichtqualität.

Die Beobachtung einer Anisotropie oberhalb der Übergangstemperatur von SRO in Manganatschichten einer Dicke von zwei bis sechs Einheitszellen weist auf eine strukturelle Kopplung über die Sauerstoffoktaederrotationen hin.

Die komplexe Wechselwirkung zwischen antiferromagnetischer Kopplung und schichtdickenabhängiger Anisotropie und dem magnetischen Moment werden in einem 2-Schichten-Modell beschrieben.

Übergitter mit Einzelschichten von weniger als drei Einheitszellen lassen sich nicht mehr mit individuellen Einzelschichten beschreiben sondern stellen einen künstlichen Ferrimagneten dar.

Bibliographic Description:

Bern, Francis

Electric and Magnetic Coupling Phenomena at Oxide Interfaces

Universität Leipzig, Dissertation

140+xii p., 376 ref., 42 fig., 1 appendix

Abstract:

Perovskite oxides show a range of physical properties in combination with high structural quality in small dimensions. The dramatic change of their properties upon small variation in stoichiometry or external influences as pressure/strain are interesting for both a deeper understanding of fundamental condensed matter physics as well as electronic applications.

In the present thesis the influence of charge transfer at interfaces, modification of the magnetic anisotropy by strain and surface effects, as well as magnetic and structural coupling was studied. In virtue of their contrasting ferromagnetic and transport properties, charge doped lanthanum manganite and strontium ruthenate (SrRuO_3) were chosen for this study. Their superior growth properties allowing atomically flat defect free interfaces make them a model system to study electronic magnetic and structural coupling phenomena in perovskite oxides – with the following findings: Charge transfer at interfaces stabilizes ferromagnetism in single layers of manganites down to one unit cell thickness similar to finite size scaling in ordinary transition metal ferromagnets.

The microscopic structure of crystalline layers can be obtained from an analysis of the symmetries present in angle dependent magnetotransport measurements, which are determined by the anisotropy.

Upon thickness reduction, the intrinsic orthorhombic symmetry in SrRuO_3 is reduced in favour of a tetragonal one owing to the symmetry breaking at the interface. Studies on the anomalous Hall effect underline its tensorial nature and show a sign dependence on both magnetic anisotropy and microstructural quality.

The observation of an in-plane anisotropy in manganite layers in the thickness range of two to six unit cells indicates a structural coupling via the oxygen octahedra.

The complex interplay of antiferromagnetic coupling and layer thickness dependent anisotropy and magnetic moment are described in a bilayer model.

Superlattices with individual layers of less than three unit cells cannot be described by the individual layer properties but represent an artificial ferrimagnet.

Contents

1	Introduction	1
2	Fundamental Concepts	5
2.1	The Material Systems	5
2.1.1	Strontium Titanate	6
2.1.2	Manganites	7
2.1.3	Ruthenates	11
2.1.4	Multilayers	14
2.2	Magnetism Fundamentals	16
2.2.1	Magnetic Anisotropy	16
2.2.2	Magnetoelasticity	18
2.3	Transport	19
2.3.1	Magnetoresistance	19
2.3.2	Anomalous Hall Effect	20
2.3.3	Transport in Multilayers	21
3	Sample Preparation and Experimental Techniques	23
3.1	Pulsed Laser Deposition	23
3.2	Structural Analysis	25
3.2.1	X-ray Diffraction	25
3.2.2	Atomic Force Microscopy	29
3.2.3	Dual Beam Microscope	30
3.2.4	Transmission Electron Microscopy	30

3.3	Transport Measurements	31
3.4	Magnetization Measurements	32
3.5	Patterning of Samples	33
3.6	Typical Artefacts	35
3.6.1	Temperature	35
3.6.2	Fluxpinning in Superconducting Solenoid	37
3.6.3	Hall Sensor	39
3.6.4	Oxygen Impurities	39
3.6.5	Magnetic Impurities and Minor Loops	41
4	Polynomial Expansion of Property Tensors in Crystals	43
4.1	Birss: Symmetry Constraints on Property Tensors	43
4.2	Döring: Analytic Functions	44
4.2.1	Series Expansion of Resistivities of Orthorhombic (110) _o Oriented Thinfilms	45
4.2.2	Series Expansion of Resistivities of Orthorhombic (101) _o Oriented Thinfilms	49
5	Magnetoelastic Coupling and Interface Effects in SrRuO₃	55
5.1	Structural Properties	55
5.2	Magnetic Properties	58
5.3	Transport Properties	58
5.3.1	Anomalous Hall Effect	62
5.4	Conclusions	66
6	La_{0.7}Sr_{0.3}MnO₃ CaRuO₃ Superlattices: T_c Stabilization	69
6.1	Sample Fabrication and Structure	70
6.2	Magnetization	71
6.3	Transport Properties	75
6.4	Discussion	80

7 Manganite Ruthenate Superlattices	81
7.1 Interlayer Coupling Strength	82
7.1.1 Magnetization	82
7.1.2 Angle Dependent Magnetoresistance	83
7.2 Ultrathin Superlattices	85
7.3 Trilayers	87
7.3.1 X-ray Magnetic Dichroism	92
7.4 Conclusions	94
8 Conclusions and Outlook	97
A Van der Pauw Measurements	101
A.1 Coordinate Transformation	101
A.2 Schwarz Christoffel Mapping	102
A.3 Resistance Calculation of a Rectangular Sample	103
Bibliography	105

List of Abbreviations

AFM atomic force microscopy

AHE anomalous Hall effect

AMR anisotropic magnetoresistance

BaTiO₃ barium titanate

CaRuO₃ calcium ruthenate

CMR colossal magnetoresistance

EDX energy dispersive x-ray spectroscopy

FC field cooled curve

HAADF-STEM high angle annular dark field scanning transmission electron microscopy

La_{0.7}Ba_{0.3}MnO₃ lanthanum barium manganite

La_{0.7}Sr_{0.3}MnO₃ lanthanum strontium manganite

LaMnO₃ lanthanum manganite

LaNiO₃ lanthanum nickelate

LSAT solid solution of (LaAlO₃)_{0.3} - (Sr₂AlTaO₆)_{0.7}

MPMS magnetic properties measurement system

PLD pulsed laser deposition

PMMA poly methyl methacrylate

RHEED refractive high energy electron diffraction

SEM scanning electron microscopy

SL superlattice

SQUID superconducting quantum interference device

SrRuO₃ strontium ruthenate

SrTiO₃ strontium titanate

STEM scanning transmission electron microscopy

TEM transmission electron microscopy

u.c. unit cell

VTI variable temperature insert

XRD x-ray diffraction

YMnO₃ yttrium manganite

ZFC zero field cooled curve

In the text appear standard chemical symbols, which have not been included in this list. The compound names have been additionally shorted to e.g. LSMO, LBMO or SRO where appropriate.

Introduction

*“Ter certeza é não estar vendo.”
(Being sure is being blind.)
(A. Caeiro)*

Oxides of the perovskite family with the general chemical formula ABO_3 show a wide variety of technologically relevant properties within a single structural form. Compatibility of the basic (pseudo) cubic building block, which moreover adapts easily to substantial lattice mismatch, allows for combining possibly a variety of material properties ranging from dielectric to ferroelectric, insulating, semiconducting, metallic or superconducting, anti- to ferromagnetic, thermoelectric and even photovoltaic properties in essentially defect free stacks [1–3]. A major issue is conservation of desirable properties upon miniaturization with the growing importance of interface effects. At the same time, these interface effects open new opportunities from emerging phenomena [4]. A prominent example is the two dimensional electron gas formed at the interface between the insulating perovskite oxides $SrTiO_3$ and $LaAlO_3$ [5].

Aim of this thesis is to gain a deeper understanding in the microscopic mechanisms responsible for the modifications of material parameters by interface related effects. The influence of charge transfer at interfaces, modification of the magnetic anisotropy by strain and surface effects, as well as magnetic and structural coupling are investigated. Methodologically we focus on magnetization and magnetotransport measurements accompanied by structural investigations by x-ray diffraction and high resolution scanning transmission electron microscopy. Superlattices allow to vary the interface density and thus the weight of interfacial effects. In virtue of their contrasting ferromagnetic and transport properties, charge doped lanthanum manganite ($LaMnO_3$) and ruthenates with their itinerant electron system were chosen for this study.

Optimally doped lanthanum strontium manganite ($La_{0.7}Sr_{0.3}MnO_3$) is a much studied colossal magnetoresistance compound and exhibits the highest transition temperature of its class. As a half metal it could play a key role in spintronics, however, broader application is hampered due to issues with degraded interfacial and surface layers. An insulating layer with predominantly antiferromagnetic coupling is formed, which results in a reduced effective thickness in magnetization and transport

as well as reduced spin polarization in tunneling magneto resistance. From a fundamental point of view the manganites are interesting since they belong to the class of strongly correlated materials. While in optimally doped stoichiometry double exchange ensures ferromagnetic order and robust conduction, small deviations may lead to localization effects with a metal to insulator transition and antiferromagnetic order. The complex interplay of spin, charge and orbital degrees of freedom makes the manganites highly sensitive to external perturbations and thus ideal candidates to observe interface effects with [6].

Strontium ruthenate (SrRuO_3) is a widely used contact material for oxides with (for an oxide) exceptionally good metallic conduction. In contrast to the double exchange driven magnetism in the manganites, the stronger delocalization of the $4d$ electrons leads to itinerant magnetism in SrRuO_3 . Reducing the A site cation size in the ARuO_3 compound by substituting strontium with calcium, the ferromagnetism gradually decreases. Calcium ruthenate (CaRuO_3) is a paramagnet on the verge of magnetic order [7]. The magnetocrystalline anisotropy of SrRuO_3 is two orders of magnitude higher than the one of $\text{La}_{0.7}\text{Sr}_{0.3}\text{MnO}_3$, while its saturation magnetization corresponds roughly to half of the saturation magnetization of $\text{La}_{0.7}\text{Sr}_{0.3}\text{MnO}_3$. The $\text{La}_{0.7}\text{Sr}_{0.3}\text{MnO}_3$ and SrRuO_3 system shows an exceptional growth behaviour allowing atomically flat and defect free interfaces and films. Thus they serve as an ideal model system to study electrical magnetic and structural coupling phenomena in perovskite oxides.

We enter this work by briefly reviewing the materials involved in this study, followed by selected aspects of magnetism and transport mechanisms. Then the experimental methods are presented with a selection of common artefacts. A newly found analytic expression allows the determination of the in-plane components of the resistivity tensor.

The structure of crystalline layers can be obtained by analysing the symmetries present in angle dependent magnetotransport measurements [8]. Since the observed symmetries depend strongly on the anisotropy, angle dependent magnetotransport serves as a tool to determine the structure of ultrathin layers and monitor changes in the anisotropy. The theoretical background of this method is reviewed and exemplified on selected samples.

The influence of substrate induced strain and interfacial symmetry breaking is investigated for SrRuO_3 thin films grown on different substrates and in superlattices with strontium titanate (SrTiO_3). Tensile strain induces a structural transition accompanied by a change of the magnetic anisotropy and a sign change of the anomalous Hall constant. In superlattices, the intrinsic orthorhombic symmetry of SrRuO_3 is reduced in favour of a tetragonal one upon thickness reduction. This transition relates to symmetry breaking at the interface. Studies on the anomalous Hall effect underline its tensorial nature and show a sign dependence on both magnetic anisotropy and microstructural quality.

Charge transfer at interfaces without simultaneous magnetic coupling effects is studied in $\text{CaRuO}_3/\text{La}_{0.7}\text{Sr}_{0.3}\text{MnO}_3$ superlattices. Ferromagnetic order is stabilized in few unit cell thick layers with a finite size scaling similar to ordinary transition metal ferromagnets.

The last chapter is dedicated to the complex interplay of antiferromagnetic coupling and layer thickness dependent anisotropy and magnetic moment in SrRuO_3 / manganite multilayers. A bilayer model qualitatively captures the phenomenology. An in-plane anisotropy in $\text{La}_{0.7}\text{Sr}_{0.3}\text{MnO}_3$ layers of two unit cells thickness indicates a structural coupling via the oxygen octahedra. Reduced interlayer strain between SrRuO_3 and lanthanum barium manganite ($\text{La}_{0.7}\text{Ba}_{0.3}\text{MnO}_3$) stabilizes orthorhombic symmetry even in $\text{La}_{0.7}\text{Ba}_{0.3}\text{MnO}_3$ layers of six unit cell thickness. When reducing the overall thickness, we find that ferromagnetic order prevails down to one unit cell thick single $\text{La}_{0.7}\text{Ba}_{0.3}\text{MnO}_3$ layers embedded in two to three unit cell thick SrRuO_3 . Finally superlattices with individual layers of less than three unit cells are also investigated. The latter show a different behaviour compared to the superlattices comprised of thicker layers and cannot be described by the individual layer properties. These superlattices represent an artificial ferrimagnet.

Most of the superlattices and films were fabricated by Dr. I. Lindfors-Vrejoiu. X-ray diffraction measurements were mainly done by Dipl.-Kryst. A. Setzer, some by Dr. I. Lindfors-Vrejoiu. HRTEM images were obtained by the group of Dr. E. Pippel and Prof. Dr. D. Hesse. The SRO films on BFSTO and STO(111) were grown by Dr. A. Herklotz and Dipl.-Ing. H. Hochmuth. Some of the measurements included were done by Prof. Dr. M. Ziese as indicated. XMCD measurements at PSI were done with the help of Dr. C. Piamonteze, Dr. M. Studniarek, and M. Sc. S.R. Avula Venkata.

Fundamental Concepts

The following sections aim to summarize the fundamental concepts which underlie the present study. We begin with the material systems, followed by a brief introduction on general concepts in magnetism and transport.

2.1 The Material Systems

According to Goldschmidt [9], ternary compounds of the form ABX_3 crystallize in a (pseudo-) cubic perovskite form if the ionic radii (Shannon radii [10]) fulfil the following relation

$$0.8 \leq \alpha \leq 1 \quad \text{with} \quad t = \frac{r_A + r_X}{\sqrt{2}(r_B + r_X)},$$

i.e. for $t = 1$ the face diagonal is $\sqrt{2}$ times the side length. The deviation of the Goldschmidt tolerance factor t from the ideal value 1 is a measure of the distortion from the ideal perovskite lattice. However, it cannot provide any indications on the symmetry of the distortion.

Since the cations are ordered basically in a cubic lattice, the symmetry of the crystal is governed by the symmetry of the oxygen octahedra. Glazer [11] established a suitable notion to describe the octahedral tilts. Denoting with a the pseudocubic lattice constant, the three possible tilt symmetries around that axis are denoted by superscripts: a^0 for zero tilt, a^+ for tilts in phase, and a^- for out of phase tilts, i.e. adjacent oxygen octahedra rotations alternate between positive and negative rotation directions. Differences in cation distances due to different tilt angles are taken into account by changing the letter describing the axis to b, c . Within a model of rigid oxygen octahedra, Glazer found 23 different tilt systems within 15 space groups.

A re-examination of Glazer's ideas [12] led Woodward [13] to correlate octahedral tilts with the A-Site coordination. Of course the bonds are not entirely ionic, so the polarizability of the species will determine the covalent bond length, as already stated by Goldschmidt [9] and recently reconsidered by Cammarata and Rondinelli [14]. Similar considerations led Lufaso and Woodward [15] to extend the rigid octahedra model by taking the coordination into account for estimation of the bond lengths and also by incorporating Jahn-Teller distorted octahedra. The validity of

their model was proven by the successful description of octahedral order in double perovskites $AA'BB'O_6$ [16].

Thus it is an interplay of valency and cation size that determines the octahedral rotations. Similar considerations are also valid for other oxide systems (see e.g. the "inverse" spinel magnetite Fe_2O_3 [17, p. 127]). Orbital hybridization and the large misfit in oxygen positions at interfaces (see Fig. 2.1(e)) may lead to electronic and crystal structure modifications. With the ability to calculate the energy associated to an octahedral distortion [18, 19] and the energy cost for displacing the oxygen from its bulk equilibrium position, tilt propagation across the interface can be modelled [20]. One may interpret the region between bulk-like octahedra rotation patterns as a structural domain wall with a material dependent characteristic width, which determines the spacial extend of octahedra rotation related interface phenomena.

2.1.1 Strontium Titanate

Most of the samples studied have been grown on the cubic perovskite $SrTiO_3$ (see Fig. 2.1(a)), a common substrate material for perovskite oxides with a lattice parameter $a = 3.905 \text{ \AA}$ at room temperature. It is synthesized as single crystals and commercially available with a variety of surface orientations¹. Single termination with TiO_2 can be achieved by soaking the substrate in deionized H_2O to form strontium hydroxides which are easily dissoluble in slightly acidic environment [21, 22] with buffered hydrofluoric acid, albeit an acid free route preventing the risk of etch pitches has been reported as equally viable [23]. Upon annealing in oxygen strontium segregation may occur at the vicinal step edges [24], which may be used for self-organized one dimensional structures [25], but may also lead to off-stoichiometry and inhomogeneous film growth.

$SrTiO_3$ shows a range of peculiar properties. Albeit normally a paraelectric, its high dielectric constant suggests that it is not ferroelectric only due to quantum fluctuations [26–28], which may be overcome by strain [29, 30]. It can be doped to a semiconducting regime with lanthanum or niobium [31, 32] as well as with cation or oxygen vacancies [33, 34], eventually becoming superconducting below 300 mK [35, 36]. Moreover, defects may result in considerable photoconductivity [37].

More significant for the present study is the phase transition from cubic to tetragonal around 105 K to 110 K [38–44] with oxygen octahedra rotations about the c-axis ($a^0a^0c^+$) decreasing the a axes. Additional elongation along the c axis results in a slightly distorted oxygen octahedron. Below around 80 K piezoelectric domainwalls appear [45, 46], possibly related to rhombohedral clusters [47], and cause surface rumpling [48]. These effects may be the reason for a previously reported orthorhombic phase [49], which has not been confirmed but sometimes appears in literature.

¹The substrates in this study have been obtained from Crystec GmbH.

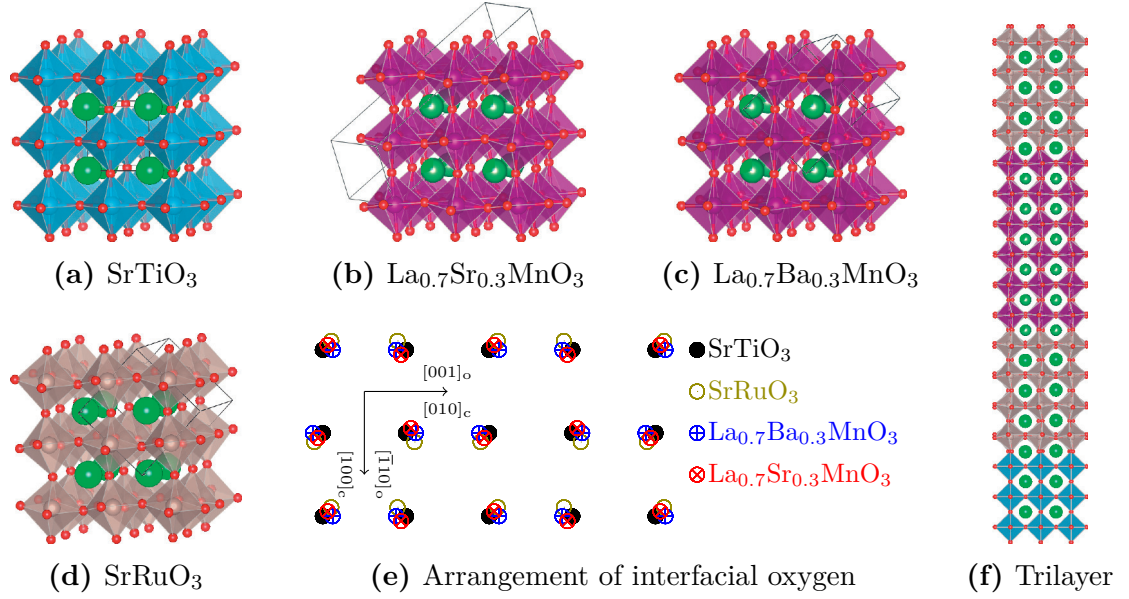


Figure 2.1: Perovskite structures viewed 15° from the pseudocubic $[010]$ direction ($[100]$ to the right, $[001]$ upwards). Thin lines indicate the actual cubic (a), rhombohedral (b), and orthorhombic (c)($Imma$), (d)($Pnma$) unit cell. In (e) the bulk positions of interfacial oxygen for the structures are superimposed. (f) Continuity of octahedral tilts viewed along the $[100]_{\text{pc}}$ direction in a SRO/LBMO/SRO trilayer. Structures drawn with VESTA [51].

It is obvious that the reported surface rumpling may have severe effects on thin films. Repeated cycling may irreversibly increase the crystalline mosaicity and lead to stacking faults as well as antiphase boundaries. This may also affect the reproducibility of an experiment. An example on how this structural transition changes the magnetic anisotropy of a thin $\text{La}_{0.7}\text{Sr}_{0.3}\text{MnO}_3$ film can be found in reference [50], which also provides evidence for substantial differences in consecutive runs.

2.1.2 Manganites

LaMnO_3 based compounds were first studied by Jonker and Van Santen [52][53], who described a transition of the antiferromagnetic and insulating parent compound to a ferromagnetic and conducting regime upon charge doping, either by introducing cation vacancies denoted as $\text{LaMnO}_{3+\delta}$, or by introducing tetravalent Mn^{4+} with doping of divalent cations on the La site with Ca^{2+} , Sr^{2+} , Ba^{2+} . Volger [54] related the appearance of ferromagnetism to the double exchange mechanism proposed by Zener [55]. His impedance measurements gave first indications on coexistence of separated conducting and insulating phases, which were studied with neutron diffraction by Wollan and Koehler [56], who concluded the existence of uncoupled disordered ferromagnetic and antiferromagnetic phases.

In the nineties of the last century, triggered by the hope to apply the huge magnetoresistance in memory devices, considerable research efforts were dedicated to a better understanding of the mixed valence manganites, which resulted in a series of review articles [6, 57–60]. The available literature on this subject is enormous, and in the following only the most basic characteristics and some more recent developments primarily focused on the situation in thin films are described while for a broader insight the reader is referred to the above mentioned reviews.

Structure

$\text{La}_{0.7}\text{Sr}_{0.3}\text{MnO}_3$ and $\text{La}_{0.7}\text{Ba}_{0.3}\text{MnO}_3$ crystallize in the rhombohedral structure $R\bar{3}c$ with lattice constants (at $T = 300\text{ K}$) of $a = 5.506\text{ \AA}$ and $c = 13.356\text{ \AA}$ (LSMO) and $a = 5.538\text{ \AA}$ and $c = 13.501\text{ \AA}$ (LBMO) corresponding to pseudocubic lattice constants of 3.88 \AA and 3.91 \AA respectively [61]. The rhombohedral distortion corresponds to a contraction along the $[111]_{pc}$ axis accompanied by out of phase octahedral rotations about that axis. Stronger distortions with the smaller cation calcium lead to a $Pnma$ orthorhombic phase in calcium doped compounds [62], but $\text{La}_{0.7}\text{Ba}_{0.3}\text{MnO}_3$ also undergoes a transition to orthorhombic $Imma$ structure below 200 K [63]. In Fig. 2.1(b) and (c) the $R\bar{3}c$ structure with pseudocubic octahedral tilt pattern $a^-a^-a^-$ and the $Imma$ structure with $a^-a^0a^-$ are shown with the actual unit cell drawn with grey lines. The richness of phases indicates that the groundstate energies of the possible distorted structures are close, allowing possibly for manipulation by moderate strains, and providing an explanation for the high sensitivity of material properties to external stress.

Magnetization and Transport

Bulk $\text{La}_{0.7}\text{Sr}_{0.3}\text{MnO}_3$ and $\text{La}_{0.7}\text{Ba}_{0.3}\text{MnO}_3$ undergo a transition from a paramagnetic semiconducting state to a ferromagnetic metallic state below $T_C = 370\text{ K}$ and $T_C = 330\text{ K}$ respectively, with an ideal saturation magnetic moment of $3.7\mu_B$ per formula unit. The main mechanism for the ferromagnetic state and the metallic conductivity is the double exchange mechanism introduced by Zener [55, 64], extended by Anderson and Hasegawa [65] and De Gennes [66]. The two configurations

$$\text{Mn}^{3+}\text{O}^{2-}\text{Mn}^{4+} \quad \text{and} \quad \text{Mn}^{4+}\text{O}^{2-}\text{Mn}^{3+}$$

are degenerate if an alignment of their spins allow transfer of the e_g electron from the Mn^{3+} to Mn^{4+} . This degeneracy lowers the energy of the system. This results in a hopping integral $t \sim \cos(\theta/2)$ depending on the angle θ between the directions of the spins. Thus the bandwidth W describing the degree of delocalization depends on both the bond lengths and the Mn-O-Mn bond angle, increasing as it approaches 180° . Goodenough described theoretically the transitions between ordered and delocalized Mn^{3+} and Mn^{4+} giving an explanation for the increased T_C with optimal doping of $\text{Mn}^{4+}/\text{Mn} = 0.31$ [67–69]. Millis et al. [70] pointed out that the double

exchange picture was likely to be incomplete and concluded on small lattice distortions effectively trapping the charge carrier above T_C , so-called small polarons [71], similar to a concept introduced in the context of ferromagnetic semiconductors [72]. But also below the critical temperature the strong correlation of lattice distortions with the bandwidth may lead to localization effects [73].

The colossal magneto resistance was ascribed to phase separation and percolation [59, 74, 75], and, especially for the low doped manganites with smaller bandwidth, to a chemical potential shift $\frac{\Delta\mu}{W} \propto \langle M \rangle^2$ proportional to the square of the mean magnetization [76]. Charge and orbital ordered phases can be metastable, as observed by temperature hysteresis of the phase transitions. The coexistence of disordered phases in strained or not optimally doped films may lead to a time and history dependence of the magneto resistance [77–79].

Optimally doped manganites are so-called half-metals with close to 100% spin polarization at the Fermi surface, since Hund’s coupling energy, which is responsible for shifting the energies of spin up and spin down states, is stronger than the bandwidth. This property made them seemingly ideal candidates for high performance tunnel magneto resistance devices and spintronic applications [80]. However, the interface towards the tunnel barrier shows inferior properties [81] that limit these prospects.

Thin Films

When grown as thin films, several strain accommodation mechanism are at play. Maurice et al. [82] studied misfit accommodation on SrTiO_3 substrates for a range of thicknesses. According to these studies, the bulk rhombohedral distortions are suppressed for thicknesses below 25 nm, above which they are recovered by forming microscopic twin domains while maintaining the in-plane lattice parameter of the substrate up to 100 nm. The thicker films show bulk-like magnetization values, while the thinner films deliver a reduced magnetic moment and transition temperature. Below a thickness of six to eight unit cells the metallic properties of $\text{La}_{0.7}\text{Sr}_{0.3}\text{MnO}_3$ are lost and the magnetic transition temperature is strongly reduced [83]. It is interesting to note that doping with titanium in thicker films results in a comparable decrease, i.e. a titanium content of 15% on the B site leads to insulating behaviour and a reduced T_C of 150 K [84]. The structure evolution in the thinner thickness range was studied by Sandiumenge et al. [85] relating the degradation of the ferromagnetic properties in the thin limit to oxygen octahedra deformations and changed orbital occupancy. Vailionis et al. [86] also described a change of the lattice parameter in the interface region with the substrate. However, they attributed the extended unit cell to a suppressed oxygen octahedral tilting at the interface. Recently a connection between ferromagnetism and octahedral tilting has been reported [87], yet, since all theoretical work indicates an increase in bandwidth for straight bonding, the tilting may rather result from distortions related to ferromagnetic order than being the reason for ordering.

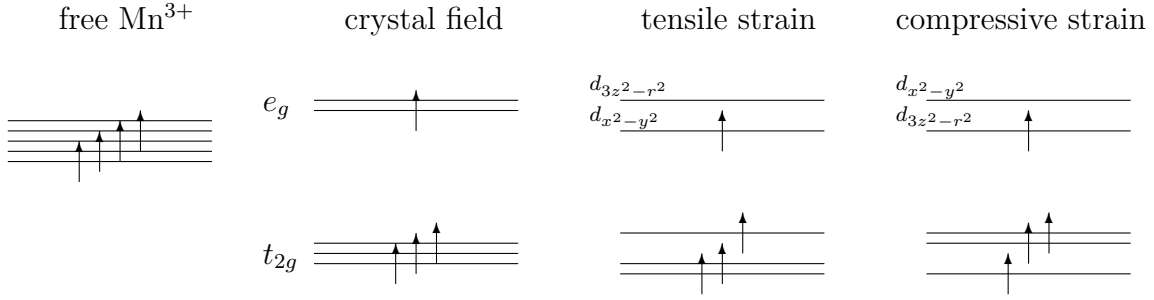


Figure 2.2: Schematically: Lifting of the octahedral degeneracy by the crystal field and shifts of the energy levels due to octahedral deformations by in-plane strains exemplified with an Mn^{3+} . The nearest neighbours lie along the x, y, and z axis. For better visibility the degenerate orbitals are also slightly offset.

There is a second explanation for the observed auxetic behaviour, which relates the strain accommodation mechanism to off-stoichiometry (see also Section 3.6.5). Herger et al. [88] observed Sr segregation from the film substrate interface, which might be related to a preferential Mn^{3+} localization at the interface. There are two reasons for this: First, epitaxial misfit may be reduced with the bigger Mn^{3+} ion at the interface instead of Mn^{4+} . The radii of Sr and La are very close and play a minor role. Second, the occupied d orbitals of Mn^{3+} may easily hybridize with the unoccupied d orbitals of Ti^{4+} . The energy gain is larger for Mn^{3+} than for Mn^{4+} . This Sr segregation may enhance T_C upon thickness reduction for films with under-doped composition, while optimally doped films degrade due to strontium excess close to the surface [89, 90]. The interface layers may be improved by the introduction of a thin LaMnO_3 layer [91, 92].

The vacuum interface as well as interfacing to a material with empty $3d$ states changes the crystal field splitting. In Fig. 2.2 the lifting of degeneracy for the $3d$ orbitals of a free manganese ion in the crystal field of a cubic structure is shown. In-plane strain leads to a splitting of the e_g orbitals. In-plane tensile strain lowers the (in-plane) $d_{x^2-y^2}$ orbital energy, and in-plane compressive strain increases it, favouring $d_{3z^2-r^2}$ occupation. Similarly one may expect that changes depend on the size and d orbital filling of the next cation along x, y, and z, albeit with some asymmetry in that case. Theoretical studies [93, 94] within a tight-binding approach indicate that the results depend crucially on the surface termination. In case of MnO_2 terminated surfaces, charge from the bulk is transferred to the lower lying $e_{3z^2-r^2}$ orbital leading to an effective Mn^{3+} oxidation state and antiferromagnetic interactions instead of double exchange. Termination with La/SrO leads to an enhancement of the $e_{x^2-y^2}$ orbital occupation and ferromagnetic coupling. Experimental studies with x-ray linear dichroism [95–97] confirm these theoretical pictures. However, the enhancement of the $e_{x^2-y^2}$ orbital occupation is weaker than predicted, possibly due to instability of the La/SrO surface layer. The effects of in-plane strain and polar discontinuities with capping layers, although detectable, seem to be of

secondary order. It should be noted that in the capping layers studied so far, the $3d$ orbitals of the B site cation were unoccupied, or, in the case of NdGaO_3 , should be preferentially occupied to fill the shell as in pure nickel or copper.

To compensate the degradation effects in thin films charge doping seems to be the means of choice. Ruthenium doping has been reported to both increase [98] and decrease [99] the transition temperature, the latter probably partially due to reduced structural quality. Direct charge doping with an electrolyte on underdoped LSMO was also successfully realized [100] proving the charge transfer concept unambiguously. Digital doping with alternating layers of LaMnO_3 and SrMnO_3 [101, 102] shows that order of the A site cations does not necessarily imply order of the B site cation, which is consistent with the theoretical model of a freely moving e_g electron in the vicinity of the interface.

2.1.3 Ruthenates

Good metallic conductivity and high crystalline quality of grown thin films make SrRuO_3 a widely used oxide electrode material. Koster et al. [103] have recently compiled a good review on structural and physical properties of SrRuO_3 thin films as well as their possible use in applications. In the following, the most important basic properties are summarized including additions to the cited review due to new research results.

Structure

SrRuO_3 and CaRuO_3 undergo phase transitions from the ideal perovskite cubic structure at high temperatures to tetragonal structure around 950 K and to the orthorhombic $Pnma$ structure at 820 K [104] with lattice constants (at $T = 300$ K) in the generally used $Pbnm$ setting of $a = 5.5567$ Å, $b = 5.5304$ Å, and $c = 7.8446$ Å (SRO) and $a = 5.359$ Å, $b = 5.5224$ Å, and $c = 7.663$ Å (CRO) [105, 106]. This corresponds to a pseudocubic lattice parameter of 3.923 Å and 3.842 Å respectively. It is worth noting the anisotropic decrease of the lattice parameters upon A site cation size reduction, which result in strong octahedral tilts about the b axis in CaRuO_3 . Adopting the pseudocubic axis settings $[100]_{\text{pc}} || [\bar{1}10]_{\text{o}}$, $[010]_{\text{pc}} || [001]_{\text{o}}$, and $[001]_{\text{pc}} || [110]_{\text{o}}$ the octahedral tilts can be described in the Glazer system as $a^-a^+a^-$, i.e. in phase rotation about the $[001]_{\text{o}}$ axis and out of phase rotation about the other two axes. The structure is visualized in Fig. 2.1(d) with the orthorhombic unit cell drawn with grey lines.

Magnetization and Transport

SrRuO_3 is a good conductor (for an oxide) and orders ferromagnetically below $T_C = 160$ K. It is one of the rare examples of $4d$ itinerant magnetism [69]. There has been some debate about the reduced saturation magnetic moment of $\sim 1.6\mu_B$

as compared to a ruthenium low spin state, especially since the moment is higher ($\sim 2.6\mu_B$) in the paramagnetic region [107, 108]. Bandstructure calculations indicate a strong hybridization of the ruthenium $4d$ and oxygen $2p$ states explaining the reduced moment [109–112]. The calculations reveal a similar density of states at the Fermi level for majority and minority spin bands ($\sim 9 - 20\%$ minority spin polarization). Worledge and Geballe [113] obtained -9.5% in a tunnel experiment, whereas Andreev reflection (not sign sensitive) yields $\sim 50\%$ [114]. The discrepancies may be related to the different Fermi velocities of majority and minority band². The spin down band has a higher Fermi velocity and thus will dominate the general transport properties [110]. An increased moment would enhance the splitting and could induce half-metallicity. Calculating a classical mean free path for the electrons yields values below 1 nm [109] implying that the classical Boltzmann theory is not valid to describe the transport properties. Klein et al. [116, 117] related this *bad metal* behaviour to the peculiar temperature dependence of the resistivity and magnetization. These are signs of weak correlations, or, in other words, only a rather weak delocalization of the $4d$ electrons.

Hall effect measurements on ruthenates show a rich phenomenology. Strong temperature dependent slope changes from negative to positive in both SrRuO_3 and CaRuO_3 were reported [118]. Later measurements on CaRuO_3 obtained generally a positive Hall coefficient suggesting predominantly hole conduction. However, Khalifah et al. [119] argued for a large positive anomalous Hall contribution in the paramagnetic phase motivated by a smooth transition over the entire $\text{Sr}_x\text{Ca}_{1-x}\text{RuO}_3$ series. Measurements of a positive Seebeck coefficient (thermoelectric power) indicate hole conduction in SrRuO_3 [120], whereas the high field slope of Hall measurements are negative, suggesting electron conduction in a simple one band model. The peculiar temperature dependence of the anomalous Hall effect in SrRuO_3 , which is positive in the paramagnetic regime and changes sign below T_C was studied intensively. It served as a model system to test the application of the Berry phase theory to the anomalous Hall effect [121–124]. The non-uniform temperature and resistivity dependence was related to the distribution of Berry curvatures, which results in a chaotic behaviour of the transverse conductivity making it very sensitive to small changes in the chemical potential.

Kanbayasi [125, 126, 127] measured the magnetic anisotropy with torque magnetometry and obtained a tetragonal magnetic anisotropy of the form

$$\mathcal{K} = K_1 \cos(\theta)^2 + K_2 \cos(\theta)^4 + K_3 \sin(\theta)^4 \cos(\phi)^2 \sin(\phi)^2,$$

with $K_1 = 0.64 \times 10^6 \text{ J m}^{-3}$, $K_2 = -1.1 \times 10^6 \text{ J m}^{-3}$ and $K_3 = 53 \times 10^3 \text{ J m}^{-3}$, with θ being the angle with respect to the easy axis. This is basically an uniaxial anisotropy. The tetragonal symmetry observation, contrary to the crystal structure, may be due to twins in the specimen. Charge doping with La in the $\text{Sr}_{1-x}\text{La}_x\text{RuO}_3$

²Generally, different methods to determine the spin polarization obtain different results. This is basically due to different definitions [115].

reduces the Curie temperature and results in a ferromagnetic to antiferromagnetic transition at $x = 0.3$ [128]. Chromium substitution on the ruthenium site increases T_C by 20 K [129, 130].

Thin Films

The above mentioned transition temperatures from cubic to tetragonal and orthorhombic phase are strongly reduced in case of thin films suggesting a cubic phase at growth temperature [131, 132]. The tetragonal to orthorhombic transition is reduced to 550 K [133]. Thus it may be feasible to re-establish long range orthorhombic ordering by moderate annealing of micro twinned films. Indications of a successful phase transition upon heating only up to 300 °C were found by Herklotz et al. [134]. One report claims suppression of the tetragonal to orthorhombic transition for films below 18 u.c. thickness on SrTiO₃ [135], however, clear orthorhombic signatures in thinner films have been observed by others, see e.g. [8]. One should note the considerable scatter in the reported phase transition temperatures in literature. Besides microscopic twinning, off-stoichiometry with ruthenium reduced phases [136] may be a possible explanation.

While single crystal growth of SrRuO₃ is challenging [137], a group around Eom found that single crystalline thin films of SrRuO₃ can be grown on SrTiO₃ with a small vicinal miscut of 0.1° to 5° and with the vicinal terraces aligned within 14° along a crystal axis [138–141]. This can be explained by the minimized lattice mismatch in this configuration. For SrRuO₃ in the *Pbnm* setting we have $a/\sqrt{2} = 3.9365$ Å, $b/\sqrt{2} = 3.9106$ Å, $c/2 = 3.9223$ Å, and $[110]_o/2 = 3.9235$ Å. The $[001]_o$ and $[\bar{1}10]_o$ axes should lie in plane, and the smaller $[010]_o$ axis aligns better with the substrates $[\bar{1}01]_c$ direction at the step edges than the $[100]_o$ axis. A small monoclinic distortion accommodates the angular misfit caused by the difference in a and b lengths [142]. It is remarkable that the one unit cell step of the terrace edge is sufficient to induce a single crystalline phase over a distance of 200 nm. Clearly, this link should become weaker with decreasing film thickness, which explains a higher amount of twin domains in few unit cells thick ultrathin films. This may be overcome by increasing the vicinal angle and thus reducing the terrace width. For thin films, a transition from monoclinic to tetragonal structure upon reduction of the oxygen partial pressure during growth was reported [143] and related to weaker linking of the (incomplete) oxygen octahedra.

For moderately tensile strained films on (110) GdScO₃ ($(001)_{pc}$) a thickness dependent transition from monoclinic in thin films to tetragonal above 17 nm was reported [144]. This indicates that for thin films the same epitaxial relationship as with SrTiO₃ is preferred due to the larger mismatch of the short orthorhombic b axis. The films also show comparable magnetic properties. With increasing thickness the symmetry changes to tetragonal and the out-of-plane direction transforms to a magnetically hard axis. Some strain relaxation might be possible through microscopic twinning, similar to the case in La_{0.7}Sr_{0.3}MnO₃. It must be noted that

the ferromagnetic transition temperature is reduced for these tensile strained films, which may hint at some off-stoichiometry [145]. The accommodation of even larger tensile strain on a KTaO_3 was explained with oxygen and possibly ruthenium vacancies while showing comparable magnetic properties [146]. Tensile strained films with in-plane easy axis on CaHfO_3 or $\text{Ba}_{0.5}\text{Sr}_{0.5}\text{TiO}_3$ did not show a T_C decrease [147, 148]. On $\text{SrTiO}_3(111)$ a high spin state was reported [149], but could neither be confirmed by our measurements nor by other groups [150]. The presented magnetization loop in Ref. [149] is reminiscent of an impurity loop (see Section 3.6.5), and no temperature dependencies showing unambiguously the transition were reported. For thin films a metal to insulator transition has been reported, and ferromagnetism is absent in films below three to four unit cells [151]. The observation of exchange bias in these magneto-optical Kerr effect studies suggested the formation of some antiferromagnetic layer. Alternatively, this exchange bias might be attributed to exchange interactions between clusters of different magnetic properties.

2.1.4 Multilayers

Interface effects render multilayer properties more than the sum of the properties of the constituent layers. The manganite ruthenium system is here of special interest since it combines materials with contrasting properties. We have rather strong correlation and localization effects in $\text{La}_{0.7}\text{Sr}_{0.3}\text{MnO}_3$ versus weak correlation and itinerant magnetism in SrRuO_3 . In the manganites we have high magnetization and small magnetocrystalline anisotropy, whereas in the ruthenates the opposite is the case.

Charge transfer between ruthenium and manganese has been studied in double perovskites and doping series [152–154], which, in case of low ruthenium concentration, results in a Ru^{5+} valence [155]. A layered geometry has the advantage of better controlling the region of charge transfer and possible spin textures [156].

Charge transfer at the interface can substantially modify the material properties in the vicinity of the interface and induces new phases in the manganite [157]. At the $\text{CaRuO}_3/\text{CaMnO}_3$ interface as well as at the $\text{SrRuO}_3/\text{SrMnO}_3$ interface charge transfer and magnetic moments on the interfacial manganese atoms were reported [158, 159]. Contrary to theoretical calculations, which confine the charge transfer at the $\text{CaRuO}_3/\text{CaMnO}_3$ interface to one unit cell [160], experimentally an extend of three to four unit cells was observed [161]. This was attributed to polaronic effects. In both solid solutions and layered systems, antiferromagnetic coupling of the ruthenium and manganese magnetic moments were observed [152, 162]. This can be understood within a strong hybridization of the ruthenium $4d$ states with the $\text{O}2p$ states and the usual antiferromagnetic alignment of the oxygen states with respect to the manganese magnetization [163, 164]. Alternatively, the predominantly negative spin polarized ruthenium states at the Fermi level [110] enhanced by an increased spin splitting due to a magnetic proximity effect [153] may be the reason. A similar antiferromagnetic coupling mediated by the interfacial oxygen is even seen with

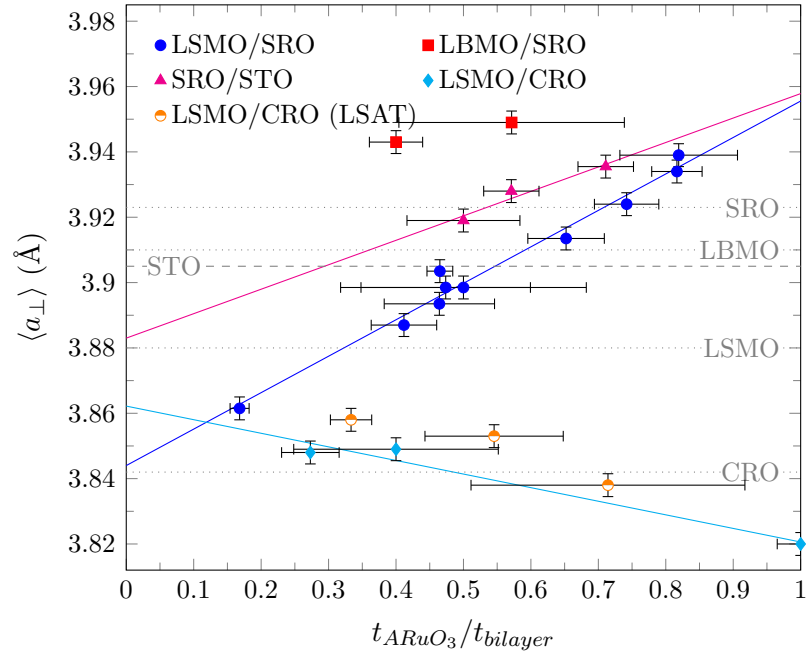


Figure 2.3: Mean lattice constants vs. $\text{SrRuO}_3(\text{CaRuO}_3)$ content in the superlattices studied. Dotted lines indicate the pseudocubic lattice constants in the bulk phase. The given x errors correspond to one unit cell uncertainty.

titanium. At manganite titanate interfaces charge transfer results in a d_x configuration of the titanium cations, and an antiferromagnetically coupled proximity effect induced magnetization was reported [165, 166].

Besides the charge transfer and the rather small lattice mismatch of the cation lattice, mismatch of the oxygen octahedral rotations can also induce property changes [20, 167, 168]. Figure 2.1(e) shows the bulk positions of the interfacial oxygen for all structures in the figure. These positions are at scale (!), visualizing the huge offset of the oxygen position of around 10% as compared to the cation mismatch $\leq 1\%$. For cubic SrTiO_3 they lie on a regular square grid. The $(a^-a^-a^-)$ tilt system in $\text{La}_{0.7}\text{Sr}_{0.3}\text{MnO}_3$ results in alternating offsets in both in-plane directions. The $(a^-a^-a^0)$ tilt system in the low temperature phase of $\text{La}_{0.7}\text{Ba}_{0.3}\text{MnO}_3$ results in alternating offsets along the $[001]_o$ direction, whereas along the $[\bar{1}10]_o$ the oxygen positions are aligned with the SrTiO_3 oxygen positions. In SrRuO_3 with $(a^-a^-a^+)$ tilt system there are additionally alternating offsets along the $[\bar{1}10]_o$ direction, which are equal for all columns along the $[001]_o$ direction. This reveals the similarity and thus probable adaptivity of the octahedral tilts. The compatibility of the tilts is shown exemplarily for a $\text{SrRuO}_3/\text{La}_{0.7}\text{Ba}_{0.3}\text{MnO}_3/\text{SrRuO}_3$ trilayer in Fig. 2.1(f) in projection along the $[\bar{1}10]_o$ direction.

Figure 2.3 summarises the results from XRD analysis of different sample series studied in the present work. The mean lattice constant of the superlattice is plotted vs. the SrRuO_3 (or CaRuO_3) content in the superlattice. Lines correspond to a lin-

ear regression of the data points. Clearly, the thin films and superlattices are in a strained state. Apart from the substrate induced strain, the slopes of the regression lines indicate as well interlayer strain. There are no indications of regimes of different strain relaxation mechanisms as described by Maurice et al. [82] for $\text{La}_{0.7}\text{Sr}_{0.3}\text{MnO}_3$, probably due to overall thicknesses ≥ 20 nm.

2.2 Magnetism Fundamentals

2.2.1 Magnetic Anisotropy

The free energy density of a uniformly magnetized system is in general a function of the temperature T , the magnetization magnitude M , the direction of magnetization \hat{m} and the stress tensor ε , $\mathcal{F}(T, M, \hat{m}, \varepsilon)$. As the experimentalist commonly manipulates the magnetization direction with an externally applied field \vec{H} , the thermodynamic potential suitable to describe a uniformly magnetized system is given by (with $H_m = \hat{m} \cdot \vec{H}$) [169, 170]

$$\mathcal{G}(T, H_m, \hat{m}, \varepsilon) = \mathcal{F}(T, M, \hat{m}, \varepsilon) - \mu_0 M H_m. \quad (2.1)$$

The temperature dependence can be explained by thermal fluctuations of the magnetization weakening the effective anisotropy [171–173]. It is important to note, that also the magnetization M is anisotropic [174] and depends on the applied field [175, 176] due to bandwidth and Fermi-level shifts in the presence of magnetoelastic deformations or interfacial spin pinning [177]. Neglecting the contributions due to stress ($\varepsilon = 0$) the free energy may be written as the sum of intrinsic crystalline anisotropy energy, the surface anisotropy energy, and the shape anisotropy

$$\mathcal{F} = \mathcal{K}_{Cryst} + \mathcal{K}_S + \mathcal{K}_{shape}. \quad (2.2)$$

The shape anisotropy is due to the long range dipolar interaction. In case of a plate of infinite lateral dimensions the demagnetization tensor is given by \hat{n} , the surface normal, and $\mathcal{K}_{shape} = K_{shape}(\hat{n} \cdot \hat{m})^2 = 1/2\mu_0 M^2 \cos(\theta)^2$ with the angle $\theta = \angle(\hat{n}, \hat{m})$ [178]. This holds equally for multilayers substituting the global average for M and \hat{m} . The shape anisotropy has the effect of an externally applied field proportional to the magnetization component directed along the surface normal of the thin film.

The crystalline anisotropy basically originates from spin-orbit coupling [179, 180]. Normally a phenomenological description based on symmetry considerations is used to describe the crystalline anisotropy, although microscopic models have already been proposed by Bloch and Gentile [179], van Vleck [180], and Néel [181]. Since the anisotropy energy only contributes a minor fraction to the total energy of the system, its proper ab-initio calculation remains a challenge in computational physics [182–

185]. Taking into account only the even terms in the magnetization direction (because of time-reversal symmetry) one may write

$$\mathcal{K}_{Cryst}(H_m, \hat{n}) = \sum_{l \text{ even}} \sum_{m=-l}^l \kappa_l^m(H_m) Y_l^m(\hat{n}), \quad (2.3)$$

expanding in spherical harmonics. While this approach has the advantage of forming a complete set of orthonormal functions, traditionally the anisotropy is rather expanded in terms of the direction cosines $(\alpha_x, \alpha_y, \alpha_z)$ of \hat{n} :

$$\mathcal{K}_{Cryst}(H_m, \hat{n}) = k_0(H_m) + \sum_{i,j} k_{ij}(H_m) \alpha_i \alpha_j + \sum_{i,j,k,l} k_{ijkl}(H_m) \alpha_i \alpha_j \alpha_k \alpha_l + \dots \quad (2.4)$$

Similarly the magnetization can be expanded with expansion coefficients related to those of the anisotropy by the Maxwell relation

$$M_{ij\dots qr}(H_m) = \frac{\partial k_{ij\dots qr}(H_m)}{\partial H_m}. \quad (2.5)$$

However, here the conventional simplification of constant (field independent) magnetization in the domains is assumed. Crystal symmetry imposes restrictions on the expansion coefficients, and a general method on how to derive the expansion coefficients of tensors of arbitrary order has been given by Birss [186]³. Ferromagnetic materials with microscopically unidirectional spin arrangements can be described by the 32 classical pointgroups. For these, Döring [192, 193] has derived generating functions for all classical point groups which allow to write down the expansion permitted by the crystal symmetry to arbitrary order (see Chapter 4). In general only few expansion terms are needed. For an orthorhombic crystal we may write the following, taking terms up to fourth order:

$$\begin{aligned} \mathcal{K}_{Cryst}^{ortho}(H_m, \hat{n}) &= k_0 + k_{11}\alpha_1^2 + k_{22}\alpha_2^2 + k_{1111}\alpha_1^4 + k_{2222}\alpha_2^4 + k_{1122}\alpha_1^2\alpha_2^2 \\ &= K_0 + \sin(\vartheta)^2(K_1 + K_2 \cos(2\phi)) \\ &\quad + \sin(\vartheta)^4(K_3 + K_4 \cos(2\phi) + K_5 \cos(4\phi)). \end{aligned} \quad (2.6)$$

The coefficients in the second line are related to those in the first line as $K_0 = k_0$, $K_1 = (k_{11} + k_{22})/2$, $K_2 = (k_{11} - k_{22})/2$, $K_3 = (3(k_{1111} + k_{2222}) + k_{1122})/8$, $K_4 = (k_{1111} - k_{2222})/2$, and $K_5 = (k_{1111} + k_{2222} - k_{1122})/8$. The choice of the expansion factors and hence the coefficients is not unique, and sometimes even more coefficients than necessary are given (see e.g. Mason [194]). Tetragonal (orthorhombic) expansion can be written in the form $\mathcal{K}^{cube} + \mathcal{K}^{uniaxial}(\alpha_3^2)(+\mathcal{K}^{uniaxial}(\alpha_2^2))$, i.e. by adding one (two) uniaxial anisotropy term(s) to the cubic expansion.

³The combination of time reversal and spatial rotation may lead to further simplification, which led to criticism [187–189] and minor corrections [190, 191] to the method.

At interfaces or surfaces, the environment of the magnetic atoms is changed as compared to the bulk leading to a symmetry breaking and potentially to the appearance of additional terms in the anisotropy energy [195]. The magnitude of this effect depends on the sort of interface atoms, while its symmetry reflects the interface symmetry [196, 197]. The cubic (001), (110) and (111) surfaces will contribute terms with tetragonal, orthorhombic and hexagonal symmetry respectively. For ultrathin films, the surface contributions to the magnetic anisotropy become the dominant terms [198]. There exists also a dipolar contribution to the surface anisotropy, but it is negligible in the case of flat surfaces [199], as is the case in our samples.

Multilayers

The multilayers studied in this work consist of stacks of identical bilayers. If they are sufficiently uniform and neglecting the surface effects, their behaviour may be described by the behaviour of a single bilayer. In a bilayer system, assuming uniform magnetization in the individual layers, the energy per area is then obtained as

$$E/A = t_A \mathcal{G}_A + t_B \mathcal{G}_B - \mathcal{J}_{AB} \hat{m}_A \cdot \hat{m}_B + 1/2 \mu_0 (t_A + t_B) (\vec{M}_{eff} \cdot \hat{n})^2, \quad (2.7)$$

with \mathcal{J}_{AB} denoting the linear exchange coupling between the layers, \hat{n} the surface normal vector and $\vec{M}_{eff} = (t_A \vec{M}_A + t_B \vec{M}_B)/(t_A + t_B)$ giving the total magnetization of the bilayer. Note that apart from the linear exchange coupling dipole interaction favours in-plane antiferromagnetic and out-of-plane ferromagnetic alignment. The shape anisotropy favours antiferromagnetic alignment in the out-of-plane direction.

2.2.2 Magnetoelasticity

As a collective phenomenon depending crucially on interatomic interaction, magnetism and magnetic properties are sensitive to deformations of the crystalline lattice. While the Heisenberg exchange interaction energy is isotropic and purely dependent on the distance, the dipolar coupling is a function of both the distance and the magnetization orientation with respect to the deformation direction [195]. The following higher order expansion terms (quadrupolar etc.) can usually be neglected. The exchange interaction is the dominant interaction, explaining why parameters like the ordering temperature can be manipulated by hydrostatic pressure. The dipolar interaction is usually much weaker and one might thus expect rather moderate changes to the magnetic anisotropy. The effect, however, may be strong if the deformation of the crystal lattice leads to a change in the orbital occupation similar to a Jahn-Teller distortion [200]. Phenomenologically, the symmetry and thus the form of the mathematical description remain the same, whereas the magnitude of the magnetoelastic coupling constants differ. Following Chikazumi [201, pp. 349], the magnetoelastic contribution to the magnetic anisotropy energy is obtained by

minimizing the elastic energy density E_{el} and the magnetoelastic energy density E_{me} which for cubic crystals are given by

$$E_{el} = \frac{c_{11}}{2} (e_{xx}^2 + e_{yy}^2 + e_{zz}^2) + \frac{c_{44}}{2} (e_{xy}^2 + e_{yz}^2 + e_{zx}^2) + c_{12} (e_{yy}e_{zz} + e_{zz}e_{xx} + e_{xx}e_{yy}) ,$$

with the elastic moduli c_{11} , c_{12} , and c_{44} , and

$$E_{me} = \frac{3}{2} \lambda_{100} (c_{12} - c_{11}) \left(e_{xx} \left(\alpha_1^2 - \frac{1}{3} \right) + e_{yy} \left(\alpha_2^2 - \frac{1}{3} \right) + e_{zz} \left(\alpha_3^2 - \frac{1}{3} \right) \right) - 3 \lambda_{111} c_{44} (e_{xy} \alpha_1 \alpha_2 + e_{yz} \alpha_2 \alpha_3 + e_{zx} \alpha_3 \alpha_1) ,$$

with the magnetoelastic constants λ_{100} and λ_{111} . Neglecting higher order coefficients of the magnetoelastic constants for films on cubic [001] substrates with strains $e_{xx} = e_{yy} = \epsilon$ and $e_{xy} = 0$ one obtains a correction to the magnetic anisotropy energy

$$\Delta E_{me} = 3 \lambda_{100} \epsilon \left(\frac{c_{12}^2}{c_{11}} - \frac{1}{2} (c_{11} + c_{12}) \right) \alpha_3^2 .$$

2.3 Transport

In the oxides studied, the classical free electron description used for metals does not hold. This is due to localization effects and readily seen from the violation of the Ioffe-Regel limit [109]. Still the temperature dependent resistivity can mainly be explained by the sum of residual resistivity ρ_0 , phonon scattering contributions $\rho_p(T)$, and a contribution due to spin disorder (magnon) scattering $\rho_m(T, M)$, which increases with decreasing long range order close to the curie temperature and above.

2.3.1 Magnetoresistance

Good conductors show a positive magnetoresistance due to the Lorentz force, which decreases the mean free path in electric field direction. Ferromagnetic materials often show a negative magneto resistance due to a reduction of spin disorder and consequently reduced spin mixing scattering events. Spin-orbit coupling results in an anisotropy of the resistivity with respect to the magnetization direction. A review in metallic ferromagnets was given by Campbell and Fert [202]. This anisotropic magnetoresistance (AMR) is due to suppression of spin mixing scattering when the magnetization is oriented perpendicular to the current. In manganites the AMR is small and only observable in films with high crystallinity [203], which makes it an indicator for film quality. The dominant effect in manganites is colossal magnetoresistance (CMR), which scales as

$$\Delta \rho / \rho_0 \sim \exp(-(M/M_S)^2) .$$

This can be understood by considering the double exchange with $\rho \sim \exp(-t^2) \sim \exp(-\cos^2(\Theta/2))$, here t is the transfer integral, which is proportional to the relative angle Θ of the magnetization direction [204]. Close to T_C phase separation mechanisms and percolation may also play a role [59, 75, 205].

Ziese [115] reviewed extrinsic effects to the magnetoresistance for a series of ferromagnetic materials. In low fields domainwalls may increase as well as decrease the resistance. This may be anisotropic since the magnetic domains orient their magnetization direction parallel to the easy axis. Thus the domainwalls between these domains run along the easy axis direction. At grain boundaries spin dependent tunneling may lead to enhanced magnetoresistance. This magnetoresistive effect shows a voltage dependence due to increased elastic scattering with loss of the spin polarization at increased currents.

2.3.2 Anomalous Hall Effect

Soon after his discovery of the effect named after him, Edward Hall found that this effect was much bigger in ferromagnetic materials [206]. This is due to the anomalous Hall effect (AHE)⁴, which may occur in systems of broken time reversal symmetry, e.g. a paramagnetic material in an applied magnetic field, or a ferromagnet showing spontaneous magnetization. Systematic studies by Pugh led to the empirical relation [207, 208]

$$\rho_{yx} = \mu_0(\rho_H H_\perp + \rho_{AHE} M_\perp),$$

where the off-diagonal part of the two dimensional resistivity tensor ρ_{yx} is a measure of the voltage drop in y direction upon the application of a current in x direction with the magnetization and magnetic field components in z direction. The two factors ρ_H and ρ_{AHE} are the ordinary and anomalous Hall constants respectively.

A first theoretical description of the anomalous Hall effect was given by Karplus and Luttinger [209], who recognized an additional contribution to the group velocity of electrons under application of an external field, which is directed perpendicular to the applied field. While this contribution normally cancels, it can survive in magnetic materials due to the spin split bands. The proportionality to magnetization arises from the fact that the splitting of the bands with opposite spin is proportional to the magnetization. This effect is present in the absence of disorder and was thus termed *intrinsic*⁵. Since $\rho_{yx} \approx \sigma_{xy}/\sigma_{xx}^2$, it is proportional to ρ_{xx}^2 . The dependence of the AHE constant on impurities led Smit [211, 212] to favour a mechanism based on asymmetric scattering from impurities due to spin orbit interactions, called *skew scattering*, which is proportional to ρ_{xx} . Berger [213, 214] argued that a second impurity related scattering mechanism should dominate, *side-jump scattering*, which is proportional to ρ_{xx}^2 .

⁴Sometimes the term extraordinary Hall effect (EHE) is used in the literature.

⁵Luttinger [210] revisited this topic and identified more intrinsic contributions.

In their recent review Nagaosa et al. [215] suggest a phenomenological parsing of the contributions to the anomalous Hall effect. Instead of relating specific microscopic scattering mechanisms to the observed effect, they classify them by their dependence on the Bloch state transport lifetime (i.e. the conductance). The recent advances in the theoretical understanding of the effect and its connection to geometric concepts of the Berry phase and Berry curvature allow in principle a quantitative comparison to experiments. The semiclassical treatment forming the link between microscopic theory and experimental observables has been reviewed by Sinitsyn [216]. Besides the Berry curvature in momentum space, contributions to the anomalous hall effect arise from noncoplanar spin structures, which give rise to a real space Berry curvature [215, 217]. While in SrRuO₃ the complex band structure with band crossings close to the Fermi surface gives rise to the anomalous Hall effect [122], in manganites the AHE was related to these noncoplanar spin configurations [218]. In this picture, thermal fluctuations of the spins induce a spin chirality acting as an additional effective field.

In single crystals the anomalous Hall effect may be anisotropic. Already Kohler [219] considered symmetry constraints on the manifestation of the Hall effect in single crystals. Based on group theoretical reasoning, the symmetry of the crystal should be reflected in the AHE [186, 220]. Only if the magnetization is directed along a high symmetry direction of the crystal, the above formula holds. In other cases the AHE "constant" is actually a function of the current, voltage measurement, and magnetization directions, $\rho_{AHE} = \rho_{AHE}(\vec{e}_j, \vec{e}_V, \vec{M})$, which could as well be rewritten as a tensor. While the current and voltage measurement directions (\vec{e}_j, \vec{e}_V) are fixed with respect to the crystal axes, the magnetization does not necessarily follow the external stimulus in small applied magnetic fields, but its direction is determined by the magnetic anisotropy. Only recently theoretical calculations appeared concerning the anisotropy [221–224]. Large anisotropy of the anomalous Hall effect may be expected for materials with strongly spin orbit coupled bands. Measurements of the anisotropy of the anomalous Hall effect provide additional parameters to test the results of *ab initio* calculations.

2.3.3 Transport in Multilayers

Most of the samples studied consist of stacks of layers of the constituent materials. As long as the electric field in these multilayers is applied parallel to the interface, the calculation of the effective resistivity tensor is straight forward. Given the two dimensional resistivity tensor and its associated conductivity tensor

$$\rho = \begin{bmatrix} \rho_{xx} & -\rho_{yx} \\ \rho_{yx} & \rho_{yy} \end{bmatrix}, \quad \sigma = \rho^{-1} = \frac{1}{|\rho|} \begin{bmatrix} \rho_{yy} & \rho_{yx} \\ -\rho_{yx} & \rho_{xx} \end{bmatrix},$$

one calculates the resulting resistivity tensor as $\rho = (t^A + t^B)(t^A \sigma^A + t^B \sigma^B)^{-1}$, where the superscripts A and B refer to the two layer materials with the layer thickness t .

Thus we obtain:

$$\begin{aligned}
 \rho_{xx} &= \left(t^A \rho_{xx}^A |\rho^B| + t^B \rho_{xx}^B |\rho^A| \right) / t' \rho'^2, \\
 \rho_{yy} &= \left(t^A \rho_{yy}^A |\rho^B| + t^B \rho_{yy}^B |\rho^A| \right) / t' \rho'^2, \\
 \rho_{yx} &= \left(t^A \rho_{yx}^A |\rho^B| + t^B \rho_{yx}^B |\rho^A| \right) / t' \rho'^2, \\
 t' \rho'^2 &= \left((t^A)^2 |\rho^B| + (t^B)^2 |\rho^A| + t^A t^B (\rho_{xx}^A \rho_{yy}^B + \rho_{xx}^B \rho_{yy}^A + 2 \rho_{yx}^A \rho_{yx}^B) \right) / (t^A + t^B).
 \end{aligned}$$

Ignoring anisotropy in $t' \rho'^2$ (take $\rho = \sqrt{\rho_{xx} \rho_{yy}}$) and omitting all ρ_{yx}^2 terms as $\rho_{yx}^2 \ll \rho$ this can be simplified to (with $i, k = x, y$)

$$\rho_{ik} = \left(t^A \rho_{ik}^A (\rho^B)^2 + t^B \rho_{ik}^B (\rho^A)^2 \right) \frac{t^A + t^B}{(t^A \rho^B + t^B \rho^A)^2}.$$

The overall transport behaviour is dominated by the layer that conducts better, but the contributions vary depending on the anisotropy.

Sample Preparation and Experimental Techniques

Since long time physical experiments rely on apparatus extending the body senses of the experimentalist. The validity of any conclusions drawn on the outcome of these experiments directly depends on the theoretical description and understanding of the experimental setup [225, Chapter 8]. The following sections concentrate on highlighting the most important aspects of sample preparation and experimental techniques. As no new technique has been introduced, the reader is referred to the given references for more details. The section on experimental artefacts gives an account of typical pitfalls and viable work-arounds implemented in the data capture and analysis procedures of the results presented hereafter. It may serve as a reader for any person new to this specific field or as a refresh.

3.1 Pulsed Laser Deposition

Pulsed laser deposition (PLD) is a widely used versatile tool, which allows growth of materials otherwise only synthesized with difficulties. It gained popularity during the advent of high- T_C superconductors, and continuous gain in understanding led to compilations [226, 227] as well as a number of reviews [228–231], which give a good account of the possibilities and limitations of this technique. As depicted in Fig. 3.1, light pulses (duration of 30 ns) with a wavelength of 248 nm are emitted from a krypton fluoride excimer laser (LPX-300, Lambda Physik/Coherent) with a variable repetition rate (typically 3 Hz to 10 Hz) and a typical pulse energy of 0.4 J to 1 J. Various apertures allow to adjust the spot size on the target according to target size and lens position as well as selecting the energetically more homogeneous central region of the beam. A newly installed attenuator allows for better control of the provided ablation energy. It would be desirable to implement computer control, as the currently used energy adjustment via the thyristor voltage leads to a varying beam profile sacrificing reproducibility [232]. With the focusing lens both the spot size on the target (typically 1 to 5 × 4 to 12 mm²) and energy density (up to 8 J cm⁻²) are controlled¹. Up to three targets can be mounted on the target manip-

¹The spot location can also be controlled by small offsets of the optical axis.

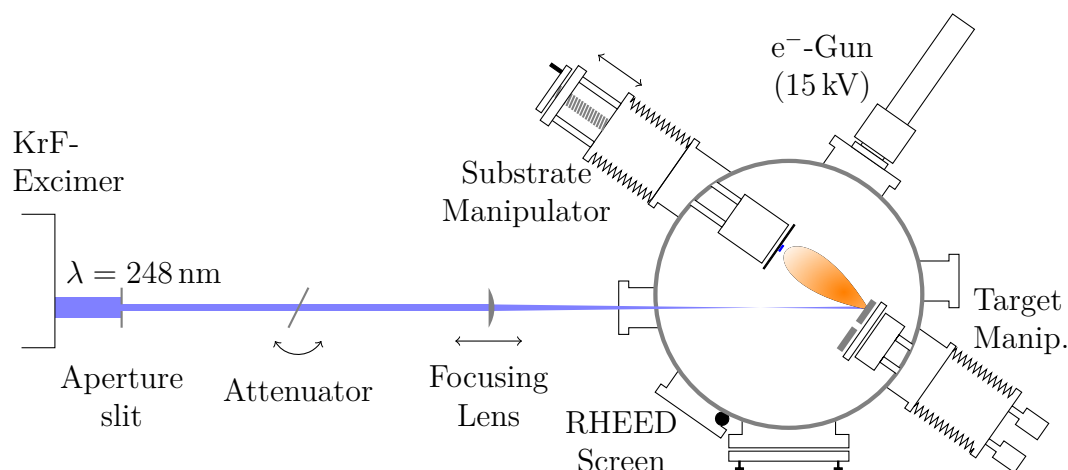


Figure 3.1: Sketch of the PLD setup (not to scale). Background gas inlet, pressure sensors and vacuum pumps are not shown.

ulator located behind the lens focus position. The angle of $\sim 45^\circ$ with the incoming beam unfortunately results in a gradient of few percent for the energy density on the target. The substrate is glued on a steel plate with silver or carbon paste and mounted in front of a resistive heater (platinum wires, $T_{\max} \sim 950^\circ\text{C}$) opposite to the target with adjustable distance (3 cm to 10 cm). For an accurate temperature control a type K thermocouple is fitted in a hole within the sample supporting plate; the actual sample surface temperature depends on the background gas flux. A shield protects the sample during initial target surface cleaning ablation. A manipulator (not shown) allows positioning of masks in front of the sample, a feature extensively used to study morphology dependence of the grown film on background gas pressure, laser spot size and laser energy. The installed RHEED² system is of no use, since the substrate manipulator cannot be rotated to align the crystallographic axes. Environment parameters (vacuum system³, oxygen partial pressure and sample temperature) are controlled manually; the PLD process is controlled via a computer interface with the ability to select pulse energy, frequency, and number of pulses⁴.

Main advantages of using a PLD setup are [229]: (i) almost any condensed matter can be ablated, (ii) growth rates can easily be controlled, (iii) ideally the stoichiometry of the target is exactly transferred to the sample, (iv) the kinetic energy of the ablated species is sufficient to promote surface diffusion but avoids bulk displacement, (v) the plasma provides species far from chemical equilibrium for alternative routes to material synthesis, (vi) the supersaturation in the plasma plume above the sample surface provides ideal conditions for initially dense nucleation and two-

²Reflection High-Energy Electron Diffraction, Staib Instruments GmbH

³Typical background pressure $< 10^{-6}$ mbar.

⁴This number is not strictly obeyed due to delays in the communication between the computer and the laser.

dimensional film growth.

Main drawbacks are: (i) possibility of particulate ejection, (ii) defects (and subimplantation) in the film caused by high kinetic energy particles, (iii) inhomogeneous angular energy and ion distribution in plume.

PLD systems vary substantially, and even more do so the optimal growth parameters published in literature. Off-stoichiometry can be induced by incongruent ablation below the ablation threshold of some species as well as different thermal diffusion lengths in the target [233, 234]. It has been known for long that species in the plasma plume are scattered differently according to their mass [235, 236], and varying the partial pressure of background gas changes the cation stoichiometry [237]. Still there is no consent as to which parameters describe the system appropriately, since most of the parameters directly accessible to the experimentalist are cross-linked. Changing the background gas pressure changes the kinetic energy of the incoming species [238, 239]. Thus one might increase the target sample distance, which in turn reduces the effective solid angle of the deposition and the growth rate. Cation stoichiometry is also changed by the spot size [240, 241], however, here also the laser fluence and deposition rate changed, which are other important growth parameters [142, 242]. The concept of plume size [243] links some of these parameters. Besides changes in bulk properties cation off-stoichiometry reduces the surface diffusivity and induces a transition from two to three dimensional growth regimes due to clustering [244] (see Section 3.5). And finally, the optimal parameters have to be precisely tuned to vicinal terrace dimensions for persistent two dimensional growth [245, 246].

3.2 Structural Analysis

3.2.1 X-ray Diffraction

X-ray diffraction (XRD) has been a valuable tool for structural analysis for more than a century. Thickness determination from interference fringes is nearly as old [247], but only with the advent of computers and the possibilities to simulate the diffractions was it made possible to extract more than the thickness of the bilayers and the averaged lattice parameter. The formalism has been worked out independently in the semiconductor [248, 249] and metallic multilayer [250, 251] community. For further review the interested reader is referred to Fewster [252]. A more accurate but less viable approach is to calculate the structure factor of a supercell consisting of the whole superlattice stack [253], which implies calculating and relaxing the positions of hundreds to thousands of atoms. Free parameters in the simulations can be reduced by measuring x-ray reflectivity curves [254].

For an appropriate description of the diffraction process in thin films the contributions from film and substrate must not be viewed independently. The electric field of the scattered light adds up and the intensity is proportional to the square of the

sum:

$$I \propto |E_{film} + E_{sub}|^2 .$$

The interference modifies the recorded spectra considerably, and ignoring the effect may lead to false conclusions regarding the lattice parameter of the film [255]⁵. The following paragraphs describe the situation in the Bragg geometry used ($\theta - 2\theta$ scan). For a full treatment of asymmetric diffraction geometries the reader may refer to the review given above or a textbook, e.g. by Holý et al. [256]. From dynamic theory [256] one obtains for the ratio r of the diffracted electromagnetic wave E_h with respect to the incoming wave E_0 for an infinitely thick crystal⁶:

$$r_{sub} = \frac{E_h}{E_0} = -\frac{\chi_h}{\sqrt{\chi_h \chi_{-h}}} (\beta \pm \sqrt{\beta^2 - 1}),$$

with

$$\beta = \frac{1}{P_A \sqrt{\chi_h \chi_{-h}}} ((\omega - \theta_B) \sin(2\theta_B) - \chi_0)$$

here E_h is the electric field scattered by the reciprocal lattice vector $h = 2\pi/d$, χ is the complex polarizability (which is derived from the structure factor [257]⁷), P_A is the polarization correction factor ($P_A = 1$ for σ polarization and $P_A = |\cos(2\theta)|$ for π polarization), $\theta_B = \arcsin(n\lambda/2a_{sub})$ the Bragg angle and ω the angle of incidence. For a thin film (which is much thinner than the extinction length) we may use a kinematic description [258]:

$$r_L = \frac{\chi_h}{2\beta_L} \left(\exp \left[-i \frac{2\pi\beta_L}{\lambda \sin(\theta_B)} t_L \right] - 1 \right) ,$$

with

$$\beta_L = (\omega - \theta_B) \sin(2\theta_B) - \chi_0 + 2 \sin(\theta_B)^2 \left(\frac{a_L}{a_{sub}} - 1 \right) ,$$

here a_L and a_{sub} are the lattice constants of the film and the substrate, and t_L is the thickness of the layer. For a thin film on a substrate we thus obtain

$$I = \left| r_{sub} \exp \left[-i \frac{2\pi\beta_L}{\lambda \sin(\theta_B)} t_L \right] + r_L \right|^2 ,$$

where the exponential is taking into account the damping and phase propagation in the thin film. For multilayers we may apply this formula recursively [258]:

$$r_k = r_{k-1} P_k + Q_k ,$$

⁵Unfortunately some of the formulas given in this paper are erroneous, although the plots were clearly obtained with correct formulas.

⁶At least thicker than the extinction length, so we can ignore backscattering from the back interface. This condition is fulfilled for our substrates of 0.5 mm.

⁷Online calculation program by Sergey Stepanov: <http://x-server.gmca.aps.anl.gov/x0h.html>

with

$$P_k = \exp \left[-i \frac{2\pi\beta_L}{\lambda \sin(\theta_B)} t_L \right] \quad \text{and} \quad Q_k = r_L = \frac{\chi_h}{2\beta_L} \left(\exp \left[-i \frac{2\pi\beta_L}{\lambda \sin(\theta_B)} t_L \right] - 1 \right).$$

From this recursive procedure we obtain

$$r_N = r_{sub} \prod_{j=1}^N P_j + \sum_{j=1}^N Q_j \prod_{k=j+1}^N P_k,$$

which simplifies in the case of an ideal superlattice (i.e. $Q_j \equiv Q, P_j \equiv P$) to

$$r_N = r_{sub} P^N + Q \frac{P^N - 1}{P - 1},$$

now with the constituents of the superlattice

$$\begin{aligned} P &= \exp \left[-i \frac{2\pi(\beta_1 t_1 + \beta_2 t_2 + \dots)}{\lambda \sin(\theta_B)} \right] \\ Q &= \frac{\chi_{h1}}{2\beta_1} \left(\exp \left[-i \frac{2\pi\beta_1}{\lambda \sin(\theta_B)} t_1 \right] - 1 \right) \\ &\quad + \frac{\chi_{h2}}{2\beta_2} \left(\exp \left[-i \frac{2\pi\beta_2}{\lambda \sin(\theta_B)} t_2 \right] - 1 \right) \exp \left[-i \frac{2\pi\beta_1}{\lambda \sin(\theta_B)} t_1 \right] + \dots \end{aligned}$$

where the order of the constituting layers (1...x) of the supercell is from the sample surface towards the substrate. The diffraction maxima of the superlattice satellites of order m are obtained from the condition

$$\sum_i \beta_i t_i = m\lambda \sin(\theta_B)/2.$$

When comparing these theoretically obtained diffraction curves of ideal superlattices with experimental ones, one has to account for, amongst others, the instrumental characteristics, interface roughness, interdiffusion, mosaicity of the sample, bilayer thickness variation and strain gradients. Measuring and fitting simultaneously three substrate peaks allows to unambiguously correct for ω (in the scan plane) and ϕ (perpendicular to scan plane) angular offsets. In practice one starts with the classically obtained Bragg-like condition

$$\sin(\theta_m) = \frac{m\lambda}{2t} + \sin(\theta_0),$$

ignoring changes in refractive indices and variation of the scattering power of the materials. Here θ_0 refers to the bragg angle of the mean out-of-plane lattice parameter of the superlattice structure as

$$\langle a_{\perp} \rangle = \sum_i a_{\perp i} t_i / t.$$

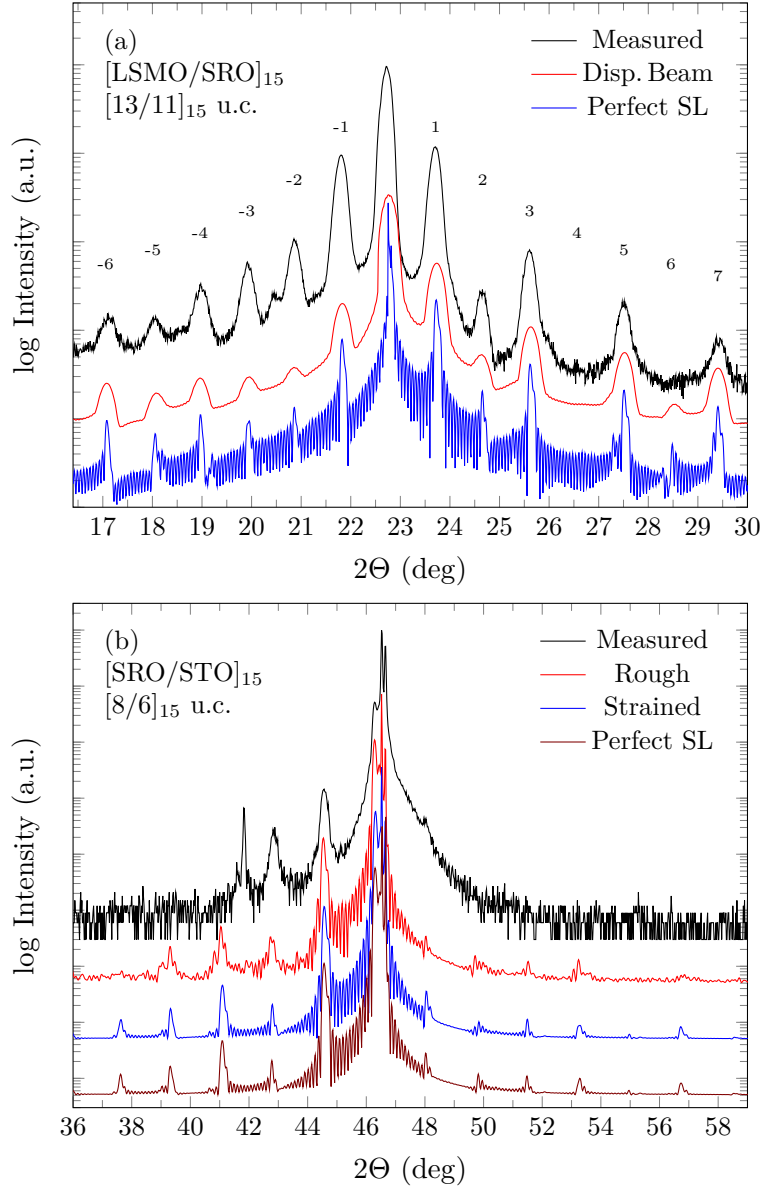


Figure 3.2: Measured and simulated diffraction curves of $\text{La}_{0.7}\text{Sr}_{0.3}\text{MnO}_3/\text{SrRuO}_3$ and $\text{SrRuO}_3/\text{SrTiO}_3$ superlattices on $\text{SrTiO}_3(001)$. Plots are vertically offset for better comparison.

These values provide a good starting point for simulating the diffraction curves. No attempt has been made in fitting, as the experimental data has been obtained by different operators on a number of diffractometers. For a direct comparison with recorded data, one has to convolute the simulated curves with the characteristics of the experimental set-up⁸. Yet it is still possible to extract valuable quantitative information from a qualitative comparison. In Fig. 3.2(a) we show the x-ray diffrac-

⁸In the simulations presented, we only account for Cu K_{α_1} and K_{α_2} with σ and π polarization.

tion of a $[\text{La}_{0.7}\text{Sr}_{0.3}\text{MnO}_3/\text{SrRuO}_3]_{15}$ superlattice (top) along simulations of an ideal superlattice without (bottom) and with (center) some beam dispersion. It is remarkable how well characteristic features of the data – like extinction of certain satellites and the variation of the intensity between the satellites – are reproduced. These characteristics are highly sensitive to the ratio of the bilayer constituents and their respective unit cell size⁹. Absence of superlattice peaks is not necessarily related to inferior quality of the samples. Figure 3.2(b) shows the example of a $\text{SrRuO}_3/\text{SrTiO}_3$ superlattice (top) around the $\text{SrTiO}_3(002)$ diffraction peak. Even the simulation assuming a perfect superlattice (bottom) shows suppression of satellites with positive index. The other two simulations exemplify the effect of strain relaxation¹⁰ and interface roughness on the order of one unit cell¹¹. Indeed, HAADF-STEM images suggest interdiffusion on the order of one to two unit cells.

One direct check for single crystals of orthorhombic SrRuO_3 is the suppression of the $(201)_o$ reflection (close to the cubic substrates (121) or (211) reflections). In superlattices however, the satellites may still be visible due to the second material involved. Unfortunately we could not perform the necessary measurements to study this effect.

3.2.2 Atomic Force Microscopy

Atomic force microscopy (AFM) is an indispensable tool when studying thin films. Valuable information concerning success of substrate pre-treatments, morphology and thin film growth modes, inclusions and crystallite size (see Section 3.6.5), as well as alignment of the vicinal miscut with respect to the crystallographic axes can be obtained. In the most frequently used tapping mode, a sharp (few nm) tip (usually Si_3N_4) at the end of an piezo driven vibrating beam is scanned across the sample surface. The vibration close to the resonance frequency of the beam is modulated due to tip surface interactions shifting amplitude and phase. Both shifts may be used as a feedback signal to adjust the vertical position of the probe to maintain a constant tip surface distance. The height, amplitude and phase signals are recorded and reveal information regarding topography and surface termination. Since the used Dimension-3000 microscope with a Nanoscope IIIa controller¹² is about 20 years old, the piezos controlling lateral and vertical positioning show considerable drifts which have to be taken into account. Recording resolution is limited to 512 points laterally and 4096 points vertically, so the piezo drive voltage range has to be adjusted to optimize height resolution while taking into account the reduced

⁹The presented simulation suggests a SrRuO_3 content of 47% (11.4 u.c.), already a change of 1% results in a +4 satellite

¹⁰ SrRuO_3 strained to the substrate assuming a Poisson ratio of 0.33, relaxes towards the surface.

¹¹Roughness was simulated by superimposing several curves with random thickness variations in the bilayers.

¹²Digital Instruments Inc., then Veeco, now Bruker.

vertical manoeuvrability to prevent damaging the scan head¹³. On transparent and reflecting substrates the optical readout by a laser focused on the oscillating beam and a quadrant photo-detector may be affected by interferences.

3.2.3 Dual Beam Microscope

Scanning electron microscopy (SEM) is a valuable instrument for nanoscale characterization. Besides the high lateral resolution its main advantages are the huge range in magnification and a large focal depth. The used FEI-200 nanolab dual beam microscope comprising a 30 kV field emission electron beam column and a Ga⁺ ion beam column allows for imaging of the topography by scanning the electron beam over the surface, and nanoscale patterning with the help of the ion beam. Cutting trenches with the ion beam and imaging the cross section with the e⁻-beam allows thickness determinations, however, the resolution is not sufficient to distinguish the sub-nanometre sized layers in this study, which were thus characterized with high resolution STEM (Section 3.2.4). Proper choice of the detector settings and the electron beam energy allows for predominantly topography or material contrast by selecting secondary or backscattered electrons.

The system is further equipped with an energy dispersive x-ray spectroscopy (EDX) detector allowing identification of the elemental composition by the characteristic x-ray energies from electron decay to beam induced holes in the lower energy levels. The limited accuracy ($\sim 1\%$) and the substantial background from the substrate in case of thin films does not allow for exact stoichiometry determination, but qualitative trends may be obtained. In combination with electron beam scanning, maps of the elemental composition can be made (see e.g. Section 3.6.5).

An attached ELPHY VI system (Raith GmbH) allows beam control for electron beam lithography. This has been used with a positive working poly methyl methacrylate (PMMA) e⁻-beam resist (AR-P 671.05 950K, All Resist GmbH) to define structures for patterning of the samples (see Section 3.5).

3.2.4 Transmission Electron Microscopy

High resolution scanning transmission electron microscopy proved to be essential in determining the sample quality. Contrast proportional to the nucleus charge obtained in high angle annular dark field (HAADF) detectors permit discrimination of the atomic species present in an atomic column. This may be further supported by simultaneously obtained EDX and electron energy loss spectroscopy (EELS), thus one can estimate atomic intermixing at the interface. The Fourier transform of the

¹³The height range determining the resolution can be adjusted to about 150 nm to 6000 nm, depending on the scan head. Missing this adjustments may result in wrong data in interleave lift modes (as magnetic force microscopy (MFM), Kelvin force microscopy (KFM, to measure the surface potential), and electric force microscopy (EFM)) as the height is not recorded correctly!

obtained images allows to visualize changes in the crystal symmetry like changing lattice parameters. Albeit oxides proved to be quite resistant against electron beam damage, care has to be taken choosing the proper probe current to avoid chemical modifications of the samples [259, 260]. In recent years, simultaneously acquired annular bright field images have allowed imaging of light atomic species like oxygen.

3.3 Transport Measurements

All the samples studied were characterized by transport measurements in a helium flow cryostat equipped with a variable temperature insert in the temperature range from 2 K to 300 K (Oxford Instruments). The cryostat was equipped with a 9 T superconducting solenoid, however, only the range up to 8 T was used in practice, as the full range is not implemented in the control software. Resistance was measured in a four point configuration either with a Lakeshore LS-370 "Resistance Bridge" or with a Keithley Model 182 voltmeter and a Keithley Model 6001 current source if the input resistance is too high ($\approx 100 \text{ k}\Omega$). In the former case a low frequency (16.2 Hz) alternating current is used, whereas in the latter case the K-6001 provides a constant current; the polarity is alternated to get rid of thermal voltages. Some transport measurements were done in a Quantum Design MPMS-7 system with the LS-370.

Most of the samples were studied in the shape of thin films, and the well-known Van-der-Pauw-Technique [261, 262] has been used for transport characterization. Van der Pauw showed that any singly connected sample with arbitrarily placed point contacts on its circumference can be mapped onto the upper half plane with the contacts placed on the x-axis and therefore fulfil the relation

$$\exp\left(-\frac{\pi R_{12,34}d}{\rho}\right) + \exp\left(-\frac{\pi R_{23,41}d}{\rho}\right) = 1,$$

where the subscripts denote the order of the contact placement on the samples circumference and $R_{12,34}$ is the resistance calculated by the voltage drop between $(V_4 - V_3)/I_{12}$. This equation can be solved iteratively, for example with the Newton method, or, with slightly less calculations, by the Banach fixed point method. The latter has been proposed recently by Cieřliński [263], who deduced from the appearance of the cross ratio in its derivation directly the useful identity $R_{12,34} + R_{13,42} + R_{23,14} = 0$. This implies for example, that if the resistivity anisotropy changes (as a function of temperature), the "cross" resistance $R_{13,42}$ may change sign.

According to a coordinate transformation originally proposed by Van der Pauw [264–266] (see Appendix A.1), an anisotropic sample is equivalent to an isotropic sample with sample dimensions multiplied by $x_i^{iso} = x_i^{ani} \sqrt{\rho_i/\rho}$, where ρ is the isotropic resistivity $\rho = \sqrt[3]{\rho_x \rho_y \rho_z}$ and the coordinate axes of the system correspond to the principal axes of the resistivity tensor.

In the special case of a rectangularly shaped sample, an analytic expression can be derived for the resistances to be measured. This has first been done by Logan [267, 268] and independently by Price [269] with the method of image charges. Both give equivalent formulas involving infinite sums or products, which can be either simplified in limiting cases [270, 271] or solved numerically [272]. However, after some additional transformations (see Appendix A) one arrives at an analytic solution

$$R_x = \frac{4}{\pi d} \sqrt{\rho_x \rho_y} \ln \left(\frac{\vartheta_3(0, q)}{\vartheta_4(0, q)} \right), \quad R_y = \frac{4}{\pi d} \sqrt{\rho_x \rho_y} \ln \left(\frac{\vartheta_3(0, q)}{\vartheta_2(0, q)} \right)$$

where the ϑ_i are the Jacobi Theta functions with nome $q = \exp \left(-\pi \sqrt{\frac{\rho_{yy} L_y}{\rho_{xx} L_x}} \right)$. With

$$\exp \left(-\frac{R_y \pi d}{\sqrt{\rho_x \rho_y}} \right) = \left(\frac{\vartheta_2(0, q)}{\vartheta_3(0, q)} \right)^4 = k^2 \quad \text{and} \quad q = \exp \left(-\pi \frac{K'(k)}{K(k)} \right)$$

the resistivities along the sample edges (which in our case correspond to the main crystallographic axes) are obtained as

$$\rho_x = \sqrt{\rho_y \rho_x} \frac{L_y K(k)}{L_x K'(k)}, \quad \rho_y = \sqrt{\rho_y \rho_x} \frac{L_x K'(k)}{L_y K(k)},$$

where $K(k)(K'(k))$ are the (complementary) complete elliptic integrals of the first kind with the elliptic modulus k .

Thus we are able to extract the in-plane components of the resistivity tensor along the sample edges, which correspond to the principal values if the samples are cut along the corresponding crystallographic directions. As a last remark we remind that the Van-der-Pauw method only yields the correct results if the samples are homogeneous (at least in the carrier concentration [273]), and the contacts are placed on the circumference of the sample and extend over the entire thickness¹⁴. A first check on the validity of the data are the reciprocity relations of the six possible contact configurations. Deviations may be either due to irregularity in the contact sizes and placements or inhomogeneity of the film [274].

3.4 Magnetization Measurements

Magnetization measurements were done in commercial magnetometers (MPMS-7 and MPMS-XL, LOT Quantum Design) with a field range of up to 7 T and a temperature range from 2 K to 390 K (800 K with an oven). The magnetic signal is detected with a radio frequency biased superconducting quantum interference device (rf-SQUID) sensor, which changes the frequency in an inductively coupled RLC-circuit proportional to the magnetic field penetrating the sensor [275]. The sample

¹⁴So the VdP method is clearly not suited for measuring e.g. microstructured graphite consisting of few weakly coupled multigraphene grains.

is moved in a second order gradiometer pick-up coil that induces a voltage which is back transformed to a magnetic field with suitable amplification at the sensor. This setup shields the sensor from the magnetic field used to magnetize the sample and removes all uniform magnetic signal within the gradiometer.

The samples are either clamped in plastic straws or glued with cryogenic varnish to slabs of glass, which ideally do not contribute to the magnetic signal, since they are uniform and extend over the gradiometer range. However, the high sensitivity readily reveals small inhomogeneities due to deformation of the plastic straw. For example, a small hole in a paramagnetic material will result in a temperature and field dependent diamagnetic signal. The obtained sample position dependent signal is fitted to the analytical curve of a magnetic point dipole in the centre of the pick-up coils with the magnetization aligned along the axis. The magnetic moment is obtained according to the fit.

Real samples are not point-like and small offsets from the axis are consequently inevitable. This has been studied by a number of authors [276–278] and geometric correction factors have been provided [279]. Contamination on edges may for example mimic an anisotropy with an out-of-plane magnetic moment enhanced by more than 20% in case of a $5 \times 5 \times 0.5 \text{ mm}^3$ sized sample, combining enhancement of the signal due to off-centring and apparent signal reduction due to the sample's spread along the measurement axis. This may be artificially further increased by subtracting a wrong diamagnetic background. Additional artefacts may arise from the superposition of substrate and sample signals [280]. In ultrathin films the substrate signal dominates the sample signal, thus the principally obtainable resolution of $10 \times 10^{-11} \text{ J T}^{-1}$ in the system may be limited due to the signal to noise ratio. The off-centred superposition of diamagnetic substrate and ferromagnetic film results in a quadrupole moment with a characteristic antisymmetric contribution to the position dependent response, which leads the fit procedure to assume a movement of the sample position. Additional hysteresis loops may appear at high fields due to hysteretic switching of the amplifier circuits and imperfect calibration. While not completely avoidable due to technical issues, most of these artefacts can be identified from parameters recorded in the data file and, if not corrected for, at least considered in the data interpretation. Additional artefacts related to the magnet, temperature control and impurities are described below (Section 3.6). A good account for possible artefacts and contaminations has been given by Garcia et al. [281]. A thorough survey on both technical issues of the apparatus and sample mounting has been given by Sawicki et al. [279].

3.5 Patterning of Samples

Since access time to the electron lithography setup was scarce, only few patterning tests could be made. In a first attempt the desired structure was directly cut with the Ga-Ion beam of the FEI-Novalab 200 setup. To protect the sample from radia-

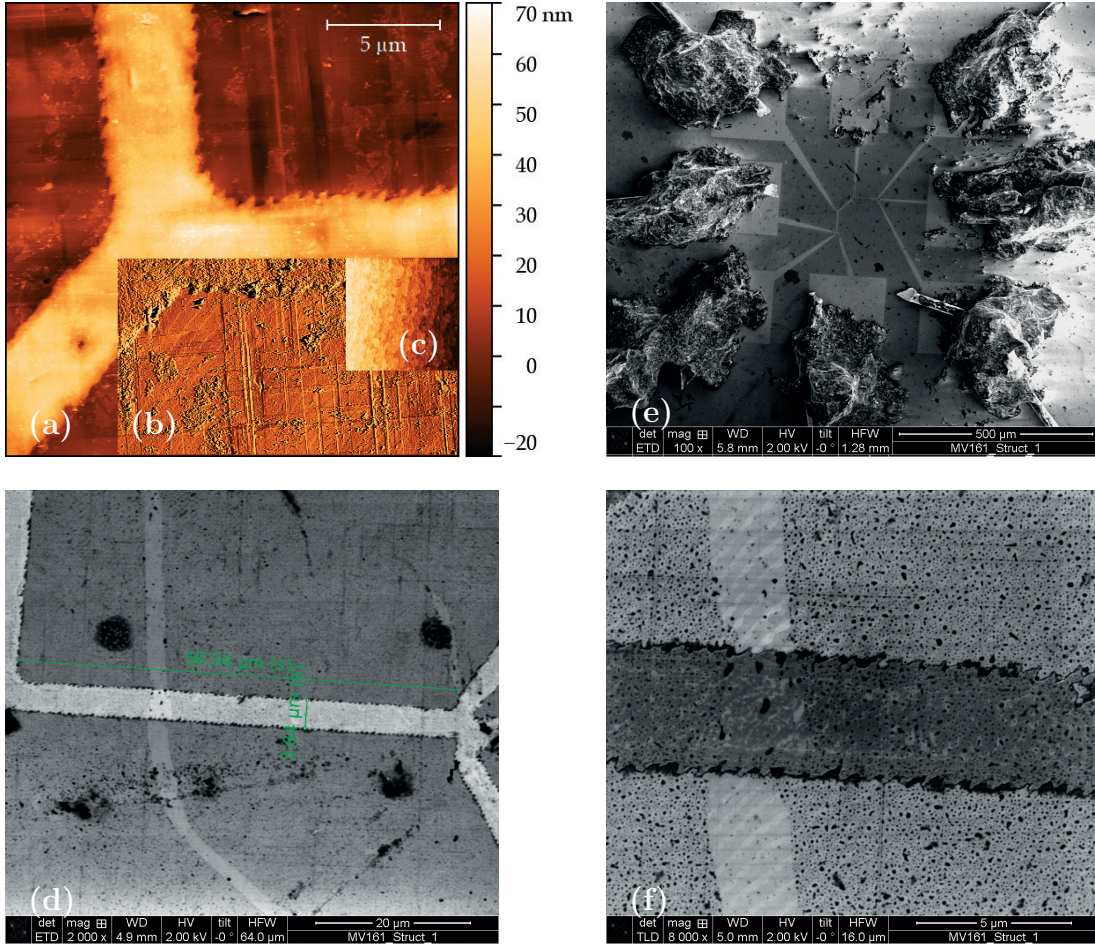


Figure 3.3: (a) AFM height image of structure defined by e-lithography and wet etching in an $[\text{LSMO } 6/\text{SRO } 4]_{15}$ SL. In the overlaid AFM amplitude image (b), the vicinal terraces are visible; for comparison in (c) the surface of the film before patterning. (d) SEM image of one arm of the defined structure. The whole structure with contacts (e). Contact pads are $200\mu\text{m}$ in size. SEM image in downhole-mode showing vicinal terraces (f). Note the irregular etching and orthogonal ruptures on the substrate.

tion damage it was covered by a $\sim 600\text{ nm}$ thick PMMA layer. The desired Hall-bar structure was defined by electron lithography in the PMMA and consequently the ion beam should cut the structure in these predefined troughs. In consequence of the huge area, this method proved to be very time consuming, requiring continuous corrections due to drifts and manual checking of failures in the cutting process, which again leads to electric leakage and shorts via intact sample material in the surrounding.

In a second approach chemical wet etching was employed. This method is more time and cost effective as it requires only one electron lithography step. While managanites are easily etched with $\text{HCl} + \text{KI}$ in H_2O [282] the Ru^{4+} ions in SrRuO_3

are not measurably attacked by any acid [283], but they can be oxidized with periodate as oxidizing agent [284]. In etching tests no significant damage of the used $\text{NaIO}_4(\text{aq})$ on the SrTiO_3 substrate or $\text{La}_{0.7}\text{Sr}_{0.3}\text{MnO}_3$ film was detected¹⁵. However, the PMMA used to define the structure is readily attacked. An easy work-around with the laboratory means at hand was found in the following procedure: (1) Definition of the desired shape with e-beam lithography in a positive working resist. (2) Sputter deposition of a thin gold layer and lift-off. (3) Etching of the superlattice (SL) not protected by Au alternating manganite and ruthenate etch solutions and rinsing in between with deionized water. (4) Finally the Au cap is dissolved in a dilute $\text{KI:I}_2:\text{H}_2\text{O}$ solution. To prevent premature dissolution of the gold, a KI free etching solution for the manganite was used. Using an ultrasonic bath and gently rubbing with a cotton stick reduces precipitates on the sample surface.

Figure 3.3 shows AFM and SEM images of a structure etched in a $[\text{LSMO}6/\text{SRO}4]_{15}$ superlattice. The images were obtained after transport measurements at cryogenic temperatures, which explains some of the dirt. Clearly a system of orthogonal lines is visible indicating enhanced etching along substrate ruptures. These ruptures are approximately aligned to the substrate edges and probably follow the principal crystallographic directions $[100]$ and $[010]$. They may be a result of repeated thermal cycling through the structural transition of SrTiO_3 (see Section 2.1.1) in the previous magnetic and transport measurements¹⁶. Another feature are cusps on the structure directed at 50° from the horizontal. A closer inspection (see Fig. 3.3(b) and (f)) reveals that these cusps are located at the edges of vicinal terraces directed along them. This reduced etching at the terrace steps may hint at stoichiometric variations close to the step edges.

3.6 Typical Artefacts

In the following we discuss some artefacts which typically may appear in transport and/or magnetization measurements.

3.6.1 Temperature

Temperature stabilization is the primordial requirement to a cryostat. Nevertheless, the exact sample temperature is often offset due to temperature gradients. In the Oxford Cryostat the gradient between the thin film exposed directly to the flowing helium gas and the copper block, which serves as thermal sink, equipped with the thermometer and a resistive heater is mainly due to the lower thermal conductivity of the circuit board used as sample support and the insulating substrate (the latter

¹⁵Albeit the formation of small amounts of permanganite cannot be excluded [285].

¹⁶The sample has been completely characterized before attempting the patterning.

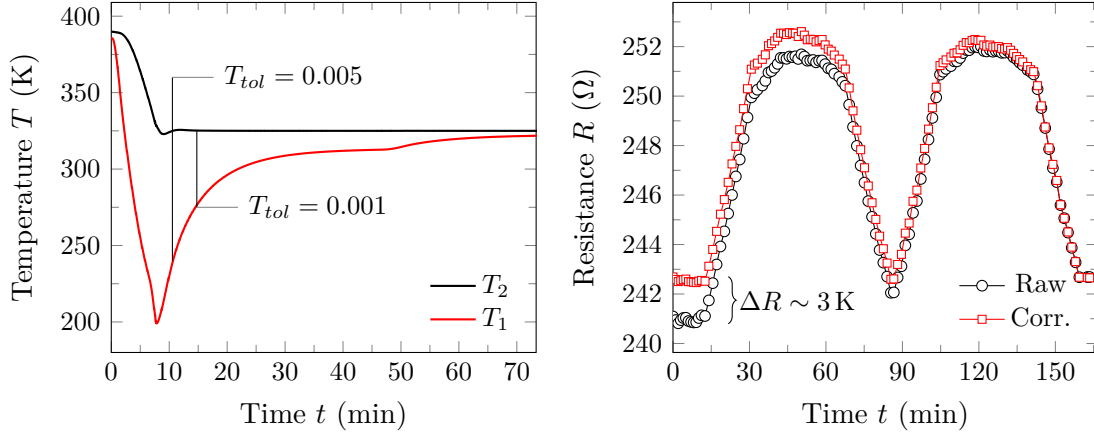


Figure 3.4: Temperature drift examples in the magnetic properties measurement system (MPMS). Left: Readings of the two thermometers in the MPMS vs. time. Marks show where the system considers the temperature to be stable according to the tolerance factors given. Right: Resistance vs. time of a R vs. H measurement at 300 K and the corrected data.

is partially shunted by the contact leads). The temperature of the helium gas is controlled by a heater installed in the variable temperature insert (VTI) at the inlet of the needle valve controlling the gas flow and adjusted to 2 K to 3 K below the setpoint. To minimize thermal gradients the cryostat is cooled below the lowest temperature of interest and allowed to stabilize. Then the temperatures of interest are set by the following procedure: first a temperature 3 K to 5 K above the temperature of interest is set and stabilized within typically 0.1 K for some minutes to allow for warming and settling of the surroundings; then the actual temperature of interest is set and stabilized within 1 mK to 4 mK for at least 20 min. Depending on the temperature step, still some drift may be observed, which may cause major resistance changes depending on the temperature coefficient of the sample. Thermal drifts were corrected assuming an exponential approach over time to some final value. It is highly recommended to measure the drift behaviour several minutes before changing another parameter (e.g. magnetic field, angle) to be able to disentangle the respective contributions. The temperature uncertainty of the CernoxTM thermometer due to the magnetic field is smaller than 1% at 4 K and negligible above 30 K [286].

In the MPMS system the situation is even more problematic, since no thermometer can be attached directly to the sample. The system comes equipped with two thermometers, T_1 at the gas inlet above the gas heater, and T_2 close to the actual sample position on the outer wall of the sample tube on top of the chamber heater. The cooling gas flows in a tube around the actual sample chamber. In Fig. 3.4 on the left the readings of the two thermometers are plotted after cooling from 390 K to 325 K. The vertical lines indicate when the software considers the temperature as stable according to the two temperature tolerance factors given. There is still a

temperature difference between the two thermometers of 86 K (50 K) for a temperature tolerance setting of 0.005 (0.001). While this may be of smaller importance in case of small samples clipped in a plastic straw for magnetization measurements, this has consequences for transport measurements, which involve a wooden sample holder with considerable heat capacity. Figure 3.4 on the right shows resistance vs. time of a R vs. H measurement at 300 K in the MPMS and the temperature drift corrected data. The drift in the resistance corresponds to a temperature drift of 3 K, although the sample was allowed to stabilize for 30 min coming from 250 K. Such a temperature drift can always mimic a hysteretic behaviour. Besides checking the data with care, an easy test is using the same sequence with a material of opposite temperature dependence. If the materials are non-magnetic and the hysteresis is reversed, it is almost certainly due to a temperature drift.

Temperature dependent measurements are often done in sweep mode to save both time and resources. These measurements are again prone to artefacts as the temperature gradient in the sample space cannot be controlled and varies from run to run. Simply subtracting a zero field cooled curve (ZFC) from a field cooled curve (FC) may thus lead to misattribution of hysteretic effects. Before claiming seemingly spectacular results one should therefore double check by measuring both FC and ZFC¹⁷ with stabilized temperatures and in the same sequence, i.e. increasing the temperature.

3.6.2 Fluxpinning in Superconducting Solenoid

The sample holders used in the laboratory's cryostats are equipped with hall sensors to correct for pinned flux in the superconducting magnet and to check the angle between sample normal and applied field. For some reason, the data acquiring software reads out the field data from the magnet power supply after reading the data of all the other devices. Thus, if the magnet is in sweeping mode, the field data saved in the datasets is ahead with respect to the acquired data. It should be noted that this is purely a software effect and not, as one might expect at first glance, due to induction in the coil (the coil is current driven). In Fig. 3.5 the difference $\Delta\mu_0 H = \mu_0 H_{Hall} - \mu_0 H_{IPS}$ between the magnetic field calculated from the Hall data and the magnet power supply is shown. On the left one can see an opening at low fields as one expects for frozen flux in the superconducting coil, i.e. the real magnetic field is ahead with respect to the drive current, which may result in inverted hysteresis loops. The temperature dependence is unexpected and can be explained by two hypothesis: (a) the Hall sensor has some superconducting part (not very probable), (b) the pumping on the sample space required to achieve these low temperatures cools down the whole helium reservoir causing a lower magnet

¹⁷ZFC measurement is done with an applied field heating up the sample after cooling in zero field. FC is normally measured during cooling in an applied field.

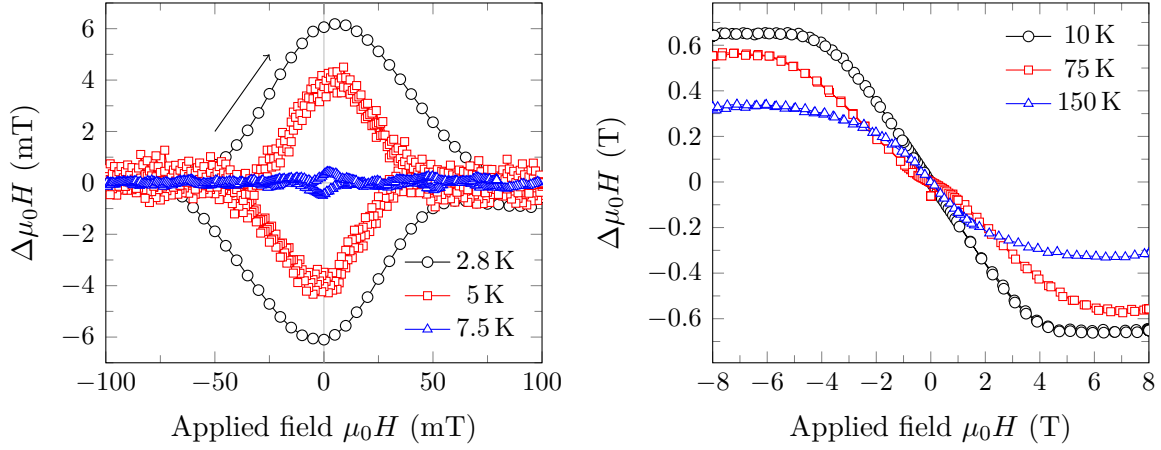


Figure 3.5: Difference $\Delta\mu_0 H$ between the magnetic fields obtained from the Hall sensor and the one provided by the magnet power supply vs. the nominal field from the magnet power supply. On the left a temperature dependent opening when operating at low temperatures. On the right the temperature dependent nonlinearity of the Hall sensor at selected temperatures.

temperature and stronger flux pinning in the NbTi solenoid¹⁸. The dataset at 2.8 K was acquired after settling the magnetic field at each point whereas the other two datasets were obtained in sweeping mode. The noise is partially due to the limited number of digits the magnet power supply can provide (resolution of 1 mT) and was reduced in the 7.5 K data by averaging.

Flux pinning is slightly worse in the MPMS and may result in inverted hysteresis loops for soft magnetic materials, initially negative magnetization after ZFC, and switching of the magnetic polarization in a remanence measurement due to a remanent field in the solenoid¹⁹. This is a major issue when continuously measuring at low fields, as flux depinning only takes place in fields ≥ 1 T. Remanence can be reduced demagnetizing the magnet by applying alternating fields with starting field ≥ 1 T²⁰, and consecutive magnet reset²¹. Alternatively, one can correct the data with reference data obtained using the same sequence with a strongly paramagnetic calibration standard (Pd or Dy₂O₃) [289, 290]. In remanence measurements one may apply a small field opposing the remanence of the solenoid effectively establishing zero field.

¹⁸It is interesting to note that this temperature dependence exactly mimics the behaviour of supposedly superconducting HOPG [287] measured in the same setup.

¹⁹Unawareness may lead to quasi-metaphysical conjectures, see e.g. [288].

²⁰Unfortunately the MPMS field setting in oscillating mode does not switch to the high resolution mode otherwise available for small fields.

²¹In a magnet reset the solenoid is heated to destroy the superconducting state.

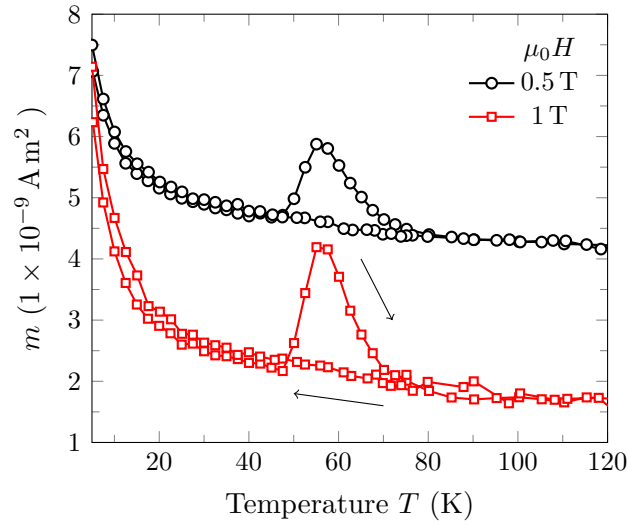


Figure 3.6: Magnetic moment m vs. temperature for a sample of multi wall carbon nanotubes showing a prominent magnetic signal around 50 K. Data courtesy of A. Setzer. Sample prepared by Dr. J. Barzola

3.6.3 Hall Sensor

The nonlinearity of the Hall sensor at high fields is shown in Fig. 3.5 on the right. This is no surprise as the used Halls sensors (Lakeshore HGT-2100 or 2101) are specified for an operating temperature from -55°C to $+125^{\circ}\text{C}$ and a field range up to 2 T (with 2% error). As the input resistance is of the order of $1\text{ k}\Omega$, instead of the nominal control current of 1 mA only $100\text{ }\mu\text{A}$ are used to avoid excessive heating. So instead of calculating the actual field from the Hall sensor data (which required an extensive set of temperature dependent parameters) the magnetic field data provided by the power supply is trusted. The Hall data, which is acquired simultaneously with the measurement of each of the multiplexer channels, is used to linearly interpolate between the actual field at time of measurement and the field saved in the data file (which is just one data entry for all channels used).

3.6.4 Oxygen Impurities

When working at cryogenic temperatures several artefacts may occur due to the condensation or freezing of gas impurities in the nominal helium atmosphere or leakage [291], the most common ones being nitrogen ($T_B = 77\text{ K}$, $T_m = 63\text{ K}$ [at normal pressure]) and oxygen (90 K, 55 K). The effects range from changes in the cooling rate in the cryostat to contact problems due to the vacuum enhancement in cryogen-free systems to small changes in the resistance of samples with high surface area. Exemplary, in Fig. 3.6 a ZFC-FC measurement of iron filled multi wall carbon nanotubes in two different applied fields is shown. The prominent

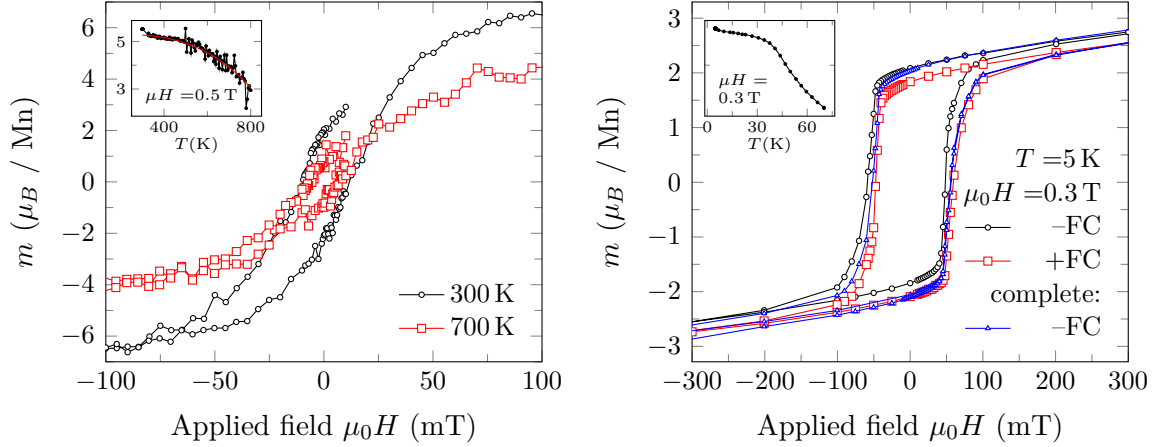


Figure 3.7: Left: Hysteresis measurements of an embedded 1 u.c. thick $\text{La}_{0.7}\text{Ba}_{0.3}\text{MnO}_3$ layer at elevated temperatures. Inset shows the temperature dependence with a mean field fit. Right: 15 nm $\text{La}_{0.7}\text{Sr}_{0.3}\text{MnO}_3$ on ~ 50 nm yttrium manganite (YMnO_3). Exchange bias shifted minor loops ($\pm 0.3\text{T}$) and a complete loop ($\pm 7\text{T}$) after field cooling in $\pm 0.3\text{T}$. Inset shows the magnetization increase around 45 K.

magnetic signal around 50 K to 70 K is probably due to condensing oxygen. During cooling, the oxygen gas condenses at the coldest point of the system at the bottom of the sample chamber outside the measurement region. Upon heating, this part is warmed up and the oxygen condenses on the colder sample with high surface area (nanotubes). Due to the reduced pressure in the sample chamber, the boiling point is reduced to about 60 K (nominal pressure 5 mmHg). In the experiment, the signal vanishes only at higher temperature, which may be due to a higher pressure in the sample space, an effectively colder sample, and surface adhesion. Oxygen in the liquid or solid γ -phase has a rather high mass susceptibility of $3.8 \times 10^{-6} \text{ m}^3 \text{ kg}^{-1}$ or $\chi = 5.2 \times 10^{-3}$ [292]. The paramagnetic moment in Fig. 3.6 corresponds to an oxygen volume of $V = m/(\chi H) = 6 \times 10^{-13} \text{ m}^3$ or a cube with sides of length 85 μm . In the gas phase this corresponds to 80 mm^3 at the reduced pressure in the sample chamber. Increasing the number of purging and flushing steps on loading the sample can slightly reduce this artefact, however, the volume at normal pressure already corresponds to only 3 ppm of the sample space gas volume. Assuming that in each purging and flushing cycle 99% of the gas volume are extracted, one ends up with at least 1 ppm air in the sample space after three cycles. The peak can be reduced by cooling more slowly, since the quantity of oxygen condensing in the part of sample space which is heated up upon heating depends on the temperature gradient. For more details on this sample see reference [293].

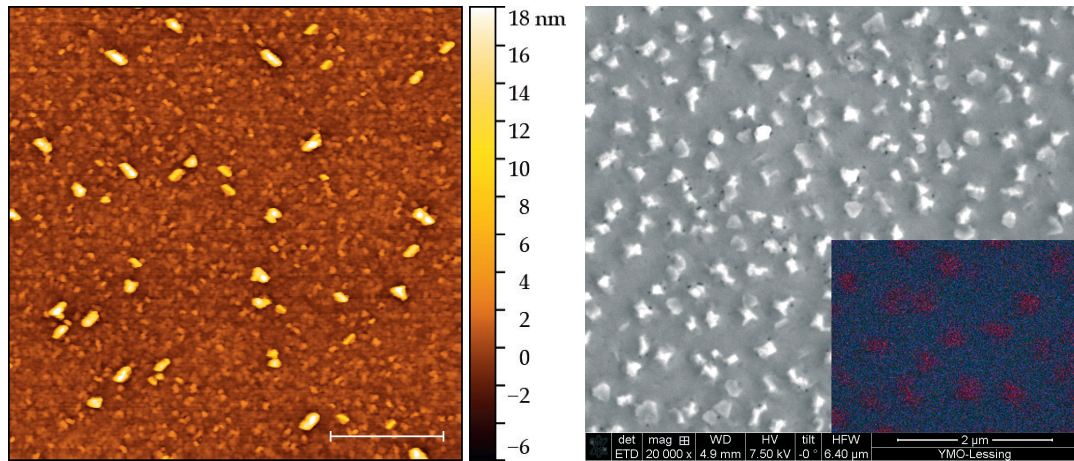


Figure 3.8: Left: Precipitates visible in AFM measurement of 15 nm $\text{La}_{0.7}\text{Sr}_{0.3}\text{MnO}_3$ on 45 nm YMnO_3 . White scale bar corresponds to 1 μm . Right: SEM image and EDX elemental map (Mn red) on ~ 300 nm YMnO_3 on SrTiO_3 grown by Dr. C. Zandalazini.

3.6.5 Magnetic Impurities and Minor Loops

The study of ultra thin films implies that the region of interest is only a minor fraction of the total sample volume. The signal of the film is small and impurities may give substantial contributions to the magnetic signal. This can be readily recognized if the coercivities of film and impurity (generally magnetically soft) are well separated, or if there is a sizeable magnetic moment above the critical temperature of the material studied. Figure 3.7 shows on the left hysteresis measurements of a one unit cell thick embedded $\text{La}_{0.7}\text{Ba}_{0.3}\text{MnO}_3$ layer at elevated temperatures. The temperature dependence in the inset was fitted within a mean field model. The obtained T_C is around 850 K, close to T_C of magnetite. Assuming magnetite as the main impurity, the measured moment corresponds to an amount less than 1×10^{-6} of the sample volume²². Most obvious sources for impurities are substrate preparation, the PLD process requiring gluing the sample to a steel support for good thermal contact, cutting the sample, and manipulation with inappropriate tools (e.g. steel tweezers) [281, 296]. Recording hysteresis loops at temperatures above the ferromagnetic transition temperature of the sample under study and subsequent subtraction of this data is a viable workaround. Before most, calculated hysteresis loops based on recorded high temperature data have been used since no additional noise is introduced.

²²Similar behaviour has been ascribed to a high temperature phase in the manganite layer [294, 295], however, this cannot be inferred without an element specific technique as e.g. XMCD. Absence of hysteresis in transport measurements also rules out the film as source of the magnetic signal.

Besides extrinsic impurities, intrinsic impurity phases may be created already during sample growth. Figure 3.7 on the right shows a $\text{La}_{0.7}\text{Sr}_{0.3}\text{MnO}_3/\text{YMnO}_3$ bilayer exhibiting exchange bias and a vertical magnetization loop shift after field cooling²³. This could be expected, since orthorhombic YMnO_3 has been reported to being antiferromagnetic with a transition temperature of around 45 K [298] (matching the peak in the inset of Fig. 3.7). Measuring up to higher fields reveals that the vertical shift is actually a minor loop effect. More recently ferromagnetic o-YMO has been reported [299, 300], but the close lying T_C of Mn_3O_4 (42 K) rises suspicion. No secondary phases could be detected by XRD, but AFM images reveal small precipitates, see Fig. 3.8. Thicker YMnO_3 films show bigger particulates and EDX elemental mapping revealed a manganese enriched phase. In LaMnO_3 films nano-sized Mn_3O_4 precipitates have been observed before [301–303]. Their coercivity increases upon size reduction to fields beyond 1 T [304], facilitating unintentional minor loops.

The YMnO_3 films presented were grown at elevated temperatures (800 °C to 850 °C), in which Mn_3O_4 is more likely to be formed than Mn_2O_3 in the pressure range available for PLD [305]²⁴. Growing at lower temperatures no particulates are formed, but unfortunately no detectable phase could be stabilized. Furthermore, no particulates were found in h-YMO films grown on Al_2O_3 under otherwise same conditions. Thus we may suspect tensile strain accommodation in the YMnO_3 film as the driving mechanism, incorporating manganese vacancies (the Mn^{3+} ion is considerably smaller than Y^{3+} [10]). Excess Mn subsequently agglomerates²⁵. This effect could be studied using a better matched substrate than SrTiO_3 , e.g. YAlO_3 .

We may conclude that experimental results are only as reliable as the knowledge of the technique used. Using complementary techniques may help gaining further understanding, albeit often at the cost of debunking apparently spectacular results.

²³This vertical shift is more accentuated when subtracting the slope at moderate fields, e.g. [297]

²⁴Only an issue if the particulates already form in the plasma.

²⁵Elevated growth temperature may assist this process by thermally activated diffusion.

Polynomial Expansion of Property Tensors in Crystals

In cases where a microscopic description of the physics involved is not feasible (either because no fundamental theory has been established, or, more commonly, because an exact description is too complicated or involves too many unknowns) one can still provide a frame for many phenomena based on group-theoretical reasoning. In the following, two approaches are briefly presented.

4.1 Birss: Symmetry Constraints on Property Tensors

In his treatise *Symmetry and Magnetism* Birss [186] shows that every crystal symmetry can be entirely characterized by a small set of generating matrices describing the symmetry operations. Any physical property of a crystal has to satisfy the same symmetry constraints as the crystal itself. A property tensor depending on the magnetization direction $\vec{a}(\hat{m})$ can be expressed as a power series with respect to the direction cosines of the magnetization $\alpha_i (i = 1..3, \hat{m} = \langle \alpha_1, \alpha_2, \alpha_3 \rangle)$. For the components $a_{i...n}$ and given generating matrices S a set of equations is obtained (Einstein sum convention applies):

$$\begin{aligned} a_{ij} &= S_{io} S_{jp} a_{op} \\ a_{ijk} \alpha_k &= |S| S_{io} S_{jp} S_{kq} a_{opq} \alpha_q \\ a_{i...n} \prod_{v=k}^n \alpha_v &= |S|^{rank-2} S_{io} \dots S_{nt} a_{o...t} \prod_{w=q}^t \alpha_w \end{aligned}$$

Here the appearance of the determinant $|S|$ as sign prefactor is due to the axial nature of the magnetization vector. In higher symmetry classes many of the components are equal to zero. Further simplification may arise due to property intrinsic symmetry (i.e. magnetostriction has to be an even function of the magnetization). This approach is very general and applies after inclusion of a time inversion operator not only to the classical 32 crystallographic classes but also to the 58 bicoloured

classes describing ferrimagnetic and some antiferromagnetic crystals¹. In Ref. [186] the non zero components up to tensors of rank four are given, McGuire and Potter [306] calculated the components for cubic crystals up to rank five. This approach has been successfully used in describing diagonal and off-diagonal magnetotransport properties [307, 308]. Limmer et al. [309] and co-workers [310–312] derived the components for cubic and monoclinic symmetry up to rank six (i.e. fourth order in magnetization) to study magnetostrictive effects in (Ga, Mn)As. For higher order expansion, a program was written in maplesoft’s Maple computer algebra software. However, the number of coefficients increases exponentially, so higher order expansion coefficients consist of sums of a large number of tensor components. Already an expansion to rank eight (i.e. sixth order in magnetization) for the point group $mmm(D_{2h})$ yields 17,214 equations, which can be reduced to 11,475 considering only the upper triangle. Identities in the equations lead to a reduction to 6,558 equations out of which 3,279 are non zero. Albeit one can reduce the number of equations by first evaluating the allowed symmetries [313, 314], these large numbers limit the practicability of this approach. As we only need the allowed symmetries up to tensors of rank two, the leaner approach of Becker and Döring was followed in this study.

4.2 Döring: Analytic Functions

Instead of first expanding a property tensor in an arbitrary polynomial and then reducing its components due to symmetry constraints, Becker and Döring [315, p. 134 et seqq.], based on previous considerations by Bethe [316], Heisenberg [317] and Gans and von Harlem [318], construct the tensor components with polynomials of functions already fulfilling the symmetry constraints. This method, initially developed for cubic symmetry, was generalized to all pointgroups for the anisotropy energy [192] and general property tensors of rank 2 [193, 319]. Further abstraction followed [320, 321], but does yet not facilitate the applicability.

According to this ansatz, the anisotropy energy and the components of a tensor fulfilling the symmetry constraints can be written as analytic function of the form

$$F(s, p) + \sum_{k=1}^3 q_k G_k(s, p),$$

where the arguments s, p, q are linearly independent polynomials of the direction cosines of the magnetization α_i . Only for the groups $\bar{1}, \bar{3},$ and $\bar{4}$ $q_2, q_3 \neq 0$, often $F(s, p)$ suffices. Döring [192] proved completeness and linear independence. In their original papers Döring and Simon had not considered further simplifications due to the axial nature of the magnetization vector. Their correction [193] oversimplifies

¹The combination of time reversal and spatial rotation may lead to further simplification, which led to criticism [187–189] and revision with only minor corrections [190, 191].

Point group of crystal	Point group in which functions of a vector have the same symmetry as functions of an axial vector in the groups on the left		Point group for symmetric phenomena (as magnetostriction, anisotropy etc.) (Laue class)	
$C_1, C_i(S_2)$	C_1	1	$C_i(S_2)$	$\bar{1}$
$C_2, C_S(C_{1h}), C_{2h}$	C_2	2	C_{2h}	$2/m$
$D_2(V), C_{2v}, D_{2h}(V_h)$	D_2	222	D_{2h}	mmm
C_4, S_4, C_{4h}	C_4	4	C_{4h}	$4/m$
$C_{4v}, D_{2d}, D_4, D_{4h}$	D_4	422	D_{4h}	$4/mmm$
$C_3, C_{3i}(S_6)$	C_3	3	C_{3i}	$\bar{3}$
D_3, C_{3v}, D_{3d}	D_3	32	D_{3d}	$\bar{3}m$
C_6, C_{3h}, C_{6h}	C_6	6	C_{6h}	$6/m$
$D_6, C_{6v}, D_{3h}, D_{6h}$	D_6	622	D_{6h}	$6/mmm$
T, T_h	T	23	T_h	$m\bar{3}$
O, T_d, O_h	O	432	O_h	$m\bar{3}m$

Table 4.1: Substitution table for the expressions obtained by Döring and Simon [319]. These equalities are also contained in the tables given by Birss [186].

in that it gives only solutions for phenomena which are even functions in the magnetization. As already stated by them, for phenomena depending on axial vectors, mirror planes have to be replaced by two-fold-rotations about an axis perpendicular to the mirror axis and the inversion is not a symmetry element. These replacements lead to the second column in Table 4.1. Due to the Onsager relations [322–324], for the resistivity $A_{ij}(\hat{m}) = A_{ji}(-\hat{m})$ holds. For the diagonal elements of the resistivity tensor (and other symmetric phenomena such as anisotropy and magnetostriction) inversion is a symmetry element resulting in column 3, which was already given in Ref. [193]. Thus, due to the axial nature of magnetization, one can only distinguish the eleven Laue classes by symmetry considerations.

4.2.1 Series Expansion of Resistivities of Orthorhombic (110)_o Oriented Thinfilms

On (100) oriented SrTiO₃ substrates with a vicinal miscut of 0.1° to 5° and with the in-plane projection of the surface normal being oriented along the [010] direction (at least within ~14° [138]), single crystalline thin films of orthorhombic SrRuO₃ can be grown [131, 139, 141]. These single crystalline films have their [001]_o axis oriented along the [100]_c axis of the substrate, which coincides with the step edge direction

of the substrate surface. The $[110]_o$ direction of the film is pointing along the $[001]_c$ direction of the substrate.

In transport measurements we apply the current in-plane along the sample edges $[\bar{1}10]_o$ and $[001]_o$. If we have the resistivity tensor with respect to the crystallographic axes, we calculate the measurable resistivity as

$$\rho = \vec{e}_V \bar{\rho} \vec{e}_j$$

with the unit vectors of the direction of applied current \vec{e}_j and measured potential drop \vec{e}_V . For the $[\bar{1}10]_o$ direction we have $\vec{e}_V = \vec{e}_j = (-1/\sqrt{2}, 1/\sqrt{2}, 0)$ and

$$\rho_{[\bar{1}10]} = 1/2(\rho_{11} + \rho_{22}) - 1/2(\rho_{12} + \rho_{21}),$$

and equally for the $[001]_o$ direction with $\vec{e}_V = \vec{e}_j = (0, 0, 1)$

$$\rho_{[001]} = \rho_{33}.$$

For the hall resistivity we measure two in plane configurations with flipped \vec{e}_V and \vec{e}_j and subtract them from each other. In this way the resistivity contributions along the current flow direction cancel. Assuming $0 \leq \angle(\vec{e}_j, \vec{e}_V) \leq \pi$ (right hand rule) we obtain

$$\rho_{yx} = 1/2 (\vec{e}_V \bar{\rho} \vec{e}_j - \vec{e}_j \bar{\rho} \vec{e}_V) / |\vec{e}_V \times \vec{e}_j| = 1/\sqrt{8}(\rho_{31} - \rho_{13} + \rho_{23} - \rho_{32}),$$

where the factor in the denominator accounts for eventual non-orthogonality.

The sample is rotated in an external magnetic field. The rotation axis is aligned with one of the sample edges. If the applied field is sufficiently large to align the magnetization to the external field and denoting with Θ the angle from the substrate normal (which is equal to $[110]_o$ within experimental resolution), we may distinguish the following cases:

Rotation in the $(001)_o$ Plane

We have

$$\begin{aligned} \alpha_1 &= (\cos(\Theta) - \sin(\Theta))/\sqrt{2}, & \alpha_1^2 &= 1/2(1 - \sin(2\Theta)), \\ \alpha_2 &= (\cos(\Theta) + \sin(\Theta))/\sqrt{2}, & \alpha_2^2 &= 1/2(1 + \sin(2\Theta)), \\ \alpha_3 &= 0, & \alpha_1 \alpha_2 &= 1/2 \cos(2\Theta). \end{aligned}$$

With $\Theta' = \Theta + \pi/4$ we may also write

$$\begin{aligned} \alpha_1 &= \cos(\Theta'), & \alpha_1^2 &= 1/2(1 + \cos(2\Theta')), \\ \alpha_2 &= \sin(\Theta'), & \alpha_2^2 &= 1 - \alpha_1^2 = 1/2(1 - \cos(2\Theta')), \\ \alpha_3 &= 0, & \alpha_1 \alpha_2 &= 1/2 \sin(2\Theta'). \end{aligned}$$

With help of the identities

$$\begin{aligned}\sin(x)^{2n+1} &= \frac{1}{2^{2n}} \sum_{j=0}^n (-1)^{n-j} \binom{2n+1}{j} \sin((2(n-j)+1)x), \\ \sin(x)^{2n} &= \frac{1}{2^{2n}} \left(2 \sum_{j=0}^n (-1)^{n-j} \binom{2n}{j} \cos(2(n-j)x) - \binom{2n}{n} \right), \\ \cos(x)^{2n} &= \frac{1}{2^{2n}} \left(2 \sum_{j=0}^n \binom{2n}{j} \cos(2(n-j)x) - \binom{2n}{n} \right),\end{aligned}$$

and recognizing that a series expansion in powers of α_i^2 consists of terms of the form (for $m \geq n$)

$$\alpha_1^{2m} \alpha_2^{2n} = 2^{-2n} \cos(2\Theta)^{2n} (1 - \sin(2\Theta))^{m-n},$$

we can write the measurable resistivities as

$$\begin{aligned}\rho_{[001]} &= K(\alpha_1^2, \alpha_2^2) = k_0 + k_1 \alpha_1^2 + k_2 \alpha_2^2 + k_3 \alpha_1^4 + k_4 \alpha_2^4 + k_5 \alpha_1^2 \alpha_2^2 \dots \\ &= \sum_{n=0}^{\infty} c_{4n} \cos(4n\Theta) + s_{4n+2} \sin((4n+2)\Theta) = \sum_{n=0}^{\infty} c'_{2n} \cos(2n\Theta'), \\ \rho_{[\bar{1}10]} &= \frac{B(\alpha_1^2, \alpha_2^2) + D(\alpha_1^2, \alpha_2^2)}{\sum c'_{4n} \cos(4n\Theta) + s'_{4n+2} \sin((4n+2)\Theta) = \sum c''_{2n} \cos(2n\Theta')} + \\ &\quad \frac{\alpha_1 \alpha_2 N(\alpha_1^2, \alpha_2^2)}{\sum s'_{4n} \sin(4n\Theta) + c'_{4n+2} \cos((4n+2)\Theta) = \sum s''_{2n} \sin(2n\Theta')} \\ &= \sum_{n=0}^{\infty} c''_{2n} \cos(2n\Theta') + s''_{2n} \sin(2n\Theta'), \\ \rho_{yx} &= \frac{\alpha_1 P(\alpha_1^2, \alpha_2^2)}{\sum c''_{2n+1} \cos((2n+1)\Theta')} + \frac{\alpha_2 R(\alpha_1^2, \alpha_2^2)}{\sum s''_{2n+1} \sin((2n+1)\Theta')} \\ &= \sum_{n=0}^{\infty} c''_{2n+1} \cos((2n+1)\Theta') + s''_{2n+1} \sin((2n+1)\Theta').\end{aligned}$$

Rotation in the $(1\bar{1}0)_o$ Plane

We have

$$\begin{aligned}\alpha_1 &= \alpha_2 = \cos(\Theta)/\sqrt{2}, & \alpha_1^2 &= \alpha_1\alpha_2 = \alpha_2^2 = 1/4(\cos(2\Theta) + 1), \\ \alpha_3 &= \sin(\Theta), & \alpha_3^2 &= 1/2(1 - \cos(2\Theta)).\end{aligned}$$

So we can write the measurable resistivities as

$$\begin{aligned}\rho_{[001]} &= K(\alpha_1^2, \alpha_2^2) = \sum_{n=0}^{\infty} c_{2n}''' \cos(2n\Theta) \\ \rho_{[\bar{1}10]} &= B(\alpha_1^2, \alpha_2^2) = \sum_{n=0}^{\infty} c_{2n}''' \cos(2n\Theta) \\ \rho_{yx} &= \sum_{n=0}^{\infty} c_{2n+1}'''' \cos((2n+1)\Theta).\end{aligned}$$

Rotation in the $(110)_o$ Plane

With $\Theta = 0$ aligned along $[001]_o$

$$\begin{aligned}\alpha_1 &= -\alpha_2 = \sin(\Theta)/\sqrt{2}, & \alpha_1^2 &= \alpha_2^2 = 1/4(1 - \cos(2\Theta)), \\ \alpha_3 &= \cos(\Theta), & \alpha_1\alpha_2 &= 1/4(\cos(2\Theta) - 1),\end{aligned}$$

we can expand the measurable resistivities as

$$\begin{aligned}\rho_{[001]} &= \sum_{n=0}^{\infty} c_{2n}'''' \cos(2n\Theta), \\ \rho_{[\bar{1}10]} &= \sum_{n=0}^{\infty} c_{2n}'''' \cos(2n\Theta), \\ \rho_{yx} &= \sum_{n=0}^{\infty} s_{2n+1}''' \sin((2n+1)\Theta).\end{aligned}$$

In Fig. 4.1 we present angle dependent magnetoresistance data at 150 K of a orthorhombic SrRuO₃ film. Data obtained by M. Ziese [8]. Note the substantial difference in symmetry after applying the geometrical corrections.

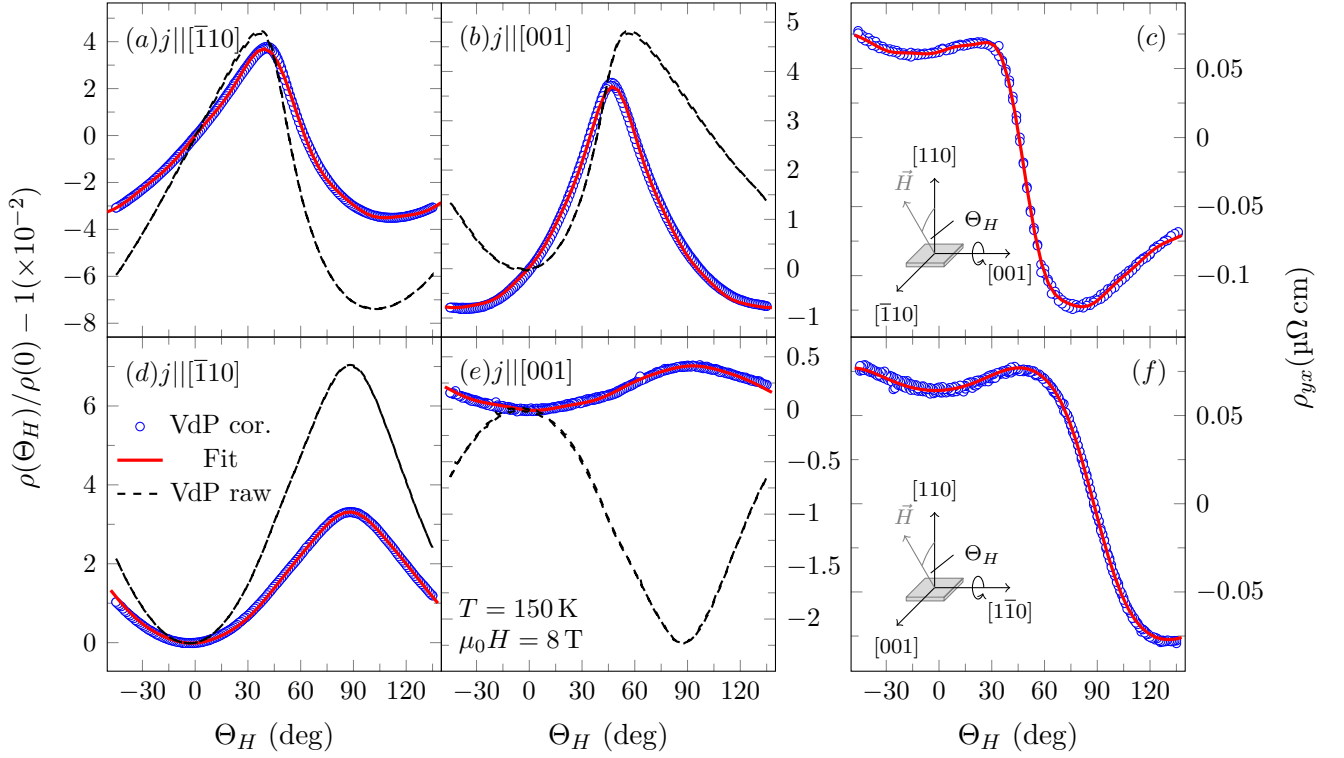


Figure 4.1: Angle dependent magnetoresistance measurements of a 40 nm thick film of SrRuO₃ with fits to the data using series expansion. Dashed lines show the raw Van der Pauw data as measured along the edges for comparison.

4.2.2 Series Expansion of Resistivities of Orthorhombic (101)_o Oriented Thinfilms

On (111)_c oriented SrTiO₃ orthorhombic SrRuO₃ has best epitaxial match in the (101)_o and (011)_o orientations, which will show the same symmetry in magnetoresistance measurements. Again we apply the current in-plane along the sample edges $[\bar{1}\bar{1}2]_c \parallel [\bar{1}01]_o$ and $[\bar{1}10]_c \parallel [010]_o$.

$$\begin{aligned}\rho_{[\bar{1}01]} &= 1/2(\rho_{11} + \rho_{33}) - 1/2(\rho_{13} + \rho_{31}), \\ \rho_{[010]} &= \rho_{22}, \\ \rho_{yx} &= 1/\sqrt{8}(\rho_{12} - \rho_{21} + \rho_{23} - \rho_{32}).\end{aligned}$$

In contrast to vicinal (001)_c oriented substrates with vicinal miscut defining an anisotropy for the crystal growth, on (111)_c oriented substrates there may be twins present in the thin film. The possible in plane crystallographic orientations are rotated by $2/3\pi$, i.e. the $[010]_o \parallel [0\bar{1}1]_c$ and $[010]_o \parallel [10\bar{1}]_c$, thus we may have contri-

butions from

$$\begin{aligned}\rho_{[\bar{1}\bar{3}\bar{1}]} &= 1/11(\rho_{11} + 9\rho_{22} + \rho_{33}) - 3/11(\rho_{12} + \rho_{21}) - 1/11(\rho_{13} + \rho_{31}) + 3/11(\rho_{23} + \rho_{32}), \\ \rho_{[\bar{1}\bar{3}\bar{1}]} &= 1/11(\rho_{11} + 9\rho_{22} + \rho_{33}) + 3/11(\rho_{12} + \rho_{21}) - 1/11(\rho_{13} + \rho_{31}) - 3/11(\rho_{23} + \rho_{32}), \\ \rho_{[\bar{1}\bar{1}\bar{1}]} &= 1/3(\rho_{11} + \rho_{22} + \rho_{33}) + 1/3(\rho_{12} + \rho_{21} - \rho_{13} - \rho_{31} - \rho_{23} - \rho_{32}), \\ \rho_{[\bar{1}\bar{1}\bar{1}]} &= 1/3(\rho_{11} + \rho_{22} + \rho_{33}) - 1/3(\rho_{12} + \rho_{21} + \rho_{13} + \rho_{31} - \rho_{23} - \rho_{32}).\end{aligned}$$

Rotation in the $(010)_o$ Plane

In the laboratory frame we have $\Theta = 0 \parallel [201]_o$ and $\Theta = \pi/2 \parallel [\bar{1}01]_o$, and

$$\alpha_1 = \sqrt{2/3} \cos(\Theta) - \sqrt{1/3} \sin(\Theta), \quad \alpha_2 = 0, \quad \alpha_3 = \sqrt{1/3} \cos(\Theta) + \sqrt{2/3} \sin(\Theta).$$

The setting $\Theta' = 0 \parallel [100]_o$ and $\Theta' = \pi/2 \parallel [001]_o$, i.e. $\Theta' = \Theta + \arccos(\sqrt{2/3})$ is more convenient, and with

$$\begin{aligned}\alpha_1 &= \cos(\Theta'), & \alpha_1^2 &= 1/2(\cos(2\Theta') + 1), \\ \alpha_2 &= 0, \\ \alpha_3 &= \sin(\Theta'), & \alpha_1\alpha_3 &= 1/2 \sin(2\Theta'),\end{aligned}$$

the measurable resistivities can be expanded as

$$\begin{aligned}\rho_{[\bar{1}01]} &= \underbrace{B(\alpha_1^2, \alpha_2^2) + K(\alpha_1^2, \alpha_2^2)}_{\sum c_{2n} \cos(2n\Theta')} + \underbrace{\alpha_1\alpha_3 T(\alpha_1^2, \alpha_2^2)}_{\sum s_{2n} \sin(2n\Theta')} \\ &= \sum_{n=0}^{\infty} c_{2n} \cos(2n\Theta') + s_{2n} \sin(2n\Theta') \\ \rho_{[010]} &= D(\alpha_1^2, \alpha_2^2) = \sum_{n=0}^{\infty} c'_{2n} \cos(2n\Theta'), \\ \rho_{yx} &= \underbrace{\alpha_3 M(\alpha_1^2, \alpha_2^2)}_{\sum s'_{2n+1} \sin((2n+1)\Theta')} + \underbrace{\alpha_1 P(\alpha_1^2, \alpha_2^2)}_{\sum c'_{2n+1} \cos((2n+1)\Theta')} \\ &= \sum_{n=0}^{\infty} c'_{2n+1} \cos((2n+1)\Theta') + s'_{2n+1} \sin((2n+1)\Theta').\end{aligned}$$

Rotation in the $(1\bar{1}\bar{1})_o$ plane: $\Theta = 0 \parallel [201]_o$ and $\Theta = \pi/2 \parallel [\bar{1}\bar{3}1]_o$

$$\begin{aligned}\alpha_1 &= \sqrt{2/3} \cos(\Theta) + \sqrt{1/12} \sin(\Theta), & \alpha_1 \alpha_2 &= 3/2(\alpha_1^2 + \alpha_2^2) - 1, \\ \alpha_2 &= -\sqrt{3/4} \sin(\Theta), & \alpha_2 \alpha_3 &= 1/\sqrt{2}(3/2\alpha_1^2 + 1/2\alpha_2^2 - 1), \\ \alpha_3 &= \sqrt{1/3} \cos(\Theta) - \sqrt{1/6} \sin(\Theta), & \alpha_1 \alpha_3 &= 1/\sqrt{2}(1/2\alpha_1^2 + 3/2\alpha_2^2 - 1).\end{aligned}$$

Rotation in the $(\bar{1}\bar{1}1)_o$ plane: $\Theta = 0 \parallel [201]_o$ and $\Theta = \pi/2 \parallel [\bar{1}31]_o$

$$\begin{aligned}\alpha_1 &= \sqrt{2/3} \cos(\Theta) + \sqrt{1/12} \sin(\Theta), & \alpha_1 \alpha_2 &= 1 - 3/2(\alpha_1^2 + \alpha_2^2), \\ \alpha_2 &= \sqrt{3/4} \sin(\Theta), & \alpha_2 \alpha_3 &= 1/\sqrt{2}(1 - 3/2\alpha_1^2 - 1/2\alpha_2^2), \\ \alpha_3 &= \sqrt{1/3} \cos(\Theta) - \sqrt{1/6} \sin(\Theta), & \alpha_1 \alpha_3 &= 1/\sqrt{2}(1/2\alpha_1^2 + 3/2\alpha_2^2 - 1).\end{aligned}$$

Since $\rho_{[\bar{1}01]}$ already possesses the most general form of a series expansion, only the resistivity $\rho_{[11\bar{1}]}$ in the twins being parallel to $\rho_{[010]}$ is considered:

$$\begin{aligned}\rho_{[11\bar{1}]} &= 1/3(B(\alpha_1^2, \alpha_2^2) + D(\alpha_1^2, \alpha_2^2) + K(\alpha_1^2, \alpha_2^2)) \\ &\quad - 1/3(\alpha_1 \alpha_2 N(\alpha_1^2, \alpha_2^2) + \alpha_1 \alpha_3 T(\alpha_1^2, \alpha_2^2) - \alpha_2 \alpha_3 Q(\alpha_1^2, \alpha_2^2)) \\ &= \sum_{n=0}^{\infty} c''_{2n} \cos(2n\Theta) + s''_{2n} \sin(2n\Theta).\end{aligned}$$

Rotation in the $(\bar{2}01)_o$ Plane

In the laboratory frame we have $\Theta = 0 \parallel [201]_o$ and $\Theta = \pi/2 \parallel [0\bar{1}0]_o$, and

$$\alpha_1 = \sqrt{2/3} \cos(\Theta), \quad \alpha_2 = -\sin(\Theta), \quad \alpha_3 = \sqrt{1/3} \cos(\Theta).$$

The measurable resistivities can be expanded as

$$\begin{aligned}\rho_{[\bar{1}01]} &= B(\alpha_1^2, \alpha_2^2) + K(\alpha_1^2, \alpha_2^2) + \alpha_1 \alpha_3 T(\alpha_1^2, \alpha_2^2) \\ &= \sum_{n=0}^{\infty} c'''_{2n} \cos(2n\Theta) \\ \rho_{[010]} &= D(\alpha_1^2, \alpha_2^2) = \sum_{n=0}^{\infty} c'''_{2n} \cos(2n\Theta), \\ \rho_{yx} &= \alpha_3 M(\alpha_1^2, \alpha_2^2) + \alpha_1 P(\alpha_1^2, \alpha_2^2) \\ &= \sum_{n=0}^{\infty} c''_{2n+1} \cos((2n+1)\Theta).\end{aligned}$$

For the twins we have $\Theta = \pi/2 \parallel [\bar{1}11]_o$, thus

$$\alpha_1 = \sqrt{2/3} \cos(\Theta) - 1/2 \sin(\Theta), \quad \alpha_2 = 1/2 \sin(\Theta), \quad \alpha_3 = \sqrt{1/3} \cos(\Theta) + \sqrt{1/2} \sin(\Theta),$$

$$\rho_{yx} = \alpha_3 M(\alpha_1^2, \alpha_2^2) + \alpha_1 P(\alpha_1^2, \alpha_2^2) = \sum_{n=0}^{\infty} c_{2n+1}''' \cos((2n+1)\Theta) + s_{2n+1}''' \sin((2n+1)\Theta),$$

and $\Theta = \pi/2 \parallel [11\bar{1}]_o$, thus

$$\alpha_1 = \sqrt{2/3} \cos(\Theta) + 1/2 \sin(\Theta), \quad \alpha_2 = 1/2 \sin(\Theta), \quad \alpha_3 = \sqrt{1/3} \cos(\Theta) - \sqrt{1/2} \sin(\Theta),$$

$$\rho_{yx} = \alpha_3 M(\alpha_1^2, \alpha_2^2) + \alpha_1 P(\alpha_1^2, \alpha_2^2) = \sum_{n=0}^{\infty} c_{2n+1}''' \cos((2n+1)\Theta) - s_{2n+1}''' \sin((2n+1)\Theta).$$

$$\begin{aligned} \rho_{[11\bar{1}]} &= 1/3 \left(B(\alpha_1^2, \alpha_2^2) + D(\alpha_1^2, \alpha_2^2) + K(\alpha_1^2, \alpha_2^2) \right. \\ &\quad \left. + \alpha_1 \alpha_2 N(\alpha_1^2, \alpha_2^2) - \alpha_1 \alpha_3 T(\alpha_1^2, \alpha_2^2) - \alpha_2 \alpha_3 Q(\alpha_1^2, \alpha_2^2) \right) \\ &= \sum_{n=0}^{\infty} c_{2n}''' \cos(2n\Theta) + s_{2n}''' \sin(2n\Theta), \\ \rho_{[1\bar{1}1]} &= 1/3 \left(B(\alpha_1^2, \alpha_2^2) + D(\alpha_1^2, \alpha_2^2) + K(\alpha_1^2, \alpha_2^2) \right. \\ &\quad \left. - \alpha_1 \alpha_2 N(\alpha_1^2, \alpha_2^2) - \alpha_1 \alpha_3 T(\alpha_1^2, \alpha_2^2) + \alpha_2 \alpha_3 Q(\alpha_1^2, \alpha_2^2) \right) \\ &= \sum_{n=0}^{\infty} c_{2n}''' \cos(2n\Theta) - s_{2n}''' \sin(2n\Theta), \\ \rho_{[13\bar{1}]} &= 1/11 \left(B(\alpha_1^2, \alpha_2^2) + 9D(\alpha_1^2, \alpha_2^2) + K(\alpha_1^2, \alpha_2^2) \right. \\ &\quad \left. + 3\alpha_1 \alpha_2 N(\alpha_1^2, \alpha_2^2) - \alpha_1 \alpha_3 T(\alpha_1^2, \alpha_2^2) - 3\alpha_2 \alpha_3 Q(\alpha_1^2, \alpha_2^2) \right) \\ &= \sum_{n=0}^{\infty} c_{2n}'''' \cos(2n\Theta) + s_{2n}'''' \sin(2n\Theta), \\ \rho_{[1\bar{3}1]} &= 1/11 \left(B(\alpha_1^2, \alpha_2^2) + 9D(\alpha_1^2, \alpha_2^2) + K(\alpha_1^2, \alpha_2^2) \right. \\ &\quad \left. - 3\alpha_1 \alpha_2 N(\alpha_1^2, \alpha_2^2) - \alpha_1 \alpha_3 T(\alpha_1^2, \alpha_2^2) + 3\alpha_2 \alpha_3 Q(\alpha_1^2, \alpha_2^2) \right) \\ &= \sum_{n=0}^{\infty} c_{2n}'''' \cos(2n\Theta) - s_{2n}'''' \sin(2n\Theta). \end{aligned}$$

If both crystallographic twins equally contribute to the resistance of the film, the $\sin(n\Theta)$ terms will cancel if the magnetization is uniform throughout the film, which can be realized close to the Curie temperature or in the paramagnetic phase. In Fig. 4.2 presents angle dependent magnetoresistance measurements of a twinned SrRuO₃ film on SrTiO₃(111). The observed asymmetry in Fig. 4.2(a) can be accounted for by a simple $\sin(2\Theta_H)$ term (dotted line, shifted). Equally ρ_{yx} in Fig. 4.2(c)

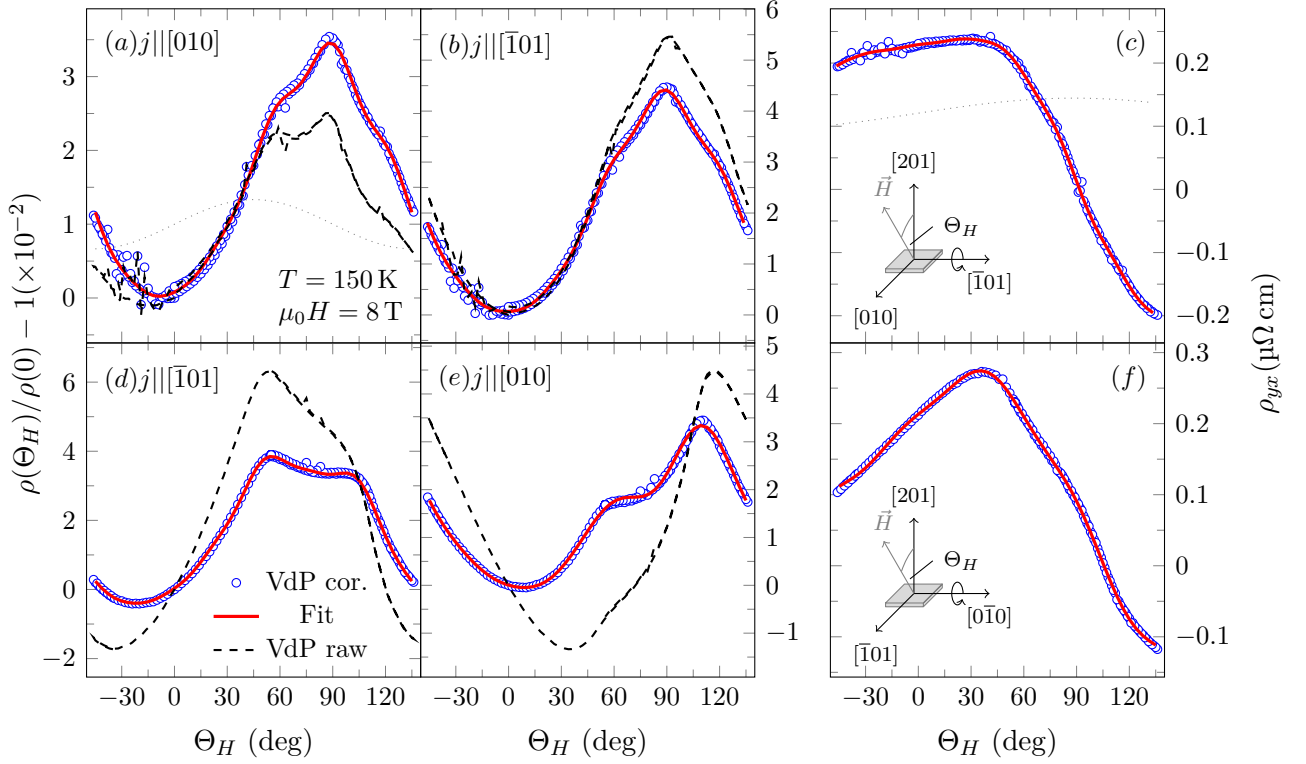


Figure 4.2: Angle dependent magnetoresistance measurements of a 60 nm thick film of SrRuO₃ on SrTiO₃(111) with fits to the data using series expansion. Note that direction descriptions are in orthorhombic setting according to the first described epitaxial relation. Dashed lines show the raw Van-der-Pauw data as measured along the edges for comparison. Grey dotted lines in (a) and (c) show the contribution of sine terms in the fit.

shows a small $\sin(\Theta_H)$ contribution (dotted line, shifted). Since no higher order sine terms are present, one may attribute these terms to a small contact asymmetry or misalignment of the sample. This suggests equal contributions from the two crystallographic twin domains. In Fig. 4.2(d)–(f) however, the contributions of the twins are clearly visible.

It is important to remember that the approximation of an isotropic magnetization amplitude is not strictly valid, adding additional dependencies due to non saturated magnetoresistance. However, the anisotropy of the magnetization has to satisfy the same symmetry constraints and thus does not change the form of the mathematical description. This implies that some care is required when trying to extract e.g. anisotropy constants from fits.

Magnetoelastic Coupling and Interface Effects in SrRuO_3

In thin films the stress exerted by the substrate on the film as well as interlayer strains may play a dominant role. Reported strong electron phonon coupling [325] suggests SrRuO_3 thin films to be highly sensitive to stress and strain acting on them. Indeed, Gan et al. [140] reported an increase of T_C and magnetic moment after lift-off and relaxation of a film from the substrate. While some strain relaxation may be expected with increasing layer thickness, this effect should be of minor importance, since the single films are at most 40 nm and in the superlattice (total thickness 100 nm) thin layers of SrTiO_3 help maintaining the strain. This view is supported by the XRD measurements (see Fig. 2.3). Thus surface and interface effects dominate the property changes within the series on STO. For tensile strained SrRuO_3 an increase in the ferromagnetic transition temperature has been reported [148], suggesting modifications in the electronic structure.

5.1 Structural Properties

Samples have been fabricated by pulsed laser deposition, with a substrate temperature of 650 °C, a laser fluence of 2 J cm^{-2} and oxygen partial pressure of 0.13 mbar (see [326]). The tensile strained sample on BSTO-buffered¹ LaAlO_3 has been grown at 700 °C in an off-axis geometry, details can be found in Ref. [327]. While we claimed the SRO/BSTO/LAO film as tetragonal, we cannot entirely exclude the possibility of the film being orthorhombic with the (orthorhombic) c-axis pointing out of plane. The tetragonal phase was inferred from reciprocal spacemaps of the pseudocubic [024] reflections family [327] corresponding to the orthorhombic [112] family, i.e. a difference between a and b cannot be inferred from these peaks. Transport and magnetization measurements were also done along the substrate edges, i.e. [110] and $[1\bar{1}0]$ and cannot discriminate between these settings. In fact, even stronger tensile strained SrRuO_3 films in the orthorhombic phase have been reported [146]. More confusingly, Gao et al. [328] reported overall tetragonal symmetry, however, with orthorhombic oxygen octahedra tilt patterns.

¹BSTO is short for $\text{Ba}_{0.5}\text{Sr}_{0.5}\text{TiO}_3$.

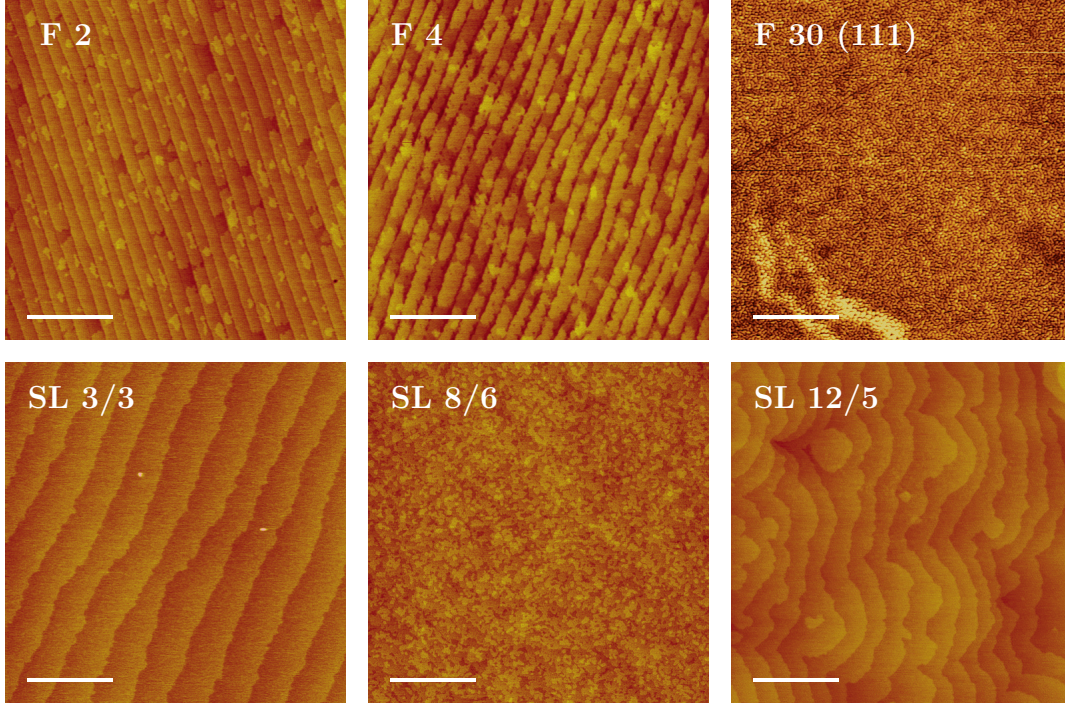


Figure 5.1: AFM images $4\mu\text{m}\times 4\mu\text{m}$ show a flat surface morphology with steps of unit cell height. Films F2 and F4 show troughs due to Sr segregation at the step edges. On $\text{SrTiO}_3(111)$, instead of terraces a fine meander structure of typically 50 nm width is observed. For SL8/6 incomplete filling of the monolayers in island growth mode is observed. The scale bars correspond to 1 μm .

In x-ray diffraction measurements of the superlattices the characteristic superlattice peaks confirming coherent growth were observed (see Fig. 3.2). AFM images Fig. 5.1 confirm the good growth morphology with unit cell high steps. Since SrTiO_3 layers grow in island growth mode, few growth pyramids can be observed on SL12/5 and the typical terraces are tattered for SL8/6 and hard to recognize. This may partially hinder the preferential alignment of the orthorhombic [001] axis along a unique in-plane axis (see Section 2.1.3). The meander structure on $\text{SrTiO}_3(111)$ suggests the formation of crystallographic twins, since there are three equivalent epitaxial relations (see Chapter 4). The ultrathin films with thicknesses of about 1.6 and 0.8 nm have troughs with typical depths of about 1 and 0.5 nm. Thus the troughs do not reach the substrate surface and the films are continuous. However, they have some tendency towards one dimensional structures with wire widths of about 200 (F4) and 160 nm (F2). One might therefore expect an in-plane anisotropy in both transport and magnetic properties. The trough formation has been ascribed to SrO diffusion to the step edges [25]. A close look at the surface of F4 reveals the formation of islands, such that we have actually a thickness distribution between 3-5 unit cells.

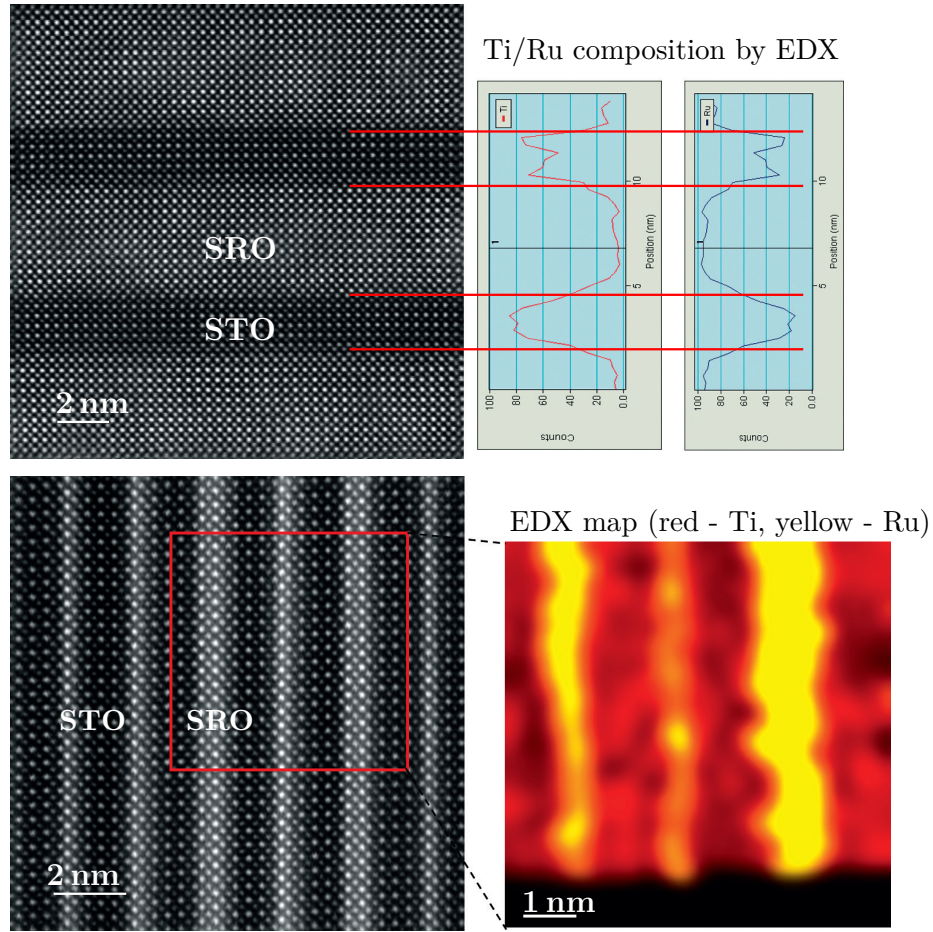


Figure 5.2: HAADF-STEM images of SL12/5 (top) with EDX line scan along the growth direction and SL3/3 (below) with an EDX elemental map. In the Z-contrast image the brighter dots correspond to Sr/Ru columns while the Ti columns correspond to the smaller dots. Note the good interface quality with only minor cation intermixing. In SL3/3 some variation in the thickness from layer to layer is observed.

Upon thickness reduction of the individual layers, the long range ordering necessary to establish a single phase [138] is reduced. This implies that upon cooling from growth temperature crystallographic twins may be formed. These have the orthorhombic c axis aligned along any of the four equivalent in-plane directions of the substrate. High resolution STEM images further confirm the overall good crystalline quality of the films with negligible intermixing, while elemental maps show some thickness variations in the thinnest superlattice (see Fig. 5.2). As already indicated by the surface morphology, SL8/6 shows more disorder at the interface (not shown).

5.2 Magnetic Properties

As can be seen in Fig. 5.3, the ferromagnetic transition temperature is reduced upon thickness reduction, which can be ascribed to finite size scaling. We confirm the critical thickness of 4 u.c. deduced from Kerr effect measurements by Xia et al. [151] for single films. This reduced magnetic moment can be understood in terms of either quenching of the magnetic moment by the presence of the interface or by antiferromagnetic order of the ruthenium moments [151]. A non-contributing layer of about 1 u.c. thickness can be inferred from the moment reduction. In the two unit cell thick films some small ferromagnetic clusters may be present, as can be seen from a finite remanent magnetic moment. At the same time the magnetic anisotropy increases strongly with the easy axis pointing out of plane. Note also the temperature dependence of the ratio M_{\parallel}/M_{\perp} for SL12/5, from which the deviation of the magnetic easy axis from the substrate normal can be deduced [117]. In the thinner samples this angle is smaller than the 11° to 45° reported before [329] for thicker films. In micro-twinned thin films as well as chromium doped films, which both destroy the long range order of the ruthenium octahedra, a similar anisotropy easy axis direction change was observed towards the out of plane direction [330]. The tetragonal film F100t has an out of plane hard axis, in accordance with the literature [147]. The structural quality seems to be somewhat worse, which manifests itself in a slope change of the FC curve around 100 K, suggesting two contributions with different T_C . Note also the rather broad transition of SL3/3.

Magnetization measurements obtained at 10 K are shown for some samples in Fig. 5.4. Besides the reduction in magnetic moment an increase in the coercivity is observed. F25(111) shows only saturation at high fields, which is a signal of a magnetization rotation process to align the magnetic moment with the field. The slanted hysteresis curve of SL3/3 indicates a distribution of coercivities in different regions of the sample.

5.3 Transport Properties

The measured resistances are highly anisotropic. This anisotropy is strongly reduced after application of the geometric corrections (see Section 3.3). Both the thin single films and the thinner multilayers SL3/3 and SL8/6 still show anisotropy after the geometric corrections, which may be due to the (extrinsic) barrier formed by troughs or off-stoichiometry close to the step edges². The temperature dependence shown in Fig. 5.5(c) and (d) indicate a transition from metallic to non-metallic like below a critical thickness of about four unit cells. The two unit cell thick film follows a 1d variable range hopping or cluster hopping between 20 K to 300 K, see inset in

²Note that the measured anisotropy ratio in R_x/R_y for F4 is on the order of 10^4 , which after application of the geometric corrections (see Appendix A) reduces to about 6 for ρ_x/ρ_y .

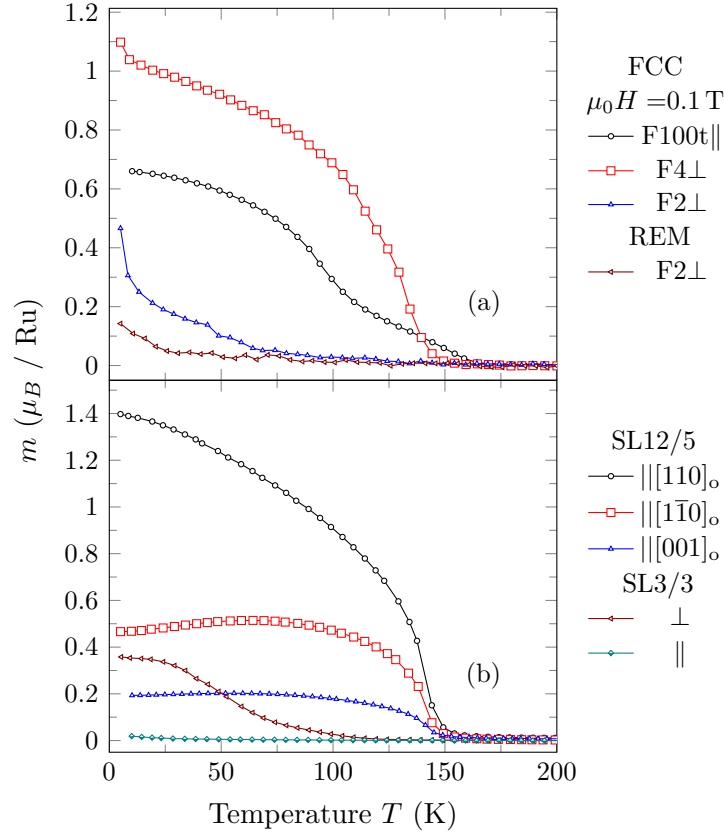


Figure 5.3: (a) FC in 0.1 T of the tetragonal film and the 4 and 2 unit cell thick films. (b) FC in 0.1 T along different crystallographic directions of SL12/5. SL3/3 does not show in plane anisotropy.

Fig. 5.5(c) with $\ln(\rho) \sim T^{-1/2}$. This combines well with the temperature dependence of the magnetization in this sample, which suggested some ferromagnetic clusters. The tensile strained film shows a slightly higher resistivity and a much weaker temperature dependence, indicating a higher degree of disorder. The high resistivity of F25(111) may hint at an effectively reduced thickness of the conducting layer and additional scattering due to the observed twin domains.

Angle dependent magnetoresistance measurements had been employed successfully before to determine the structural symmetry of thin films [8]. This method is based on series expansion of both, the magnetocrystalline anisotropy as well as the magnetoresistance in powers of direction cosines of the magnetization (for further details see Chapter 4). This can be a powerful method for a global structure determination in cases where the films are too thin to be analysed by XRD in contrast to local techniques as STEM. However, the full description with possibly orthorhombic symmetry in both the magnetic anisotropy energy and the resistivity series expansion, and additionally taking into account possible twin domains, provides a large number of parameters making fits without further constraints infeasible. Thus, in Fig. 5.6

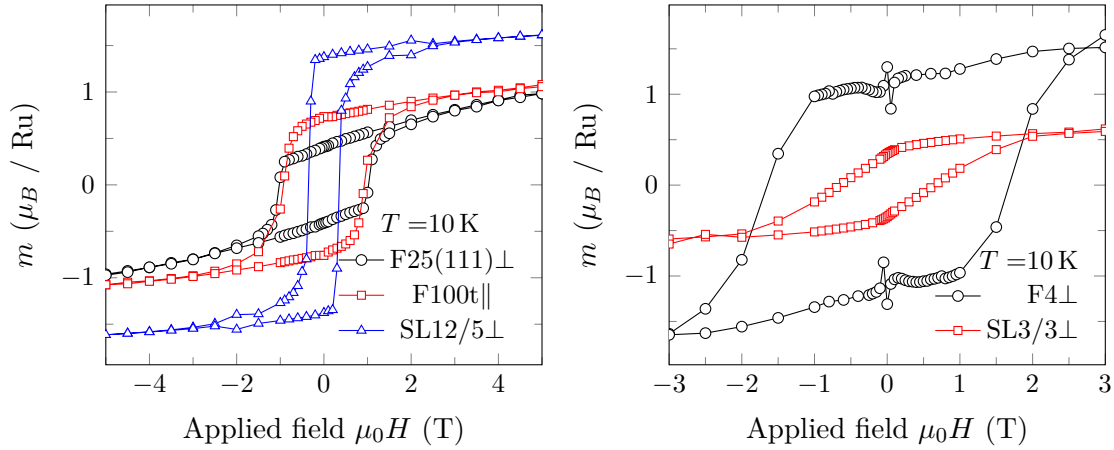


Figure 5.4: Magnetization vs. applied field at 10K. F100t measured with the field applied parallel to the sample surface, others with field applied parallel to substrate normal. For F25(111) and F4 a considerable magnetic moment from impurities was measured at 200 K and subtracted from the data (see Section 3.6.5).

a fit was not attempted, but one can still recognize the presence of orthorhombic symmetry as indicated by sketches with smaller amounts of contributions from all of the four possible twin domains. The position of hard axes are most easily recognized in the Hall data through steps. With increasing temperature, the hard axis in the (001) plane moves a few degrees into the direction of the substrate normal and, by implication, the easy axis moves away from the substrate normal, in accordance with magnetization data. In Fig. 5.7 angle dependent magnetoresistance of SL 3/3 are shown. The striking feature is the similarity of the angle dependence measured in the different directions suggesting a tetragonal symmetry. Due to the strong anisotropy, in a first approximation, only uniaxial anisotropy is considered to first order, i.e. $E_K = K_U \cos(\theta)^2$ with θ being the angle between the magnetization and the easy axis (close to the surface normal) and the uniaxial magnetocrystalline constant $K_U < 0$. Minimizing the total energy (Eq. (2.1)) and assuming a simple angle dependent magnetoresistivity of the form $\rho(\theta) = \rho(0) + \Delta\rho \cos(\theta)^2$ ³ and further $\rho_{yx} = \rho_{AHE} \cos(\theta) + \rho_H \cos(\Theta_H)$ the 50 K data was fitted in a global fit. The 10 K data shows small maxima around $\Theta = 0$ and, more prominently, a cusp at the same position in the Hall resistivity. This indicates a deviation of the easy axis from the substrate normal or a superposition with another effect (see also Section 5.3.1). The anisotropy field of 5.8 T obtained from the fitting is huge. Similar fits on F4 give an anisotropy field as large as 6 T even at 100 K. One mechanism capable to explain this strong increase in anisotropy is magnetostriction. Assuming a fully strained state, with the pseudocubic lattice constants $a_{\text{SRO}} = 3.92\text{\AA}$ and $a_{\text{STO}} = 3.898\text{\AA}$ below 100 K and $\epsilon = (a_{\text{SRO}} - a_{\text{STO}})/a_{\text{SRO}} = 0.0056$, the additional anisotropy field

³As usually encountered in polycrystalline samples, but also the first order expansion in single crystals.

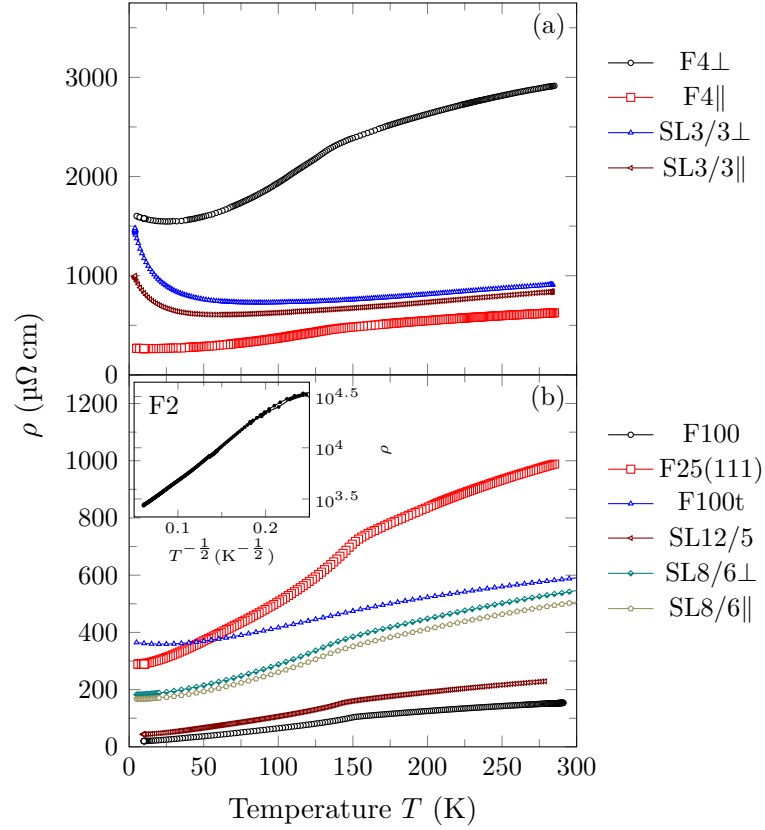


Figure 5.5: Resistivity is plotted vs. the temperature. Symbols indicate the measurement direction parallel \parallel or perpendicular \perp to the vicinal terraces.

due to magnetostriction is given by (see Section 2.2.2, [331]⁴):

$$\Delta H_A = \frac{3\lambda_{100}}{\mu_0 M_S} (c_{11} - c_{12}) \left(1 + \frac{2c_{12}}{c_{11}} \right) \epsilon.$$

With the saturation magnetization $\mu_0 M_S \approx 0.3$ T, the elastic moduli $c_{11} = 252$ GPa and $c_{12} = 132$ GPa [332], and the above obtained anisotropy fields $\Delta H_A \approx 6$ T, we can estimate the magnetostriction constant as $\lambda_{100} = 3.5 \times 10^{-4}$. This is in very good agreement with the values estimated by Dabrowski et al. [333] (3×10^{-4} to 5×10^{-4}). This is especially surprising, since the uncertainty of the elastic moduli, which were obtained in polycrystalline specimens, is large. A second mechanism capable to explain this anisotropy increase is the surface or interface induced anisotropy. Recently an increase in the ruthenium orbital moment was observed upon thickness reduction of SrRuO₃ films [334], which may partially explain the anisotropy increase [182].

⁴There is a typo in Eq. 8 in this paper, c_{11} and c_{12} are interchanged in the fraction.

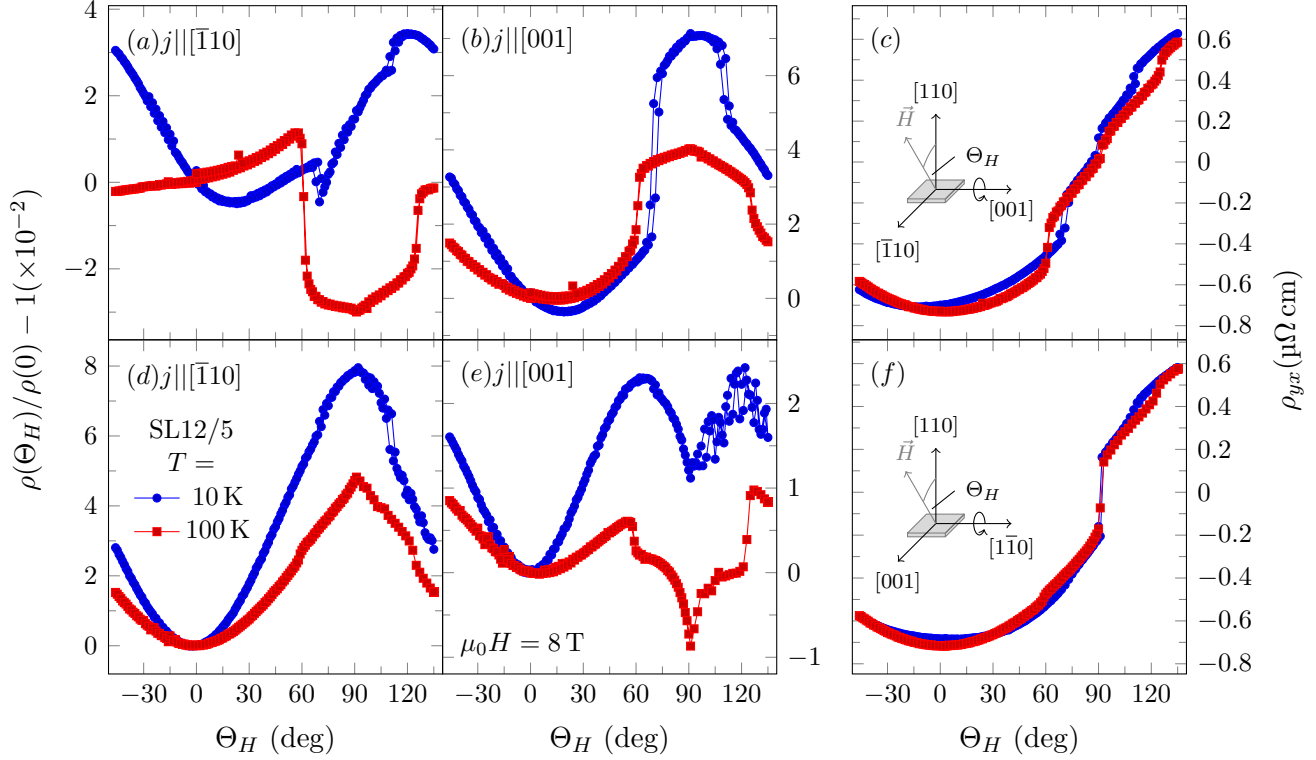


Figure 5.6: Angle dependent magnetoresistance of SL12/5 at 10 and 100 K. Current direction and rotational indications are according to the dominant contributions. However, the manifestation of several magnetically hard axes at the same positions in both rotation directions indicate twinning of the film along the four equivalent in-plane directions. The positions of the hard axes show a clear temperature dependence.

5.3.1 Anomalous Hall Effect

The anomalous Hall effect in SrRuO₃ has attracted considerable interest in recent years as it was a prototype for testing theoretical models for the intrinsic (Berry-phase curvature related) contributions to the anomalous Hall effect [122, 123]. As described earlier (Section 2.3.2), it is now consensus that in high quality SrRuO₃ the intrinsic band structure related contributions to the AHE dominate. However, the relatively high resistivity as a bad metal puts it at the limit between intrinsically and extrinsically dominated ρ_{AHE} [215]. The irregular and spiky dependence of the calculated σ_{AHE} on the density of states can explain the rich phenomenology.

In Fig. 5.8(a) the temperature dependence of the anomalous effect is plotted. We did not succeed in performing the rescaling procedure described by Haham et al. [124]. The reason for this may be the relatively high resistivity, placing this sample series in a range in which both the internal and the external sources for the anomalous Hall effect have similar contributions. Figure 5.8(b) depicts the number of carriers obtained from a one band model ($n = 1/R_H e$) with the ordinary Hall constant R_H

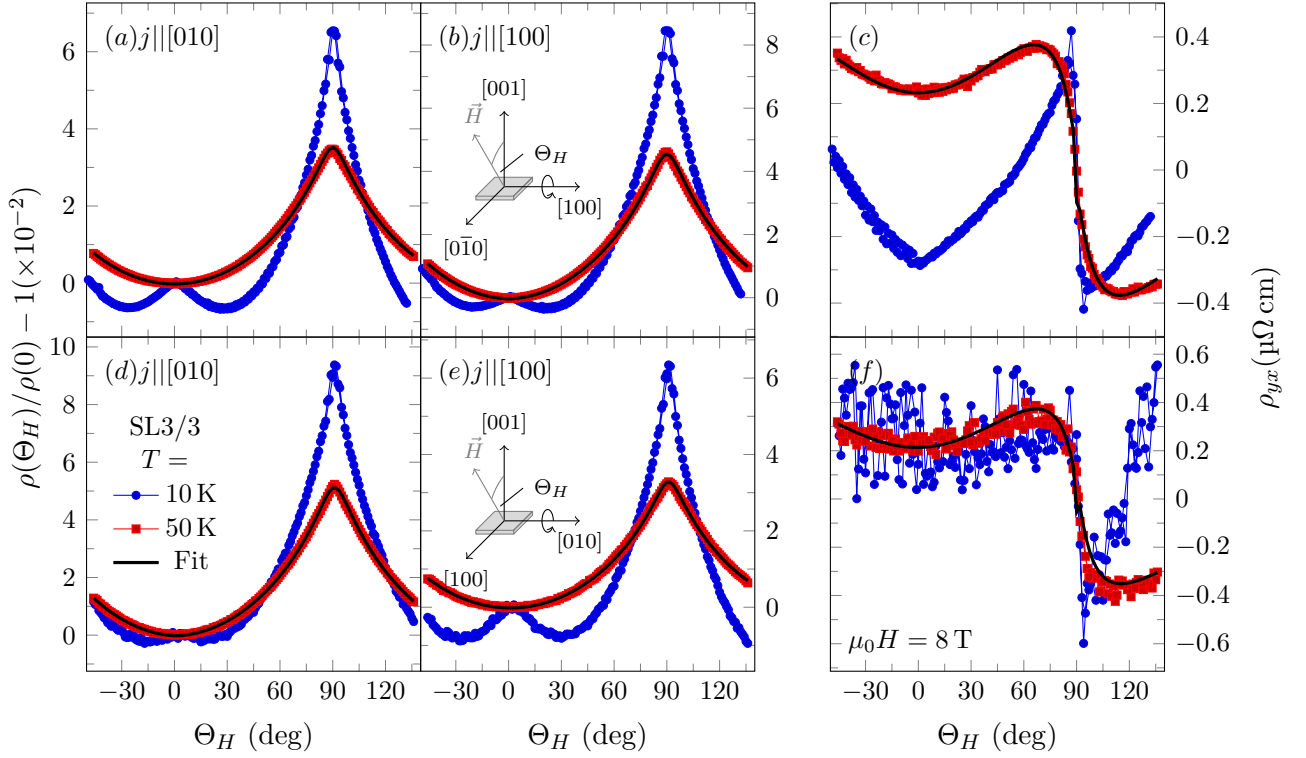


Figure 5.7: Angle dependent magnetoresistance of SL3/3 at 10 and 50 K. The apparent symmetry is tetragonal. Current direction and rotational indications are according to the substrate directions. The fit lines of the curves measured at 50 K are according to the simple model described in the text.

obtained from a linear fit to the high field slope. This gives in general reasonable values of around one electron per unit cell. Strong and unphysical variation with temperature, which is most prominent in the sample grown on SrTiO₃(111), is due to non-saturation of the magnetization even in fields of 8 T, i.e. contributions to the apparently linear slope from the AHE due to magnetization rotation. This can also be seen in Fig. 5.9. The measured diagonal resistivity of the single layers and thin films is plotted. While all the films on SrTiO₃(001) show quite similar behaviour, the tensile strained tetragonal film F100t grown on the BSTO buffer shows a positive AHE with a gradual rotation of the magnetization towards the hard out of plane axis only saturating at high fields. The thinnest superlattice SL3/3 also shows a positive ρ_{AHE} , albeit with a very different shape. In this sample the easy axis is close to the substrate normal. The thin film grown on SrTiO₃(111) shows an enhancement of ρ_{yx} at low fields due to rotation of the magnetization away from the substrate normal towards the easy axes of the (twinned) film. This demonstrates that the empirically established relation $\rho_{yx} = \mu_0(H_{\perp}\rho_H + M_{\perp}\rho_{AHE})$ is not strictly valid but should rather read as

$$\rho_{yx} = \mu_0(H_{\perp}\rho_H + \rho_{AHE}(\vec{M}))$$

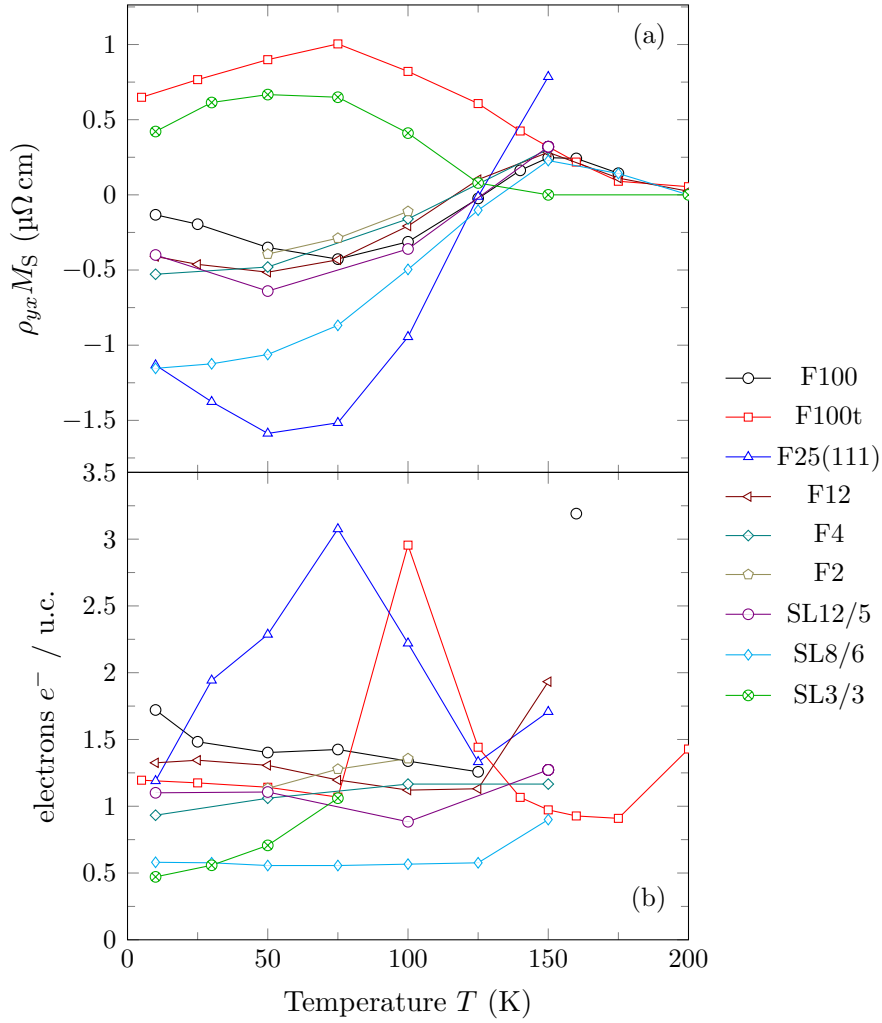


Figure 5.8: (a) Temperature dependence of the anomalous Hall constant $\rho_{yx}M_S$ vs. temperature. SL3/3 and F100t show a positive AHE. (b) Charge carrier density. Strong variation may indicate an influence of magnetization orientation effects.

which can be reduced only to the former equation in case of magnetization along high symmetry axes. This is actually obvious from the allowed symmetries in a crystal. The observed increase of ρ_{AHE} at low fields is related to the magnetization increase along the easy axis increasing the splitting of the spin up and spin down bands. This anisotropic nature of the ρ_{AHE} tensor is not only related to the intrinsic mechanism, but may also be observed for extrinsic contributions if the additional scatterers are anisotropic.

We observed spikes in the anomalous Hall effect of SL3/3 at 10 K, see Fig. 5.10. Similar features in SrRuO₃/SrIrO₃ bilayers led Matsuno et al. [335] to infer a topological Hall effect due to the formation of skyrmions. The proposed mechanism can be excluded in our sample, since SrRuO₃ is embedded symmetrically in SrTiO₃

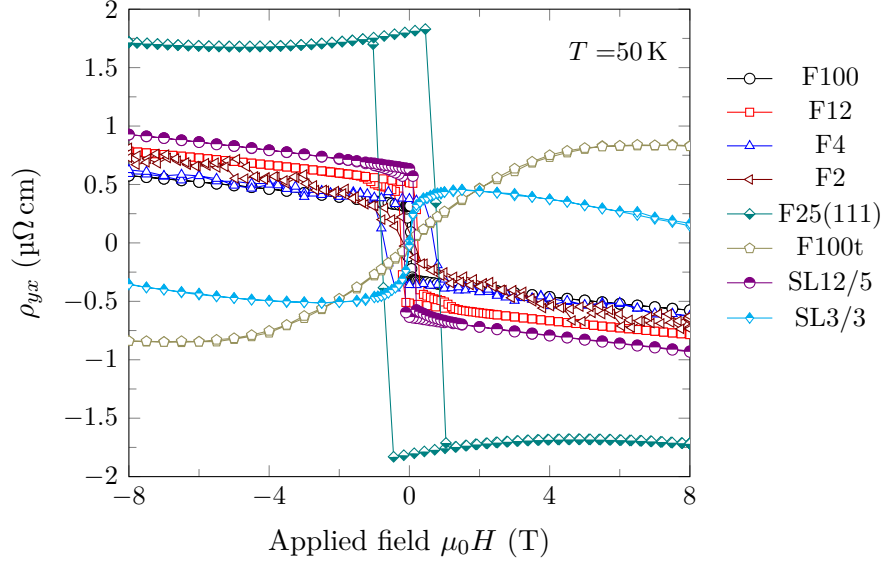


Figure 5.9: Hall effect measurements at 50 K for the thin films and superlattices. The increase at small fields for F25(111) manifests magnetization rotation.

layers, which should cancel the proposed interfacial Dzyaloshinski-Moriya interaction leading to the formation of skyrmions. Thus a different mechanism should be at play: Already early studies on SrRuO₃ indicate strong spin fluctuations due to comparatively weak exchange interactions as one reason for a reduced magnetic moment [108, 127]. Strong spin-orbit coupling and increased orbital anisotropy at the SrRuO₃/SrTiO₃ interface may lead to a modified phase at the interface with different magnetic and transport properties. Already the magnetization of SL3/3 (see Fig. 5.4) is slanted, which either indicates a deviation from the easy axis or a distribution of the switching field. Thus we may assume at least two different phases in the superlattice. It is irrelevant to the model whether these phases are due to the described variation in layer thickness or interface related. We model ρ_{yx} with two independent hysteresis loops, one with a positive contribution and one with a negative contribution to ρ_{AHE} with different switching fields. Simultaneously we fit the magnetization with the magnetization of the two contributions. A phenomenological description of the hysteresis curve with the error function is used⁵. The fit is shown in Fig. 5.10. For comparison a conventional modelling rescaling the magnetization is also put on display. From the switching fields we may infer that the phase with negative ρ_{AHE} contributes about one third of the magnetic moment and has a higher coercive field. SL8/6 is shown along to exemplify how well normally the modelling with a proportionality to the magnetization works.

⁵i.e. $M(H) = M_S \text{erf}(a(H - H_C))$ with the saturation magnetization M_S , the coercive field H_C and the parameter a describing the width of the gaussian distribution of switching fields. Equivalently one might use other standard function, i.e. $\tanh(x)$ or the Langevin function, however, these show a slower saturation behaviour.

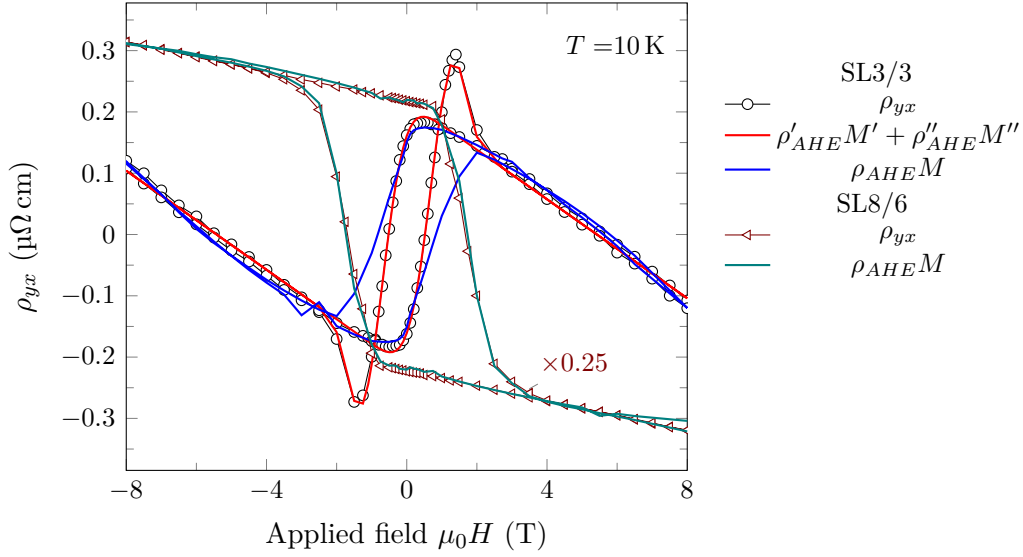


Figure 5.10: Measurement of SL3/3 and SL8/6 at 10 K along with fits according to the conventional equation and a bilayer model for SL3/3. The model was fitted simultaneously to the magnetization to assure that $M = M' + M''$ always holds.

5.4 Conclusions

This work was partially motivated by the prediction of a highly confined spin polarized two dimensional electron gas for 1 u.c. thick SrRuO₃ embedded in SrTiO₃ [336, 337]. No indications for this predicted two dimensional electron gas was observed in the 2–3 u.c. thick layers in the superlattice. However, the observed changes in the anomalous Hall effect support their view of the importance of the shape of the electronic density of states, i.e. the topological nature of the intrinsic contribution to the anomalous Hall effect. The obtained results clearly show the anisotropic nature of the ρ_{AHE} tensor underlining the importance of taking this into account in interpretations of transversal resistivity measurements. Observation of negative ρ_{AHE} in both compressively and tensile strained tetragonal thin films of SrRuO₃ on NdGaO₃ and SmScO₃ [338] counter-indicate a simple relation of the sign of ρ_{AHE} with the structure. For thicker films, in which the intrinsic contribution is expected to dominate, the sign change of ρ_{AHE} is apparently linked to a change in magnetic anisotropy (see Refs. [144, 167, 339]), as in our SRO/BSTO/LAO sample. Of course, electronic structure and magnetic anisotropy are intimately related. One can as well relate the sign change of the anomalous Hall effect in SrRuO₃ for orthorhombic and tetragonal structure to the crystal orientation with respect to the surface normal. In the tetragonal SrRuO₃ the c-axis corresponding to two pseudocubic unit cells is oriented along the surface normal. Assuming that the electronic modifications between tetragonal and orthorhombic SrRuO₃ is rather small, since the changes in lattice constants is rather small, there remains a big difference: In

(110)_o oriented films we measure $\rho_{yx} = 1/\sqrt{8}(\rho_{31} - \rho_{13} + \rho_{23} - \rho_{32})$, whereas in the tensile strained (001)_t oriented films we measure $\rho_{yx} = 1/2(\rho_{12} - \rho_{21})$. For this notation the same unit cell is assumed. To settle this question, measurements of (001)_o oriented films would be necessary. Another possibility to completely map the anomalous Hall effect tensor would be the measurements of lamellas with defined crystallographic orientations cut with a dual beam microscope from micrometer thick single crystalline films.

We may also note, that the anomalous Hall effect is positive for thicker SrRuO₃ films in proximity to T_C , and that the sign reversal temperature lowers with decreasing crystalline quality. Thus the observed positive anomalous Hall constant of SL3/3 might be explained considering the rather low magnetic moment and high resistivity. The peculiar susceptibility behaviour in the Ca_{1-x}Sr_xRuO₃ series has been related to a Griffiths' phase of a dilute ferromagnet [7, 340, 341]. Similar processes may be at play in the SrRu_{1-x}Ti_xO₃ series [342] or simply due to thickness reduction [151]. Thus we conclude that the observed anomalous Hall effect in the SL3/3 may be related to an interfacial phase with modified electronic properties or even a superposition of layers or areas with different electronic and magnetic properties. A simple bilayer model successfully fitted the unusual ρ_{yx} vs. $\mu_0 H$ curves. An exact determination of the magnitude of the interfacial effect requires band structure and Berry phase curvature calculations of embedded SrRuO₃ layers. In an experimental approach one may discriminate between the suggested models by (a) studying single layers to avoid parallel transport, embedded in (b) symmetric and (c) asymmetric systems to disentangle the individual contributions of non-collinear spin arrangements and band structure modifications at the interface.

The symmetry of angle dependent magnetoresistance measurements can serve as a fingerprint for structural information. However, as a global measurement technique, the superposition of twinned structures can blur the characteristic features. Furthermore, it crucially depends on the magnetic anisotropy. If the magnetic anisotropy is dominated by a tetragonal symmetry, irrelevant of its origin from micro-twinning, magnetoelastic coupling or surface anisotropy, only a tetragonal symmetry can be observed.

La_{0.7}Sr_{0.3}MnO₃ / CaRuO₃ Superlattices: Stabilization of Ferromagnetic Transition Temperature

Generally speaking good bulk ferromagnetic properties deteriorate fatally upon dimensional reduction. Several mechanisms responsible may be simultaneously at play, such as finite size scaling [343], electronic phase separation [59, 75], and issues with sample fabrication and microstructure [344]. This decline in magnetic properties has been one main obstacle to the implementation of La_{0.7}Sr_{0.3}MnO₃ in spintronic devices [80]. As mentioned before, manganites exhibit a strong coupling between electron, orbital, spin, and phonon degrees of freedom [58], which leads to the formation of antiferromagnetic and insulating states in thin layers of natively conducting ferromagnets [97]. This can be understood by orbital ordering due to strain [345–348] or surface/interface symmetry breaking [95], or by an interfacially driven electronic phase separation [349, 350].

Several methods have been suggested to prevent the degradation of the manganite ferromagnetic properties. Simply interfacing with a good conductor to promote an indirect double exchange may actually be counter-productive [351]. Charge doping of the interfacial layer showed some improvements [91, 352] and can also be employed dynamically with a ferroelectric [353]. Capping layers can successfully modulate the orbital occupancy [255]. Doping with the 4d transition metal ruthenium may lead to improvements of the ferromagnetic properties, but actually both a T_C decrease [99] and a moderate increase [98] have been observed. The former results might be understood by structural deformations. At the CaMnO₃/CaRuO₃ interface a charge transfer was observed [158]. The predicted interfacial two dimensional electron gas [160] appeared to be rather three dimensional in experiment [161], with an effective electron delocalization of 3–4 unit cells.

CaRuO ₃	Thickness (u.c.)	$m_{\text{CRO}} (\mu_B/\text{Ru})$		
C30	30	<0.1 (for H=1T)		
LSMO/CRO	Thickness (u.c.)	$T_{\text{C,LSMO}} (\text{K})$	$m_{\text{LSMO}} (\mu_B/\text{Mn})$	Substrate
LC1.5/1.5	[1-2/1-2] ₂₂	225	2.5	STO
LC8/3	[8/3] ₁₅	250-280	3.2	STO
LC2/3 l	[2-3/3] ₁₅	265	2.7	LSAT
LC2/3 l	[8/3] ₁₅	320	3.5	LSAT
LC1/3 l	[1/3] ₁₅	225	2.7	LSAT
Ru:LSMO	Thickness (u.c.)	$T_{\text{C,LSMO}} (\text{K})$	$m_{\text{LSMO}} (\mu_B/\text{Mn})$	
Ru:LSMO100	100	340	3.3	
LSMO/STO	Thickness (u.c.)	$T_{\text{C,LSMO}} (\text{K})$	$m_{\text{LSMO}} (\mu_B/\text{Mn})$	
Ru:L/St	[3/2] ₁₅	58	1	
LSt3/3	[3/3] ₁₅	35	0.6	
LNb:St	[3/8] ₁₅	20	1.0	
LaNiO ₃	Thickness (u.c.)	$T_{\text{C,LSMO}} (\text{K})$	$m_{\text{LSMO}} (\mu_B/\text{Mn})$	$T_{\text{C,SRO}} (\text{K})$
LSMOLNO	[3/4] ₁₅	95	0.7	
SROLNO	[3/4] ₁₅			<20
LSMO/SRO	Thickness (u.c.)	$T_{\text{C,LSMO}} (\text{K})$	$m_{\text{LSMO}} (\mu_B/\text{Mn})$	$T_{\text{C,SRO}} (\text{K})$
LS10/2	[10/2] ₁₅	320/290	3.8	108
LS2/8	[2/8] ₁₅	230	2.5	144
LStSSt	[2/2/2/2] ₁₅	139	1	46

Table 6.1: List of samples with key properties. Subscripts in the second column give the number of repetitions. In the sample names L stands for La_{0.7}Sr_{0.3}MnO₃, C for CaRuO₃, S for SrRuO₃, St for SrTiO₃, Ru: for ruthenium doping, and LNO for lanthanum nickelate. The small l denotes samples grown on LSAT substrates.

6.1 Sample Fabrication and Structure

We studied a series of La_{0.7}Sr_{0.3}MnO₃/CaRuO₃ superlattices and compared it to alternative approaches stabilizing the ferromagnetic transition: Ruthenium doping of the La_{0.7}Sr_{0.3}MnO₃ layer and interfacing with the reasonably conducting oxide LaNiO₃. One might expect a modification due to the changed polarity at the La_{0.7}Sr_{0.3}MnO₃ LaNiO₃ interface. Three samples with SrRuO₃ layers have been included for comparison. The samples have been denoted by a code for the materials used and numbers describing the layer thickness, see Table 6.1. All samples were

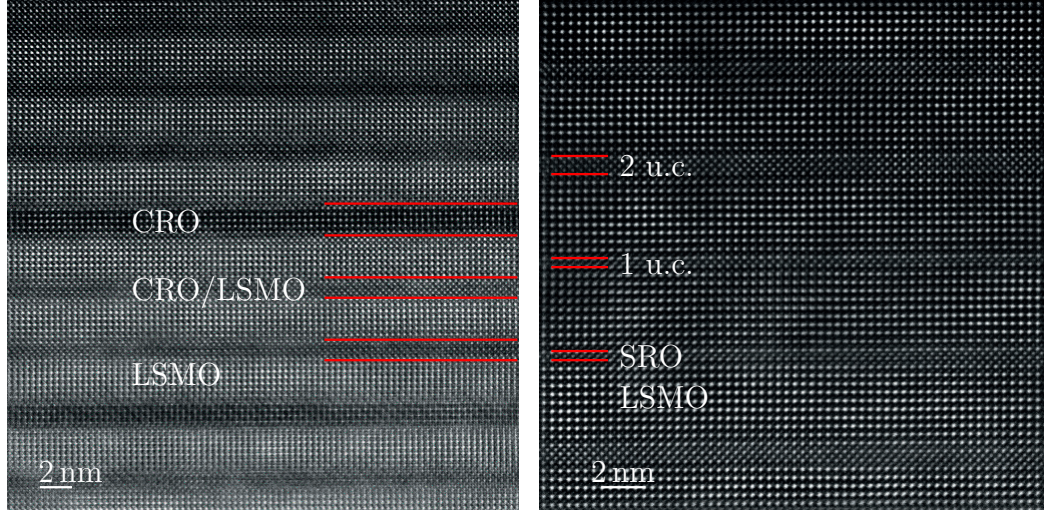


Figure 6.1: HAADF-STEM image of LC8/2 (left) and LS10/2 (right). In the La_{0.7}Sr_{0.3}MnO₃/CaRuO₃ superlattice some intermixing occurs and the layer thickness vary by 1 u.c.. In LS10/2 the SrRuO₃ layers with a thickness of 1 or 2 u.c. are sharply defined.

fabricated by PLD with a substrate temperature of 650 °C and an oxygen partial pressure of 0.14 mbar. SrTiO₃ substrates were TiO₂ terminated.

X-ray diffraction measurements showed characteristic superlattice peaks confirming homogeneous growth. HAADF-STEM images confirmed the layer thicknesses determined from XRD. The La_{0.7}Sr_{0.3}MnO₃/CaRuO₃ interface is more prone to intermixing than the La_{0.7}Sr_{0.3}MnO₃/SrRuO₃ interface, see Fig. 6.1. The thinner superlattices LC1.5/1.5, LC1/3 \bar{l} and LC2/3 \bar{l} show regions with layer thickness distributions as 1/1, 1/2, 2/1, or in the latter ones 1/3, 2/3. The smaller unit cell of CaRuO₃ results in a stronger distortion of the oxygen octahedra and may induce some structural degradation due to the larger lattice misfit with the commonly used SrTiO₃ substrate. Indeed, samples grown on LSAT substrates show some enhancement in T_C. The interface properties may also improve with the structurally better matching La_{1-x}Ca_xMnO₃ as manganite layer.

6.2 Magnetization

Magnetic moment vs. temperature of the La_{0.7}Sr_{0.3}MnO₃ / CaRuO₃ superlattices are shown in Fig. 6.2 (a). In contrast to the previous study with ferromagnetic SrRuO₃ layers [354], the paramagnetic moment of the CaRuO₃ is negligible. The inset in Fig. 6.2(c) shows the linear temperature dependence of the inverse susceptibility characteristic for paramagnetic materials. No sign was observed for an antiferromagnetic [107] or ferromagnetic [355] state in the CaRuO₃ thin film. The measured magnetic moment was converted to Bohr magnetons per manganese ion, allowing

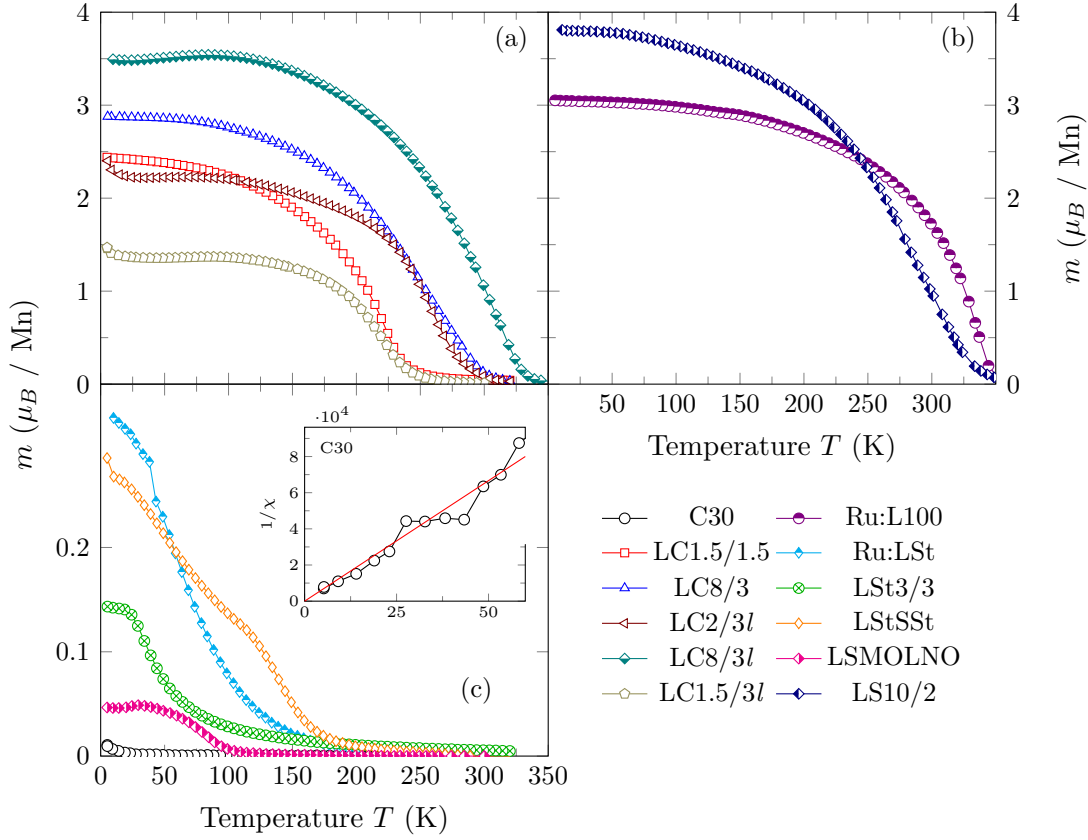


Figure 6.2: (a) M vs. T for the La_{0.7}Sr_{0.3}MnO₃/CaRuO₃ series. (b) Ru:L100, and LS10/2 show clear transitions. The saturation moment of the Ru:L100 is somewhat reduced. In (c) the samples with strongly reduced T_C are shown. The inset shows the inverse susceptibility of the CaRuO₃ film.

for a quick comparison¹. The transition temperatures are apparently increased on the LSAT substrates, probably due to improved homogeneity. In Fig. 6.2(b) the Ru:LSMO shows a high T_C but some moment reduction. Superlattices with strongly reduced T_C and smaller magnetic moments are depicted in Fig. 6.2(c). In superlattices with SrTiO₃ the T_C is strongly reduced and the magnetic moment is quenched. In the ruthenium doped superlattice Ru:LSt with three unit cell thick manganite layers, the effect of ruthenium doping is comparable to ruthenate layers separated by a two unit cell SrTiO₃ spacer layer (Sample LStSSSt). The paramagnetic and reasonably conducting strongly correlated oxide LaNiO₃ does not improve the magnetic properties of thin La_{0.7}Sr_{0.3}MnO₃ layers, probably due to the stronger localized Ni 3d electron states as compared to Ru 4d.

¹In case of the CaRuO₃ thin film μ_B per ruthenium ion.

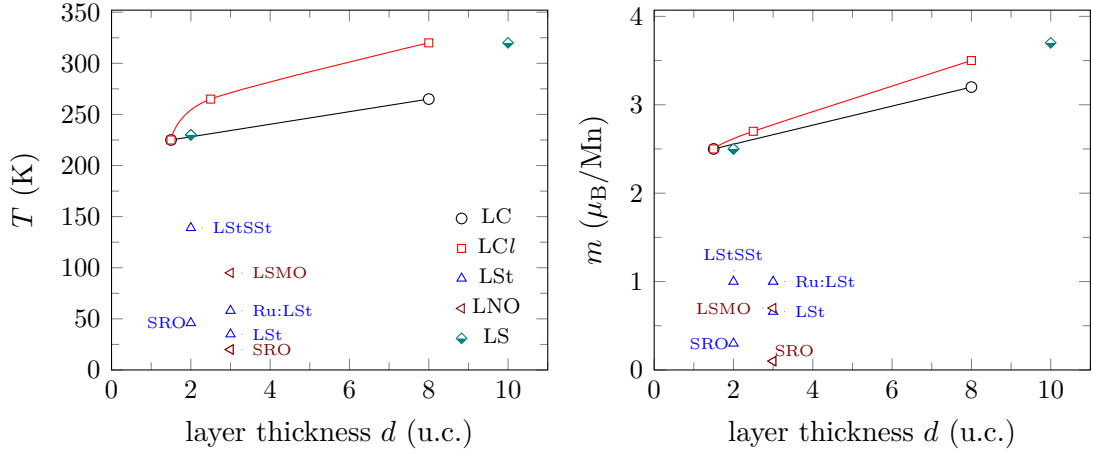


Figure 6.3: Relation of (a) T_C and (b) M with La_{0.7}Sr_{0.3}MnO₃ layer thickness in unit cells. The samples are grouped according to the series: LSMO/CRO on STO, LSMO/CRO on LSAT, STO intercalated layers, superlattices with LNO, and LSMO/SRO on STO.

For an easy comparison the transition temperature and saturation magnetic moment are plotted versus layer thickness in Fig. 6.3. The Curie temperature was obtained as the minimum in the temperature derivative of the field cooled curve in 0.1 T. With this procedure a mean Curie temperature is obtained, i.e. it generally underestimates T_C , but it will better describe the global sample properties than a Curie point determined by slope extrapolation. Indeed, also in the derivative one may obtain several minima or a very broad minimum indicating regions with varying properties. In these cases the mean was assumed. Clearly the presented samples fall into two groups. The superlattices with CaRuO₃ layers remain ferromagnetic up to relatively high temperatures with sizeable magnetic moments. When interfaced with SrTiO₃, the magnetic moment of La_{0.7}Sr_{0.3}MnO₃ is quenched, as is the Curie temperature. Ruthenium doping gives only moderate enhancements. Also interfacing with LaNiO₃ quenches the magnetization. The additional charge that might be transferred from the interfacial La³⁺ is apparently not sufficient to stabilize ferromagnetism. The effect of LaNiO₃ is even stronger on SrRuO₃ suppressing nearly completely the ferromagnetic transition. While one might relate this to the interfacial lanthanum [128], this can only be half of the answer, since between La_{0.7}Sr_{0.3}MnO₃ layers the suppression is not as strong. Most interestingly, the La_{0.7}Sr_{0.3}MnO₃/SrRuO₃ superlattice with intercalated SrTiO₃ layers (Sample LStSSt) shows a T_C of nearly 140 K indicating a small charge transfer even through two unit cell thick insulating SrTiO₃. This gives a hint on the spatial extension of the Ru 4d states.

The structural quality of the La_{0.7}Sr_{0.3}MnO₃ layers also influences the coercivity. While generally a rather soft magnet with coercive fields of less than 1 mT in case of high quality films, the coercive field of La_{0.7}Sr_{0.3}MnO₃ is sensitive to structural

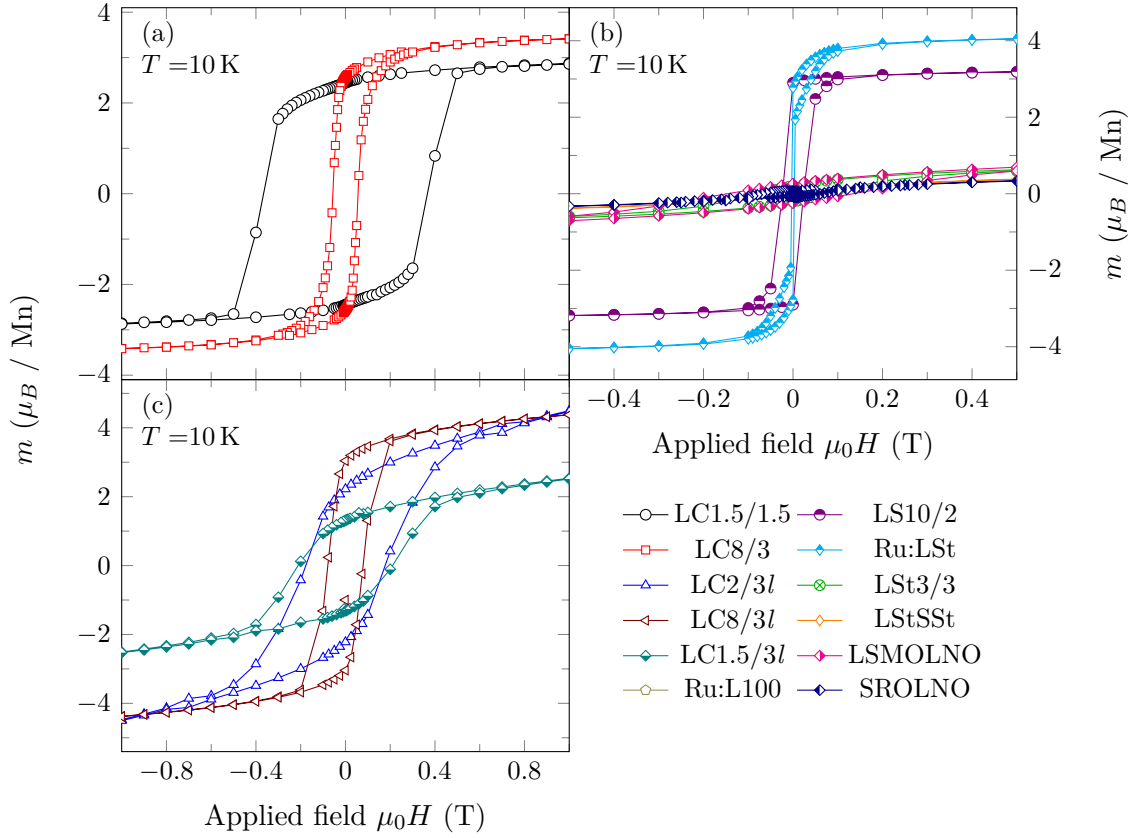


Figure 6.4: M vs. H at 10 K for the La_{0.7}Sr_{0.3}MnO₃/CaRuO₃ series on STO (a), on LSAT (c). In (b) the samples Ru:L100, and LS10/2, as well as the samples with reduced moment are depicted.

inhomogeneities. In case of ultrathin films, some parts of the sample may order antiferromagnetically, and there are also reports on surface spin glass states for nanoparticles [356]. Ruthenium doping has been employed before to enhance the coercivity of La_{0.6}Sr_{0.4}MnO₃ [98]. In Fig. 6.4 hysteresis curves obtained at 10 K with the magnetic field applied in the film plane are shown. In (b) the sample LS10/2 with high structural quality is shown along with the Ru:L100 film. Both samples show very small coercivity (note that the measurement points for Ru:L100 are more coarse artificially increasing the hysteretic opening). The samples with quenched moment are shown for comparison. For the LC superlattices depicted in (a) and (c) we may note the similarity of the two samples LC8/3 (a) and LC8/3l (c) indicating negligible influence of substrate strain. There is a trend of increasing coercivity with decreasing La_{0.7}Sr_{0.3}MnO₃ layer thickness, which may be related to structural degradation also observed in the resistivity measurements. LC2/3l and LC 1.5/3l show slanted hysteresis curves, probably related to the observed thickness distribution of the layers. Note that the samples grown on LSAT show a paramagnetic contribution which was not subtracted.

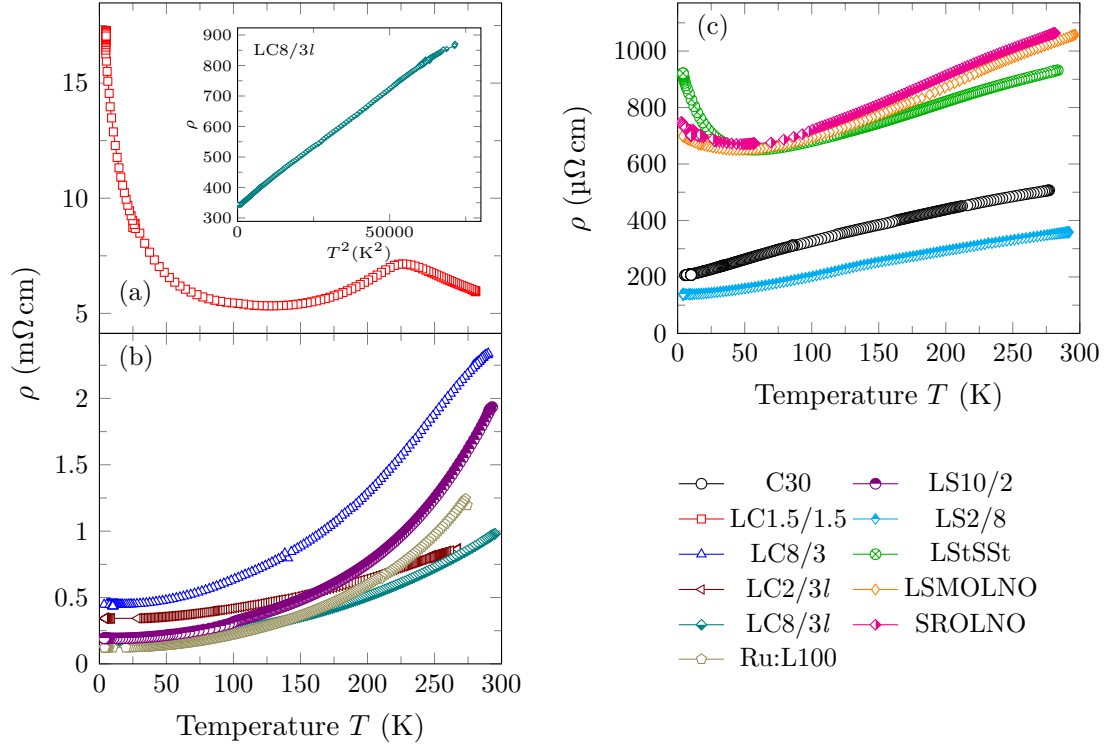


Figure 6.5: Resistivity vs. temperature of the samples studied. The samples on the left are La_{0.7}Sr_{0.3}MnO₃-like. Only LC1.5/1.5 in (a) shows an increasingly insulating behaviour upon cooldown. The quadratic temperature dependence is exemplified for LC8/3l in the inset in (a). In (c) the CaRuO₃ film, LS2/8, where the SrRuO₃ dominates, the superlattices with LaNiO₃, and LStSSst with intercalated SrTiO₃ layers are depicted.

6.3 Transport Properties

Transport measurements on the samples were done with the described Van-der-Pauw method with geometrical correction to obtain the resistivities along the two substrate edge directions (see Section 3.3). The observed anisotropy was small, and thus only the mean resistivities as obtained by the conventional Van-der-Pauw method are presented in Fig. 6.5. In contrast to superlattices with highly conducting SrRuO₃ layers [354], in which the SrRuO₃ dominates the transport properties, in superlattices of La_{0.7}Sr_{0.3}MnO₃ and CaRuO₃ the transport is to a great extent alike La_{0.7}Sr_{0.3}MnO₃. In the inset LC8/3l is plotted vs. the temperature squared to exemplify the typical T^2 dependence. In LC1.5/1.5 the ferromagnetic transition temperature is clearly indicated by a peak, which is a characteristic for the ferromagnetic manganites [6]. The transition temperatures of the other samples were outside of the measurement range. The resistivity of LC1.5/1.5 is about ten times higher than the resistivity of the other samples and increases with decreasing tem-

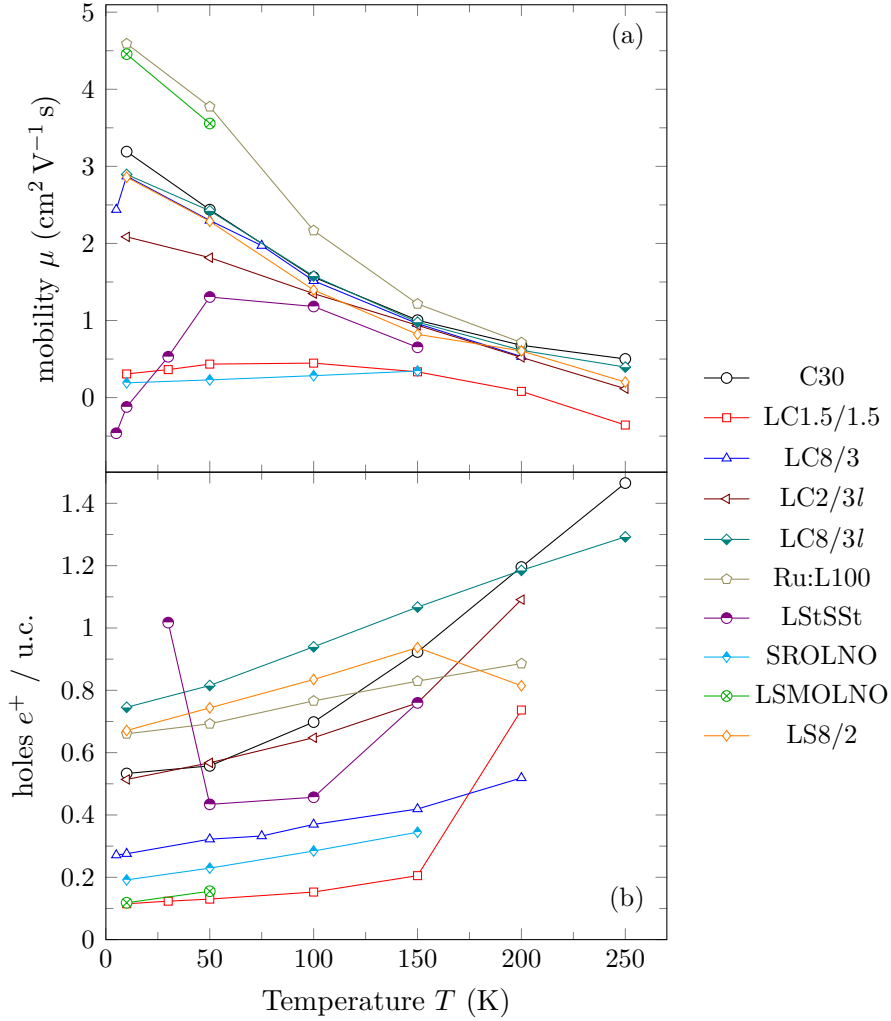


Figure 6.6: Mobility μ vs. temperature. Number of charge carriers per unit cell vs. temperature.

perature below 120 K. This indicates a rather high degree of disorder or even some phase separation. The samples grown on LSAT show enhanced conductivity, which correlates with the higher critical temperature and magnetic moment. Figure 6.5(c) shows the temperature dependence of the CaRuO₃ thin film along with conducting non-magnetic superlattices and LS2/8 with SrRuO₃ layers. The superlattices with LaNiO₃ mimic the temperature dependence of LaNiO₃ solely, with the characteristic resistivity enhancement below 50 K. Their resistivity is in a similar range as the superlattices indicating that conductivity enhancement is not a sufficient condition to promote ferromagnetic order in manganites. The sample LStSSt with intercalated SrTiO₃ layers shows similarity with SrRuO₃/SrTiO₃ superlattices (see Chapter 5) with no sign of La_{0.7}Sr_{0.3}MnO₃ contributions to the transport properties. Other samples were rather insulating with resistances exceeding 10 GΩ when lowering the

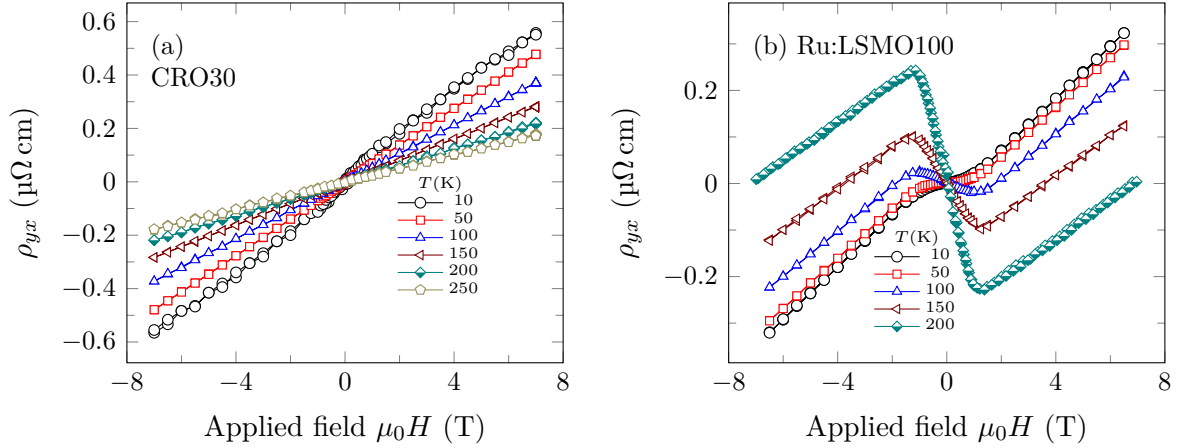


Figure 6.7: ρ_{yy} vs. magnetic field at several temperatures for the CaRuO₃ (a) and Ru:La_{0.7}Sr_{0.3}MnO₃ (b) films.

temperature and are not shown.

The mobility and charge carrier density plotted in Fig. 6.6 were extracted from resistivity data and the high field slope of the Hall data within a conventional one band model. At high temperatures the field dependence of the diagonal resistivity is affected by the large anomalous Hall effect saturating only in high fields, which disguises the ordinary Hall contribution and explains the scatter in the data in Fig. 6.6(b). The general trend is an increase of charge carrier density and a decrease in mobility with increasing temperature. Albeit the general transport properties in the LaNiO₃ superlattices are dominated by the hole conducting nickelate, one can see the apparent increase in charge carriers and decrease in mobility due to compensation effects in the superlattice with the electron conductor SrRuO₃.

To further elucidate the interplay of charge transfer and magnetism we studied the anomalous Hall effect which correlates with the magnetization. Figure 6.7 presents measurements of the diagonal resistivity of the CaRuO₃ and Ru:La_{0.7}Sr_{0.3}MnO₃ thin films. The high field slope is positive in both cases, which indicates hole conduction in a one band model. There is a small curvature in the CaRuO₃ data at low temperatures, which may indicate a shortcoming of the one band model [357] or paramagnetic AHE contributions [119]. The Ru:La_{0.7}Sr_{0.3}MnO₃ film in Fig. 6.7(b) shows the typical behaviour for manganites with a maximum of ρ_{AHE} close to the Curie temperature which vanishes at low temperature.

Depending on the La_{0.7}Sr_{0.3}MnO₃ layer thickness, the CaRuO₃/La_{0.7}Sr_{0.3}MnO₃ superlattices show a different behaviour: While the thicker superlattices LC8/3 and LC8/3l are similar to La_{0.7}Sr_{0.3}MnO₃ films (see Fig. 6.8 (a)), albeit with an enhanced anomalous Hall coefficient, the thinner samples show an increase of the AHE contribution with decreasing temperature, with even further increased anomalous Hall coefficient as compared to the thicker superlattices. Even more stunningly, the curves get rounded, eventually saturating in fields >4 T. This rounding contribu-

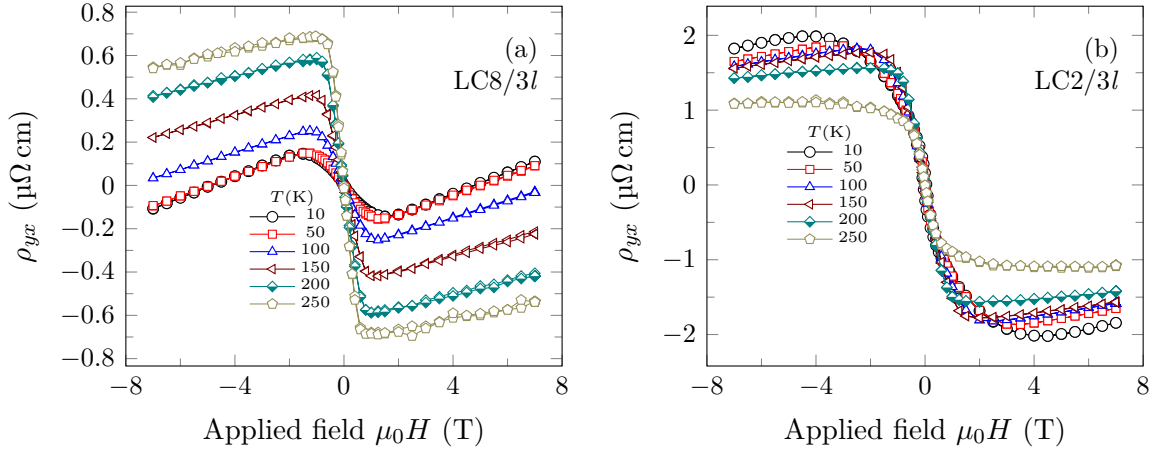


Figure 6.8: ρ_{yx} vs. magnetic field at several temperatures for (a) LC8/3 and (b) L/C2.5/3. Note the similarity to La_{0.7}Sr_{0.3}MnO₃ in (a), while for (b) there is only a small change of ρ_{AHE} with temperature. Note also the rounding of the loops at low temperatures in (b).

tion is too large to be ascribed to a two band conduction only. There might even be some magnetic proximity effect onto the ruthenium ions. In supposedly ferromagnetic CaRuO₃ a small AHE has been observed [355]. Another possible explanation might be a change in the magnetic anisotropy of the La_{0.7}Sr_{0.3}MnO₃ layers due to antiferromagnetic coupling to the ruthenium ions.

These mentioned trends are seen more clearly in Fig. 6.9. The given samples fall into three groups. LC8/3l, LS10/2 and Ru:L100 are alike La_{0.7}Sr_{0.3}MnO₃, with a decreasing AHE upon temperature reduction. The samples LC8/3 and LC2/3l show a weak temperature dependence and a small decrease of the AHE with increasing temperature respectively. These two samples also belong to a medium residual resistivity range of 400 $\mu\Omega$ cm to 500 $\mu\Omega$ cm (see Fig. 6.5). LC1.5/1.5 has, similar to its resistivity, an anomalous Hall coefficient enhanced by a factor of ten. Note the scaling of LC1.5/1.5 in Fig. 6.9(a), which also implies a temperature dependence a factor of ten higher than the other samples. Upon lowering the temperature $\rho_{AHE}M_S$ is enhanced. The positive $\rho_{AHE}M_S$ observed for LStSSr corroborates the assumption that conduction is dominated by the SrRuO₃ layers.

The double logarithmic representation of $-\rho_{AHE}$ vs. ρ in Fig. 6.9(b) shows a scaling effect with the longitudinal resistivity. This kind of scaling is often observed for disordered materials with hopping conduction [215]. For the samples with intermediate resistivity (LC8/3 and LC2/3l), which do not follow the scaling observed for the other samples, there might be competing effects at play. In manganites different scaling behaviours have been proposed, and the actually observed anomalous Hall effect depends on the several contributions. A scaling with the magnetization was proposed by Lyanda-Geller et al. [218] and described nicely the behaviour close to the ferromagnetic transition temperature for a range of manganites. Ye

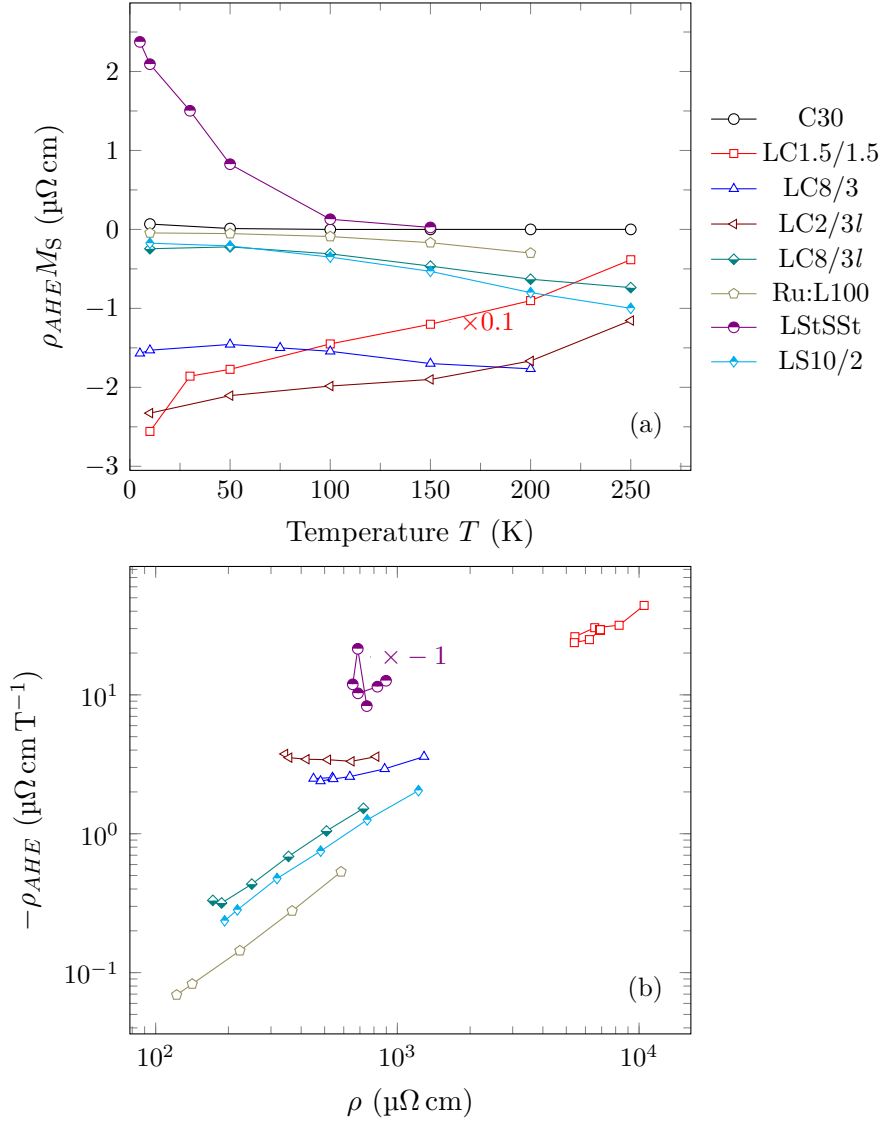


Figure 6.9: (a) Anomalous Hall coefficient $\rho_{AHE} M_S$ vs. temperature. (b) Anomalous Hall coefficient ρ_{AHE} vs. longitudinal resistivity ρ .

et al. [358] calculated different scaling behaviours depending on the temperature, and Matl et al. [359] reported scaling with resistivity, as observed here. Albeit the data is normalized by the magnetization, this does not account for possible sample inhomogeneities, which may also contribute to deviations. The SrRuO₃ confined in layers of SrTiO₃ in sample LStSSSt (multiplied by -1) does not follow a scaling of this kind.

6.4 Discussion

Similar to the ferromagnetic electron conductor SrRuO₃ [354], also the paramagnetic hole conductor CaRuO₃ can stabilize ferromagnetism in ultrathin La_{0.7}Sr_{0.3}MnO₃. Long range RKKY²-like exchange coupling across the CaRuO₃ layers should be of minor importance, as similar results were also obtained in embedded single layers [360] and no clear thickness dependence of the coupling was observed. After successful suppression of the *dead layer* formation, the manganites follow a finite size scaling similar to the 3d transition metal ferromagnets with a T_C reduced by a factor of two for one unit cell thick films [343]. The negative result with a LaNiO₃ superlattice underline the importance of strongly delocalized 4d electron states for charge transfer. Molybdenum or rhodium might be other candidates possibly without antiferromagnetic coupling [361, 362], albeit with less reductive potential than ruthenium [363]. The observed scaling of the anomalous Hall effect is another confirmation of bulk like properties in La_{0.7}Sr_{0.3}MnO₃ layers when interfaced with CaRuO₃, an effect that was concealed in the previous study with SrRuO₃ [354] due to the magnetic coupling.

The observed small effect in the LStSSt sample with intercalated SrTiO₃ layers gives a lower limit for the extension of the charge transfer of at least two unit cells. The effect is greater in superlattices than by disordered doping in films, possibly due to better structural coherence. A secondary effect of the layered structure may be that the large ruthenium atoms have the inverse effect compared to a free surface: The extended Ru 4d states rise the energy of the Mn *t*_{2g} orbitals strengthening the *e*_g occupation and increasing the bandwidth. Hall effect measurements show an unusual rounding up to applied fields of 4 T, which implies a modification of the effective magnetic anisotropy or a magnetic proximity effect on the CaRuO₃. Interfacial ruthenate layers may be a feasible way to preserve the unique properties of La_{0.7}Sr_{0.3}MnO₃ in device fabrication. Perspectively, further studies are needed to evaluate the degree of spin polarization of ruthenium layer enhanced La_{0.7}Sr_{0.3}MnO₃ and how the delocalized ruthenium states affect the La_{0.7}Sr_{0.3}MnO₃ band structure.

²Rudermann-Kittel-Koriya-Yoshida exchange via spin polarization of itinerant electrons.

Manganite Ruthenate Superlattices

In the previous chapters we studied the effects of charge transfer at oxide interfaces and the modification of the magnetic anisotropy due to strain and interfacial symmetry breaking. Now we add an additional degree of freedom due to magnetic coupling in all ferromagnetic systems. Disentanglement of the various parameters is complicated as the microscopic structure of each layer with a well defined symmetry has eventually a smaller influence on the global properties than the interfacial anisotropy and the apparent anisotropy due to coupling to the adjacent layer.

Let us first resume some of the contrasting material properties of the constituting layers presented in more detail in Chapter 2: $\text{La}_{0.7}\text{Sr}_{0.3}\text{MnO}_3$ only has a small magnetic anisotropy [364] with a high magnetic moment of ideally $3.7 \mu_B/\text{Mn}$. In thin films generally the shape anisotropy dominates the magnetic behaviour, albeit there are some small contributions due to magnetoelastic coupling [331]. It exhibits hopping transport characteristic for double exchange ferromagnets with hole-like charge carriers and relatively high resistivity. SrRuO_3 shows contrasting properties. While having a factor of two smaller magnetic moment ($1.8 \mu_B/\text{Ru}$), it has a high magnetocrystalline anisotropy. In thin film form, this anisotropy is further increased by a strong surface anisotropy resulting in a basically uniaxial anisotropy with out of plane easy axis. Although considered a *bad metal*, it shows a high electron-like conductivity for an oxide. As all layers were grown on (001) oriented SrTiO_3 , the interfaces will introduce a tetragonal symmetry. Due to the higher magnetic moment of the manganite, strong magnetic coupling can enhance the effect of the applied field on the SrRuO_3 by orders of magnitude, reducing the apparent anisotropy.

The manganese and ruthenium atoms couple antiferromagnetically via the bonding oxygen atom. This antiferromagnetic coupling can be understood as due to strong hybridization of the Ru 4d states with the oxygen orbitals [163]. Or with view on band structure calculations [109] with the fact that SrRuO_3 is a spin minority conductor.

In the following section we present samples categorized into three groups: First the results of superlattices with rather thick individual layers are presented, which can be understood by an interplay of magnetic and structural coupling. The second section is comprised of superlattices in the ultrathin limit with three, two, and one unit cell thickness, which clearly show properties going beyond their individual

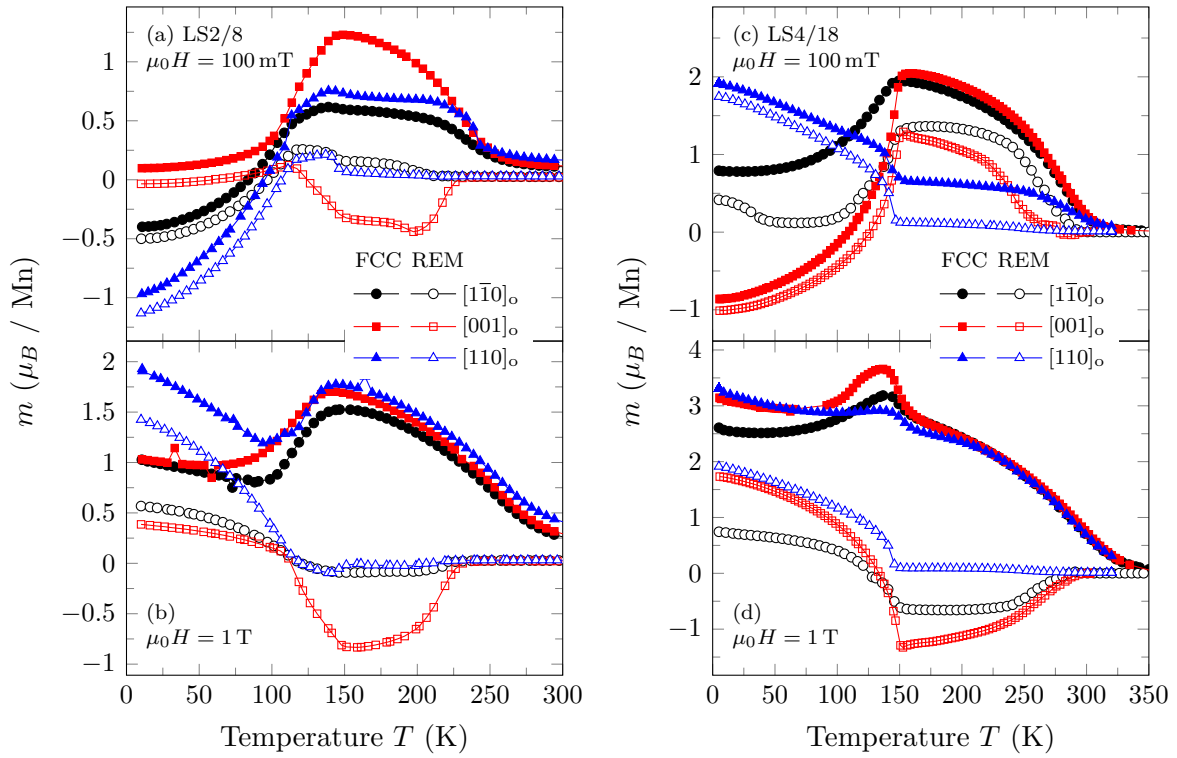


Figure 7.1: Field cooled curves and in an applied field of 0.1 T (a,b) and 1 T (c,d) and the consecutive remanence curves obtained heating the samples in zero field for LS2/8 and LS4/8

constituents. Finally, ultrathin trilayers with SrRuO_3 embedding $\text{La}_{0.7}\text{Ba}_{0.3}\text{MnO}_3$ layers are presented showing some surface effect as well. Here we employed XMCD to probe the individual layer magnetization.

7.1 Interlayer Coupling Strength

7.1.1 Magnetization

In thick superlattices the individual material properties dominate over the coupling, i.e. the system can be described by adding the magnetic energies of the two constituent materials and a coupling constant (Eq. (2.1)). The strength of the coupling may be changed by changing the number of interfaces. Here we compare two $[\text{La}_{0.7}\text{Sr}_{0.3}\text{MnO}_3/\text{SrRuO}_3]_{15}$ superlattices, LS2/8 and LS4/18, where the numbers indicate the thickness of the individual layers in unit cells. They have a similar thickness ratio, however, the first has an interface density a factor of two higher than the second one. Thus one might expect a factor of 2 stronger coupling in the first superlattice. In Fig. 7.1 field cooled and the consecutively obtained remanence

curves in fields of 0.1 and 1 T are presented. Most remarkably, the antiferromagnetic coupling of the two superlattices may lead to negative magnetization.

In both systems, the total magnetic moment of the SrRuO_3 layers is higher than that of the $\text{La}_{0.7}\text{Sr}_{0.3}\text{MnO}_3$ layers at low temperatures. There is a difference in the magnetic coupling and the magnetocrystalline anisotropy of the SrRuO_3 layers. When cooling in a moderate field of 100 mT the antiferromagnetic coupling dominates over the Zeeman energy in the vicinity of the ferromagnetic transition of SrRuO_3 resulting in the SrRuO_3 layers being magnetized antiparallel with respect to the applied field. This antiparallel alignment is stabilized by the magnetocrystalline anisotropy. LS4/18 however, shows ferromagnetic-like coupling and a positive magnetic moment for the out of plane direction indicating a contribution to the total energy from the antiferromagnetic coupling between ruthenium and manganese.

Application of a higher field of 1 T during the field cool aligns the SrRuO_3 layers with the applied field. The decrease in overall magnetic moment due to the antiferromagnetic coupling is more pronounced in LS2/8, a further evidence of the stronger antiferromagnetic coupling in this sample.

There is a notable anisotropy for the two in plane directions at elevated temperatures above the T_C of SrRuO_3 with a reduction of the magnetic moment in plane to a value comparable with the out of plane moment for LS2/8. This unexpected in-plane anisotropy of the $\text{La}_{0.7}\text{Sr}_{0.3}\text{MnO}_3$ layers can only be explained by a structural coupling on the microscopic level and consequently a transfer of the orthorhombic structure of the SrRuO_3 layer to the $\text{La}_{0.7}\text{Sr}_{0.3}\text{MnO}_3$ layer. As the cations are ordered in the cubic perovskite structure and follow the square lattice of the substrate, it is the oxygen octahedra which determine the structure by their tilt angles. In the Glazer classification of tilt systems [11] SrRuO_3 can be described as $a^-a^-c^+$, i.e. out of phase rotations about the a and b pseudocubic axes and in phase rotation about the c axis (see also Chapter 2). $\text{La}_{0.7}\text{Sr}_{0.3}\text{MnO}_3$, on the other hand, is described by a $a^-a^-a^-$ tilt pattern. The in plane easy axis of the $\text{La}_{0.7}\text{Sr}_{0.3}\text{MnO}_3$ layers is along the orthorhombic c -axis of the SrRuO_3 as identified by the magnetically hard axis of the SrRuO_3 layers and by angular magnetoresistance. The microscopic origin of the $\text{La}_{0.7}\text{Sr}_{0.3}\text{MnO}_3$ magnetic hard axis along the $[1\bar{1}0]_o$ axis may be related to the anisotropy of the tilt angles resulting in an anisotropic bandwidth for the double exchange mechanism.

7.1.2 Angle Dependent Magnetoresistance

From the symmetry of angle dependent magnetoresistance measurements the structural symmetry of the sample may be determined following the ansatz of Döring [192] or Birss [186] as described in detail in Chapter 4. In case of magnetically coupled systems this approach is complicated by the fact that not only the magnetocrystalline anisotropy of the single layer, but also magnetic coupling and eventual parallel transport processes have to be taken into account. However, the symmetry

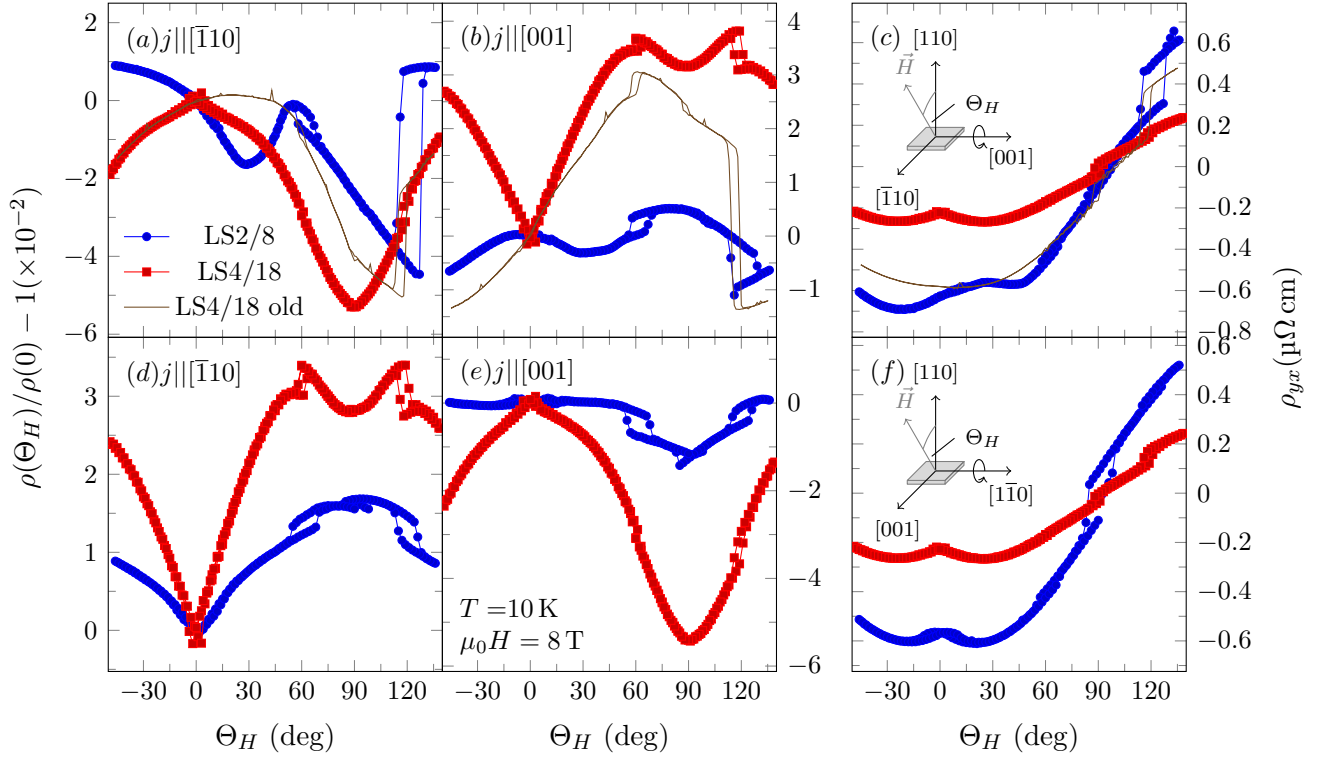


Figure 7.2: Angle dependent magnetoresistance at 10 K for LS2/8 and LS4/18. The latter one severely twinned. Lines show an older measurement with less twins (measurement by M. Ziese). Note also the reduction in ρ_{yx} .

might readily be recognized in a known system by characteristic features without a complete fit. In Fig. 7.2 the measured magnetoresistance curves have been indexed accordingly by comparing to a 40 nm thick orthorhombic SrRuO₃ film. The characteristic orthorhombic symmetry with one hard axis at 60° respectively 120° from the substrate normal is clearly seen LS2/8. There are deviations from the pure orthorhombic curve due to the antiferromagnetic coupled La_{0.7}Sr_{0.3}MnO₃. Furthermore, there is a number of crystallographic twins present as seen by the hysteretic behaviour around 60° in the (001) plane and 60° and 120° in the (110) plane, and corresponding steps in the Hall measurement. LS4/18 is severely twinned. Albeit there are still the characteristic steps and openings at the right angular positions the curves in the two rotation planes look equivalent. We may conclude that the sample consists of roughly equal fractions of the four possible epitaxial relations of the SrRuO₃ (110)_o oriented orthorhombic unit cell with the cubic substrate. The thin line is a first measurement of LS4/18 made two years before the other measurements. These measurements indicate that the sample had been in a nearly single crystalline form. Note that this breaking up into crystallographic twins affects both the coupling and the Hall effect. The reason for this structural transformation upon

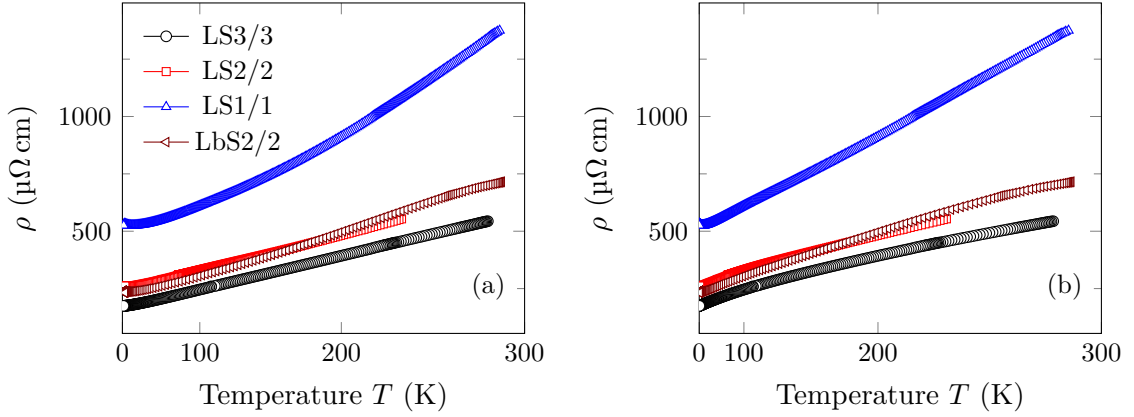


Figure 7.3: Temperature dependence of the resistivity for the ultrathin superlattices LSMO/SRO[3/3]₁₅, LSMO/SRO[2/2]₁₅, LSMO/SRO[1/1]₂₂, and LBMO/SRO[2/2]₂₂. The temperature axis is scaled according to $T^{3/2}$ in (a) and T^2 in (b).

ageing could be related to microscopic cracks formed during thermal cycles through the SrTiO₃ substrates structural phase transition (see Section 3.5).

7.2 Ultrathin Superlattices

Three superlattices with ultrathin layers of one, two and three unit cell thickness for each of the constituting layers La_{0.7}Sr_{0.3}MnO₃ and SrRuO₃ were fabricated with the usual PLD parameters described earlier. In the following they are referred to by LS1/1, LS2/2, and LS3/3, where the numbers indicate the individual layer thicknesses. The bilayers were repeated 15 times (LS3/3, LS2/2) or 22 times (LS1/1). In a fourth superlattice (LbS2/2) with La_{0.7}Ba_{0.3}MnO₃ as manganite layer, the inter-layer strain is reduced. This superlattice consists of 22 bilayers. These superlattices show a distinct behaviour with no noticeable signature of the parent materials. HAADF-STEM images show homogeneous growth with sharp interfaces, so inter-mixing effects can be excluded. However, as discussed earlier (Section 6.4), an extension of the Ru 4*d* states about two unit cells away from the interface may yield a coupling of the ruthenium electronic states throughout the samples.

Contrary to samples with thicker individual layers, the temperature dependence does not show any slope change in vicinity of the SrRuO₃ ferromagnetic transition, instead one may fit the data with a power law, similar to the case of the La_{0.7}Sr_{0.3}MnO₃ / CaRuO₃ superlattices described earlier. In Fig. 7.3 the resistivity of the four ultrathin superlattices is plotted vs. the temperature on different scales. The sample LS1/1 shows a temperature dependence with $\rho \sim T^2$, whereas the other samples are well described with a $\rho \sim T^{3/2}$ relation. Both exponents are typically found in magnetic systems. From the absence of a slope change one could infer that

the contribution to the conductivity of both materials is similar. On the other hand, this could be taken as an indication of the strong magnetic coupling between the layers. The characteristic kink close to T_C is related to the onset of magnetic order and a slow magnon freeze out at lower temperatures. If the magnetic excitations of the manganite and ruthenate couple, we may expect a uniform behaviour.

As already observed in the Section 7.1, the interlayer coupling increases with the interface density. As these superlattices are composed of equal numbers of layers of the two materials the manganite magnetization will always dominate over the ruthenate magnetization. Due to the strength of the antiferromagnetic coupling it is impossible to align the SrRuO_3 magnetization with the external field. Thus we may see these superlattices as well as an artificial ferrimagnet.

Above the T_C of the SrRuO_3 layers the manganite properties dominate: the samples have a magnetic hard axis along the substrate normal. At low temperatures the hysteresis curves measured in the sample plane are slanted, whereas the out of plane hysteresis curves show a square shape with rather low coercive fields. The anomalous Hall effect shows only a weak temperature dependence, similar to the LSMO/CRO superlattices discussed earlier. Thus we may infer, that SrRuO_3 does not play a significant role in the size of the AHE. The high field slope of the Hall measurements is positive and very small. From this, one might conclude on a high charge carrier density and a hypothetical interfacial hole gas, however, in view of the system being composed of an electron conductor and a hole conductor, it seems more probable that compensation effects are at play.

In angle dependent magnetoresistance measurements a tetragonal symmetry is observed. This might be related to microscopic twinning, as discussed before, but, more importantly, the square lattice forming the interface imprints a tetragonal symmetry. In Fig. 7.4 the angle dependent magnetoresistance in a magnetic field of 8 T at a temperature of 10 K is shown. Current directions and the rotation axis are indicated with respect to the substrates cubic system, equivalent to a possible tetragonal system of the samples. Rotation in the (010) plane is equivalent and is not shown. Interestingly, the angle dependent magnetoresistance measurements indicate that both, the in-plane axis as well as the out-of-plane axis are magnetically hard. The evolution of the easy magnetization direction depends on the layer thickness. Sample LS3/3 has the easy axis in plane, whereas LS2/2 is magnetically hard in plane, as seen from the cusps in the magneto resistance. This is even more evident from the corresponding measurements of the off-diagonal resistivity ρ_{yx} shown in Fig. 7.5. Since the $\text{La}_{0.7}\text{Sr}_{0.3}\text{MnO}_3$ magnetization in LS3/3 is considerably higher ($\sim 3.2\mu_B$ per Mn vs. $\sim 2.5\mu_B$ in LS2/2) the following interpretation seems most probable. In LS3/3 the overall anisotropy is dominated by the anisotropy of the $\text{La}_{0.7}\text{Sr}_{0.3}\text{MnO}_3$ layer, which is mainly due to shape anisotropy and partly due to magnetostriction from the tensile strain. In LS2/2 the strontium ruthenates' magnetic anisotropy, enhanced by in-plane compressive strain, dominates. The out-of-plane easy axis in LS2/2 may also partially be caused by a stronger coupling and partial hybridization of the Mn 3d states with the Ru 4d states reducing the out-

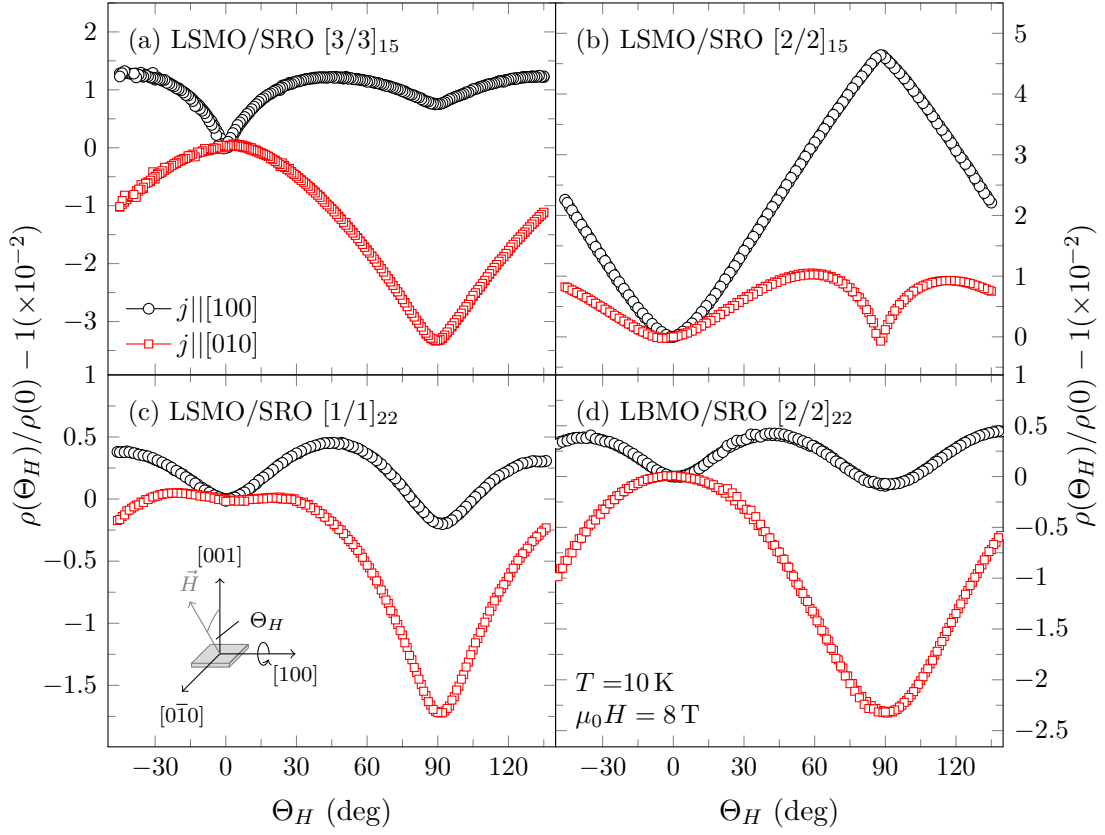


Figure 7.4: Angle dependent magnetoresistance of ultrathin superlattices at 10 K in an applied field of $\mu_0 H = 8$ T. (a) LSMO/SRO $[3/3]_{15}$, (b) LSMO/SRO $[2/2]_{15}$, (c) LSMO/SRO $[1/1]_{22}$, and (d) LBM/SRO $[2/2]_{22}$.

of-plane hard axis of $\text{La}_{0.7}\text{Sr}_{0.3}\text{MnO}_3$ as already observed for the $\text{La}_{0.7}\text{Sr}_{0.3}\text{MnO}_3 / \text{CaRuO}_3$ system (Chapter 6). In LS3/3 there persists one manganite layer without interface contact, whereas in LS2/2 every manganese has a ruthenium neighbour and vice versa. The angle dependent magnetoresistance of LS1/1 and LbS2/2 depicted in Fig. 7.4(c) and (d) suggest contributions of the two materials to the overall magnetic anisotropy which are nearly in equilibrium. The strong antiferromagnetic coupling of the layers forms one single system which is rotated uniformly by the applied magnetic field with only minor spin canting.

7.3 Trilayers

To exclude interlayer coupling, trilayers of $\text{La}_{0.7}\text{Ba}_{0.3}\text{MnO}_3$ with a thickness from 1 to 5 u.c. embedded in 3 u.c. thick SrRuO_3 were fabricated by the already mentioned PLD process. One additional sample has thickness reduced embedding layers between 1 and 2 u.c. SrRuO_3 to minimize the SrRuO_3 contributions to the transport

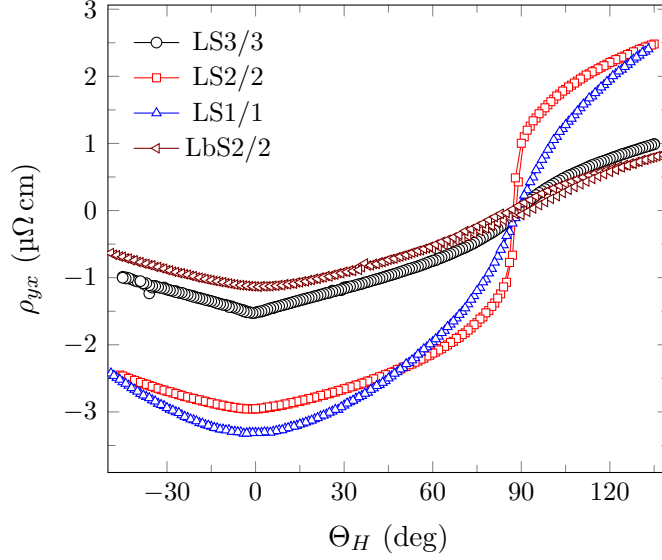


Figure 7.5: Angle dependent ρ_{yx} of ultrathin superlattices at 10 K in an applied field of $\mu_0 H = 8$ T of the ultrathin superlattices LSMO/SRO[3/3]₁₅, LSMO/SRO[2/2]₁₅, LSMO/SRO[1/1]₂₂, and LbMO/SRO[2/2]₂₂.

properties. The FC magnetization in an applied field of 0.1 T parallel (perpendicular) to the film plane are shown in Fig. 7.6 (a) and (b). They show exceptionally high ferromagnetic transition temperatures and the characteristic antiferromagnetic coupling of the embedding SrRuO₃ layers due to the antiferromagnetic coupling of the Ru⁴⁺ via the interfacing oxygen to the Mn^{3+/4+}. From the remanence curves we may infer the magnetization state at low temperature, i.e. whether the SrRuO₃ or the La_{0.7}Ba_{0.3}MnO₃ layers are oriented along the measurement direction. Generally they follow closely the field cooled curves and are not presented. From these we conclude that the film with the easy magnetization direction parallel to the applied field aligns the magnetization as expected, i.e. La_{0.7}Ba_{0.3}MnO₃ is aligned to the applied field for the in-plane measurement, and SrRuO₃ for the out-of-plane measurement. The case is different for the samples T313 and T323. Here the antiferromagnetic coupling of the SrRuO₃ to the La_{0.7}Ba_{0.3}MnO₃ dominates over the Zeeman energy close to the T_C of the SrRuO₃. Thus it is oriented opposite to the applied field and remains in this antiparallel configuration due to the strong perpendicular magnetic anisotropy. As the other samples have in principle the same SrRuO₃ layer properties, it is remarkable that only the thinnest layers show this strong antiferromagnetic coupling, particularly as the Zeeman energy difference between SrRuO₃ and La_{0.7}Ba_{0.3}MnO₃ increases. Note that the La_{0.7}Ba_{0.3}MnO₃ magnetization along the surface normal for T131 and T323 is enhanced in comparison to the other samples, which implies a modification of the anisotropy of the manganite layer. This may also lead to an enhanced coupling as the $d_{z^2-r^2}$ have a higher occupation. In view of the delocalization of the ruthenium d states, the thinnest layers might be

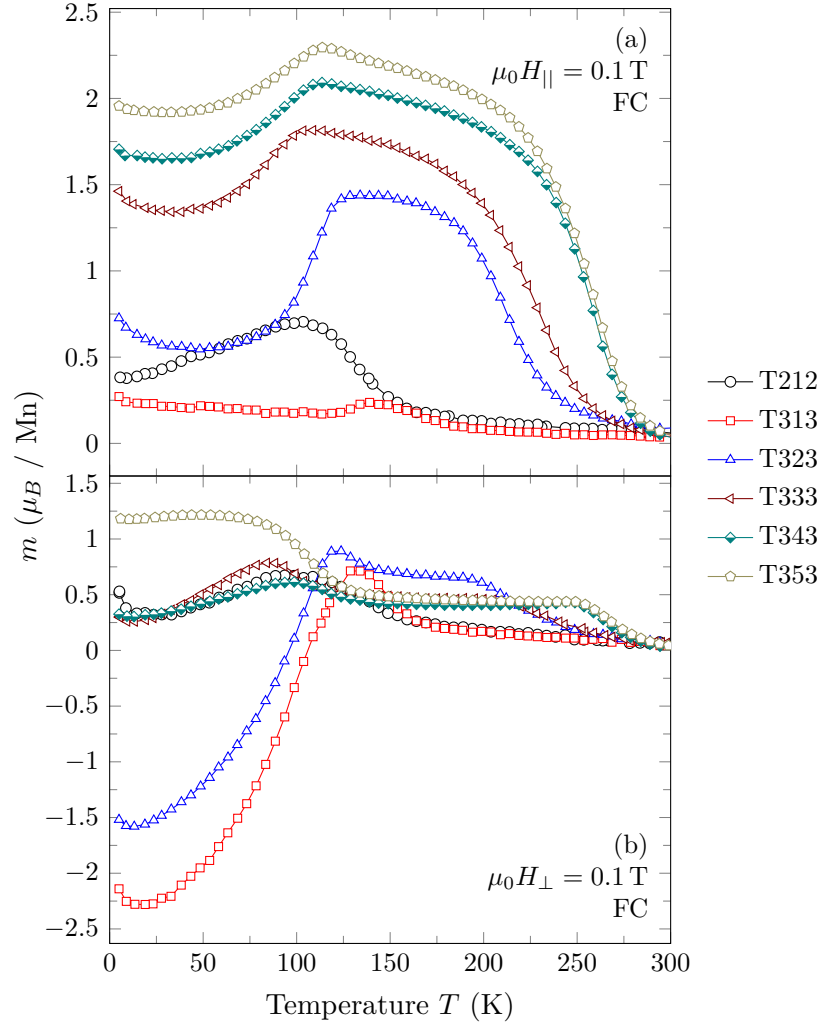


Figure 7.6: Field cooled curves in an applied field of 0.1 T in the film plane (a) and along the substrate normal (b).

viewed not as a system of independent layers, but rather a hybrid system, similar to the case of the thinner superlattices.

As the magnetization data show substantial temperature independent impurity contributions from the substrate, and the overall magnetic signal of the layers is rather small, we take the Hall data to study the field dependence of the magnetization. In Fig. 7.7 the measured ρ_{yx} of selected samples are presented. Both materials exhibit a negative anomalous hall contribution, albeit SrRuO_3 may also have a positive ρ_{AHE} depending on temperature and structural quality (see Chapter 5). The possible magnetization configurations depend on the anisotropies $K_i(T)$, the strength of the antiferromagnetic coupling J_{ab} , and the magnetization and field dependent Zeeman energy $\mu_0 H M_i(T)$ as parameters. Besides the applied field, $\text{La}_{0.7}\text{Ba}_{0.3}\text{MnO}_3$ layer thickness and temperature variations allow the navigation through this parameter

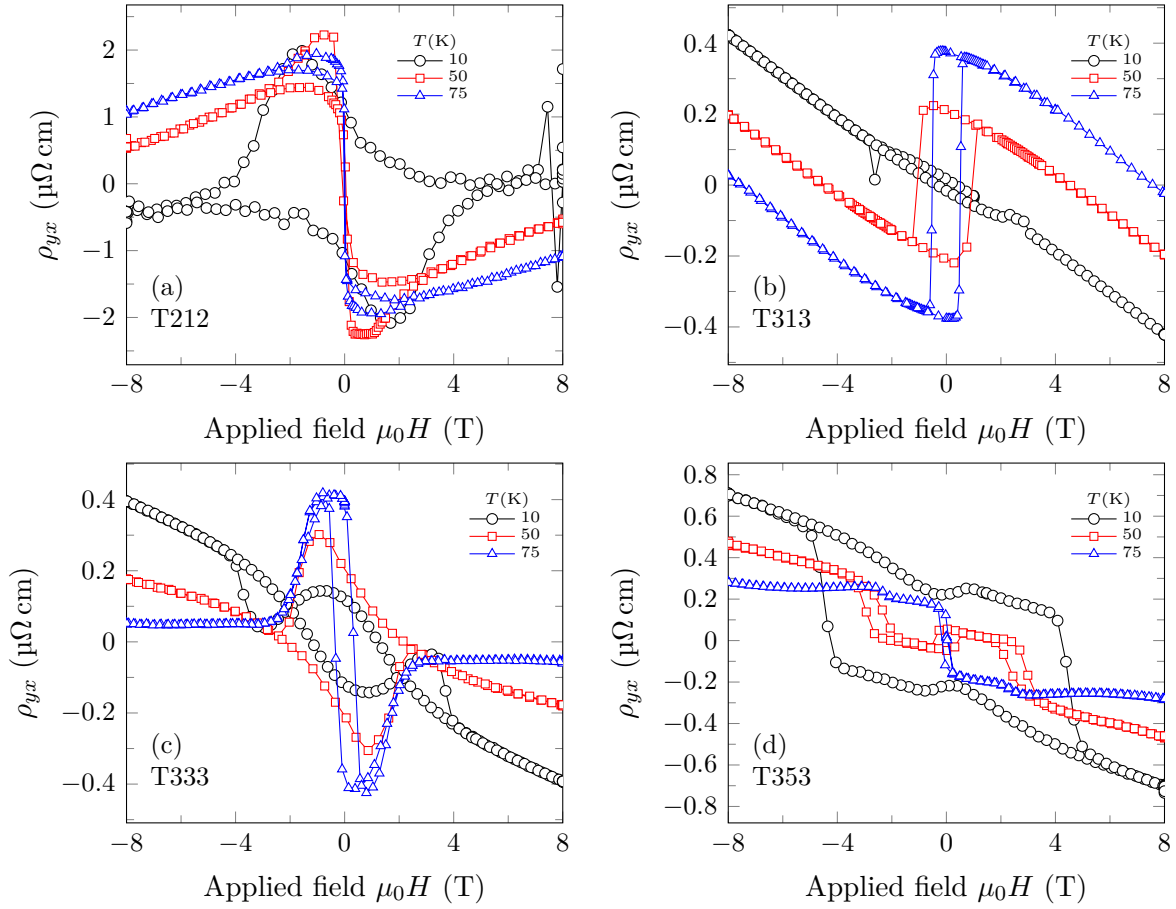


Figure 7.7: ρ_{yx} of samples T212, T313, T333, T353 at selected temperatures.

space. Easiest to understand is the sample T353. Looking at the data recorded at 50 K we see three switching events. In high fields we may assume that both materials have their magnetic moment aligned along the applied field. Upon reduction of the field, the antiferromagnetic coupling becomes similar in size as the Zeeman energy, thus switching the ruthenate layers with the lower total magnetic moment antiparallel to the applied field. Reversing the field, all the layers switch the magnetization direction together, conserving the antiparallel alignment. Further increasing the field in the negative field direction will eventually align both layers again parallel to the applied field. With this model we may understand the 10 K data of T353 with a small dip at fields below 2 T as due to the onset of a magnetization rotation of the SrRuO₃ layers. However, the manganite layer reverses the magnetization in vicinity to the zero crossing of the applied field, and the antiferromagnetic coupling stabilizes the antiparallel alignment of the ruthenate layers with respect to the applied field. Since the magnetization reversal of the manganite layer has no significant influence on the measured ρ_{yx} , we may conclude that either the transport is dominated by the SrRuO₃ layers, or the anomalous Hall effect of the

five unit cell thick $\text{La}_{0.7}\text{Ba}_{0.3}\text{MnO}_3$ layer is very small, which would indicate high structural quality.

In the sample T313 (Fig. 7.7(b)), the magnetic moment of the SrRuO_3 layers is higher than that of the $\text{La}_{0.7}\text{Ba}_{0.3}\text{MnO}_3$ layer. Thus the $\text{La}_{0.7}\text{Ba}_{0.3}\text{MnO}_3$ remain antiferromagnetically coupled to the SrRuO_3 layers throughout the hysteresis loop. The positive anomalous Hall coefficient might point at a large contribution from the antiferromagnetically coupled $\text{La}_{0.7}\text{Ba}_{0.3}\text{MnO}_3$ layer with its intrinsically negative anomalous Hall coefficient. In the two samples T212 and T333 (Fig. 7.7(a) and (c)) the different energies at play have similar magnitude resulting in a continuous magnetization rotation process. The two processes described above are superimposed. Close to zero field the Zeeman energy is negligible, but the magnetocrystalline anisotropy of the ruthenate layers is larger than that of the $\text{La}_{0.7}\text{Ba}_{0.3}\text{MnO}_3$, thus forcing the $\text{La}_{0.7}\text{Ba}_{0.3}\text{MnO}_3$ layers to switch before reaching zero field.

The anomalous Hall constants $\mu_0 MR_{AHE}$ of the two constituting materials were determined by comparing the extrapolation of the high field Hall effect to zero field with the measured AHE at zero applied field. Based on the assumption of antiferromagnetic coupling and neglecting possible weighting differences due to relative field dependent resistivity changes, the individual contributions may be disentangled with

$$\mu_0 MR_{AHE} = \mu_0 M^a R_{AHE}^a + \mu_0 M^b R_{AHE}^b$$

and $M^a \parallel M^b \parallel \mu_0 H$ in the high field limit and $M^a \nparallel M^b \parallel \mu_0 H$ in the low field limit. The carrier density was calculated from the slope ρ_H of the high field Hall data within a one band model ($n = 1/R_H e$). The corresponding values are shown in Fig. 7.8. The separation of the two anomalous Hall constants is not satisfactory in case of the 3 u.c. thick film due to a magnetization rotation process at low fields. The temperature dependence of the anomalous Hall constant attributed to SRO is reminiscent of ultrathin orthorhombic SRO films (Chapter 5), while the LBMO films contribute a negative, weakly temperature dependent term as observed before for $\text{La}_{0.7}\text{Sr}_{0.3}\text{MnO}_3$ (Chapter 6). The anomalous Hall effect of the embedded LBMO films is relatively easy to understand as a superposition of the contributions from the constituent layers in contrast to the case in LSMO / SRO superlattices (Section 7.2). The carrier density appears to indicate a transition from electron dominated conduction at low temperatures to hole dominated conduction at high temperatures. One has to keep in mind, however, that the high field slope of single SRO films also shows a sign change from negative to positive values due to the positive contribution of the anomalous Hall effect in the paramagnetic phase. It is hardly possible to disentangle the ordinary Hall effect above the T_C of the SrRuO_3 layers.

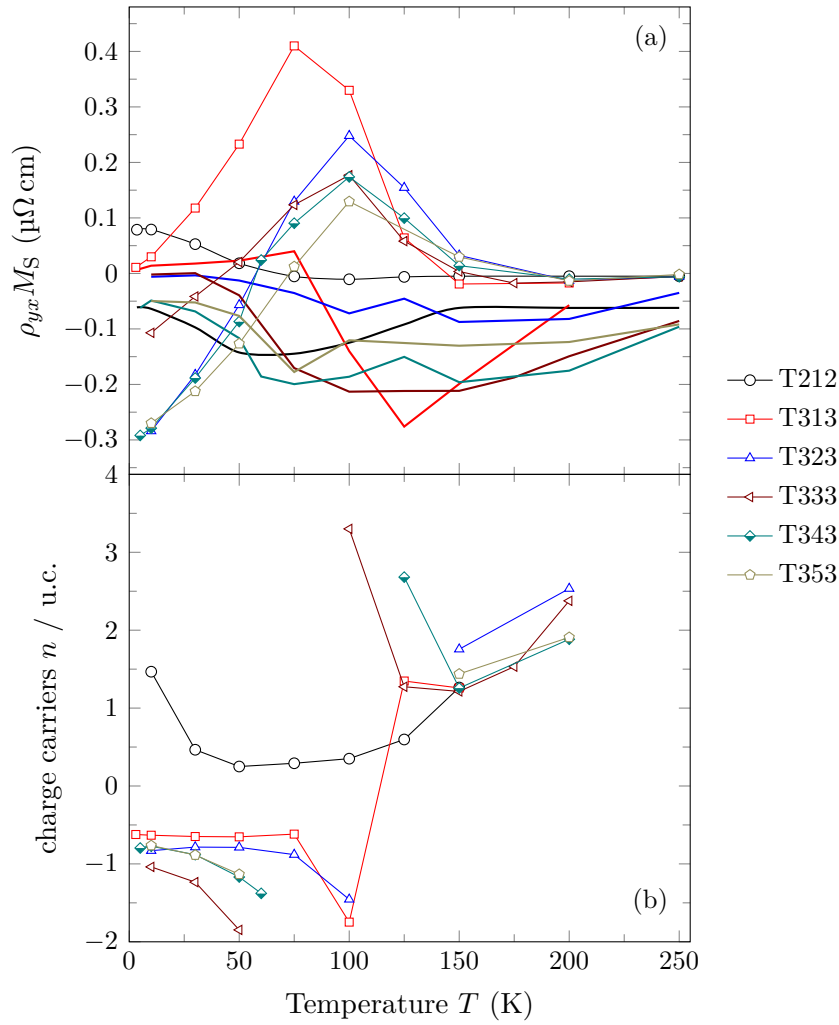


Figure 7.8: (a) Temperature dependence of the anomalous Hall constants of the SrRuO_3 (line and symbol) and $\text{La}_{0.7}\text{Sr}_{0.3}\text{MnO}_3$ (only line) layers. The data of sample T212 was scaled with a factor of 0.1 to fit together with the other data. (b) Number of charge carriers per unit cell determined from the high field slope of the ρ_{yx} .

7.3.1 X-ray Magnetic Dichroism

Since X-ray magnetic circular dichroism (XMCD) allows elementally resolved magnetization determination, it is a most versatile technique to study magnetism in coupled layers [365]. The absorption of circularly polarized x-rays depends on the magnetization with respect to the direction of the incident beam. From the difference in absorption of left and right circularly polarized x-rays the magnetic moment can be deduced. From the shape of the absorption one can even obtain the spin

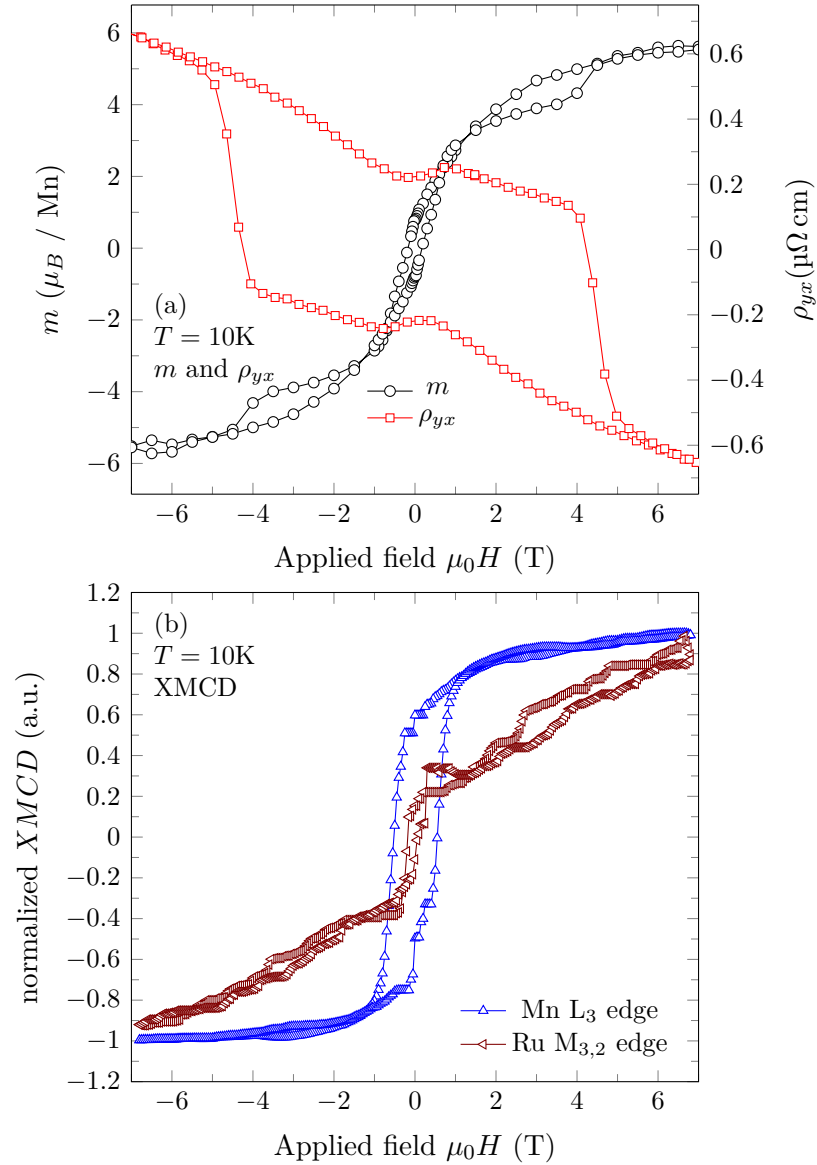


Figure 7.9: (a) Magnetization and Hall resistivity of trilayer T353 at 10 K. (b) XMCD hysteresis measurements on the manganese L_3 and ruthenium $M_{3,2}$ edges. The switching fields do not match.

and orbital moment according to the sum-rules established by Thole et al. [366] and Carra et al. [367]. Depending on Jahn-Teller distortion and hybridization effects these rather simple rules need to be corrected with the help of simulations [368, 369]. In the following the discussion is only limited to element specific hysteresis curves.

Some trilayer samples were studied by XMCD at Paul Scherrer Institute, Villigen, CH. Details on the experimental setup can be found in Ref. [370]. In Fig. 7.9 hysteresis curves of sample T353 obtained by different techniques are compared. One

full XMCD hysteresis consists actually of four hysteresis cycles. For each element and each polarization one has to measure a hysteresis curve. Polarization and energy are controlled by the relative positions of undulator magnets. During a hysteresis measurement the energy is always toggled between the absorption edge and the pre edge region to correct for possible drifts. Since the ruthenium M edge is superimposed by the titanium L edge of the substrate and the signal of the M edge is rather weak, noise improvement was attempted by comparing M_3 and M_2 edges, which give an opposite XMCD signal.

In panel (a) of Fig. 7.9 magnetization and Hall resistivity data obtained at 10 K are shown. Coming from positive field, there is a dip before reaching zero field, but then the initial slope line is followed until a switching process between four and five tesla. As described before, this large loop was attributed to the SRO layer. This is in accordance with the magnetization measurement. The round hysteresis loop shape indicates a rotation process. The magnetic moment of the manganite switches the magnetization direction after passing the zero field, the antiferromagnetically coupled SRO layer switches only at a higher field between four and five tesla. The manganite hysteresis measured by XMCD (Fig. 7.9 (b)) follows qualitatively this interpretation, albeit with an unusually high coercive field. Unexpectedly, the SRO dichroism signal does not follow the described path, but shows a significant slope, which indicates non-saturation. Furthermore, the magnetization switches sign at small fields. There is no signature in the XMCD data of a magnetization reversal process at four to five tesla.

The orbital moment extracted from XMCD spectra at small, medium, and high applied field, does not show a significant change. Thus, the magnetization process of coupled manganite ruthenate layers is not simply described by the sum of the manganese and ruthenium contribution. Okamoto et al. [371] measured a magnetic moment of the oxygen t_{2g} and e_g states in the $\text{Ca}_{1-x}\text{Sr}_x\text{RuO}_3$ series, which are strongly hybridized with the ruthenate $4d$ states [110]. However, a significant magnetization contribution in the order of one Bohr magneton is most unusual. Further experimental investigation has to unravel these puzzling observations.

7.4 Conclusions

For thin manganite layers we observed a transfer of the symmetry from the orthorhombic SrRuO_3 layers to the manganite layers. As this anisotropy modification results in an in-plane anisotropy of the magnetic properties of the manganite above the Curie temperature of the SrRuO_3 layers, its origin is due to a micro-structural modification. Since the cations are restricted to the square lattice of the substrate, the oxygen octahedral tilt patterns are transferred. This shows the close vicinity of the ground state energies of possible crystallographic structures in the manganites explaining partially their sensitivity to external influences, but also opening a way to interface engineered property modifications.

In principle, the complicated shapes of the measurement curves can be modelled considering the magnetic properties of the individual layers and a coupling between them. The behaviour depends on the relative energies of the antiferromagnetic coupling, anisotropy energies and Zeeman energies. In practice, there are too many unknown parameters, but qualitatively they can be described. Besides the isotropic Heisenberg exchange coupling an anisotropic Dzyaloshinskii-Moriya [372, 373] like exchange coupling may arise due to the asymmetry of the oxygen octahedra tilt patterns in plane and spin canting effects. Strong magnetic coupling mimics a composed symmetry, masking the symmetry of individual layers.

While in thicker layers only an interface layer is affected by the charge transfer from the Ru^{4+} and possible hybridization due to the delocalized 4d states, the range of this modification may exceed the actual layer thickness for the ultrathin superlattices. Thus a hybrid state is formed with modified electronic structure, stronger coupling, and modified anisotropy. The anisotropy of the parent materials superimpose in this case with negative (SrRuO_3) and positive ($\text{La}_{0.7}\text{Sr}_{0.3}\text{MnO}_3$) anisotropy energy along the surface normal. This results in a overall anisotropy reduction, which may explain the unusual phenomenology of the ultrathin superlattices representing an artificial ferrimagnet.

Conclusions and Outlook

“The best way to have a good idea is to have a lot of ideas”
(L. Pauling)

The aim of this thesis was to gain a deeper understanding on the mechanisms of interface related phenomena leading to modified material properties. The perovskite oxide family with its rich phase diagram offers a plethora of physical properties from metallic to insulating, ferro- to antiferromagnetic, ferroelectric and multiferroic, offering the possibility of tailored material properties meeting future electronic application needs. The increasing importance of interface and surface effects with continuous miniaturization requires special attention. A deeper understanding of the microscopic mechanisms responsible for the property modifications is a prerequisite for deterministic design and for the ability to predict emerging phenomena at oxide interfaces.

Experimental

Ruthenate and manganite layers were grown by pulsed laser deposition from stoichiometric targets onto TiO_2 -terminated SrTiO_3 substrates with a vicinal miscut $<0.2^\circ$. The chosen SrTiO_3 substrate has a small lattice mismatch to allow high interface quality and is a common substrate for perovskites. However, in the course of these studies we found hints on structural degradation, probably related to repeated cycles through the cubic to tetragonal phase transition of the substrate. The thickness of the manganite layers was controlled by monitoring RHEED oscillations during growth, while for the ruthenates the number of pulses needed for one layer was calibrated, since RHEED oscillations are absent in the observed step-flow growth mode.

Surface morphology was monitored by atomic force microscopy measurements showing generally atomically flat surfaces with unit cell high steps along the vicinal terraces. The observed superlattice peaks in x-ray diffraction confirmed homogeneous layer thicknesses with coherent interfaces. High resolution scanning transmission electron microscopy in combination with electron dispersive x-ray emission allowed monitoring of the interface quality and possible intermixing effects on the microscopic level as well as a second measurement of the layer thickness.

Magnetization measurements were done in a commercial SQUID magnetometer. Special attention was put on measuring the magnetization above the T_C of the multilayers to identify ubiquitous magnetic signals from impurities and correct for them. Angle dependent magneto transport measurements in a helium flow cryostat with a home-built rotation stage and in magnetic fields up to 8 T were done with a low frequency alternating current with a four point method in Van-der-Pauw geometry. The rectangular sample shape allows for a newly derived analytic deduction of the resistivities along the sample edges (mathematical details in Appendix A). This in turn permits a comparison of the obtained angle dependence of the resistivities with the allowed symmetries of the crystal to determine the structure. The method of series expansions in terms of the magnetization direction, introduced by Döring and Simon [319], has been reviewed to include the tensor elements odd in \vec{M} as described with examples in Chapter 4.

Charge Transfer, Induced Anisotropy, and Magnetic Coupling

In the preceding chapters we discussed experimentally obtained results showing the importance of interfacial charge transfer, strain and symmetry breaking as well as the possibility of anisotropy modifications by magnetic coupling. By varying the layer thicknesses and the interface density the weights of the different influences was varied, albeit not completely distinguishable.

Interfacial charge transfer at the ruthenate manganite interface stabilizes ferromagnetism in $\text{La}_{0.7}\text{Sr}_{0.3}\text{MnO}_3$ down to 1–2 unit cell thick layers, i.e. a finite size scaling similar to conventional 3d metal ferromagnets is achieved. The degradation of the ferromagnetic and metallic properties hampers the realization of possible spintronic applications due to a pervasive antiferromagnetically ordered surface or interface layer in $\text{La}_{0.7}\text{Sr}_{0.3}\text{MnO}_3$. Embedding the $\text{La}_{0.7}\text{Sr}_{0.3}\text{MnO}_3$ layer in a ruthenate system may therefore improve substantially the efforts. In contrast to conventional charge doping in the bulk phase, the layered design allows for specific charge doping where it is most needed: at the interface. The possibility to adapt the lattice parameter over a wide range in the Ba-Sr-Ca ruthenate series allows to transfer these results to other systems. Future experiments have to show how the delocalized Ru 4d states affect the tunneling process in spin valve devices. Besides the charge transfer based T_C stabilization, a modification of the magnetic anisotropy was observed, probably related to changes in the energy of the d orbitals as manifested by a rounding of the magnetization and ρ_{yx} versus applied magnetic field curves.

A transfer of the orthorhombic structure from SrRuO_3 to $\text{La}_{0.7}\text{Sr}_{0.3}\text{MnO}_3$ and $\text{La}_{0.7}\text{Ba}_{0.3}\text{MnO}_3$ layers of six unit cell thickness is manifested by an in-plane uniaxial anisotropy with the easy axis in the manganite parallel to the SrRuO_3 [001]_o axis. This structural coupling can only be due to a transfer of the oxygen octahedra

tilt pattern. The agreement of the experimentally deduced length of tilt transfer with theoretical calculations [20] is exceptional. Recent advances in scanning transmission electron microscopy in the annular bright field mode allow direct observation of the oxygen octahedra and make major progress in this field tangible. Oxygen octahedra rotations may also be seen within a layer averaged potential model as charge transfer along the c-axis within the ABO_3 perovskite unit cell from the BO_2 layers to the AO layer. Since changes in the octahedral environment affect the energy levels and thereby the local bandstructure, the range of these tilt transfers is crucial in the understanding of emergent phenomena at oxide interfaces.

Orthorhombic and tetragonal SrRuO_3 films on different substrates as well as in superlattices with SrTiO_3 have been studied with special attention to the symmetry observable in angle dependent magnetoresistance and the anomalous Hall effect. Microscopic twinning and the strong surface anisotropy obstruct unequivocal structure determination from magnetotransport data, but the continuous trend upon thickness reduction suggest conservation of the orthorhombic structure with a small monoclinic tilt to adapt to the square lattice of the substrate. The field dependent measurements underline the importance of taking the tensorial nature of the anomalous Hall resistivity into account. As measurements on single crystals are out of reach, a systematic study, with thin films oriented along the principal axes of the unit cell, would allow for a complete characterization of the anisotropic anomalous Hall effect tensor. Unusual spikes in the ρ_{yx} vs. $\mu_0 H$ curves, which had been ascribed to skyrmions in similar systems, can be simply explained within a parallel conduction model on the basis of a modified interface structure. Besides the change in the cation environment at the interface, the frustration of oxygen octahedra tilt may again be an important parameter [167]. The connection of the interface related transport and the observed surface anisotropy may advance the understanding of the microscopic mechanism responsible for the surface anisotropy in future research and call for band structure calculations of heterostructures.

Antiferromagnetic coupling in manganite ruthenate superlattices leads to a phenomenologically rich temperature and field dependent behaviour. Varying the thickness ratio and temperature the balance between the magnetic anisotropy energies is changed. This magnitude of the anisotropy energy per unit area $\mathcal{K}_i t_i$ determines the groundstate at zero applied field, whereas the Zeeman energy per unit area $\mu_0 \vec{M}_i \cdot \vec{H} t_i$ determines the dominant contribution at moderate fields. The complicated composed magnetic anisotropy may dominate over the structural anisotropy of the constituting layers. The antiferromagnetic coupling can enhance the coercivity by orders of magnitude, thus a design based on artificial ferrimagnets may be interesting to increase the magnetic energy. By proper choice of the layer thickness ratio artificial frustrated system can be designed. Systems composed of layers with different thickness ratios allow tuning of graded anisotropies, which are potentially important in the emergent field of skyrmionics. In the ultrathin superlattices a hy-

bridized state of matter emerges, characterized by a superposition of the magnetic anisotropies of the parent materials. These systems can be seen as an artificial ferromagnet with relatively weak coupling of the sublattices. In contrast to the thicker layers there are no clearly separated regimes of dominance of particular parameters, but the strong interlayer coupling results in gradual changes.



Van der Pauw Measurements on a Rectangular Sample

A.1 Coordinate Transformation for Anisotropic Samples

In the following we reproduce the coordinate transformation proposed by Van der Pauw [264] to map an anisotropic sample onto an isotropic one. Assume we have chosen the coordinate system such that we have the resistivity tensor in it's diagonal form:

$$\vec{E} = \begin{bmatrix} \rho_{xx} & \rho_{xy} & \rho_{xz} \\ \rho_{yx} & \rho_{yy} & \rho_{yz} \\ \rho_{zx} & \rho_{zy} & \rho_{zz} \end{bmatrix} \vec{j}$$

Now we perform a transformation with $x' = \alpha x, y' = \beta y, z' = \gamma z$. If we want the electrostatic potentials in the corresponding points to be the same, we have:

$$E'_x = -\frac{\partial U}{\partial x'} = -\frac{\partial U}{\alpha \partial x} = \frac{1}{\alpha} E_x; \quad E'_y = \frac{1}{\beta} E_y; \quad E'_z = \frac{1}{\gamma} E_z.$$

As we want the resistances to be the same, $R' = R$, we require that the current per corresponding surface element is conserved under the transformation:

$$j'_x dy' dz' = j_x dy dz \Rightarrow j'_x = \frac{1}{\beta \gamma} j_x; \quad j'_y = \frac{1}{\gamma \alpha} j_y; \quad j'_z = \frac{1}{\alpha \beta} j_z.$$

With the mean resistivity $\rho_m = \sqrt[3]{\rho_{xx}\rho_{yy}\rho_{zz}}$ and

$$\alpha^2 = \frac{\rho_{xx}}{\rho_m}, \quad \beta^2 = \frac{\rho_{yy}}{\rho_m}, \quad \gamma^2 = \frac{\rho_{zz}}{\rho_m},$$

we obtain the resistivity tensor for the scaled isotropic medium showing the same resistance values as the anisotropic one:

$$\vec{E}' = \begin{bmatrix} \rho_m & \rho_{xy} \sqrt{\frac{\rho_{zz}}{\rho_m}} & \rho_{xz} \sqrt{\frac{\rho_{yy}}{\rho_m}} \\ \rho_{yx} \sqrt{\frac{\rho_{zz}}{\rho_m}} & \rho_m & \rho_{yz} \sqrt{\frac{\rho_{xx}}{\rho_m}} \\ \rho_{zx} \sqrt{\frac{\rho_{yy}}{\rho_m}} & \rho_{zy} \sqrt{\frac{\rho_{xx}}{\rho_m}} & \rho_m \end{bmatrix} \vec{j}'.$$

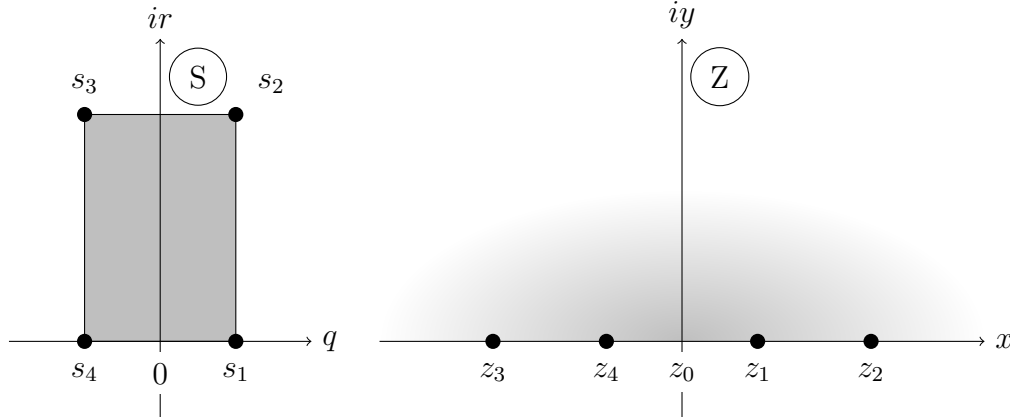


Figure A.1: Illustration of the changes of the coordinate system by (inverse) Schwarz-Christoffel mapping.

In the case of a thin film we normally measure the sheet resistance $R_s = \rho_m/t' = \sqrt{\rho_{xx}\rho_{yy}}/t$ according to the Van der Pauw formula [261].

A.2 Schwarz-Christoffel Transformation

The Schwarz-Christoffel Transformation maps the complex upper half plane to the interior of a polygon and the real axis to the boundary of the polygon (see Fig. A.1).

$$s(z) = A + B \int_{z_0}^z \prod_{n=1}^N \frac{1}{(t - z_n)^{\alpha_n}} dt,$$

here the prevertices z_n on the real axis, A and B are the parameters, the α_n denote the change in direction from one polygon side to the following one in units of π . For a simple rectangle we obtain

$$s(z) = a \int_0^z \frac{dt}{\sqrt{(t^2 - 1)(t^2 - a^2)}} = \int_0^z \frac{dt}{\sqrt{(1 - t^2)(1 - k^2 t^2)}} = F(z, k),$$

with $A = 0, B = a$, prevertices $z_3 = -a, z_4 = -1, z_1 = 1, z_2 = a, z_0 = 0$ and $k = 1/a$. This is the Jacobi elliptic integral of the first kind with the modulus k . Using the short notation

$$K(k) = \int_0^1 \frac{dt}{\sqrt{(1 - t^2)(1 - k^2 t^2)}}$$

for the complete elliptic integral of the first kind, and $K'(k) = K(k')$ the complementary complete elliptic integral with $k' = \sqrt{1 - k^2}$, we obtain (with $F(1/k, k) =$

$K(k) + iK'(k)$ [374]):

$$\begin{aligned} s_1 = s(1) &= K(k), & s_2 = s(1/k) &= K(k) + iK'(k), \\ s_3 = s(-1/k) &= -K(k) + iK'(k), & s_4 = s(-1) &= -K(k). \end{aligned}$$

The inverse mapping can be done analytically in the case of the rectangle [375] with the Jacobi elliptic function SN,

$$z(s) = \text{JacobiSN}(s, k).$$

The modulus k is obtained by

$$k = \frac{\vartheta_2^2(0, q)}{\vartheta_3^2(0, q)} \quad \text{with} \quad q = \exp\left(-\pi \frac{K'(k)}{K(k)}\right) = \exp\left(-\pi \frac{2L_y}{L_x}\right).$$

Unfortunately the method of conformal mapping is not as present in physics teaching curricula nowadays as it has been before. Only recently its use has been proposed in determining the resistivity constants in highly anisotropic layered materials, such as in High- T_C superconductors or graphite [376].

A.3 Resistance Calculation of a Rectangular Sample

Denoting with L_y/L_x the dimensions ratio of the sample after the coordinate transformation described in section Appendix A.1 Logan [267] arrived with the method of image charges and the contacts placed at the corners of the sample at

$$\begin{aligned} R_x &= \frac{4\rho}{\pi d} \sum_{l=0}^{\infty} \frac{2}{(2l+1) \sinh[\pi(2l+1) \frac{L_y}{L_x}]} & \left| \text{with } q = \exp\left(-\pi \frac{L_y}{L_x}\right) \right. \\ &= \frac{16\rho}{\pi d} \sum_{l=0}^{\infty} \frac{q^{2l+1}}{(2l+1)(1-q^{4l+2})} & \left| \frac{x}{1-x^2} = \sum_{n=0}^{\infty} x^{2n+1} \right. \\ &= \frac{16\rho}{\pi d} \sum_{l=0}^{\infty} \sum_{n=0}^{\infty} \frac{1}{2l+1} (q^{2l+1})^{2n+1} & \left| 2 \sum_{n=0}^{\infty} \frac{1}{2n+1} x^{2n+1} = \ln\left(\frac{1+x}{1-x}\right) \right. \\ &= \frac{8\rho}{\pi d} \sum_{n=0}^{\infty} \ln\left(\frac{1+q^{2n+1}}{1-q^{2n+1}}\right) & \left| = -\frac{8\rho}{\pi d} \ln\left[\prod_{n=0}^{\infty} \tanh\left(\frac{\pi L_y}{2L_x}(2n+1)\right)\right] \right. \\ &= \frac{4\rho}{\pi d} \ln\left(\prod_{n=1}^{\infty} \frac{(1+q^{2n-1})^2(1-q^{2n})}{(1-q^{2n-1})^2(1-q^{2n})}\right) & \left| \vartheta_3(0, q) = \prod_{n=1}^{\infty} (1+q^{2n-1})^2(1-q^{2n-1})^2 \right. \\ &= \frac{4\rho}{\pi d} \ln\left(\frac{\vartheta_3(0, q)}{\vartheta_3(0, -q)}\right) \\ &= \frac{\rho}{\pi d} \ln\left(\frac{\vartheta_3^4(0, q)}{\vartheta_4^4(0, q)}\right) = \frac{\rho}{\pi d} \ln\left(\frac{1}{k'^2}\right). \end{aligned}$$

Line four on the right hand gives the result obtained by Price [269]. Equally one obtains

$$\exp\left(-\frac{R_y \pi d}{\sqrt{\rho_x \rho_y}}\right) = \left(\frac{\vartheta_2(0, q)}{\vartheta_3(0, q)}\right)^4 = k^2,$$

where k denotes the elliptic modulus and $q = \exp\left(-\pi \frac{L_y}{L_x}\right) = \exp\left(-\pi \frac{K'(k)}{K(k)}\right)$. Thus the resistivity along the sample edges can be evaluated from

$$\rho_x = \sqrt{\rho_x \rho_y} \sqrt{\frac{\rho_x}{\rho_y}}, \quad \text{and} \quad \rho_y = \sqrt{\rho_x \rho_y} / \sqrt{\frac{\rho_x}{\rho_y}},$$

with $\sqrt{\rho_x \rho_y}$ obtained from solving the van der Pauw equation and

$$\sqrt{\frac{\rho_x}{\rho_y}} = \frac{L'_y K(k)}{L'_x K(k')},$$

where the L' denote the physical dimensions of the sample.

Using conformal mapping (see the previous Appendix A.2), we can write

$$\begin{aligned} R_x = R_{41,23} &= \frac{\rho}{\pi d} \ln \left(\frac{(z_3 - z_1)(z_2 - z_4)}{(z_2 - z_1)(z_3 - z_4)} \right) = \frac{\rho}{\pi d} \ln \left(\frac{(k+1)^2}{(k-1)^2} \right), \\ R_y = R_{34,12} &= \frac{\rho}{\pi d} \ln \left(\frac{(z_1 - z_3)(z_2 - z_4)}{(z_2 - z_3)(z_1 - z_4)} \right) = \frac{\rho}{\pi d} \ln \left(\frac{(k+1)^2}{4k} \right), \\ R_x - R_y = R_{42,13} &= \frac{\rho}{\pi d} \ln \left(\frac{(z_3 - z_2)(z_1 - z_4)}{(z_1 - z_2)(z_4 - z_3)} \right) = \frac{\rho}{\pi d} \ln \left(\frac{4k}{(k-1)^2} \right), \end{aligned}$$

here $k = k(q') = \vartheta_2^2(0, q') / \vartheta_3^2(0, q')$ with $q' = \exp\left(-\pi \frac{K'(k)}{K(k)}\right) = \exp\left(-\pi \frac{2L_y}{L_x}\right) = q^2$.

With the Landen transformations [374]

$$K'(k) = \frac{2}{1+k} K\left(\frac{1-k}{1+k}\right) \quad \text{and} \quad K(k) = \frac{1}{1+k} K\left(\frac{2\sqrt{k}}{1+k}\right)$$

we obtain the previous result with $k(q) = 2\sqrt{k(q^2)}/(1+k(q^2))$.

$$\begin{aligned} R_x = R_{41,23} &= \frac{\rho}{\pi d} \ln \left(\frac{(k(q^2) + 1)^2}{(k(q^2) - 1)^2} \right) = \frac{\rho}{\pi d} \ln \left(\frac{1}{k'^2(q)} \right), \\ R_y = R_{34,12} &= \frac{\rho}{\pi d} \ln \left(\frac{(k(q^2) + 1)^2}{4k(q^2)} \right) = \frac{\rho}{\pi d} \ln \left(\frac{1}{k^2(q)} \right), \\ R_x - R_y = R_{42,13} &= \frac{\rho}{\pi d} \ln \left(\frac{4k(q^2)}{(k(q^2) - 1)^2} \right) = \frac{\rho}{\pi d} \ln \left(\frac{k^2(q)}{k'^2(q)} \right). \end{aligned}$$

Bibliography

“The world is a never-ending cross-reference.”
(C. Nooteboom in: *The following Story*, 1991)

- [1] I. Vrejoiu, M. Alexe, D. Hesse, and U. Gösele. Functional Perovskites - From Epitaxial Films to Nanostructured Arrays. *Adv. Funct. Mater.*, 18(24):3892–3906, 2008. doi:10.1002/adfm.200800560.
- [2] J. G. Bednorz and K. A. Müller. Perovskite-type oxides—The new approach to high- T_c superconductivity. *Rev. Mod. Phys.*, 60(3):585, 1988.
- [3] I. Grinberg, D. V. West, M. Torres, G. Gou, D. M. Stein, L. Wu, G. Chen, E. M. Gallo, A. R. Akbashev, P. K. Davies, J. E. Spanier, and A. M. Rappe. Perovskite oxides for visible-light-absorbing ferroelectric and photovoltaic materials. *Nature*, 503(7477):509–512, 2013. doi:10.1038/nature12622.
- [4] H. Y. Hwang, Y. Iwasa, M. Kawasaki, B. Keimer, N. Nagaosa, and Y. Tokura. Emergent phenomena at oxide interfaces. *Nat. Mater.*, 11(2):103–113, 2012. doi:10.1038/nmat3223.
- [5] A. Ohtomo and H. Y. Hwang. A high-mobility electron gas at the $\text{LaAlO}_3/\text{SrTiO}_3$ heterointerface. *Nature*, 427:423, 2004. doi:10.1038/nature02308.
- [6] M. B. Salamon and M. Jaime. The physics of manganites: Structure and transport. *Rev. Mod. Phys.*, 73(3):583, 2001.
- [7] C.-Q. Jin, J.-S. Zhou, J. B. Goodenough, Q. Q. Liu, J. G. Zhao, L. X. Yang, Y. Yu, R. C. Yu, T. Katsura, A. Shatskiy, and others. High-pressure synthesis of the cubic perovskite BaRuO_3 and evolution of ferromagnetism in ARuO_3 ($A = \text{Ca, Sr, Ba}$) ruthenates. *Proc. Natl. Acad. Sci.*, 105(20):7115–7119, 2008.

- [8] M. Ziese, I. Vrejoiu, and D. Hesse. Structural symmetry and magnetocrystalline anisotropy of SrRuO₃ films on SrTiO₃. *Phys. Rev. B*, 81(18), 2010. doi:10.1103/PhysRevB.81.184418.
- [9] V. M. Goldschmidt. Die Gesetze der Krystallochemie. *Naturwissenschaften*, 14(21):477–485, 1926.
- [10] R. D. Shannon. Revised effective ionic radii and systematic studies of interatomic distances in halides and chalcogenides. *Acta Crystallogr. A*, 32(5): 751–767, 1976.
- [11] A. M. Glazer. Simple ways of determining perovskite structures. *Acta Crystallogr. A*, 31(6):756–762, 1975.
- [12] P. M. Woodward. Octahedral tilting in perovskites. I. Geometrical considerations. *Acta Crystallogr. B*, 53(1):32–43, 1997.
- [13] P. M. Woodward. Octahedral tilting in perovskites. II. Structure stabilizing forces. *Acta Crystallogr. B*, 53(1):44–66, 1997.
- [14] A. Cammarata and J. M. Rondinelli. Covalent dependence of octahedral rotations in orthorhombic perovskite oxides. *J. Chem. Phys.*, 141(11):114704, 2014.
- [15] M. W. Lufaso and P. M. Woodward. Prediction of the crystal structures of perovskites using the software program SPuDS. *Acta Cryst. B*, 57:725–738, 2001. doi:10.1107/S0108768101015282.
- [16] M. W. Lufaso and P. M. Woodward. Jahn–Teller distortions, cation ordering and octahedral tilting in perovskites. *Acta Crystallogr. B*, 60(1):10–20, 2004. doi:10.1107/S0108768103026661.
- [17] R. C. O’Handley. *Modern Magnetic Materials: Principles and Applications*. John Wiley and Sons, 2000. ISBN 0-471-15566-7.
- [18] B. J. Campbell, H. T. Stokes, D. E. Tanner, and D. M. Hatch. ISODISPLACE : A web-based tool for exploring structural distortions. *J. Appl. Crystallogr.*, 39(4):607–614, 2006. doi:10.1107/S0021889806014075.
- [19] A. B. Harris. Landau theory of tilting of oxygen octahedra in perovskites. *Phys. Rev. B*, 85(17):174107, 2012.
- [20] J. He, A. Borisevich, S. V. Kalinin, S. J. Pennycook, and S. T. Pantelides. Control of Octahedral Tilts and Magnetic Properties of Perovskite Oxide Heterostructures by Substrate Symmetry. *Phys. Rev. Lett.*, 105(22), 2010. doi:10.1103/PhysRevLett.105.227203.

- [21] M. Kawasaki, K. Takahashi, T. Maeda, R. Tsuchiya, M. Shinohara, O. Ishiyama, T. Yonezawa, M. Yoshimoto, and H. Koinuma. Atomic Control of the SrTiO_3 Crystal Surface. *Science*, 266(5190):1540, 1994. doi:10.1126/science.266.5190.1540.
- [22] G. Koster, G. Rijnders, D. H. A. Blank, and H. Rogalla. Surface morphology determined by (0 0 1) single-crystal SrTiO_3 termination. *Phys. C*, 339:215–230, 2000.
- [23] J. G. Connell, B. J. Isaac, G. B. Ekanayake, D. R. Strachan, and S. S. A. Seo. Preparation of atomically flat SrTiO_3 surfaces using a deionized-water leaching and thermal annealing procedure. *Appl. Phys. Lett.*, 101(25):251607, 2012. doi:10.1063/1.4773052.
- [24] K. Szot and W. Speier. Surfaces of reduced and oxidized SrTiO_3 from atomic force microscopy. *Phys. Rev. B*, 60(8):5909, 1999.
- [25] R. Bachelet, F. Sánchez, J. Santiso, C. Munuera, C. Ocal, and J. Fontcuberta. Self-assembly of $\text{SrTiO}_3(001)$ chemical-terminations: A route for oxide-nanostructure fabrication by selective growth. *Chem. Mater.*, 21(12):2494–2498, 2009.
- [26] K. A. Müller and H. Burkard. SrTiO_3 : An intrinsic quantum paraelectric below 4 K. *Phys. Rev. B*, 19(7):3593, 1979.
- [27] K. A. Müller, W. Berlinger, and E. Tosatti. Indication for a novel phase in the quantum paraelectric regime of SrTiO_3 . *Z. Für Phys. B Condens. Matter*, 84(2):277–283, 1991.
- [28] S. E. Rowley, L. J. Spalek, R. P. Smith, M. P. M. Dean, M. Itoh, J. F. Scott, G. G. Lonzarich, and S. S. Saxena. Ferroelectric quantum criticality. *Nat. Phys.*, 10(5):367–372, 2014. doi:10.1038/nphys2924.
- [29] J. H. Haeni, P. Irvin, W. Chang, R. Uecker, P. Reiche, Y. Li, S. Choudhury, W. Tian, M. Hawley, B. Craigo, A. Tagantsev, X. Q. Pan, S. Streiffer, L.-Q. Chen, S. Kirchhofer, J. Levy, and D. G. Schlom. Room-temperature ferroelectricity in strained SrTiO_3 . *Nature*, 430:758, 2004.
- [30] D. Lee, H. Lu, Y. Gu, S.-Y. Choi, S. Li, S. Ryu, T. Paudel, K. Song, E. Mikheev, S. Lee, S. Stemmer, D. Tenne, S. Oh, E. Y. Tsymbal, X. Wu, L.-Q. Chen, A. Gruverman, and C. B. Eom. Emergence of room-temperature ferroelectricity at reduced dimensions. *Science*, 349(6254):1314, 2015. doi:10.1126/science.aac9411.
- [31] K. Uematsu, O. Sakurai, N. Mizutani, and M. Kato. Electrical properties of La-doped SrTiO_3 (La: 0.1 to 2.0 at%) single crystals grown by xenon-arc image floating zone method. *J. Mater. Sci.*, 19(11):3671–3679, 1984.

- [32] A. Ohtomo and H. Y. Hwang. Surface depletion in doped SrTiO_3 thin films. *Appl. Phys. Lett.*, 84(10):1716, 2004. doi:10.1063/1.1668329.
- [33] C. Lee, J. Destry, and J. L. Brebner. Optical absorption and transport in semiconducting SrTiO_3 . *Phys. Rev. B*, 11(6):2299, 1975.
- [34] M. E. Zvanut, S. Jeddy, E. Towett, G. M. Janowski, C. Brooks, and D. Schlom. An annealing study of an oxygen vacancy related defect in SrTiO_3 substrates. *J. Appl. Phys.*, 104(6):064122, 2008. doi:10.1063/1.2986244.
- [35] J. F. Schooley, W. R. Hosler, and M. L. Cohen. Superconductivity in Semiconducting SrTiO_3 . *Phys. Rev. Lett.*, 12(17):474, 1964.
- [36] X. Lin, Z. Zhu, B. Fauqué, and K. Behnia. Fermi Surface of the Most Dilute Superconductor. *Phys. Rev. X*, 3(2), 2013. doi:10.1103/PhysRevX.3.021002.
- [37] M. C. Tarun, F. A. Selim, and M. D. McCluskey. Persistent Photoconductivity in Strontium Titanate. *Phys. Rev. Lett.*, 111(18), 2013. doi:10.1103/PhysRevLett.111.187403.
- [38] H. Unoki and T. Sakudo. Electron Spin Resonance of Fe^{3+} in SrTiO_3 with Special Reference to the 110°K Phase Transition. *J. Phys. Soc. Jpn.*, 23: 546–552, 1967. doi:10.1143/JPSJ.23.546.
- [39] K. A. Müller, W. Berlinger, and F. Waldner. Characteristic Structural Phase Transition in Perovskite-Type Compounds. *Phys. Rev. Lett.*, 21:814, 1968. doi:https://doi.org/10.1103/PhysRevLett.21.814.
- [40] P. A. Fleury, J. F. Scott, and J. M. Worlock. Soft Phonon Modes and the 110°K Phase Transition in SrTiO_3 . *Phys. Rev. Lett.*, 21(1):16, 1968.
- [41] Y. Yamada and G. Shirane. Neutron scattering and nature of the soft optical phonon in SrTiO_3 . *J. Phys. Soc. Jpn.*, 26:396–403, 1969. doi:10.1143/JPSJ.26.396.
- [42] B. Alefeld. Die Messung der Gitterparameteränderung von Strontiumtitanat am Phasenübergang bei 108°K . *Z. Für Phys. Hadrons Nucl.*, 222(2):155–164, 1969.
- [43] J. C. Slonczewski and H. Thomas. Interaction of elastic strain with the structural transition of strontium titanate. *Phys. Rev. B*, 1(9):3599, 1970.
- [44] A. Heidemann and H. Wettengel. Die Messung der Gitterparameteränderung von SrTiO_3 . *Z. Für Phys. Hadrons Nucl.*, 258(5):429–438, 1973.
- [45] J. F. Scott, E. K. H. Salje, and M. A. Carpenter. Domain Wall Damping and Elastic Softening in SrTiO_3 : Evidence for Polar Twin Walls. *Phys. Rev. Lett.*, 109(18), 2012. doi:10.1103/PhysRevLett.109.187601.

- [46] E. K. H. Salje, O. Aktas, M. A. Carpenter, V. V. Laguta, and J. F. Scott. Domains within Domains and Walls within Walls: Evidence for Polar Domains in Cryogenic SrTiO_3 . *Phys. Rev. Lett.*, 111(24), 2013. doi:10.1103/PhysRevLett.111.247603.
- [47] R. Blinc, B. Zalar, V. V. Laguta, and M. Itoh. Order-Disorder Component in the Phase Transition Mechanism of O 18 Enriched Strontium Titanate. *Phys. Rev. Lett.*, 94(14), 2005. doi:10.1103/PhysRevLett.94.147601.
- [48] S. Singh, T.-Y. Chien, J. R. Guest, and M. R. Fitzsimmons. Correlation between surface rumpling and structural phase transformation in SrTiO_3 . *Phys. Rev. B*, 85(11), 2012. doi:10.1103/PhysRevB.85.115450.
- [49] F. W. Lytle. X-Ray Diffractometry of Low-Temperature Phase Transformations in Strontium Titanate. *J. Appl. Phys.*, 35(7):2212–2215, 1964. doi:10.1063/1.1702820.
- [50] M. Ziese, I. Vrejoiu, A. Setzer, A. Lotnyk, and D. Hesse. Coupled magnetic and structural transitions in $\text{La}_{0.7}\text{Sr}_{0.3}\text{MnO}_3$ films on SrTiO_3 . *New J. Phys.*, 10(6):063024, 2008. doi:10.1088/1367-2630/10/6/063024.
- [51] K. Momma and F. Izumi. *VESTA 3* for three-dimensional visualization of crystal, volumetric and morphology data. *J. Appl. Crystallogr.*, 44(6):1272–1276, 2011. doi:10.1107/S0021889811038970.
- [52] G. H. Jonker and J. H. Van Santen. Ferromagnetic compounds of manganese with perovskite structure. *Physica*, 16(3):337–349, 1950. doi:10.1016/0031-8914(50)90033-4.
- [53] J. H. Van Santen and G. H. Jonker. Electrical conductivity of ferromagnetic compounds of manganese with perovskite structure. *Physica*, 16(7-8):599–600, 1950.
- [54] J. Volger. Further Experimental Investigations on some Ferromagnetic Oxidic Compounds of Manganese with Perovskite Structure. *Physica*, 20(1):49–66, 1954.
- [55] C. Zener. Interaction between the d shells in the transition metals. *Phys. Rev.*, 81(3):440, 1951.
- [56] E. O. Wollan and W. C. Koehler. Neutron Diffraction Study of the Magnetic Properties of the Series of Perovskite-Type Compounds $[(1-x)\text{La}, x\text{Ca}]\text{MnO}_3$. *Phys. Rev.*, 100(2):545, 1955.
- [57] J. M. D. Coey, M. Viret, and S. von Molnár. Mixed-valence manganites. *Adv. Phys.*, 48(2):167–293, 1999. doi:10.1080/000187399243455.

- [58] Y. Tokura and Y. Tomioka. Colossal magnetoresistive manganites. *J. Magn. Magn. Mater.*, 200(1):1–23, 1999.
- [59] E. Dagotto, T. Hotta, and A. Moreo. Colossal magnetoresistant materials: The key role of phase separation. *Phys. Rep.*, 344(1):1–153, 2001.
- [60] E. Nagaev. Colossal-magnetoresistance materials: Manganites and conventional ferromagnetic semiconductors. *Physics Reports*, 346(6):387–531, 2001. doi:10.1016/S0370-1573(00)00111-3.
- [61] P. G. Radaelli, G. Iannone, M. Marezio, H. Y. Hwang, S. W. Cheong, J. D. Jorgensen, and D. N. Argyriou. Structural effects on the magnetic and transport properties of perovskite $A_{1-x}A'_x\text{MnO}_3$ ($x=0.25, 0.30$). *Phys. Rev. B*, 56(13):8265, 1997.
- [62] P. G. Radaelli, M. Marezio, H. Y. Hwang, S. W. Cheong, and B. Batlogg. Charge localization by static and dynamic distortions of the MnO_6 octahedra in perovskite manganites. *Phys. Rev. B*, 54(13):8992, 1996.
- [63] P. G. Radaelli, M. Marezio, H. Y. Hwang, and S.-W. Cheong. Structural Phase Diagram of Perovskite $A_{0.7}A'_{0.3}\text{MnO}_3$ ($A=\text{La, Pr}$; $A'=\text{Ca, Sr, Ba}$): A New Imma Allotype. *J. Solid State Chem.*, 122(2):444–447, 1996.
- [64] C. Zener and R. R. Heikes. Exchange interactions. *Rev. Mod. Phys.*, 25(1):191, 1953.
- [65] P. W. Anderson and H. Hasegawa. Considerations on double exchange. *Phys. Rev.*, 100(2):675, 1955.
- [66] P.-G. De Gennes. Effects of double exchange in magnetic crystals. *Phys. Rev.*, 118(1):141, 1960.
- [67] J. B. Goodenough. Theory of the Role of Covalence in the Perovskite-Type Manganites $[\text{La, M(II)}]\text{MnO}_3$. *Phys. Rev.*, 100:564, 1955. doi:10.1103/PhysRev.100.564.
- [68] J. B. Goodenough. *Magnetism and the Chemical Bond*. John Wiley and Sons, New York, 1963.
- [69] J. B. Goodenough. Covalency Criterion for Localized vs Collective Electrons in Oxides with the Perovskite Structure. *J. Appl. Phys.*, 37(3):1415, 1966. doi:10.1063/1.1708496.
- [70] A. J. Millis, P. B. Littlewood, and B. I. Shraiman. Double exchange alone does not explain the resistivity of $\text{La}_{1-x}\text{Sr}_x\text{MnO}_3$. *Phys. Rev. Lett.*, 74(25):5144, 1995.

- [71] A. J. Millis. Lattice effects in magnetoresistive manganese perovskites. *Nature*, 392(6672):147–150, 1998.
- [72] E. L. Nagaev. Ferromagnetic Domains in a Semiconducting Antiferromagnet. *JETP*, 27:122, 1968.
- [73] J. M. D. Coey, M. Viret, L. Ranno, and K. Ounadjela. Electron localization in mixed-valence manganites. *Phys. Rev. Lett.*, 75(21):3910, 1995.
- [74] E. L. Nagaev. On the giant magnetoresistance for degenerate ferromagnetic semiconductors of LaMnO_3 -type. *Phys. Lett. A*, 211(5):313–317, 1996.
- [75] E. L. Nagaev. Phase-separation mechanism for giant magnetoresistance of lanthanum manganites. *Phys. Lett. A*, 218(3):367–372, 1996.
- [76] N. Furukawa. Anomalous Shift of Chemical Potential in the Double-Exchange Systems. *J. Phys. Soc. Jpn.*, 66:2523, 1997.
- [77] R. von Helmolt, J. Wecker, T. Lorenz, and K. Samwer. Magnetoresistance in $\text{La}_{2/3}\text{Ca}_{1/3}\text{MnO}_{3+\delta}$: Dependence on magnetic history. *Appl. Phys. Lett.*, 67(14):2093, 1995. doi:10.1063/1.115089.
- [78] M. Ziese, C. Sritiwirawong, and C. Shearwood. Extrinsic magnetoresistance and resistance relaxation in $\text{La}_{0.7}\text{Ca}_{0.3}\text{MnO}_3$ and Fe_3O_4 films and heterostructures. *J. Phys. Condens. Matter*, 10(38):L659, 1998.
- [79] M. G. Blamire, B.-S. Teo, J. H. Durrell, N. D. Mathur, Z. H. Barber, J. M. Driscoll, L. F. Cohen, and J. E. Evetts. Strain-induced time-dependent magnetic disorder in ultra-thin $\text{La}_{0.7}\text{Ca}_{0.3}\text{MnO}_3$ films. *J. Magn. Magn. Mater.*, 191(3):359–367, 1999.
- [80] M. Bibes, J. E. Villegas, and A. Barthélémy. Ultrathin oxide films and interfaces for electronics and spintronics. *Adv. Phys.*, 60(1):5–84, 2011. doi:10.1080/00018732.2010.534865.
- [81] F. Pailloux, D. Imhoff, T. Sikora, A. Barthélémy, J.-L. Maurice, J.-P. Contour, C. Colliex, and A. Fert. Nanoscale analysis of a SrTiO_3 / $\text{La}_{2/3}\text{Sr}_{1/3}\text{MnO}_3$ interface. *Phys. Rev. B*, 66(1), 2002. doi:10.1103/PhysRevB.66.014417.
- [82] J.-L. Maurice, F. Pailloux, A. Barthélémy, O. Durand, D. Imhoff, R. Lyonnet, A. Rocher, and J.-P. Contour. Strain relaxation in the epitaxy of $\text{La}_{2/3}\text{Sr}_{1/3}\text{MnO}_3$ grown by pulsed-laser deposition on SrTiO_3 (001). *Philos. Mag.*, 83(28):3201–3224, 2003. doi:10.1080/14786430310001603436.
- [83] M. Huijben, L. W. Martin, Y.-H. Chu, M. B. Holcomb, P. Yu, G. Rijnders, D. H. A. Blank, and R. Ramesh. Critical thickness and orbital ordering in ultrathin $\text{La}_{0.7}\text{Sr}_{0.3}\text{MnO}_3$ films. *Phys. Rev. B*, 78(9), 2008. doi:10.1103/PhysRevB.78.094413.

- [84] M. S. Kim, J. B. Yang, Q. Cai, X. D. Zhou, W. J. James, W. B. Yelon, P. E. Parris, D. Buddhikot, and S. K. Malik. Structure, magnetic, and transport properties of Ti-substituted $\text{La}_{0.7}\text{Sr}_{0.3}\text{MnO}_3$. *Phys. Rev. B*, 71(1), 2005. doi:10.1103/PhysRevB.71.014433.
- [85] F. Sandiumenge, J. Santiso, L. Balcells, Z. Konstantinovic, J. Roqueta, A. Pomar, J. P. Espinós, and B. Martínez. Competing Misfit Relaxation Mechanisms in Epitaxial Correlated Oxides. *Phys. Rev. Lett.*, 110(10):107206, 2013. doi:10.1103/PhysRevLett.110.107206.
- [86] A. Vailionis, H. Boschker, Z. Liao, J. R. A. Smit, G. Rijnders, M. Huijben, and G. Koster. Symmetry and lattice mismatch induced strain accommodation near and away from correlated perovskite interfaces. *Appl. Phys. Lett.*, 105(13):131906, 2014. doi:10.1063/1.4896969.
- [87] X. Li, I. Lindfors-Vrejoiu, M. Ziese, A. Gloter, and P. A. van Aken. Impact of interfacial coupling of oxygen octahedra on ferromagnetic order in $\text{La}_{0.7}\text{Sr}_{0.3}\text{MnO}_3/\text{SrTiO}_3$ heterostructures. *Sci. Rep.*, 7:40068, 2017. doi:10.1038/srep40068.
- [88] R. Herger, P. R. Willmott, C. M. Schlepütz, M. Björck, S. A. Pauli, D. Martoccia, B. D. Patterson, D. Kumah, R. Clarke, Y. Yacoby, and M. Döbeli. Structure determination of monolayer-by-monolayer grown $\text{La}_{1-x}\text{Sr}_x\text{MnO}_3$ thin films and the onset of magnetoresistance. *Phys. Rev. B*, 77(8), 2008. doi:10.1103/PhysRevB.77.085401.
- [89] L. Jin, C.-L. Jia, I. Lindfors-Vrejoiu, X. Zhong, H. Du, and R. E. Dunin-Borkowski. Direct Demonstration of a Magnetic Dead Layer Resulting from A-Site Cation Inhomogeneity in a $(\text{La},\text{Sr})\text{MnO}_3$ Epitaxial Film System. *Adv. Mater. Interfaces*, page 1600414, 2016. doi:10.1002/admi.201600414.
- [90] J. Krempaský, V. N. Strocov, L. Patthey, P. R. Willmott, R. Herger, M. Falub, P. Blaha, M. Hoesch, V. Petrov, M. C. Richter, O. Heckmann, and K. Hricovini. Effects of three-dimensional band structure in angle- and spin-resolved photoemission from half-metallic $\text{La}_{2/3}\text{Sr}_{1/3}\text{MnO}_3$. *Phys. Rev. B*, 77(16), 2008. doi:10.1103/PhysRevB.77.165120.
- [91] H. Yamada, Y. Ogawa, Y. Ishii, H. Sato, M. Kawasaki, A. Hiroshi, and Y. Tokura. Engineered Interface of Magnetic Oxides. *Science*, 305(5684):646–648, 2004. doi:10.1126/science.1098867.
- [92] J. J. Kavich, M. P. Warusawithana, J. W. Freeland, P. Ryan, X. Zhai, R. H. Kodama, and J. N. Eckstein. Nanoscale suppression of magnetization at atomically assembled manganite interfaces: XMCD and XRMS measurements. *Phys. Rev. B*, 76(1), 2007. doi:10.1103/PhysRevB.76.014410.

- [93] M. J. Calderón, L. Brey, and F. Guinea. Surface electronic structure and magnetic properties of doped manganites. *Phys. Rev. B*, 60(9):6698, 1999.
- [94] H. Zenia, G. A. Gehring, G. Banach, and W. M. Temmerman. Electronic and magnetic properties of the (001) surface of hole-doped manganites. *Phys. Rev. B*, 71(2), 2005. doi:10.1103/PhysRevB.71.024416.
- [95] C. Aruta, G. Ghiringhelli, V. Bisogni, L. Braicovich, N. B. Brookes, A. Tebano, and G. Balestrino. Orbital occupation, atomic moments, and magnetic ordering at interfaces of manganite thin films. *Phys. Rev. B*, 80(1), 2009. doi:10.1103/PhysRevB.80.014431.
- [96] D. Pesquera, G. Herranz, A. Barla, E. Pellegrin, F. Bondino, E. Magnano, F. Sánchez, and J. Fontcuberta. Surface symmetry-breaking and strain effects on orbital occupancy in transition metal perovskite epitaxial films. *Nat. Commun.*, 3:1189, 2012. doi:10.1038/ncomms2189.
- [97] S. Valencia, L. Peña, Z. Konstantinovic, L. Balcells, R. Galceran, D. Schmitz, F. Sandiumenge, M. Casanove, and B. Martínez. Intrinsic antiferromagnetic/insulating phase at manganite surfaces and interfaces. *J. Phys. Condens. Matter*, 26(16):166001, 2014. doi:10.1088/0953-8984/26/16/166001.
- [98] H. Yamada, M. Kawasaki, and Y. Tokura. Ru-doped $\text{La}_{0.6}\text{Sr}_{0.4}\text{MnO}_3$ thin films as a coercivity tunable electrode for magnetic tunnel junctions. *Appl. Phys. Lett.*, 86(19):192505, 2005. doi:10.1063/1.1923199.
- [99] R. K. Sahu and S. S. Manoharan. Magnetic pair-making double exchange coupling in Ru substituted orthomanganites $\text{La}_{0.7}\text{A}_{0.3}\text{Mn}_{0.9}\text{Ru}_{0.1}\text{O}_3$. *Appl. Phys. Lett.*, 77(15):2382–2384, 2000. doi:10.1063/1.1317539.
- [100] A. K. Mishra, A. J. Darbandi, P. M. Leufke, R. Kruk, and H. Hahn. Room temperature reversible tuning of magnetism of electrolyte-gated $\text{La}_{0.75}\text{Sr}_{0.25}\text{MnO}_3$ nanoparticles. *J. Appl. Phys.*, 113(3):033913, 2013. doi:10.1063/1.4778918.
- [101] H. Yamada, M. Kawasaki, T. Lottermoser, T. Arima, and Y. Tokura. $\text{LaMnO}_3/\text{SrMnO}_3$ interfaces with coupled charge-spin-orbital modulation. *Appl. Phys. Lett.*, 89(5):052506, 2006. doi:10.1063/1.2266863.
- [102] C. Adamo, X. Ke, P. Schiffer, A. Soukiassian, M. Warusawithana, L. Maritato, and D. G. Schlom. Electrical and magnetic properties of $(\text{SrMnO}_3)_n/(\text{LaMnO}_3)_{2n}$ superlattices. *Appl. Phys. Lett.*, 92(11):112508, 2008. doi:10.1063/1.2842421.
- [103] G. Koster, L. Klein, W. Siemons, G. Rijnders, J. S. Dodge, C.-B. Eom, D. H. A. Blank, and M. R. Beasley. Structure, physical properties, and applications of SrRuO_3 thin films. *Rev. Mod. Phys.*, 84(1):253–298, 2012. doi:10.1103/RevModPhys.84.253.

- [104] B. J. Kennedy and B. A. Hunter. High-temperature phases of SrRuO_3 . *Phys. Rev. B*, 58(2):653, 1998.
- [105] C. Jones, P. Battle, P. Lightfoot, and W. T. A. Harrison. The Structure of SrRuO_3 by Time-of-Flight Neutron Powder Diffraction. *Acta Crystallogr.*, C45:365–367, 1989.
- [106] H. Kobayashi, M. Nagata, R. Kanno, and Y. Kawamoto. Structural characterization of the orthorhombic perovskites: $[\text{ARuO}_3$ (A= Ca, Sr, La, Pr)]. *Mater. Res. Bull.*, 29(12):1271–1280, 1994.
- [107] J. M. Longo, P. Raccach, and J. B. Goodenough. Magnetic Properties of SrRuO_3 and CaRuO_3 . *J. Appl. Phys.*, 39(2):1327, 1968. doi:10.1063/1.1656282.
- [108] T. Gibb, R. Greatrex, N. N. Greenwood, D. C. Puxley, and K. G. Snowdon. A study of the magnetic superexchange interactions in the solid-solution series $\text{Ca}_x\text{Sr}_{1-x}\text{RuO}_3$ by ruthenium-99 Mössbauer spectroscopy. *J. Solid State Chem.*, 11:17–25, 1974.
- [109] P. B. Allen, H. Berger, O. Chauvet, L. Forro, T. Jarlborg, A. Junod, B. Revaz, and G. Santi. Transport properties, thermodynamic properties, and electronic structure of SrRuO_3 . *Phys. Rev. B*, 53(8):4393, 1996.
- [110] D. J. Singh. Electronic and magnetic properties of the 4d itinerant ferromagnet SrRuO_3 . *J. Appl. Phys.*, 79(8):4818, 1996. doi:10.1063/1.361618.
- [111] I. I. Mazin and D. J. Singh. Electronic structure and magnetism in Ru-based perovskites. *Phys. Rev. B*, 56(5):2556, 1997.
- [112] I. I. Mazin and D. J. Singh. Erratum: Electronic structure and magnetism in Ru-based perovskites [Phys. Rev. B **56** , 2556 (1997)]. *Phys. Rev. B*, 73(18), 2006. doi:10.1103/PhysRevB.73.189903.
- [113] D. C. Worledge and T. H. Geballe. Negative spin-polarization of SrRuO_3 . *Phys. Rev. Lett.*, 85(24):5182, 2000.
- [114] M. Foerster, S. Piano, F. Rigato, C. J. Mellor, and J. Fontcuberta. Andreev reflection and spin polarization of SrRuO_3 thin films on SrTiO_3 (111). *J. Phys. Conf. Ser.*, 303:012068, 2011. doi:10.1088/1742-6596/303/1/012068.
- [115] M. Ziese. Extrinsic magnetotransport phenomena in ferromagnetic oxides. *Rep. Prog. Phys.*, 65:143, 2002.
- [116] L. Klein, J. S. Dodge, C. H. Ahn, G. J. Snyder, T. H. Geballe, M. R. Beasley, and A. Kapitulnik. Anomalous spin scattering effects in the badly metallic itinerant ferromagnet SrRuO_3 . *Phys. Rev. Lett.*, 77(13):2774, 1996.

- [117] L. Klein, J. S. Dodge, C. H. Ahn, J. W. Reiner, L. Mieville, T. H. Geballe, M. R. Beasley, and A. Kapitulnik. Transport and magnetization in the badly metallic itinerant ferromagnet SrRuO_3 . *J. Phys.: Condens. Matter*, 8:10111–10126, 1996.
- [118] S. C. Gausepohl, M. Lee, R. A. Rao, and C. B. Eom. Hall-effect sign reversal in CaRuO_3 and SrRuO_3 thin films. *Phys. Rev. B*, 54(13):8996, 1996.
- [119] P. Khalifah, I. Ohkubo, B. C. Sales, H. M. Christen, D. Mandrus, and J. Cerne. Composition dependence of the anomalous Hall effect in $\text{Ca}_x\text{Sr}_{1-x}\text{RuO}_3$ films. *Phys. Rev. B*, 76(5), 2007. doi:10.1103/PhysRevB.76.054404.
- [120] Y. Klein, S. Hébert, A. Maignan, S. Kolesnik, T. Maxwell, and B. Dabrowski. Insensitivity of the band structure of substituted SrRuO_3 as probed by Seebeck coefficient measurements. *Phys. Rev. B*, 73(5), 2006. doi:10.1103/PhysRevB.73.052412.
- [121] L. Klein, J. R. Reiner, T. H. Geballe, M. R. Beasley, and A. Kapitulnik. Extraordinary Hall effect in SrRuO_3 . *Phys. Rev. B*, 61(12):R7842, 2000.
- [122] Z. Fang. The Anomalous Hall Effect and Magnetic Monopoles in Momentum Space. *Science*, 302(5642):92–95, 2003. doi:10.1126/science.1089408.
- [123] R. Mathieu, A. Asamitsu, H. Yamada, K. S. Takahashi, M. Kawasaki, Z. Fang, N. Nagaosa, and Y. Tokura. Scaling of the Anomalous Hall Effect in $\text{Sr}_{1-x}\text{Ca}_x\text{RuO}_3$. *Phys. Rev. Lett.*, 93(1), 2004. doi:10.1103/PhysRevLett.93.016602.
- [124] N. Haham, Y. Shperber, M. Schultz, N. Naftalis, E. Shimshoni, J. W. Reiner, and L. Klein. Scaling of the anomalous Hall effect in SrRuO_3 . *Phys. Rev. B*, 84(17):1774439, 2011. doi:10.1103/PhysRevB.84.174439.
- [125] A. Kanbayasi. Magnetic Properties of SrRuO_3 Single Crystal. *J. Phys. Soc. Jpn.*, 41(6):1876, 1976.
- [126] A. Kanbayasi. Magnetocrystalline Anisotropy of SrRuO_3 . *J. Phys. Soc. Jpn.*, 41:1879, 1976. doi:10.1143/JPSJ.41.1879.
- [127] A. Kanbayasi. Magnetic Properties of SrRuO_3 Single Crystal. II. *J. Phys. Soc. Jpn.*, 44:89–95, 1978. doi:10.1143/JPSJ.44.89.
- [128] R. J. Bouchard and J. F. Weiher. $\text{La}_x\text{Sr}_{1-x}\text{RuO}_3$: A new perovskite series. *J. Solid State Chem.*, 4(1):80–86, 1972.
- [129] B. Dabrowski, S. Kolesnik, O. Chmaissem, T. Maxwell, J. Mais, and J. D. Jorgensen. Magnetic properties of substituted SrRuO_3 . *Phys. Status Solidi B*, 243(1):13–20, 2006. doi:10.1002/pssb.200562525.

- [130] J. A. Rodgers, A. J. Williams, M. J. Martinez-Lope, J. A. Alonso, and J. P. Attfield. Magnetic Order from Cation Disorder in $\text{SrCr}_x\text{Ru}_{1-x}\text{O}_3$ Perovskite Oxides. *Chem. Mater.*, 20(15):4797–4799, 2008.
- [131] J.-P. Maria, H. L. McKinstry, and S. Trolier-McKinstry. Origin of preferential orthorhombic twinning in SrRuO_3 epitaxial thin films. *Appl. Phys. Lett.*, 76(23):3382, 2000. doi:10.1063/1.126654.
- [132] J.-G. Cheng, J.-S. Zhou, and J. B. Goodenough. Lattice effects on ferromagnetism in perovskite ruthenates. *Proc. Natl. Acad. Sci.*, 110(33):13312–13315, 2013. doi:10.1073/pnas.1311871110.
- [133] K. J. Choi, S. H. Baek, H. W. Jang, L. J. Belenky, M. Lyubchenko, and C.-B. Eom. Phase-Transition Temperatures of Strained Single-Crystal SrRuO_3 Thin Films. *Adv. Mater.*, 22(6):759–762, 2010. doi:10.1002/adma.200902355.
- [134] A. Herklotz, A. T. Wong, T. Meyer, M. D. Biegalski, H. N. Lee, and T. Z. Ward. Controlling Octahedral Rotations in a Perovskite via Strain Doping. *Sci. Rep.*, 6:26491, 2016. doi:10.1038/srep26491.
- [135] S. H. Chang, Y. J. Chang, S. Y. Jang, D. W. Jeong, C. U. Jung, Y.-J. Kim, J.-S. Chung, and T. W. Noh. Thickness-dependent structural phase transition of strained SrRuO_3 ultrathin films: The role of octahedral tilt. *Phys. Rev. B*, 84(10), 2011. doi:10.1103/PhysRevB.84.104101.
- [136] W. Siemons, G. Koster, A. Vailionis, H. Yamamoto, D. H. A. Blank, and M. R. Beasley. Dependence of the electronic structure of SrRuO_3 and its degree of correlation on cation off-stoichiometry. *Phys. Rev. B*, 76(7), 2007. doi:10.1103/PhysRevB.76.075126.
- [137] N. Kikugawa, R. Baumbach, J. S. Brooks, T. Terashima, S. Uji, and Y. Maeno. Single-Crystal Growth of a Perovskite Ruthenate SrRuO_3 by the Floating-Zone Method. *Cryst. Growth Des.*, 15(11):5573–5577, 2015. doi:10.1021/acs.cgd.5b01248.
- [138] Q. Gan, R. A. Rao, and C. B. Eom. Control of the growth and domain structure of epitaxial SrRuO_3 thin films by vicinal (001) SrTiO_3 substrates. *Appl. Phys. Lett.*, 70(15):1962, 1997. doi:10.1063/1.118792.
- [139] R. A. Rao, Q. Gan, and C. B. Eom. Growth mechanisms of epitaxial metallic oxide SrRuO_3 thin films studied by scanning tunneling microscopy. *Appl. Phys. Lett.*, 71(9):1171, 1997. doi:10.1063/1.119616.
- [140] Q. Gan, R. A. Rao, C. B. Eom, J. L. Garrett, and M. Lee. Direct measurement of strain effects on magnetic and electrical properties of epitaxial SrRuO_3 thin films. *Appl. Phys. Lett.*, 72(8):978, 1998. doi:10.1063/1.120603.

- [141] Q. Gan, R. A. Rao, C. B. Eom, L. Wu, and F. Tsui. Lattice distortion and uniaxial magnetic anisotropy in single domain epitaxial (110) films of SrRuO_3 . *J. Appl. Phys.*, 85(8):5297, 1999. doi:10.1063/1.369859.
- [142] D. Kan and Y. Shimakawa. Strain Effect on Structural Transition in SrRuO_3 Epitaxial Thin Films. *Cryst. Growth Des.*, 11(12):5483–5487, 2011. doi:10.1021/cg201070n.
- [143] W. Lu, P. Yang, W. D. Song, G. M. Chow, and J. S. Chen. Control of oxygen octahedral rotations and physical properties in SrRuO_3 films. *Phys. Rev. B*, 88(21), 2013. doi:10.1103/PhysRevB.88.214115.
- [144] D. Kan, R. Aso, H. Kurata, and Y. Shimakawa. Thickness-Dependent Structure-Property Relationships in Strained (110) SrRuO_3 Thin Films. *Adv. Funct. Mater.*, 23(9):1129–1136, 2013. doi:10.1002/adfm.201202402.
- [145] B. Dabrowski, O. Chmaissem, P. W. Klamut, S. Kolesnik, M. Maxwell, J. Mais, Y. Ito, B. D. Armstrong, J. D. Jorgensen, and S. Short. Reduced ferromagnetic transition temperatures in $\text{SrRu}_{1-x}\text{O}_3$ perovskites from Ru-site vacancies. *Phys. Rev. B*, 70(1), 2004. doi:10.1103/PhysRevB.70.014423.
- [146] W. Lu, W. Song, P. Yang, J. Ding, G. M. Chow, and J. Chen. Strain Engineering of Octahedral Rotations and Physical Properties of SrRuO_3 Films. *Sci. Rep.*, 5:10245, 2015. doi:10.1038/srep10245.
- [147] C. U. Jung, H. Yamada, M. Kawasaki, and Y. Tokura. Magnetic anisotropy control of SrRuO_3 films by tunable epitaxial strain. *Appl. Phys. Lett.*, 84(14): 2590–2592, 2004. doi:10.1063/1.1695195.
- [148] K. Terai, T. Ohnishi, M. Lippmaa, H. Koinuma, and M. Kawasaki. Magnetic properties of strain-controlled SrRuO_3 thin films. *Jpn. J. Appl. Phys.*, 43(2A): L227, 2004.
- [149] A. J. Grutter, F. J. Wong, E. Arenholz, A. Vailionis, and Y. Suzuki. Evidence of high-spin Ru and universal magnetic anisotropy in SrRuO_3 thin films. *Phys. Rev. B*, 85(13), 2012. doi:10.1103/PhysRevB.85.134429.
- [150] S. Agrestini, Z. Hu, C.-Y. Kuo, M. W. Haverkort, K.-T. Ko, N. Hollmann, Q. Liu, E. Pellegrin, M. Valvidares, J. Herrero-Martin, P. Gargiani, P. Gegenwart, M. Schneider, S. Esser, A. Tanaka, A. C. Komarek, and L. H. Tjeng. Electronic and spin states of SrRuO_3 thin films: An x-ray magnetic circular dichroism study. *Phys. Rev. B*, 91(7), 2015. doi:10.1103/PhysRevB.91.075127.
- [151] J. Xia, W. Siemons, G. Koster, M. R. Beasley, and A. Kapitulnik. Critical thickness for itinerant ferromagnetism in ultrathin films of SrRuO_3 . *Phys. Rev. B*, 79(14), 2009. doi:10.1103/PhysRevB.79.140407.

- [152] R. A. Ricciardo, H. L. Cuthbert, P. M. Woodward, Q. Zhou, B. J. Kennedy, Z. Zhang, M. Avdeev, and L.-Y. Jang. Structure and Properties of $\text{Sr}_{1-x}\text{Ca}_x\text{Mn}_{0.5}\text{Ru}_{0.5}\text{O}_3$ Perovskites: Using Chemical Pressure to Control Mn/Ru Mixed Valency. *Chem. Mater.*, 22(11):3369–3382, 2010. doi:10.1021/cm903848h.
- [153] K. Terai, K. Yoshii, Y. Takeda, S.-i. Fujimori, Y. Saitoh, K. Ohwada, T. Inami, T. Okane, M. Arita, K. Shimada, H. Namatame, M. Taniguchi, K. Kobayashi, M. Kobayashi, and A. Fujimori. Electronic structure and magnetism of $\text{CaMn}_{1-x}\text{Ru}_x\text{O}_3$ thin films. *J. Magn. Magn. Mater.*, 310(2):1070–1072, 2007. doi:10.1016/j.jmmm.2006.10.261.
- [154] T. Taniguchi, S. Mizusaki, N. Okada, Y. Nagata, S. H. Lai, M. D. Lan, N. Hiraoka, M. Itou, Y. Sakurai, T. C. Ozawa, Y. Noro, and H. Samata. Crystallographic and magnetic properties of the mixed-valence oxides $\text{CaRu}_{1-x}\text{Mn}_x\text{O}_3$. *Phys. Rev. B*, 77(1), 2008. doi:10.1103/PhysRevB.77.014406.
- [155] D. H. Kim, E. Lee, H. W. Kim, S. Kolesnik, B. Dabrowski, C.-J. Kang, M. Kim, B. I. Min, H.-K. Lee, J.-Y. Kim, and J.-S. Kang. Correlation between Mn and Ru valence states and magnetic phases in $\text{SrMn}_{1-x}\text{Ru}_x\text{O}_3$. *Phys. Rev. B*, 91(7), 2015. doi:10.1103/PhysRevB.91.075113.
- [156] P. Yordanov, A. V. Boris, J. W. Freeland, J. J. Kavich, J. Chakhalian, H. N. Lee, and B. Keimer. Far-infrared and dc magnetotransport of CaMnO_3 - CaRuO_3 superlattices. *Phys. Rev. B*, 84(4), 2011. doi:10.1103/PhysRevB.84.045108.
- [157] Z. Sefrioui, C. Visani, M. J. Calderón, K. March, C. Carrétéro, M. Walls, A. Rivera-Calzada, C. León, R. L. Anton, T. R. Charlton, F. A. Cuellar, E. Iborra, F. Ott, D. Imhoff, L. Brey, M. Bibes, J. Santamaria, and A. Barthélémy. All-Manganite Tunnel Junctions with Interface-Induced Barrier Magnetism. *Adv. Mater.*, 22(44):5029–5034, 2010. doi:10.1002/adma.201002067.
- [158] K. S. Takahashi, M. Kawasaki, and Y. Tokura. Interface ferromagnetism in oxide superlattices of $\text{CaMnO}_3/\text{CaRuO}_3$. *Appl. Phys. Lett.*, 79(9):1324–1326, 2001. doi:10.1063/1.1398331.
- [159] Y. Choi, Y. Z. Yoo, O. Chmaissem, A. Ullah, S. Kolesnik, C. W. Kimball, D. Haskel, J. S. Jiang, and S. D. Bader. Ferromagnetic Mn moments at $\text{SrRuO}_3/\text{SrMnO}_3$ interfaces. *Appl. Phys. Lett.*, 91(2):022503, 2007. doi:10.1063/1.2753100.
- [160] B. R. K. Nanda, S. Satpathy, and M. S. Springborg. Electron Leakage and Double-Exchange Ferromagnetism at the Interface between a Metal and an

- Antiferromagnetic Insulator: CaRuO_3 / CaMnO_3 . *Phys. Rev. Lett.*, 98(21), 2007. doi:10.1103/PhysRevLett.98.216804.
- [161] J. W. Freeland, J. Chakhalian, A. V. Boris, J.-M. Tonnerre, J. J. Kavich, P. Yordanov, S. Grenier, P. Zschack, E. Karapetrova, P. Popovich, H. N. Lee, and B. Keimer. Charge transport and magnetization profile at the interface between the correlated metal CaRuO_3 and the antiferromagnetic insulator CaMnO_3 . *Phys. Rev. B*, 81(9), 2010. doi:10.1103/PhysRevB.81.094414.
- [162] X. Ke, M. S. Rzchowski, L. J. Belenky, and C. B. Eom. Positive exchange bias in ferromagnetic $\text{La}_{0.67}\text{Sr}_{0.33}\text{MnO}_3/\text{SrRuO}_3$ bilayers. *Appl. Phys. Lett.*, 84(26):5458, 2004. doi:10.1063/1.1767955.
- [163] F. Weigand, S. Gold, A. Schmid, J. Geissler, E. Goering, K. Dörr, G. Krabbes, and K. Ruck. Antiparallel ruthenium coupling in doped $\text{La}_{1.2}\text{Sr}_{1.8}\text{Mn}_{2-x}\text{Ru}_x\text{O}_7$. *Appl. Phys. Lett.*, 81(11):2035–2037, 2002. doi:10.1063/1.1506792.
- [164] Y. Lee, B. Caes, and B. Harmon. Role of Oxygen 2p states for antiferromagnetic interfacial coupling and positive exchange bias of ferromagnetic LSMO/SRO bilayers. *J. Alloys Compd.*, 450(1-2):1–6, 2008. doi:10.1016/j.jallcom.2006.10.085.
- [165] J. Garcia-Barriocanal, F. Y. Bruno, A. Rivera-Calzada, Z. Sefrioui, N. M. Nemes, M. Garcia-Hernández, J. Rubio-Zuazo, G. R. Castro, M. Varela, S. J. Pennycook, C. Leon, and J. Santamaria. “Charge Leakage” at LaMnO_3 / SrTiO_3 Interfaces. *Adv. Mater.*, 22(5):627–632, 2010. doi:10.1002/adma.200902263.
- [166] F. Y. Bruno, J. Garcia-Barriocanal, M. Varela, N. M. Nemes, P. Thakur, J. C. Cezar, N. B. Brookes, A. Rivera-Calzada, M. Garcia-Hernandez, C. Leon, S. Okamoto, S. J. Pennycook, and J. Santamaria. Electronic and Magnetic Reconstructions in $\text{La}_{0.7}\text{Sr}_{0.3}\text{MnO}_3$ / SrTiO_3 Heterostructures: A Case of Enhanced Interlayer Coupling Controlled by the Interface. *Phys. Rev. Lett.*, 106(14), 2011. doi:10.1103/PhysRevLett.106.147205.
- [167] D. Kan, R. Aso, R. Sato, M. Haruta, H. Kurata, and Y. Shimakawa. Tuning magnetic anisotropy by interfacially engineering the oxygen coordination environment in a transition metal oxide. *Nat. Mater.*, 2016. doi:10.1038/nmat4580.
- [168] Z. Liao, M. Huijben, Z. Zhong, N. Gauquelin, S. Macke, R. J. Green, S. Van Aert, J. Verbeeck, G. Van Tendeloo, K. Held, G. A. Sawatzky, G. Koster, and G. Rijnders. Controlled lateral anisotropy in correlated manganite heterostructures by interface-engineered oxygen octahedral coupling. *Nat. Mater.*, 15(4):425–431, 2016. doi:10.1038/nmat4579.

- [169] G. Aubert. Torque Measurements of the Anisotropy of Energy and Magnetization of Nickel. *J. Appl. Phys.*, 39(2):504, 1968. doi:10.1063/1.2163505.
- [170] P. Bruno. Physical origins and theoretical models of magnetic anisotropy. In R. Hölzle, editor, *Magnetismus von Festkörpern Und Grenzflächen: Vorlesungsmanuskripte Des 24. IFF-Ferienkurses Vom 8. Bis 19. März 1993 Im Forschungszentrum Jülich*, volume 24 of *Institut für Festkörperforschung Jülich: Vorlesungsmanuskripte des IFF-Ferienkurses*. Forschungszentrum Jülich, 1993.
- [171] N. Akulov. Zur Quantentheorie der Temperaturabhängigkeit der Magnetisierungskurve. *Z. Für Phys.*, 100(3-4):197–202, 1936.
- [172] C. Zener. Classical theory of the temperature dependence of magnetic anisotropy energy. *Phys. Rev.*, 96(5):1335, 1954.
- [173] H. B. Callen and E. R. Callen. The present status of the temperature dependence of magnetocrystalline anisotropy, and the $l(l+1)2$ power law. *J. Phys. Chem. Solids*, 27(8):1271–1285, 1966.
- [174] E. R. Callen and H. B. Callen. Anisotropic magnetization. *J. Phys. Chem. Solids*, 16(3):310–328, 1960. doi:10.1016/0022-3697(60)90161-X.
- [175] F. Ono. Fermi-level dependence of magnetocrystalline anisotropy in 3d-transition metals. *J. Magn. Magn. Mater.*, 31:841–842, 1983.
- [176] F. Ono. Magnetic field dependence of the magnetocrystalline anisotropy in Fe. *J. Magn. Magn. Mater.*, 54:907–908, 1986.
- [177] I. Barsukov, Y. Fu, A. M. Gonçalves, M. Spasova, M. Farle, L. C. Sampaio, R. E. Arias, and I. N. Krivorotov. Field-dependent perpendicular magnetic anisotropy in CoFeB thin films. *Appl. Phys. Lett.*, 105(15):152403, 2014. doi:10.1063/1.4897939.
- [178] S. Blundell. *Magnetism in Condensed Matter*. Oxford Master Series in Physics. Oxford University Press, Oxford, 2001. ISBN 978-0-19-850591-4.
- [179] F. Bloch and G. Gentile. Zur Anisotropie der Magnetisierung Ferromagnetischer Einkristalle. *Z. Für Phys.*, 70(5-6):395–408, 1931.
- [180] J. H. van Vleck. On the anisotropy of cubic ferromagnetic crystals. *Phys. Rev.*, 52(11):1178, 1937.
- [181] L. Néel. L’anisotropie superficielle des substances ferromagnetiques. *C. r. hebd. séances Acad. sci.*, 237:1468–1470, 1953.

- [182] P. Bruno. Tight-binding approach to the orbital magnetic moment and magnetocrystalline anisotropy of transition-metal monolayers. *Phys. Rev. B*, 39(1):865, 1989.
- [183] L. Szunyogh, B. Újfalussy, and P. Weinberger. Magnetic anisotropy of iron multilayers on Au (001): First-principles calculations in terms of the fully relativistic spin-polarized screened KKR method. *Phys. Rev. B*, 51(15):9552, 1995.
- [184] G. Schneider. *Calculation of Magnetocrystalline Anisotropy*. Thesis, Oregon State University, Corvallis, Oregon, 1999.
- [185] A. Sakuma, Y. Manabe, and Y. Kota. First Principles Calculation of Magnetocrystalline Anisotropy Energy of MnBi and MnBi_{1-x}Sn_x. *J. Phys. Soc. Jpn.*, 82(7):073704, 2013.
- [186] R. R. Birss. *Symmetry and Magnetism*. North-Holland, Amsterdam, 1966.
- [187] A. P. Cracknell. Symmetry Properties of the Transport Coefficients of Magnetic Crystals. *Phys. Rev. B*, 7(5):2145, 1973.
- [188] W. Kleiner. Space-Time Symmetry of Transport Coefficients. *Phys. Rev.*, 142(2):318, 1966.
- [189] W. Kleiner. Space-Time Symmetry Restrictions on Transport Coefficients II. Two Theories Compared. *Phys. Rev.*, 153(3):726, 1967.
- [190] H.-D. Butzal and R. R. Birss. Time reversal and magnetic reversal in crystal physics. *Phys. Stat. Mech. Its Appl.*, 114(1-3):518–521, 1982.
- [191] H.-D. Butzal. Magnetic symmetry and the electrical conductivity tensor. *Phys. Stat. Mech. Its Appl.*, 114(1-3):522–525, 1982.
- [192] W. Döring. Die Richtungsabhängigkeit der Kristallenergie. *Ann. Phys.*, 456(1-3):102–109, 1957.
- [193] W. Döring and G. Simon. Berichtigung und Ergänzung der Arbeiten „Die Richtungsabhängigkeit der Kristallenergie“ und „Die Richtungsabhängigkeit der Magnetostriktion“. *Ann. Phys.*, 463(3-4):144–145, 1961. doi:10.1002/andp.19614630304.
- [194] W. P. Mason. Derivation of Magnetostriction and Anisotropic Energies for Hexagonal, Tetragonal, and Orthorhombic Crystals. *Phys. Rev.*, 96:302, 1954.
- [195] L. Néel. Anisotropie magnétique superficielle et surstructures d’orientation. *J. Phys. Radium*, 15(4):225–239, 1954.

- [196] P. Bruno. Magnetic surface anisotropy of cobalt and surface roughness effects within Neel's model. *J. Phys. F Met. Phys.*, 18(6):1291, 1988.
- [197] P. Bruno and J.-P. Renard. Magnetic surface anisotropy of transition metal ultrathin films. *Appl. Phys. A*, 49(5):499–506, 1989.
- [198] C. Chappert, K. Le Dang, P. Beauvillain, H. Hurdequint, and D. Renard. Ferromagnetic resonance studies of very thin cobalt films on a gold substrate. *Phys. Rev. B*, 34(5):3192, 1986.
- [199] P. Bruno. Dipolar magnetic surface anisotropy in ferromagnetic thin films with interfacial roughness. *J. Appl. Phys.*, 64(6):3153, 1988. doi:10.1063/1.341530.
- [200] H. A. Jahn and E. Teller. Stability of Polyatomic Molecules in Degenerate Electronic States. I. Orbital Degeneracy. *Proc. R. Soc. Lond. A*, 161:220–235, 1937. doi:10.1098/rspa.1937.0142.
- [201] S. Chikazumi. *Physics of Ferromagnetism*. Number 91 in International series of monographs on physics. Oxford University Press, Oxford, 1997. ISBN 0-19-851776-9.
- [202] I. A. Campbell and A. Fert. Transport Properties of Ferromagnets. In E. P. Wohlfarth, editor, *Ferromagnetic Materials Vol.3*, page 747. North-Holland, 1982. ISBN 978-0-444-86378-2.
- [203] M. Ziese and S. P. Sena. Anisotropic magnetoresistance of thin $\text{La}_{0.7}\text{Ca}_{0.3}\text{MnO}_3$ films. *J. Phys. Condens. Matter*, 10(12):2727, 1998.
- [204] J. O'Donnell, M. Onellion, M. S. Rzchowski, J. N. Eckstein, and I. Bozovic. Magnetoresistance scaling in MBE-grown $\text{La}_{0.7}\text{Ca}_{0.3}\text{MnO}_3$ thin films. *Phys. Rev. B*, 54(10):R6841, 1996.
- [205] E. L. Nagaev. Magnetoimpurity theory of manganites and other colossal magnetoresistance materials. *Aust. J. Phys.*, 52(2):305–317, 1999.
- [206] E. Hall. XVIII. On the “Rotational Coefficient” in nickel and cobalt. *Philos. Mag.*, 12(74):157–172, 1881. doi:10.1080/14786448108627086.
- [207] E. M. Pugh. Hall effect and the magnetic properties of some ferromagnetic materials. *Phys. Rev.*, 36(9):1503, 1930.
- [208] E. M. Pugh and N. Rostoker. Hall effect in ferromagnetic materials. *Rev. Mod. Phys.*, 25(1):151, 1953.
- [209] R. Karplus and J. M. Luttinger. Hall effect in ferromagnetics. *Phys. Rev.*, 95(3):1154, 1954.

- [210] J. M. Luttinger. Theory of the Hall effect in ferromagnetic substances. *Phys. Rev.*, 112(3):739, 1958.
- [211] J. Smit. The spontaneous Hall effect in ferromagnetics I. *Physica*, 21(6-10): 877–887, 1955.
- [212] J. Smit. The spontaneous Hall effect in ferromagnetics II. *Physica*, 24:39, 1958.
- [213] L. Berger. Influence of spin-orbit interaction on the transport processes in ferromagnetic nickel alloys, in the presence of a degeneracy of the 3d band. *Physica*, 30(6):1141–1159, 1964.
- [214] L. Berger. Side-jump mechanism for the Hall effect of ferromagnets. *Phys. Rev. B*, 2(11):4559, 1970.
- [215] N. Nagaosa, J. Sinova, S. Onoda, A. H. MacDonald, and N. P. Ong. Anomalous Hall effect. *Rev. Mod. Phys.*, 82(2):1539–1592, 2010. doi:10.1103/RevModPhys.82.1539.
- [216] N. A. Sinitsyn. Semiclassical theories of the anomalous Hall effect. *J. Phys. Condens. Matter*, 20(2):023201, 2008. doi:10.1088/0953-8984/20/02/023201.
- [217] M. Onoda, G. Tatara, and N. Nagaosa. Anomalous Hall Effect and Skyrmion Number in Real and Momentum Spaces. *J. Phys. Soc. Jpn.*, 73(10):2624–2627, 2004. doi:10.1143/JPSJ.73.2624.
- [218] Y. Lyanda-Geller, S. H. Chun, M. B. Salamon, P. M. Goldbart, P. D. Han, Y. Tomioka, A. Asamitsu, and Y. Tokura. Charge transport in manganites: Hopping conduction, the anomalous Hall effect, and universal scaling. *Phys. Rev. B*, 63(18), 2001. doi:10.1103/PhysRevB.63.184426.
- [219] M. Kohler. Magnetischer Halleffekt in kristallinen Medien. *Ann. Phys.*, 412 (8):878–890, 1934.
- [220] C. Hurd. Galvanomagnetic effects in anisotropic metals. *Adv. Phys.*, 23(2): 315–433, 1974. doi:10.1080/00018737400101361.
- [221] E. Roman, Y. Mokrousov, and I. Souza. Orientation Dependence of the Intrinsic Anomalous Hall Effect in hcp Cobalt. *Phys. Rev. Lett.*, 103(9), 2009. doi:10.1103/PhysRevLett.103.097203.
- [222] Y. Mokrousov, H. Zhang, F. Freimuth, B. Zimmermann, N. H. Long, J. Weis-chenberg, I. Souza, P. Mavropoulos, and S. Blügel. Anisotropy of spin relax-ation and transverse transport in metals. *J. Phys. Condens. Matter*, 25(16): 163201, 2013. doi:10.1088/0953-8984/25/16/163201.

- [223] R. Bianco, R. Resta, and I. Souza. How disorder affects the Berry-phase anomalous Hall conductivity: A reciprocal-space analysis. *Phys. Rev. B*, 90(12), 2014. doi:10.1103/PhysRevB.90.125153.
- [224] Y. Zhang, Y. Sun, H. Yang, J. Železný, S. P. P. Parkin, C. Felser, and B. Yan. Strong anisotropic anomalous Hall effect and spin Hall effect in the chiral antiferromagnetic compounds Mn_3X ($\text{X} = \text{Ge}, \text{Sn}, \text{Ga}, \text{Ir}, \text{Rh}, \text{and Pt}$). *Phys. Rev. B*, 95(7), 2017. doi:10.1103/PhysRevB.95.075128.
- [225] P. M. M. Duhem. *Ziel und Struktur der physikalischen Theorien*. J. A. Barth, Leipzig, 1 edition, 1908.
- [226] D. B. Chrisey and G. K. Hubler, editors. *Pulsed Laser Deposition of Thin Films*. John Wiley and Sons, New York, 1994. ISBN 978-0-471-59218-1.
- [227] R. Eason, editor. *Pulsed Laser Deposition of Thin Films - Applications-Led Growth of Functional Materials*. John Wiley and Sons, Hoboken, 2007. ISBN 978-0-471-44709-2.
- [228] J. Klein, C. Höfener, L. Alff, and R. Gross. Laser ablation of manganite thin films monitored by in situ RHEED. *J. Magn. Magn. Mater.*, 211(1):9–15, 2000.
- [229] P. R. Willmott and J. R. Huber. Pulsed laser vaporization and deposition. *Rev. Mod. Phys.*, 72(1):315, 2000.
- [230] H. M. Christen and G. Eres. Recent advances in pulsed-laser deposition of complex oxides. *J. Phys. Condens. Matter*, 20(26):264005, 2008. doi:10.1088/0953-8984/20/26/264005.
- [231] M. Opel. Spintronic oxides grown by laser-MBE. *J. Phys. Appl. Phys.*, 45(3):033001, 2012. doi:10.1088/0022-3727/45/3/033001.
- [232] P. C. Dowden, Z. Bi, and Q. X. Jia. Method for controlling energy density for reliable pulsed laser deposition of thin films. *Rev. Sci. Instrum.*, 85(2):025111, 2014. doi:10.1063/1.4865716.
- [233] B. Dam, J. H. Rector, J. Johansson, J. Huijbregtse, and D. G. De Groot. Mechanism of incongruent ablation of SrTiO_3 . *J. Appl. Phys.*, 83(6):3386–3389, 1998. doi:10.1063/1.367106.
- [234] T. Ohnishi, K. Shibuya, T. Yamamoto, and M. Lippmaa. Defects and transport in complex oxide thin films. *J. Appl. Phys.*, 103(10):103703, 2008. doi:10.1063/1.2921972.
- [235] K. L. Saenger. On the origin of spatial nonuniformities in the composition of pulsed-laser-deposited films. *J. Appl. Phys.*, 70(10):5629, 1991. doi:10.1063/1.350178.

- [236] S. I. Anisimov, D. Bäuerle, and B. S. Luk'yanchuk. Gas dynamics and film profiles in pulsed-laser deposition of materials. *Phys. Rev. B*, 48(16):12076, 1993.
- [237] S. Ryu, J. Lee, E. Ahn, J. Kim, A. Herklotz, J.-S. Bae, H. N. Lee, Y. Kim, J.-Y. Kim, T.-Y. Jeon, J. Cho, S. Park, and H. Jeon. Growth of electronically distinct manganite thin films by modulating cation stoichiometry. *Appl. Phys. Lett.*, 110(26):261601, 2017. doi:10.1063/1.4989578.
- [238] S. Amoruso, C. Aruta, R. Bruzzese, D. Maccariello, L. Maritato, F. M. Granozio, P. Orgiani, U. Scotti di Uccio, and X. Wang. Optimization of $\text{La}_{0.7}\text{Ba}_{0.3}\text{MnO}_{3-\delta}$ complex oxide laser ablation conditions by plume imaging and optical emission spectroscopy. *J. Appl. Phys.*, 108(4):043302, 2010. doi:10.1063/1.3467770.
- [239] P. Orgiani, R. Ciancio, A. Galdi, S. Amoruso, and L. Maritato. Physical properties of $\text{La}_{0.7}\text{Ba}_{0.3}\text{MnO}_{3-\delta}$ complex oxide thin films grown by pulsed laser deposition technique. *Appl. Phys. Lett.*, 96(3):032501, 2010. doi:10.1063/1.3292588.
- [240] J. H. Song, T. Susaki, and H. Y. Hwang. Enhanced thermodynamic stability of epitaxial oxide thin films. *Adv. Mater.*, 20(13):2528–2532, 2008. doi:10.1002/adma.200701919.
- [241] L. F. Kourkoutis, J. H. Song, H. Y. Hwang, and D. A. Muller. Microscopic origins for stabilizing room-temperature ferromagnetism in ultra-thin manganite layers. *Proc. Natl. Acad. Sci.*, 107(26):11682–11685, 2010. doi:10.1073/pnas.1005693107.
- [242] H. Guo, D. Sun, W. Wang, Z. Gai, I. Kravchenko, J. Shao, L. Jiang, T. Z. Ward, P. C. Snijders, L. Yin, J. Shen, and X. Xu. Growth diagram of $\text{La}_{0.7}\text{Sr}_{0.3}\text{MnO}_3$ thin films using pulsed laser deposition. *J. Appl. Phys.*, 113(23):234301, 2013. doi:10.1063/1.4811187.
- [243] M. Strikovski and J. H. Miller. Pulsed laser deposition of oxides: Why the optimum rate is about 1 Å per pulse. *Appl. Phys. Lett.*, 73(12):1733, 1998. doi:10.1063/1.122260.
- [244] C. Xu, S. Wicklein, A. Sambri, S. Amoruso, M. Moors, and R. Dittmann. Impact of the interplay between nonstoichiometry and kinetic energy of the plume species on the growth mode of SrTiO_3 thin films. *J. Phys. Appl. Phys.*, 47(3):034009, 2014. doi:10.1088/0022-3727/47/3/034009.
- [245] W. Hong, H. N. Lee, M. Yoon, H. M. Christen, D. H. Lowndes, Z. Suo, and Z. Zhang. Persistent Step-Flow Growth of Strained Films on Vicinal Substrates. *Phys. Rev. Lett.*, 95(9), 2005. doi:10.1103/PhysRevLett.95.095501.

- [246] D. Estève, T. Maroutian, V. Pillard, and P. Lecoeur. Step velocity tuning of SrRuO₃ step flow growth on SrTiO₃. *Phys. Rev. B*, 83(19), 2011. doi:10.1103/PhysRevB.83.193401.
- [247] H. Kiessig. Interferenz von Röntgenstrahlen an dünnen Schichten. *Ann. Phys.*, 402(7):769–788, 1931.
- [248] W. J. Bartels, J. Hornstra, and D. J. W. Lobeek. X-ray diffraction of multilayers and superlattices. *Acta Crystallogr. A*, 42(6):539–545, 1986.
- [249] P. F. Fewster and C. J. Curling. Composition and lattice-mismatch measurement of thin semiconductor layers by x-ray diffraction. *J. Appl. Phys.*, 62(10):4154, 1987. doi:10.1063/1.339133.
- [250] I. K. Schuller. New class of layered materials. *Phys. Rev. Lett.*, 44(24):1597, 1980.
- [251] E. E. Fullerton, I. K. Schuller, H. Vanderstraeten, and Y. Bruynseraede. Structural refinement of superlattices from x-ray diffraction. *Phys. Rev. B*, 45(16):9292, 1992.
- [252] P. F. Fewster. X-ray analysis of thin films and multilayers. *Rep. Prog. Phys.*, 59(11):1339, 1996. doi:10.1088/0034-4885/59/11/001.
- [253] M. Grundmann and A. Krost. Atomic structure based simulation of X-ray scattering from strained superlattices. *Phys. Status Solidi B*, 218(2):417–423, 2000. doi:10.1002/1521-3951(200004)218:2<417::AID-PSSB417>3.0.CO;2-Q.
- [254] J. Birch, J.-E. Sundgren, and P. F. Fewster. Measurement of the lattice parameters in the individual layers of single-crystal superlattices. *J. Appl. Phys.*, 78(11):6562, 1995. doi:10.1063/1.360476.
- [255] D. Pesquera, X. Marti, V. Holý, R. Bachelet, G. Herranz, and J. Fontcuberta. X-ray interference effects on the determination of structural data in ultrathin La_{2/3}Sr_{1/3}MnO₃ epitaxial thin films. *Appl. Phys. Lett.*, 99(22):221901, 2011. doi:10.1063/1.3663574.
- [256] V. Holý, U. Pietsch, and T. Baumbach. *High-Resolution X-Ray Scattering from Thin Films and Multilayers*. Number 149 in Springer Tracts in Modern Physics. Springer-Verlag, Berlin Heidelberg, 1999. ISBN 978-3-540-62029-7.
- [257] O. Lugovskaya and S. A. Stepanov. Calculation of the polarizabilities of crystals for diffraction of x-rays of the continuous spectrum at wavelengths of 0.1-10 Å. *Sov Phys Crystallogr.*, 36:478–481, 1991.
- [258] V. Holý, J. Kuběna, and K. Ploog. X-Ray Analysis of Structural Defects in a Semiconductor Superlattice. *Phys. Status Solidi B*, 162(2):347–361, 1990.

- [259] L. Jones, S. Wenner, M. Nord, P. H. Ninive, O. M. Løvvik, R. Holmestad, and P. D. Nellist. Optimising multi-frame ADF-STEM for high-precision atomic-resolution strain mapping. *Ultramicroscopy*, 179:57–62, 2017. doi:10.1016/j.ultramic.2017.04.007.
- [260] M. Nord, P. E. Vullum, I. Hallsteinsen, T. Tybell, and R. Holmestad. Assessing electron beam sensitivity for SrTiO_3 and $\text{La}_{0.7}\text{Sr}_{0.3}\text{MnO}_3$ using electron energy loss spectroscopy. *Ultramicroscopy*, 169:98–106, 2016. doi:10.1016/j.ultramic.2016.07.004.
- [261] L. Van der Pauw. A method of measuring specific resistivity and Hall effect of discs of arbitrary shape. *Philips Res Rep*, 13(1):334, 1958.
- [262] L. Van der Pauw. A method of measuring the resistivity and Hall coefficient on lamellae of arbitrary shape. *Philips Tech Rev*, 20(8):220, 1958.
- [263] J. L. Cieřliński. Modified van der Pauw method based on formulas solvable by the Banach fixed point method. *Thin Solid Films*, 522:314–317, 2012. doi:10.1016/j.tsf.2012.09.018.
- [264] L. Van der Pauw. Determination of resistivity tensor and hall tensor of anisotropic conductors. *Philips Res Rep*, 16:187–195, 1961.
- [265] J. Wasscher. Note on four-point resistivity measurements on anisotropic conductors. *Philips Res. Rep.*, 16(4):301–306, 1961.
- [266] W. L. V. Price. Extension of van der Pauw’s theorem for measuring specific resistivity in discs of arbitrary shape to anisotropic media. *J. Phys. D*, 5(6):1127, 1972.
- [267] B. F. Logan. Series for computing current flow in a rectangular block. *J. Appl. Phys.*, 42(7):2975, 1971. doi:10.1063/1.1660657.
- [268] H. C. Montgomery. Method for measuring electrical resistivity of anisotropic materials. *J. Appl. Phys.*, 42(7):2971, 1971. doi:10.1063/1.1660656.
- [269] W. L. V. Price. Electric potential and current distribution in a rectangular sample of anisotropic material with application to the measurement of the principal resistivities by an extension of van der Pauw’s method. *Solid-State Electron.*, 16(7):753–762, 1973.
- [270] S. H. Simon. Comment on “Evidence for an Anisotropic State of Two-Dimensional Electrons in High Landau Levels”. *Phys. Rev. Lett.*, 83(20):4223, 1999.

- [271] C. A. M. dos Santos, A. de Campos, M. S. da Luz, B. D. White, J. J. Neumeier, B. S. de Lima, and C. Y. Shigue. Procedure for measuring electrical resistivity of anisotropic materials: A revision of the Montgomery method. *J. Appl. Phys.*, 110(8):083703, 2011. doi:10.1063/1.3652905.
- [272] O. Bierwagen, R. Pomraenke, S. Eilers, and W. T. Masselink. Mobility and carrier density in materials with anisotropic conductivity revealed by van der Pauw measurements. *Phys. Rev. B*, 70(16):165307, 2004. doi:10.1103/PhysRevB.70.165307.
- [273] O. Bierwagen, T. Ive, C. G. Van de Walle, and J. S. Speck. Causes of incorrect carrier-type identification in van der Pauw–Hall measurements. *Appl. Phys. Lett.*, 93(24):242108, 2008. doi:10.1063/1.3052930.
- [274] A. Segal, O. Shaya, M. Karpovski, and A. Gerber. Asymmetric field dependence of magnetoresistance in magnetic films. *Phys. Rev. B*, 79(14), 2009. doi:10.1103/PhysRevB.79.144434.
- [275] S. N. Ern , H.-D. Hahlbohm, and H. L bbig. Theory of rf-biased superconducting quantum interference device for nonhysteretic regime. *J. Appl. Phys.*, 47(12):5440–5442, 1976. doi:10.1063/1.322574.
- [276] A. Zi ba. Image and sample geometry effects in SQUID magnetometers. *Rev. Sci. Instrum.*, 64(12):3357, 1993. doi:10.1063/1.1144306.
- [277] L. L. Miller. The response of longitudinal and transverse pickup coils to a misaligned magnetic dipole. *Rev. Sci. Instrum.*, 67(9):3201, 1996. doi:10.1063/1.1147493.
- [278] P. Stamenov and J. M. D. Coey. Sample size, position, and structure effects on magnetization measurements using second-order gradiometer pickup coils. *Rev. Sci. Instrum.*, 77(1):015106, 2006. doi:10.1063/1.2149190.
- [279] M. Sawicki, W. Stefanowicz, and A. Ney. Sensitive SQUID magnetometry for studying nanomagnetism. *Semicond. Sci. Technol.*, 26(6):064006, 2011. doi:10.1088/0268-1242/26/6/064006.
- [280] A. Ney, T. Kammermeier, V. Ney, K. Ollefs, and S. Ye. Limitations of measuring small magnetic signals of samples deposited on a diamagnetic substrate. *J. Magn. Magn. Mater.*, 320(23):3341–3346, 2008. doi:10.1016/j.jmmm.2008.07.008.
- [281] M. A. Garcia, E. Fernandez Pinel, J. de la Venta, A. Quesada, V. Bouzas, J. F. Fern ndez, J. J. Romero, M. S. Mart n Gonz lez, and J. L. Costa-Kr mer. Sources of experimental errors in the observation of nanoscale magnetism. *J. Appl. Phys.*, 105(1):013925, 2009. doi:10.1063/1.3060808.

- [282] G. Bridoux, J. Barzola-Quiquia, F. Bern, W. Böhlmann, I. Vrejoiu, M. Ziese, and P. Esquinazi. An alternative route towards micro- and nano-patterning of oxide films. *Nanotechnology*, 23(8):085302, 2012. doi:10.1088/0957-4484/23/8/085302.
- [283] A. F. Marshall, L. Klein, J. S. Dodge, C. H. Ahn, J. W. Reiner, L. Mieville, L. Antagonazza, A. Kapitulnik, T. H. Geballe, and M. R. Beasley. Lorentz transmission electron microscope study of ferromagnetic domain walls in SrRuO₃: Statics, dynamics, and crystal structure correlation. *J. Appl. Phys.*, 85(8):4131, 1999. doi:10.1063/1.370322.
- [284] D. Weber, R. Vőfély, Y. Chen, Y. Mourzina, and U. Poppe. Variable resistor made by repeated steps of epitaxial deposition and lithographic structuring of oxide layers by using wet chemical etchants. *Thin Solid Films*, 533:43–47, 2013. doi:10.1016/j.tsf.2012.11.118.
- [285] R. U. Lemieux and E. von Rudloff. Periodate–Permanganate Oxidations: I. Oxidation of Olefins. *Can. J. Chem.*, 33(11):1701–1709, 1955.
- [286] B. L. Brandt, D. W. Liu, and L. G. Rubin. Low temperature thermometry in high magnetic fields. VII. CernoxTM sensors to 32 T. *Rev. Sci. Instrum.*, 70(1):104, 1999. doi:10.1063/1.1149549.
- [287] P. Esquinazi, N. García, J. Barzola-Quiquia, P. Rödiger, K. Schindler, J.-L. Yao, and M. Ziese. Indications for intrinsic superconductivity in highly oriented pyrolytic graphite. *Phys. Rev. B*, 78(13):134516, 2008. doi:10.1103/PhysRevB.78.134516.
- [288] B. Sarkar, B. Dalal, and S. K. De. Temperature induced magnetization reversal in SrRuO₃. *Appl. Phys. Lett.*, 103(25):252403, 2013. doi:10.1063/1.4850737.
- [289] MPMS Application Note 1014-208 Remnant fields in MPMS superconducting magnets, 2001.
- [290] G. Mastrogiacomo, J. F. Löffler, and N. R. Dilley. Soft-magnetic materials characterized using a superconducting solenoid as magnetic source. *Appl. Phys. Lett.*, 92(8):082501, 2008. doi:10.1063/1.2838733.
- [291] MPMS Application Note 1014-210 Oxygen contamination, 1997.
- [292] R. J. Meier, C. J. Schinkel, and A. De Visser. Magnetisation of condensed oxygen under high pressures and in strong magnetic fields. *J. Phys. C Solid State Phys.*, 15(5):1015, 1982.
- [293] J. Barzola-Quiquia, P. Esquinazi, M. Lindel, D. Spemann, M. Muallem, and G. Nessim. Magnetic order and superconductivity observed in

- bundles of double-wall carbon nanotubes. *Carbon*, 88:16–25, 2015. doi:10.1016/j.carbon.2015.02.062.
- [294] A. Sadoc, B. Mercey, C. Simon, D. Grebille, W. Prellier, and M.-B. Lepetit. Large Increase of the Curie Temperature by Orbital Ordering Control. *Phys. Rev. Lett.*, 104(4), 2010. doi:10.1103/PhysRevLett.104.046804.
- [295] H. Boschker, J. Kautz, E. P. Houwman, W. Siemons, D. H. A. Blank, M. Huijben, G. Koster, A. Vailionis, and G. Rijnders. High-Temperature Magnetic Insulating Phase in Ultrathin $\text{La}_{0.67}\text{Sr}_{0.33}\text{MnO}_3$ Films. *Phys. Rev. Lett.*, 109(15), 2012. doi:10.1103/PhysRevLett.109.157207.
- [296] M. Khalid, A. Setzer, M. Ziese, P. Esquinazi, D. Spemann, A. Pöpl, and E. Goering. Ubiquity of ferromagnetic signals in common diamagnetic oxide crystals. *Phys. Rev. B*, 81(21), 2010. doi:10.1103/PhysRevB.81.214414.
- [297] C. Zandalazini, P. Esquinazi, G. Bridoux, J. Barzola-Quiquia, H. Ohldag, and E. Arenholz. Uncompensated magnetization and exchange-bias field in $\text{La}_{0.7}\text{Sr}_{0.3}\text{MnO}_3/\text{YMnO}_3$ bilayers: The influence of the ferromagnetic layer. *J. Magn. Magn. Mater.*, 323(22):2892–2898, 2011. doi:10.1016/j.jmmm.2011.06.053.
- [298] V. Wood, E. Austin, E. Collings, and K. Brog. Magnetic properties of heavy-rare-earth orthomanganites. *J. Phys. Chem. Solids*, 34:859–868, 1973.
- [299] X. Marti, V. Skumryev, A. Cattoni, R. Bertacco, V. Laukhin, C. Ferrater, M. García-Cuenca, M. Varela, F. Sánchez, and J. Fontcuberta. Ferromagnetism in epitaxial orthorhombic YMnO_3 thin films. *J. Magn. Magn. Mater.*, 321(11):1719–1722, 2009. doi:10.1016/j.jmmm.2009.02.025.
- [300] M. Nakamura, Y. Tokunaga, M. Kawasaki, and Y. Tokura. Multiferroicity in an orthorhombic YMnO_3 single-crystal film. *Appl. Phys. Lett.*, 98(8):082902, 2011. doi:10.1063/1.3555462.
- [301] A. Bosak, C. Dubourdieu, M. Audier, J. Sénateur, and J. Pierre. Compositional effects on the structure and magnetotransport properties of lacunar $\text{La}_{1-x}\text{MnO}_{3-\delta}$ films ($x>0$) grown by MOCVD. *Appl. Phys. A*, 79(8):1979–1984, 2004. doi:10.1007/s00339-003-2179-4.
- [302] T. Higuchi, T. Yajima, L. F. Kourkoutis, Y. Hikita, N. Nakagawa, D. A. Muller, and H. Y. Hwang. Mn_3O_4 precipitates in laser-ablated manganite films. *Appl. Phys. Lett.*, 95(4):043112, 2009. doi:10.1063/1.3193667.
- [303] A. Pomar, Z. Konstantinović, N. Bagués, J. Roqueta, L. López-Mir, L. Balcells, C. Frontera, N. Mestres, A. Gutiérrez-Llorente, M. Šćepanović, N.

- Lazarević, Z. V. Popović, F. Sandiumenge, B. Martínez, and J. Santiso. Formation of Self-Organized Mn_3O_4 Nano-inclusions in LaMnO_3 Films. *Front. Phys.*, 4, 2016. doi:10.3389/fphy.2016.00041.
- [304] W. S. Seo, H. H. Jo, K. Lee, B. Kim, S. J. Oh, and J. T. Park. Size-Dependent Magnetic Properties of Colloidal Mn_3O_4 and MnO Nanoparticles. *Angew. Chem. Int. Ed.*, 43(9):1115–1117, 2004. doi:10.1002/anie.200352400.
- [305] S. Fritsch and A. Navrotsky. Thermodynamic Properties of Manganese Oxides. *J. Am. Ceram. Soc.*, 79(7):1761, 1996.
- [306] T. R. McGuire and R. Potter. Anisotropic Magnetoresistance in Ferromagnetic 3d Alloys. *IEEE Trans. Magn.*, MAG-11(4):1018, 1975.
- [307] P. K. Muduli, K.-J. Friedland, J. Herfort, H.-P. Schönherr, and K. H. Ploog. Antisymmetric contribution to the planar Hall effect of Fe_3Si films grown on GaAs (113) A substrates. *Phys. Rev. B*, 72(10), 2005. doi:10.1103/PhysRevB.72.104430.
- [308] W. Limmer, M. Glunk, J. Daeubler, T. Hummel, W. Schoch, R. Sauer, C. Bihler, H. Huebl, M. S. Brandt, and S. T. B. Goennenwein. Angle-dependent magnetotransport in cubic and tetragonal ferromagnets: Application to (001)- and (113) A-oriented (Ga, Mn)As. *Phys. Rev. B*, 74(20), 2006. doi:10.1103/PhysRevB.74.205205.
- [309] W. Limmer, J. Daeubler, L. Dreher, M. Glunk, W. Schoch, S. Schwaiger, and R. Sauer. Advanced resistivity model for arbitrary magnetization orientation applied to a series of compressive- to tensile-strained (Ga, Mn) As layers. *Phys. Rev. B*, 77(20), 2008. doi:10.1103/PhysRevB.77.205210.
- [310] M. Glunk, J. Daeubler, W. Schoch, R. Sauer, and W. Limmer. Scaling relation of the anomalous Hall effect in (Ga,Mn)As. *Phys. Rev. B*, 80(12), 2009. doi:10.1103/PhysRevB.80.125204.
- [311] M. Glunk, J. Daeubler, L. Dreher, S. Schwaiger, W. Schoch, R. Sauer, W. Limmer, A. Brandlmaier, S. T. B. Goennenwein, C. Bihler, and M. S. Brandt. Magnetic anisotropy in (Ga,Mn)As: Influence of epitaxial strain and hole concentration. *Phys. Rev. B*, 79(19), 2009. doi:10.1103/PhysRevB.79.195206.
- [312] L. Dreher, D. Donhauser, J. Daeubler, M. Glunk, C. Rapp, W. Schoch, R. Sauer, and W. Limmer. Strain, magnetic anisotropy, and anisotropic magnetoresistance in (Ga, Mn)As on high-index substrates: Application to (113) A-oriented layers. *Phys. Rev. B*, 81(24), 2010. doi:10.1103/PhysRevB.81.245202.
- [313] Y. C. Akgoz and G. A. Saunders. Space-time symmetry restrictions on the form of transport tensors. II. Thermomagnetic effects. *J. Phys. C Solid State Phys.*, 8(18):2962, 1975.

- [314] Y. C. Akgoz and G. A. Saunders. Space-time symmetry restrictions on the form of transport tensors. I. Galvanomagnetic effects. *J. Phys. C Solid State Phys.*, 8(9):1387, 1975.
- [315] R. Becker and W. Döring. *Ferromagnetismus*. Julius Springer Verlag, Berlin, 1939. ISBN 978-3-642-47112-4.
- [316] H. Bethe. Termaufspaltung in Kristallen. *Ann. Phys.*, 395(2):133–208, 1929.
- [317] W. Heisenberg. Zur Theorie der Magnetostriktion und der Magnetisierungskurve. *Z. Für Phys.*, 69(5):287, 1931. doi:10.1007/BF01391350.
- [318] R. Gans and J. von Harlem. Widerstandsänderung ferromagnetischer Kristalle. *Ann. Phys.*, 407(5):516–526, 1932. doi:10.1002/andp.19324070503.
- [319] W. Döring and G. Simon. Die Richtungsabhängigkeit der Magnetostriktion. *Ann. Phys.*, 460(7-8):373–387, 1960.
- [320] J. Patera, R. T. Sharp, and P. Winternitz. Polynomial irreducible tensors for point groups. *J. Math. Phys.*, 19(11):2362, 1978. doi:10.1063/1.523595.
- [321] E. Ascher and D. Gay. Relative invariants of crystallographic point groups. *J. Phys. Math. Gen.*, 18:397, 1985. doi:https://doi.org/10.1088/0305-4470/18/3/016.
- [322] L. Onsager. Reciprocal relations in irreversible processes. I. *Phys. Rev.*, 37: 405, 1931.
- [323] L. Onsager. Reciprocal relations in irreversible processes. II. *Phys. Rev.*, 38: 2265, 1931.
- [324] R. Fieschi, S. R. De Groot, and P. Mazur. Thermodynamical theory of galvanomagnetic and thermomagnetic phenomena. I: Reciprocal relations in anisotropic metals. *Physica*, 20(1):67–76, 1954.
- [325] M. N. Iliev, A. P. Litvinchuk, H.-G. Lee, C. L. Chen, M. L. Dezaneti, C. W. Chu, V. G. Ivanov, M. V. Abrashev, and V. N. Popov. Raman spectroscopy of SrRuO₃ near the paramagnetic-to-ferromagnetic phase transition. *Phys. Rev. B*, 59(1):364, 1999.
- [326] F. Bern, M. Ziese, A. Setzer, E. Pippel, D. Hesse, and I. Vrejoiu. Structural, magnetic and electrical properties of SrRuO₃ films and SrRuO₃ /SrTiO₃ superlattices. *J. Phys. Condens. Matter*, 25(49):496003, 2013. doi:10.1088/0953-8984/25/49/496003.
- [327] A. Herklotz. *Einfluss reversibler epitaktischer Dehnung auf die ferroische Ordnung dünner Schichten*. PhD thesis, IFW Dresden, 2012.

- [328] R. Gao, Y. Dong, H. Xu, H. Zhou, Y. Yuan, V. Gopalan, C. Gao, D. D. Fong, Z. Chen, Z. Luo, and L. W. Martin. Interfacial Octahedral Rotation Mismatch Control of the Symmetry and Properties of SrRuO₃. *ACS Appl. Mater. Interfaces*, 8(23):14871–14878, 2016. doi:10.1021/acsami.6b02864.
- [329] M. Schultz, S. Levy, J. W. Reiner, and L. Klein. Magnetic and transport properties of epitaxial films of SrRuO₃ in the ultrathin limit. *Phys. Rev. B*, 79(12):125444, 2009. doi:10.1103/PhysRevB.79.125444.
- [330] S. Kolesnik, Y. Z. Yoo, O. Chmaissem, B. Dabrowski, T. Maxwell, C. W. Kimball, and A. P. Genis. Effect of crystalline quality and substitution on magnetic anisotropy of SrRuO₃ thin films. *J. Appl. Phys.*, 99(8):08F501, 2006. doi:10.1063/1.2165132.
- [331] M. Ziese, H. C. Semmelhack, and P. Busch. Sign reversal of the anisotropy in La_{0.7}A_{0.3}MnO₃ (A=Ca, Sr, Ba, □) films. *J. Magn. Magn. Mater.*, 246:327, 2002.
- [332] S. Yamanaka, T. Maekawa, H. Muta, T. Matsuda, S.-i. Kobayashi, and K. Kurosaki. Thermophysical properties of SrHfO₃ and SrRuO₃. *J. Solid State Chem.*, 177(10):3484–3489, 2004. doi:10.1016/j.jssc.2004.05.039.
- [333] B. Dabrowski, M. Avdeev, O. Chmaissem, S. Kolesnik, P. W. Klamut, M. Maxwell, and J. D. Jorgensen. Freezing of octahedral tilts below the Curie temperature in SrRu_{1-x}O₃ perovskites. *Phys. Rev. B*, 71(10), 2005. doi:10.1103/PhysRevB.71.104411.
- [334] K. Ishigami, K. Yoshimatsu, D. Toyota, M. Takizawa, T. Yoshida, G. Shibata, T. Harano, Y. Takahashi, T. Kadono, V. K. Verma, V. R. Singh, Y. Takeda, T. Okane, Y. Saitoh, H. Yamagami, T. Koide, M. Oshima, H. Kumigashira, and A. Fujimori. Thickness-dependent magnetic properties and strain-induced orbital magnetic moment in SrRuO₃ thin films. *Phys. Rev. B*, 92(6), 2015. doi:10.1103/PhysRevB.92.064402.
- [335] J. Matsuno, N. Ogawa, K. Yasuda, F. Kagawa, W. Koshibae, N. Nagao, Y. Tokura, and M. Kawasaki. Interface-driven topological Hall effect in SrRuO₃-SrIrO₃ bilayer. *Sci. Adv.*, 2(7):e1600304–e1600304, 2016. doi:10.1126/sciadv.1600304.
- [336] M. Verissimo-Alves, P. García-Fernández, D. I. Bilc, P. Ghosez, and J. Junquera. Highly Confined Spin-Polarized Two-Dimensional Electron Gas in SrTiO₃/SrRuO₃ Superlattices. *Phys. Rev. Lett.*, 108(10), 2012. doi:10.1103/PhysRevLett.108.107003.

- [337] P. García-Fernández, M. Verissimo-Alves, D. I. Bilc, P. Ghosez, and J. Junquera. First-principles modeling of the thermoelectric properties of $\text{SrTiO}_3/\text{SrRuO}_3$ superlattices. *Phys. Rev. B*, 86(8), 2012. doi:10.1103/PhysRevB.86.085305.
- [338] R. Aso, D. Kan, Y. Fujiyoshi, Y. Shimakawa, and H. Kurata. Strong Dependence of Oxygen Octahedral Distortions in SrRuO_3 Films on Types of Substrate-Induced Epitaxial Strain. *Cryst. Growth Des.*, 14(12):6478–6485, 2014. doi:10.1021/cg501340e.
- [339] D. Kan, R. Aso, H. Kurata, and Y. Shimakawa. Epitaxial strain effect in tetragonal SrRuO_3 thin films. *J. Appl. Phys.*, 113(17):173912, 2013. doi:10.1063/1.4803869.
- [340] R. B. Griffiths. Nonanalytic behavior above the critical point in a random Ising ferromagnet. *Phys. Rev. Lett.*, 23(1):17, 1969.
- [341] A. J. Bray. Nature of the Griffiths phase. *Phys. Rev. Lett.*, 59(5):586, 1987.
- [342] J. Kim, J.-Y. Kim, B.-G. Park, and S.-J. Oh. Photoemission and x-ray absorption study of the electronic structure of $\text{SrRu}_{1-x}\text{Ti}_x\text{O}_3$. *Phys. Rev. B*, 73(23), 2006. doi:10.1103/PhysRevB.73.235109.
- [343] F. Huang, M. T. Kief, G. J. Mankey, and R. F. Willis. Magnetism in the few-monolayers limit: A surface magneto-optic Kerr-effect study of the magnetic behavior of ultrathin films of Co, Ni, and Co-Ni alloys on Cu (100) and Cu (111). *Phys. Rev. B*, 49(6):3962, 1994.
- [344] A. Galdi, P. Orgiani, L. Maritato, and L. Méchin. Correlation between structural properties and resistivity critical behavior in SrRuO_3 thin films. *J. Phys. Condens. Matter*, 24(43):435603, 2012. doi:10.1088/0953-8984/24/43/435603.
- [345] Y. Konishi, Z. Fang, M. Izumi, T. Manako, M. Kasai, H. Kuwahara, M. Kawasaki, K. Terakura, and Y. Tokura. Orbital-state-mediated phase-control of manganites. *J. Phys. Soc. Jpn.*, 68(12):3790–3793, 1999.
- [346] Z. Fang, I. V. Solovyev, and K. Terakura. Phase diagram of tetragonal manganites. *Phys. Rev. Lett.*, 84(14):3169, 2000.
- [347] A. Tebano, C. Aruta, P. G. Medaglia, F. Tozzi, G. Balestrino, A. A. Sidorenko, G. Allodi, R. De Renzi, G. Ghiringhelli, C. Dallera, L. Braicovich, and N. B. Brookes. Strain-induced phase separation in $\text{La}_{0.7}\text{Sr}_{0.3}\text{MnO}_3$ thin films. *Phys. Rev. B*, 74(24), 2006. doi:10.1103/PhysRevB.74.245116.
- [348] P. Orgiani, A. Y. Petrov, R. Ciancio, A. Galdi, L. Maritato, and B. A. Davidson. Evidence of direct correlation between out-of-plane lattice parameter

- and metal-insulator transition temperature in oxygen-depleted manganite thin films. *Appl. Phys. Lett.*, 100(4):042404, 2012. doi:10.1063/1.3676268.
- [349] M.-H. Jo, N. D. Mathur, N. K. Todd, and M. G. Blamire. Very large magnetoresistance and coherent switching in half-metallic manganite tunnel junctions. *Phys. Rev. B*, 61(22):R14905, 2000.
- [350] M. Bibes, L. Balcells, S. Valencia, J. Fontcuberta, M. Wojcik, E. Jedryka, and S. Nadolski. Nanoscale Multiphase Separation at $\text{La}_{2/3}\text{Ca}_{1/3}\text{MnO}_3/\text{SrTiO}_3$ Interfaces. *Phys. Rev. Lett.*, 87(6), 2001. doi:10.1103/PhysRevLett.87.067210.
- [351] S. Brivio, C. Magen, A. A. Sidorenko, D. Petti, M. Cantoni, M. Finazzi, F. Ciccacci, R. De Renzi, M. Varela, S. Picozzi, and R. Bertacco. Effects of Au nanoparticles on the magnetic and transport properties of $\text{La}_{0.67}\text{Sr}_{0.33}\text{MnO}_3$ ultrathin layers. *Phys. Rev. B*, 81(9), 2010. doi:10.1103/PhysRevB.81.094410.
- [352] R. Peng, H. C. Xu, M. Xia, J. F. Zhao, X. Xie, D. F. Xu, B. P. Xie, and D. L. Feng. Tuning the dead-layer behavior of $\text{La}_{0.67}\text{Sr}_{0.33}\text{MnO}_3/\text{SrTiO}_3$ via interfacial engineering. *Appl. Phys. Lett.*, 104(8):081606, 2014. doi:10.1063/1.4866461.
- [353] D. Preziosi, I. Fina, E. Pippel, D. Hesse, X. Marti, F. Bern, M. Ziese, and M. Alexe. Tailoring the interfacial magnetic anisotropy in multiferroic field-effect devices. *Phys. Rev. B*, 90(12):125155, 2014. doi:10.1103/PhysRevB.90.125155.
- [354] M. Ziese, F. Bern, E. Pippel, D. Hesse, and I. Vrejoiu. Stabilization of Ferromagnetic Order in $\text{La}_{0.7}\text{Sr}_{0.3}\text{MnO}_3\text{--SrRuO}_3$ Superlattices. *Nano Lett.*, 12(8):4276–4281, 2012. doi:10.1021/nl301963a.
- [355] S. Tripathi, R. Rana, S. Kumar, P. Pandey, R. S. Singh, and D. S. Rana. Ferromagnetic CaRuO_3 . *Sci. Rep.*, 4(1):3877, 2015. doi:10.1038/srep03877.
- [356] T. Zhu, B. G. Shen, J. R. Sun, H. W. Zhao, and W. S. Zhan. Surface spin-glass behavior in $\text{La}_{1-x}\text{Sr}_x\text{MnO}_3$ nanoparticles. *Appl. Phys. Lett.*, 78(24):3863, 2001. doi:10.1063/1.1379597.
- [357] Y. Kumar, F. Bern, J. Barzola-Quiquia, I. Lorite, and P. Esquinazi. Study of non-linear Hall effect in nitrogen-grown ZnO microstructure and the effect of H^+ -implantation. *Appl. Phys. Lett.*, 107(2):022403, 2015. doi:10.1063/1.4926856.
- [358] J. Ye, Y. B. Kim, A. J. Millis, B. I. Shraiman, P. Majumdar, and Z. Tešanović. Berry phase theory of the anomalous Hall effect: Application to colossal magnetoresistance manganites. *Phys. Rev. Lett.*, 83(18):3737, 1999.

- [359] P. Matl, N. P. Ong, Y. Yan, Y. Li, D. Studebaker, T. Baum, and G. Doubinina. Hall effect of the colossal magnetoresistance manganite $\text{La}_{1-x}\text{Ca}_x\text{MnO}_3$. *Phys. Rev. B*, 57:10248, 1998.
- [360] F. Bern, M. Ziese, I. Vrejoiu, X. Li, and P. A. van Aken. Magnetic and magnetotransport properties of ultrathin $\text{La}_{0.7}\text{Ba}_{0.3}\text{MnO}_3$ epitaxial films embedded in SrRuO_3 . *New J. Phys.*, 18(5):053021, 2016. doi:10.1088/1367-2630/18/5/053021.
- [361] L. Pi, S. Hébert, C. Martin, A. Maignan, and B. Raveau. Comparison of $\text{CaMn}_{1-x}\text{Ru}_x\text{O}_3$ and $\text{CaMn}_{1-y}\text{Mo}_y\text{O}_3$ perovskites. *Phys. Rev. B*, 67(2), 2003. doi:10.1103/PhysRevB.67.024430.
- [362] A. Maignan, C. Martin, M. Hervieu, B. Raveau, and J. Hejtmanek. Probing the underlying charge ordering: Ruthenium-doped $\text{Sm}_{1-x}\text{Sr}_x\text{MnO}_3$ perovskite manganites. *J. Appl. Phys.*, 89(4):2232–2236, 2001. doi:10.1063/1.1342188.
- [363] B. Raveau, S. Hébert, A. Maignan, R. Frésard, M. Hervieu, and D. Khomskii. Rhodium doped manganites: Ferromagnetism and metallicity. *J. Appl. Phys.*, 90(3):1297–1302, 2001. doi:10.1063/1.1380412.
- [364] M. Ziese. Magnetocrystalline anisotropy transition in $\text{La}_{0.7}\text{Sr}_{0.3}\text{MnO}_3$ films. *Phys. Status Solidi B*, 242(13):R116–R117, 2005. doi:10.1002/pssb.200541266.
- [365] J. Stöhr. Exploring the microscopic origin of magnetic anisotropies with X-ray magnetic circular dichroism (XMCD) spectroscopy. *J. Magn. Magn. Mater.*, 200:470, 1999.
- [366] B. T. Thole, P. Carra, F. Sette, and G. van der Laan. X-ray circular dichroism as a probe of orbital magnetization. *Phys. Rev. Lett.*, 68(12):1943, 1992.
- [367] P. Carra, B. T. Thole, M. Altarelli, and X. Wang. X-ray circular dichroism and local magnetic fields. *Phys. Rev. Lett.*, 70:694, 1993.
- [368] C. Piamonteze, P. Miedema, and F. M. F. de Groot. Accuracy of the spin sum rule in XMCD for the transition-metal L edges from manganese to copper. *Phys. Rev. B*, 80(18), 2009. doi:10.1103/PhysRevB.80.184410.
- [369] K. Kuepper, M. Raekers, C. Taubitz, M. Uhlarz, C. Piamonteze, F. M. F. de Groot, E. Arenholz, V. R. Galakhov, Y. M. Mukovskii, and M. Neumann. The x-ray magnetic circular dichroism spin sum rule for $3d^4$ systems: Mn^{3+} ions in colossal magnetoresistance manganites. *J. Phys. Condens. Matter*, 24(43):435602, 2012. doi:10.1088/0953-8984/24/43/435602.
- [370] C. Piamonteze, U. Flechsig, S. Rusponi, J. Dreiser, J. Heidler, M. Schmidt, R. Wetter, M. Calvi, T. Schmidt, H. Pruchova, J. Krempasky, C. Quitmann, H. Brune, and F. Nolting. X-Treme beamline at SLS: X-ray magnetic circular and

- linear dichroism at high field and low temperature. *J. Synchrotron Radiat.*, 19(5):661–674, 2012. doi:10.1107/S0909049512027847.
- [371] J. Okamoto, T. Okane, Y. Saitoh, K. Terai, S.-I. Fujimori, Y. Muramatsu, K. Yoshii, K. Mamiya, T. Koide, A. Fujimori, Z. Fang, Y. Takeda, and M. Takano. Soft x-ray magnetic circular dichroism study of $\text{Ca}_{1-x}\text{Sr}_x\text{RuO}_3$ across the ferromagnetic quantum phase transition. *Phys. Rev. B*, 76(18), 2007. doi:10.1103/PhysRevB.76.184441.
- [372] I. Dzyaloshinsky. A thermodynamic theory of “weak” ferromagnetism of antiferromagnetics. *J. Phys. Chem. Solids*, 4(4):241–255, 1958.
- [373] T. Moriya. New mechanism of anisotropic superexchange interaction. *Phys. Rev. Lett.*, 4(5):228, 1960.
- [374] F. W. Olver, D. W. Lozier, R. F. Boisvert, and C. W. Clark. *NIST Handbook of Mathematical Functions*. Cambridge University Press, New York, 2010. ISBN 978-0-521-14063-8.
- [375] W. P. Calixto, B. Alvarenga, J. C. da Mota, L. d. C. Brito, M. Wu, A. J. Alves, L. M. Neto, and C. F. R. L. Antunes. Electromagnetic problems solving by conformal mapping: A mathematical operator for optimization. *Math. Probl. Eng.*, 2010:1–19, 2010. doi:10.1155/2010/742039.
- [376] M. Suzuki and H. Katsui. Method for measuring anisotropic electrical resistivity. *Jpn. J. Appl. Phys.*, 51:123102, 2012. doi:10.1143/JJAP.51.123102.

Own and Contributed Publications

- [1] F. Bern, M. Ziese, I. Vrejoiu, X. Li, and P. A. van Aken. Magnetic and magnetotransport properties of ultrathin $\text{La}_{0.7}\text{Ba}_{0.3}\text{MnO}_3$ epitaxial films embedded in SrRuO_3 . *New J. Phys.*, 18(5):053021, 2016. doi:10.1088/1367-2630/18/5/053021.
- [2] I. Razdolski, R. R. Subkhangulov, D. G. Gheorghe, F. Bern, I. Vrejoiu, A. V. Kimel, A. Kirilyuk, M. Ziese, and T. Rasing. Laser-induced magnetisation dynamics in $\text{La}_{0.7}\text{Sr}_{0.3}\text{MnO}_3/\text{SrRuO}_3$ superlattices. *Phys. Status Solidi RRL - Rapid Res. Lett.*, 9(10):583–588, 2015. doi:10.1002/pssr.201510272.
- [3] Y. Kumar, F. Bern, J. Barzola-Quiquia, I. Lorite, and P. Esquinazi. Study of non-linear Hall effect in nitrogen-grown ZnO microstructure and the effect of H⁺-implantation. *Appl. Phys. Lett.*, 107(2):022403, 2015. doi:10.1063/1.4926856.
- [4] D. Preziosi, I. Fina, E. Pippel, D. Hesse, X. Marti, F. Bern, M. Ziese, and M. Alexe. Tailoring the interfacial magnetic anisotropy in multiferroic field-effect devices. *Phys. Rev. B*, 90(12):125155, 2014. doi:10.1103/PhysRevB.90.125155.
- [5] A. Paul, C. Reitinger, C. Autieri, B. Sanyal, W. Kreuzpaintner, J. Jutimoosik, R. Yimnirun, F. Bern, P. Esquinazi, P. Korelis, and P. Böni. Exotic exchange bias at epitaxial ferroelectric-ferromagnetic interfaces. *Appl. Phys. Lett.*, 105(2):022409, 2014. doi:10.1063/1.4885316.
- [6] A. Ballestar, P. Esquinazi, J. Barzola-Quiquia, S. Dusari, F. Bern, R. da Silva, and Y. Kopelevich. Possible superconductivity in multi-layer-graphene by application of a gate voltage. *Carbon*, 72:312–320, 2014. doi:10.1016/j.carbon.2014.02.011.
- [7] M. Lorenz, V. Lazenka, P. Schwinkendorf, F. Bern, M. Ziese, H. Modarresi, A. Volodin, M. J. Van Bael, K. Temst, A. Vantomme, and M. Grundmann. Multiferroic BaTiO_3 – BiFeO_3 composite thin films and multilayers: Strain engineering and magnetoelectric coupling. *J. Phys. Appl. Phys.*, 47(13):135303, 2014. doi:10.1088/0022-3727/47/13/135303.
- [8] G. Grinblat, F. Bern, J. Barzola-Quiquia, M. Tirado, D. Comedi, and P. Esquinazi. Luminescence and electrical properties of single ZnO/MgO core/shell nanowires. *Appl. Phys. Lett.*, 104(10):103113, 2014. doi:10.1063/1.4868648.
- [9] J. Gräfe, M. Welke, F. Bern, M. Ziese, and R. Denecke. Magnetoelastic coupling in epitaxial cobalt ferrite/barium titanate heterostructures. *J. Magn. Magn. Mater.*, 339:84–88, 2013. doi:10.1016/j.jmmm.2013.02.046.
- [10] F. Bern, M. Ziese, K. Dörr, A. Herklotz, and I. Vrejoiu. Hall effect of tetragonal and orthorhombic SrRuO_3 films. *Phys. Status Solidi RRL - Rapid Res. Lett.*, 7(3): 204–206, 2013. doi:10.1002/pssr.201206500.
- [11] F. Bern, M. Ziese, A. Setzer, E. Pippel, D. Hesse, and I. Vrejoiu. Structural, magnetic and electrical properties of SrRuO_3 films and $\text{SrRuO}_3/\text{SrTiO}_3$ superlattices. *J. Phys. Condens. Matter*, 25(49):496003, 2013. doi:10.1088/0953-8984/25/49/496003.

- [12] F. Bern and M. Ziese. Magnetotransport and Hall effect studies of $\text{SrRuO}_3/\text{SrTiO}_3$ superlattices. *EPJ Web Conf.*, 40:15013, 2013. doi:10.1051/epjconf/20134015013.
- [13] M. Ziese, F. Bern, and I. Vrejoiu. Exchange bias in manganite/ SrRuO_3 superlattices. *J. Appl. Phys.*, 113(6):063911, 2013. doi:10.1063/1.4790877.
- [14] M. Ziese, F. Bern, A. Setzer, E. Pippel, D. Hesse, and I. Vrejoiu. Existence of a magnetically ordered hole gas at the $\text{La}_{0.7}\text{Sr}_{0.3}\text{MnO}_3/\text{SrRuO}_3$ interface. *Eur. Phys. J. B*, 86(2):42, 2013. doi:10.1140/epjb/e2012-30646-4.
- [15] P. K. Muduli, J. Barzola-Quiquia, S. Dusari, A. Ballestar, F. Bern, W. Böhlmann, and P. Esquinazi. Large local Hall effect in pin-hole dominated multigraphene spin-valves. *Nanotechnology*, 24(1):015703, 2013. doi:10.1088/0957-4484/24/1/015703.
- [16] J. Barzola-Quiquia, A. Lessig, A. Ballestar, C. Zandalazini, G. Bridoux, F. Bern, and P. Esquinazi. Revealing the origin of the vertical hysteresis loop shifts in an exchange biased Co/YMnO_3 bilayer. *J. Phys. Condens. Matter*, 24(36):366006, 2012. doi:10.1088/0953-8984/24/36/366006.
- [17] G. Bridoux, J. Barzola-Quiquia, F. Bern, W. Böhlmann, I. Vrejoiu, M. Ziese, and P. Esquinazi. An alternative route towards micro- and nano-patterning of oxide films. *Nanotechnology*, 23(8):085302, 2012. doi:10.1088/0957-4484/23/8/085302.
- [18] M. Ziese, F. Bern, E. Pippel, D. Hesse, and I. Vrejoiu. Stabilization of Ferromagnetic Order in $\text{La}_{0.7}\text{Sr}_{0.3}\text{MnO}_3\text{-SrRuO}_3$ Superlattices. *Nano Lett.*, 12(8):4276–4281, 2012. doi:10.1021/nl301963a.
- [19] N. García, Z. Yan, A. Ballestar, J. Barzola-Quiquia, F. Bern, and P. Esquinazi. Disordered electrical potential observed on the surface of SiO_2 by electric field microscopy. *J. Phys. Condens. Matter*, 22(4):045002, 2010. doi:10.1088/0953-8984/22/4/045002.
- [20] J. Barzola-Quiquia, S. Dusari, G. Bridoux, F. Bern, A. Molle, and P. Esquinazi. The influence of Ga^+ irradiation on the transport properties of mesoscopic conducting thin films. *Nanotechnology*, 21(14):145306, 2010. doi:10.1088/0957-4484/21/14/145306.
- [21] R. P. Borges, M. M. Cruz, R. C. da Silva, F. Bern, P. Venezuela, M. D. Moreira, A. T. Costa, and M. Godinho. Magnetism in wide band gap semiconductors implanted with non-magnetic ions. *J. Phys. Conf. Ser.*, 153:012044, 2009. doi:10.1088/1742-6596/153/1/012044.

Acknowledgements

This page is dedicated to the people who helped me to accomplish this thesis.

First I would like to express my sincere gratitude to my advisor Prof. Dr. Michael Ziese for his collegial collaboration and vast knowledge of literature, almost always having a reference at hand when I came up with a question.

My deepest thanks go also to Dr. Ionela Lindfors-Vrejoiu, who provided the samples studied in this thesis. Her profound understanding of the pulsed laser deposition process allowed her to fabricate single crystalline samples and multilayer structures with minimal interfacial intermixing crucial for the presented study.

Furthermore I would like to thank

- Prof. Dr. D. Hesse and Dr. E. Pippel as well as Prof. P. A. van Aken and Dr. X. Li for high resolution TEM measurements on the samples.
- Dipl.-Kryst. A. Setzer for x-ray diffraction measurements and collaboration in SQUID measurements. Office sharing with her was most appreciable.
- Dr. C. Piamonteze and collaborators from PSI for the help in XMCD measurements.
- Dr. W. Böhlmann for an introduction to the dual beam microscope and advice regarding chemicals.
- Prof. Dr. Pablo Esquinazi for offering the position which allowed the work on this thesis.
- Mr. Schlayer, Mr. Moschkowitz, and Mr. Lenzner for providing liquefied helium for the experiments.
- The Leipzig university library for providing access to so many papers.
- Universität Tübingen for hosting my writing session.
- Mr. Schlueter for establishing a good work environment.
- My fellow colleagues of the sum group, guests, and students for discussions on a variety of subjects in physics.
- My family for their confidence, support and patience.